Virginia Commonwealth University
VCU Scholars Compass

Theses and Dissertations | Graduate School

2020

MODEL-BASED IN-VITRO PK/PD PROFILING OF NOVEL SYNTHETIC ALLOSTERIC EFFECTORS OF HEMOGLOBIN (AEH) AS POTENTIAL SICKLE CELL DISEASE (SCD) THERAPEUTICS

Xiaomeng Xu
VCU, School of Pharmacy

Follow this and additional works at: https://scholarscompass.vcu.edu/etd

Part of the Medicinal Chemistry and Pharmaceutics Commons, Pharmaceutics and Drug Design Commons, and the Pharmacology Commons

© The Author

Downloaded from
https://scholarscompass.vcu.edu/etd/6424

This Dissertation is brought to you for free and open access by the Graduate School at VCU Scholars Compass. It has been accepted for inclusion in Theses and Dissertations by an authorized administrator of VCU Scholars Compass. For more information, please contact libcompass@vcu.edu.

© Xiaomeng Xu 2020

All Rights Reserved

MODEL-BASED *IN-VITRO* PK/PD PROFILING OF NOVEL SYNTHETIC ALLOSTERIC EFFECTORS OF HEMOGLOBIN (AEH) AS POTENTIAL SICKLE CELL DISEASE (SCD) THERAPEUTICS

A Dissertation submitted in partial fulfillment of the requirements for the degree of Doctor of Philosophy at Virginia Commonwealth University

by

XIAOMENG XU

B.S., Pharmacy, Shenyang Pharmaceutical University, China, 2013

M.S., Pharmaceutical Science, University of Pittsburgh, 2015

Major Directors: Jürgen Venitz, M.D., Ph.D., Professor, Department of Pharmaceutics

Martin K. Safo, Ph.D., Professor, Department of Medicinal Chemistry

Virginia Commonwealth University

Richmond, Virginia

August 2020

ACKNOWLEDGEMENTS

First and foremost, I would like to express my deep and sincere gratitude to my advisor and mentor, Dr. Jürgen Venitz, for his dedicated support of my Ph.D. study and research, for his patience, motivations, insights, enthusiasm, empathy, immense knowledge, his philosophy and great sense of humor. His rigorous scientific attitude has inspired me throughout my Ph.D. research. It is a great honor, privilege and enjoyment to study under his guidance.

Sincere thanks also go to my co-advisor, Dr. Martin K. Safo for his patient guidance to my research project and constructive feedback on the writing of this dissertation. Special thanks to Dr. Osheiza Y. Abdulmalik for collaboration on this sickle cell disease project. My completion of this Ph.D. program could not have been accomplished without the continuous support and encouragement from my committee members. I offer my heartfelt appreciation to Dr. Philip Gerk, Dr. Matthew Halquist and Dr. Yan Zhang.

Many thanks to all faculties and staff in School of Pharmacy. Special thanks go to Keyetta, Laura and Sha-kim for their kindly help.

I am grateful to VCU alumni, Bishoy, Mengyao, Vijay, Gopichand, Jocelyn, Angela for their wise career advices. I would like to thank my graduate school friends, Mengyao, Bishoy, Omar, Emmanuel, Zaneera, Palak, Younan, Hanming, Emma, Yuan, Cat and all of others. Many thanks for always being there, helpful and caring for me.

Last but not least, I would like to thank my parents and my elder sister for their love, prayers, caring, understanding and supporting throughout my life.

TABLE OF CONTENT

ACKNOWLEDGEMENTS ..... **iii**

LIST OF TABLES ..... **xi**

LIST OF FIGURES ..... **xiv**

LIST OF ABBREVIATIONS ..... **xx**

ABSTRACT ..... **xxix**

INTRODUCTION **1**

1.1 Sickle Cell Disease (SCD) 1

1.1.1 Prevalence 1

1.1.2 Pathophysiology 2

1.1.3 Clinical Manifestations 4

1.1.4 Hemoglobin (Hb) 6

1.2 Therapeutic Strategies for SCD 7

1.2.1 Hydroxyurea (Pharmacological Reactivation of Hemoglobin F (HbF)) 7

1.2.2 Voxelotor (GBT-440, Anti-Sickling Agent) 10

1.2.3 Crizanlizumab (Anti-Adhesion Agent) 11

1.2.4 L-Glutamine (Modulator of Oxidative Stress) 12

1.2.5 Pain Management (NSAIDs, Opioids) 13

1.2.6 Blood Transfusion 15

1.2.7 Infection Prevention 15

1.3 Allosteric Effectors of Hb (AEH) 16

1.3.1 Mechanism of Action (MOA) of AEH 16

1.3.2 Clinical Findings of Voxelotor (GBT-440) 17

1.3.2.1. Clinical Pharmacokinetics (PK) 18

1.3.2.2. Clinical Pharmacodynamics (PD) 22

1.4 Relevant Metabolic Enzymes 25

1.4.1 Aldehyde Dehydrogenase (ALDH) 25

1.4.2 Other Metabolic Enzymes for Aldehydes 26

1.4.3 Cytochrome P450 (CYP450) 28

HYPOTHESES, SPECIFIC AIMS, AND SIGNICANCE 32

2.1. Hypotheses 32

2.2. Specific Aims 33

2.3. Significance 35

***IN-VITRO* SS CONCENTRATION- AND TIME-DEPENDENCY OF HBA-AEH ADDUCT FORMATION IN HBA SOLUTION 38**

3.1 Introduction 38

3.2 Methods 45

3.2.1 Materials and Reagents 45

3.2.2 Equipment 47

3.2.3 Preparation of Solutions 49

3.2.4 Sample Preparation and Experimental Design 51

3.2.4.1 Sample Preparation 51

3.2.4.2 Pilot Experimental Design for SS Concentration- and Time-Dependency of HbA-AEH Adduct Formation in HbA Solution 51

3.2.4.3 Definitive Experimental Design for SS Concentration- and Time-Dependency of HbA-AEH adduct Formation in HbA Solution 52

3.2.5 HPLC-UV/Vis Conditions 56

3.2.6 Partial Validation of HPLC-UV/Vis Assay Method 57

3.2.6.1 Selectivity and Representative Chromatograms 57

3.2.6.2 UV Spectra of HbA and HbA-AEH Adduct 57

3.2.6.3 Linearity 58

3.2.6.4 Mass Balance 58

3.2.6.5 Comparison to the Reference Assay Method using 5-HMF 58

3.2.7 Data Analysis and Modeling 59

3.2.7.1. Data Analysis 59

3.2.7.2. Modeling of SS Concentration-Dependency of HbA-AEH Adduct Formation and HbA Loss 60

3.2.7.3. Modeling of Time-dependency of HbA-AEH Adduct Formation 62

3.2.7.4. Sensitivity Analysis for the Simple Kinetic Binding Model 64

3.3 Results 66

3.3.1. Partial Validation of HPLC-UV/Vis Assay Method 66

3.3.1.1. Selectivity and Representative Chromatograms 66

3.3.1.2. UV Spectra of HbA and HbA-AEH Adduct 66

3.3.1.3. Linearity 70

3.3.1.4. Mass Balance 71

3.3.1.5. Comparison to the Previous Reference Assay Method using 5-HMF . 74

3.3.2. Sensitivity Analysis for the Simple Kinetic Binding Model..... 75

3.3.3. Pilot Study of SS Concentration- and Time-Dependency of HbA-AEH Adduct in Formation HbA Solution 82

3.3.4. Definitive Study of SS Concentration- and Time-Dependency of HbA-AEH Adduct Formation in HbA Solution 89

3.3.4.1 Definitive Study of SS Concentration-Dependency of HbA-AEH Adduct Formation in HbA solution 89

3.3.4.2 Definitive Study of Time-dependency of HbA-AEH adduct Formation in HbA Solution..... 95

3.4 Discussion and Conclusions 104

***IN-VITRO* METABOLISM OF AEH IN HUMAN LIVER CYTOSOL (HLC)..... 110**

4.1. Introduction 110

4.2. Methods 115

4.2.1. Materials and Reagents..... 115

4.2.2. Equipment 117

4.2.3. Sample Preparation and Experimental Design 118

4.2.4. UV/Vis Spectrophotometric (Warburg) Measurement Procedure 120

4.2.5. Validation of ALDH and ADH Activity in HLC 121

4.2.6. Optimization of Experimental Conditions 121

4.2.7. Oxidative and Reductive Metabolism of AEH in HLC 122

4.3. Results 124

4.3.1. Calibration of UV/Vis Spectrophotometer 124

4.3.2. Selectivity of Assay Technique 126

4.3.3. Optimization of Experimental Conditions 128

4.3.4. Validation of ALDH and ADH Activity 129

4.3.5. Oxidative Metabolism of AEH in HLC 133

4.3.6. Reductive Metabolism of AEH in HLC 137

4.4. Discussion and Conclusions 140

***IN-VITRO* DISPOSITION OF VZHE-039 AND 5-HMF IN WB 148**

5.1 Introduction 148

5.2 Methods 153

5.2.1. Materials and Reagents 153

5.2.2. Equipment 154

5.2.3. Preparation of Solutions 156

5.2.4. Experimental Design 158

5.2.4.1. HbA-AEH Adduct Quantification in WB 158

5.2.4.2. VZHE-039 Quantification in Plasma 159

5.2.5. HPLC-UV/Vis Conditions 160

5.2.5.1. HbA-AEH Adduct Quantification in WB 160

5.2.5.2. VZHE-039 Quantification in Plasma 160

5.2.6. Partial Validation of HPLC-UV/Vis Assay Methods 163

5.2.6.1 HbA-AEH Adduct Quantification in WB 163

5.2.6.2 VZHE-039 Quantification in Plasma 163

5.2.7. Data Analysis and Modeling 165

5.2.7.1 Non-compartmental analysis (NCA) of c_p -t and HbA-AEH adduct – t profiles for VZHE-039 and 5-HMF 165

5.2.7.2 Modeling of SS Concentration-Dependency of HbA-AEH Adduct Profiles for VZHE-039 and 5-HMF 167

5.2.7.3 Modeling of Time-Dependency of HbA-AEH Adduct Profiles for VZHE-039 167

5.2.7.4 Modeling of Time-dependency of HbA-AEH Adduct Profiles for 5-HMF 171

5.3 Results 176

5.3.1 Partial Validation of HPLC-UV/Vis Assay Methods 176

5.3.1.1 HbA-AEH Adduct Quantification in WB 176

5.3.1.2 VZHE-039 Quantification in Plasma 184

5.3.2 WB disposition of VZHE-039 189

5.3.2.1 NCA Analysis of c_p – t Profile 189

5.3.2.2 SS Concentration- and Time- Dependency of HbA-AEH Adduct Formation in WB 193

5.3.2.3 Disposition of VZHE-039 between Plasma and RBC 204

5.3.3 WB Disposition of 5-HMF 208

5.3.3.1 NCA Analysis of HbA-AEH adduct – t Profile 208

5.3.3.2 Apparent SS Concentration- and Time-dependency of HbA-AEH Adduct Formation in WB 210

5.4 Discussion and Conclusions 229

OVERALL CONCLUSIONS AND FUTURE DIRECTIONS 233

LIST OF REFERENCES 254

APPENDIX A 268

APPENDIX B 272

APPENDIX C 307

APPENDIX D 316

VITA 324

LIST OF TABLES

Table: **Page:**

Table 1.1. Classification of CYP450 based on major substrate class..... 31

Table 1.2. Functions of CYP450 gene families. 31

Table 3.1. Definitive experimental design for SS concentration- and time-dependency of HbA-AEH adduct formation in HbA solution. 55

Table 3.2. HPLC conditions for HbA and HbA-AEH adduct quantification in HbA solution. 56

Table 3.3. Comparison of the final parameter estimates of SS concentration-dependency of HbA-AEH adduct formation for 5-HMF by the sigmoidal B_{max}-model, using two different HPLC-UV/Vis assay methods. 74

Table 3.4. Assessment of outcome metrics from sensitivity analysis for the simple kinetic binding model.…..... 77

Table 3.5. Comparison of the final parameter estimates of SS concentration-dependency of HbA-AEH adduct formation for 5-HMF, TD-7, and VZHE-039, using the sigmoidal B_{max}-model and hyperbolic B_{max}-model. 83

Table 3.6. Final parameter estimates of SS concentration-dependency of HbA-AEH adduct formation in HbA solution using sigmoidal B_{max}-model. 91

Table 3.7. Final parameter estimates of time -dependency of HbA-AEH adduct formation in HbA solution, using the simple kinetic binding model. 96

Table 3.8. Comparison of the final K_D and $K_D^{kinetic}$ estimates from SS concentration- and time-dependency of HbA-AEH adduct formation in HbA solution, using sigmoidal B_{max}-model and simple kinetic binding model, respectively. 97

Table 4.1. Molar absorptivity of AEH at λ of 340 nm. 127

Table 4.2. Final parameter estimates of oxidative metabolism of AEH as well as acetaldehyde and ethanol (prototypical substrates of ALDH and ADH enzyme) in HLC, using linear regression for AEH and modified MM model. 136

Table 4.3. Final parameter estimates of reductive metabolism of AEH in HLC, using the modified MM model. 139

Table 5.1. HPLC conditions for HbA and HbA-AEH adduct quantification in WB. 161

Table 5.2. HPLC conditions for VZHE-039 quantification in plasma. 162

Table 5.3. *Post hoc* sensitivity analyses for the simple metabolism kinetic binding model of 5-HMF. 175

Table 5.4. Linearity, precision, and accuracy assessment for VZHE-039 in net solution (Water:ACN = 1:1) (n = 3). 187

Table 5.5. Linearity, precision, accuracy and absolute recovery assessment for VZHE-039 in plasma (n = 3). 188

Table 5.6. Final parameters estimated from NCA analysis for VZHE-039 in plasma. . 192

Table 5.7. Final parameter estimates of time-dependency of HbA-AEH adduct formation for VZHE-039 in WB, using different kinetic binding models, and compared to the PE in HbA solution. 200

Table 5.8. Final parameter estimates of time-dependency of HbA-AEH adduct formation for 5-HMF in WB and in HbA solution, using the simple metabolism kinetic binding model and the simple kinetic binding model, respectively. 215

Table 5.9. Assessment of the outcome metrics for HbA-AEH adduct in RBC from sensitivity analysis of the simple metabolism kinetic binding model. 218

Table 5.10. Assessment of the outcome metrics of 5-HMF in RBC from sensitivity analysis of the simple metabolism kinetic binding model. 218

Table 5.11. Summary table of VZHE-039 and 5-HMF disposition in WB. 231

Table 6.1. Summary table of HbA binding kinetics of AEH in HbA solution and their oxidative metabolism in HLC. 236

Table 6.2. Summary table of the disposition of VZHE-039 and 5-HMF in WB 241

Table 6.3. PK parameters for VZHE-039 and GBT-440 in mice (n = 2-3). 247

LIST OF FIGURES

Figure: **Page:**

Figure 3.1. Structure of selected AEH. 43

Figure 3.2. AEH selection: *in-vitro* concentration-dependency of HbS-AEH adduct formation in SCD WB at 2 hrs.. 44

Figure 3.3. Representative chromatogram of 0.003 mM HbA solution. 67

Figure 3.4. Representative chromatogram of HbA-AEH adduct and HbA separation for 0.25 mM of 5-HMF in HbA solution (0.2 mM) at 3 hrs. 67

Figure 3.5. Representative chromatogram of HbA-AEH adduct and HbA separation for 8 mM of 5-HMF in HbA solution (0.2 mM) at 8 hrs. 68

Figure 3.6. Representative chromatogram of HbA-AEH adduct and HbA separation for 0.2 mM of TD-7 in HbA solution (0.2 mM) at 0.8 hr. 68

Figure 3.7. Representative UV spectra (λ = 200 – 600 nm) of HbA-AEH adduct and HbA for 0.2 mM of TD-7 in HbA solution (0.2 mM) at 0.8 hr. 69

Figure 3.8. Representative calibration curve of HbA in water/stopping solution (V:V = 1:1) in presence of 2%DMSO. 70

Figure 3.9. Mass balance assessment for VZHE-039 in HbA solution for 0.4 hr. 72

Figure 3.10. Mass balance assessment for GBT-440 in HbA solution for 0.03 hr. 73

Figure 3.11. Simulation of time-dependent HbA-AEH adduct formation using the simple kinetic binding model by changing $[HbA]_0$ (25-fold). 78

Figure 3.12. Simulation of time-dependent HbA-AEH adduct formation using the simple kinetic binding model by changing k_{on} (25-fold). 78

Figure 3.13. Simulation of time-dependent HbA-AEH adduct formation using the simple kinetic binding model by changing k_{off} (25-fold). 79

Figure 3.14. Simulation of SS concentration-dependency of HbA-AEH adduct formation using the simple kinetic binding model by changing $[HbA]_0$ (25-fold). 80

Figure 3.15. Simulation of SS concentration-dependency of HbA-AEH adduct formation using the simple kinetic binding model by changing k_{on} (25-fold). 80

Figure 3.16. Simulation of SS concentration-dependency of HbA-AEH adduct formation using the simple kinetic binding model by changing k_{off} (25-fold). 81

Figure 3.17. Simulation of SS concentration-dependency of HbA-AEH adduct formation using the simple kinetic binding model by changing k_{off} and k_{on} simultaneously (25-fold). 81

Figure 3.18. Pilot study of SS concentration- and time-dependency of HbA-AEH adduct formation for VZHE-039 in HbA solution (0.2 mM).. 84

Figure 3.19. Pilot study of SS concentration- and time-dependency of HbA-AEH adduct formation for vanillin in HbA solution (0.2 mM). 86

Figure 3.20. Pilot study of SS concentration- and time-dependency of HbA-AEH adduct formation for GBT-440 in HbA solution (0.2 mM). 88

Figure 3.21. Definitive study of SS concentration-dependency of HbA-AEH adduct formation for the selected AEH in HbA solution (0.2 mM). 90

Figure 3.22. Definitive study of SS concentration-dependency of HbA-AEH adduct formation for 5-HMF and 2,5-DMF in HbA solution (0.2 mM). 92

Figure 3.23. Definitive study of SS concentration-dependency of HbA -AEH adduct formation for TD isomers, as well as 5-HMF and vanillin in HbA solution. 93

Figure 3.24. Definitive study of SS concentration-dependency of HbA -AEH adduct formation for high affinity AEH, as well as 5-HMF and Vanillin in HbA solution..... 94

Figure 3.25. Definitive study of time-dependency of HbA-AEH adduct formation for 5-HMF in HbA solution (0.2 mM). 99

Figure 3.26. Definitive study of time-dependency of HbA-AEH adduct formation for TD-7 in HbA solution (0.2 mM). 100

Figure 3.27. Definitive study of time-dependency of HbA-AEH adduct formation for VZHE-039 in HbA solution (0.1 mM). 101

Figure 3.28. Log-log correlation of k_{on} and k_{off} for AEH..... 103

Figure 4.1. Representative calibration curve of NADH at λ of 340 nm. 125

Figure 4.2. Concentration-dependent oxidative metabolism of acetaldehyde in HLC with/without 0.5%DMSO..... 131

Figure 4.3. Concentration-dependent oxidative metabolism of ethanol in HLC. 132

Figure 4.4. Concentration-dependent oxidative metabolism of 5-HMF in HLC..... 134

Figure 4.5. Concentration-dependent oxidative metabolism of TD-7 and VZHE-039 in HLC. 135

Figure 4.6. Concentration-dependent reductive metabolism of 5-HMF and 2,5-DMF in HLC. 138

Figure 4.7 .SAR of oxidative metabolism in HLC for the selected benzaldehydes. 145

Figure 5.1. Representative chromatograms for blank WB sample (a) and 0.125 mM of HbA solution (b). 177

Figure 5.2. Representative chromatogram of HbA-AEH adduct and HbA separation for 0.3 mM of VZHE-039 in WB at 15 hrs. 178

Figure 5.3. Representative chromatogram of HbA-AEH adduct and HbA separation for 2 mM of 5-HMF in WB at 2 hrs. 178

Figure 5.4. Representative chromatogram of HbA-AEH adduct and HbA separation for 2 mM of 5-HMF in WB at 14 hrs. 179

Figure 5.5. Representative calibration curve of HbA in water/stopping solution (V:V = 1:5).. 180

Figure 5.6. Mass balance assessment for VZHE-039 in WB for 24 hrs..... 182

Figure 5.7. Mass balance assessment for 5-HMF in WB for 24 hrs. 183

Figure 5.8. Representative chromatograms for blank and 2 mM of $[\text{VZHE-039}]_0$ in neat solution (Water:ACN = 1:1) and plasma. 185

Figure 5.9. Representative calibration curves of VZHE-039 in neat solution and plasma. 186

Figure 5.10. c_p-t profiles (linear and log-scale) for VZHE-039.. 190

Figure 5.11. Dose-proportionality assessment for VZHE-039 in plasma. 191

Figure 5.12. Time-dependency of HbA-AEH adduct formation for VZHE-039 in WB. . 195

Figure 5.13. Dose-proportionality assessment for HbA-AEH adduct of VZHE-039 in WB. 195

Figure 5.14. SS concentration-dependency of HbA-AEH adduct formation for VZHE-039 in WB and the extrapolation (dashed line) using the final PE from the sigmoidal B_{max}-model in HbA solution. 197

Figure 5.15. Simulation of the zero-order dissolution process using the final k_0 estimate from the simple dissolution model in WB..... 201

Figure 5.16. Initial portion of the time-dependency of HbA-AEH adduct formation for VZHE-039 in WB, using the simple kinetic binding model (Figure 5.16a) and the simple dissolution kinetic binding model (Figure 5.16b). 202

Figure 5.17. Full time-dependency of HbA-AEH adduct formation for VZHE-039 in WB, using the simple kinetic binding model (Figure 5.16a) and the simple dissolution kinetic binding model (Figure 5.16b). 203

Figure 5.18. Time-dependent VZHE-039 disposition in plasma and RBC for low and high $[VZHE\text{-}039]_0$ (Figure a, 0.3 mM; Figure b, 7.8 mM). 206

Figure 5.19. Disposition of VZHE-039 in plasma and RBC at equilibrium (at 24 hrs).. 207

Figure 5.20. Dose-proportionality assessment for HbA-AEH adduct of 5-HMF in WB. 209

Figure 5.21. Apparent SS concentration-dependency HbA-AEH adduct of 5-HMF in WB and the extrapolation (dashed line) from HbA solution. 211

Figure 5.22. Time -dependency of HbA-AEH adduct formation for 5-HMF in WB. 214

Figure 5.23. Reference case: Simulation of the disposition of 5-HMF (2 mM) in WB ($[HbA]_0$ of 2.0 mM) from the simple metabolism kinetic binding model using the final PE (k_{on}' =0.56 mM^{-1} hr^{-1}, k_{off}' =0.11 hr^{-1}, k_{met}' =2.2 hr^{-1}, K_D' = 0.2 mM)..... 217

Figure 5.24. Scenario 1a: Simulation of the disposition of 5-HMF (2 mM) in WB ($[HbA]_0$ of 2.0 mM) from the simple metabolism kinetic binding model by changing k_{on}' to 0.14 mM^{-1} hr^{-1} (K_D' = 0.79 mM). 220

Figure 5.25. Scenario 1b: Simulation of the disposition of 5-HMF (2 mM) in WB ($[HbA]_0$ of 2.0 mM) from the simple metabolism kinetic binding model by changing k_{on}' to 2.24 mM^{-1} hr^{-1} (K_D' = 0.05 mM). 221

Figure 5.26. Scenario 2a: Simulation of the disposition of 5-HMF (2 mM) in WB ($[HbA]_0$ of 2.0 mM) from the simple metabolism kinetic binding model by changing k_{off}' to 0.03 hr^{-1} (K_D' = 0.05 mM) 223

Figure 5.27. Scenario 2b: Simulation of the disposition of 5-HMF (2 mM) in WB ($[HbA]_0$ of 2.0 mM) from the simple metabolism kinetic binding model by changing k_{off}' to 0.44 hr^{-1} (K_D' = 0.79 mM) 224

Figure 5.28. Scenario 3a: Simulation of the disposition of 5-HMF (2 mM) in WB ($[HbA]_0$ of 2.0 mM) from the simple metabolism kinetic binding model by changing k_{met}' to 0.55 hr^{-1}(K_D' = 0.20 mM) 226

Figure 5.29. Scenario 3b: Simulation of the disposition of 5-HMF (2 mM) in WB ($[HbA]_0$ of 2.0 mM) from the simple metabolism kinetic binding model by changing k_{met}' to 8.8 hr^{-1}(K_D' = 0.20 mM) 227

Figure 6.1. Time-dependency of HbA-AEH adduct formation for VZHE-039 in WB.. .. 240

Figure 6.2. Time-dependent HbA-AEH adduct formation for 5-HMF in WB. 240

Figure 6.3. Simulation of SS concentration-dependency of HbA-AEH adduct formation for VZHE-039 (solid line) and 5-HMF (dashed line) in HbA solution (red lines) and in WB (blue lines), using the final PE from the sigmoidal B_{max}-model (as discussed in Chapter 3 and 5) and scaled up to the same $[HbA]_0$ (2.0 mM) in WB. 244

LIST OF ABBREVIATIONS

%Hct	%Hematocrit
$[AEH]_0$	Initial AEH concentrations, at time=0
$[HbA]_0$	Initial HbA concentration, at time=0
2,3-DPG	2,3-Diphosphoglycerate
2,5-DMF	2,5-Diformylfuran (2,5-Furandicarboxaldehyde, DFF)
5-HMF	5-Hydroxymethylfurfural
ACN	Acetonitrile
ADH	Alcohol dehydrogenase
ADME	Absorption, distribution, metabolism and exretion
AEH	Allosteric effector(s) of hemoglobin
AEs	Adverse events
ALDH	Aldehyde dehydrogenase
AO	Aldehyde oxidase
AUC	Area under the curve
AUC_∞	Area under the curve up to time infinity
AUC^{adduct}	Area under the curve of HbA-AEH adduct

$AUC^{5\text{-}HMF}$	Area under the curve of 5-HMF
$AUC^{VZHE\text{-}039}$	Area under the curve of VZHE-039
AUC_{trap}	Area under the curve calculated by trapezoidal rule
AUC_{extra}	Extrapolated area under the curve calculated by terminal slope
$AUC_{0\text{-}24hr}$	Area under the curve up to 24 hrs
$AUC_{0\text{-}4hr}$	Area under the curve up to 4 hrs
B_{max}	Maximal binding capacity
CC	Calibration curve
CI	Confident interval
CL	Clearance
CrCL	Creatinine clearance
CL_{hep}	Hepatic clearance
$CL_{int}^{in\text{-}vitro}$	*In-vitro* intrinsic clearance
cIogP	Calculated logarithm of octanol-to-water partition coefficient
$CL_{plasma}^{in\text{-}vitro}$	*In-vitro* plasma clearance
CL_{tot}	*In-vivo* total body clearance
C_{max}	Peak concentration (in plasma or blood)
CO_2	Carbon dioxide

COV	Coefficient of variation
CYP450	Cytochrome P450
DFN	Difference from nominal
DMSO	Dimethyl sulfoxide
EC_{50}	Concentration at half-maximal effect
eLOQ	Experimental limit of quantitation
ER_{hep}	Hepatic extraction ratio
EX	Experimental observation
FC	Fold-change of the simulation results from the (simple or metabolism) kinetic binding model
F.D.A.	Food and Drug Administration
f_e	Fraction of dose excreted unchanged in urine
FIH	First-in-human (study)
F_{oral}	Oral bioavailability
f_u	Unbound fraction of drug in plasma/blood
f_b	Bound fraction of drug in plasma/blood
GBT-440	Voxelotor
Hb	Hemoglobin
HbA	(Normal) Adult hemoglobin

HbAS	Hemoglobin with one HbA gene and one HbS gene
HbA-AEH adduct	Hemoglobin AEH adduct
HbA-AEH adduct$_\infty$	Hemoglobin AEH adduct at equilibrium
HbC	Hemoglobin C (abnormal isoform)
HbF	Fetal hemoglobin
HbS	Sickle hemoglobin
HbSS	Sickle hemoglobin with two HbS genes
HbSC	Hemoglobin with one HbS gene and one HbC gene
HbS-β	Hemoglobin with one HbS gene and Hb$\beta^{0/+}$ gene
HLC	Human liver cytosol
HLM	Human liver microsome
HMFA	5-Hydroxmethyl-2-furoic acid
HPLC	High performance liquid chromatography
HU	Hydroxyurea
I.V.	Intravenous (route of administration)
IVIVE	*In-vitro-in-vivo* extrapolation
k_{cat}	Catalytic activity
K_D	Dissociation (equilibrium) constant, estimated from SS concentration-dependency study in HbA

K_D'	Apparent dissociation (equilibrium) constant, estimated from SS concentration-dependency study in WB
$K_D^{kinetic}$	Dissociation (equilibrium) constant, estimated from time-dependency study in HbA
$K_D^{kinetic'}$	Apparent dissociation (equilibrium) constant, estimated from time-dependency study in WB
k^{ass}	(Apparent first-order) association rate constant, determined by k_{on} estimated from time-dependency study and $[HbA]_0$ in HbA
$k^{ass'}$	Apparent (first-order) association rate constant, determined by k_{on} estimated from time-dependency study and $[HbA]_0$ in WB
k^{diss}	(First-order) dissociation rate constant, determined by k_{off} estimated from time-dependency study in HbA
$k^{diss'}$	Apparent (first-order) dissociation rate constant, determined by k_{off} estimated from time-dependency study in WB
k^{eq}	(First-order) equilibration rate constant in HbA
$k^{eq'}$	Apparent (first-order) equilibration rate constant in WB
K_i	Affinity constant for inhibitor
K_m	Michaelis-Menten metabolic affinity constant
k_{met}'	Apparent metabolic rate constant, estimated from time-dependency study in WB
k_{off}	(First-order) dissociation rate constant, estimated from time-dependency study in HbA
k_{off}'	Apparent (first-order) dissociation rate constant estimated from time-dependency study in WB
k_{on}	(Second-order) association rate constant, estimated from time-dependency study in HbA
k_{on}'	Apparent (second-order) association rate constant, estimated from time-dependency study in WB
LL	Lower limit

MAD	Multiple ascending dose
MCV	Mean corpuscular volume of RBC
MeOH	Methanol
MM	Michaelis-Menten
MOA	Mechanism of action
MSC	Model selection criterion
n	Hill coefficient
$NaBH_3CN$	Sodium cyanoborohydride
$NaBH_4$	Sodium borohydride
NAD^+	Oxidized nicotinamide adenine dinucleotide
NADH	Reduced nicotinamide adenine dinucleotide
NCA	Non-compartmental (PK) analysis
NMDA	N-methyl-D-aspartate
NO	Nitric oxide
NSAID	Non-steroidal anti-inflammatory drugs
NSB	Nonspecific binding
O_2	Oxygen
OEC	Oxygen equilibrium curve

PD	Pharmacodynamics
PE	Point estimate
Penicillin VK	Penicillin V potassium
pH	Negative log of hydrogen ion concentration
pI	Isoelectric point of protein
PK	Pharmacokinetics
PK/PD	Pharmacokinetics and pharmacodynamics
pKa	Negative log of the acid association constant
pO_2	Partial pressure of oxygen/oxygen tension
PPB	Plasma protein binding
Q_{hep}	Hepatic blood flow
r	Correlation coefficient
r^2	Coefficient of determination
RBC	Red blood cell(s)
R-state	Relaxed (oxygenated) state of Hb
SAD	Single ascending dose
SAR	Structure activity relationship
SCD	Sickle cell disease

SCT	Sickle cell trait
SD	Standard deviation
SPE	Solid phase extraction
SS	Steady-state
SS cells	Red blood cells containing HbS, “sickle cells”
ST	Simulation from the final point estimates from simple metabolism kinetic binding model
$t_{1/2}$	Half-life
$t_{1/2}^{ass}$	Association half-life in HbA solution
$t_{1/2}^{ass'}$	Apparent association half-life in WB
$t_{1/2}^{diss}$	Dissociation half-life in HbA solution
$t_{1/2}^{diss'}$	Apparent dissociation half-life in WB
$t_{1/2}^{eq}$	Equilibration half-life in HbA solution
$t_{1/2}^{eq'}$	Apparent equilibration half-life in WB
$t_{/2}^{term}$	Terminal half-life
TDs	TD-7, TD-8 and TD-9
t_{max}	Time to peak concentration (in plasma/blood)
t_R	Retention time
T-state	Tense (deoxygenated) state of hemoglobin

UL	Upper limit
UV/Vis	Ultraviolet /Visible spectrophotometry
v_0	Baseline reaction rate, without addition of substrate
V_{dss}	Steady-state volume of distribution
v_i	Initial reaction rate
v_{max}	Maximal rate of metabolism
WB	WB
ε_{340}	Extinction coefficient at 340 nm
ε_{max}	Extinction coefficient at wavelength of maximal extinction
ε_{NADH}	Extinction coefficient of NADH at 340 nm

ABSTRACT

MODEL-BASED *IN-VITRO* PK/PD PROFILING OF NOVEL SYNTHETIC ALLOSTERIC EFFECTORS OF HEMOGLOBIN (AEH) AS POTENTIAL SICKLE CELL DISEASE (SCD) THERAPEUTICS

By Xiaomeng Xu, B.Pharm., M.S.

A Dissertation submitted in partial fulfillment of the requirements for the degree of Doctor of Philosophy at Virginia Commonwealth University

Virginia Commonwealth University, 2020

Major Directors: Jürgen Venitz, M.D., Ph.D., Professor, Department of Pharmaceutics

Martin K. Safo, Ph.D., Professor, Department of Medicinal Chemistry

Introduction: Allosteric effectors of hemoglobin (AEH) represent a class of synthetic aromatic aldehydes that transiently form covalent interactions (Schiff-base) with hemoglobin (Hb) to form Hb-AEH adduct, preventing the HbS polymerization and sickling of red blood cells (RBC). The overall objective of this research was to aid in the optimization of novel AEH by understanding their target-site disposition of AEH in relevant biological matrices, e.g., HbA solution, whole blood (WB) and human liver cytosol (HLC), a surrogate of aldehyde dehydrogenase (ALDH)-mediated oxidative metabolism.

Methods: A “universal” HPLC-UV/Vis assay method was developed for the quantitation of HbA-AEH adduct for chemically different AEH in HbA solution and in WB. Steady-state (SS) concentration-dependence and time- dependence HbA binding were characterized by a sigmoidal B_{max}-model (K_D) and a kinetic binding model (k_{on}, k_{off}). The Warburg method was used to assess the enzymatic oxidation of selected AEH in HLC. WB disposition of 5-HMF (VCU lead, terminated in Phase 2) and VZHE-039 (current top candidate, pre-IND) was assessed by measuring their HbA-AEH adduct in WB and plasma exposures.

Results: All vanillin-derived benzaldehydes exhibit enhanced binding affinity in HbA solution, primarily due to their faster k_{on}. Across AEH, i.e., benzaldehydes and furaldehydes studied, k_{on} and k_{off} values are strongly (log-log) correlated (r=0.993, n=7), suggesting that the molecular modifications of the current AEH scaffold enhance their interactions with Hb (as intended), but also (inadvertently) increase their Hb-AEH adduct dissociation.

In HLC, some AEH showed oxidative metabolism (CL_{int}: 5-HMF < TD-7 < INN-310 < acetaldehyde, prototypical substrate). Presence of the meta-methoxy group (in TD-7) favors ALDH-mediated oxidation, while the ortho-hydroxy group (in VZHE-039) protects the aldehyde group/AEH from metabolism.

In WB, Hb-AEH adduct concentrations for VZHE-039 are sustained in WB for 24 hrs, confirming its resistance to ALDH metabolism in RBC. A less than proportional increase in plasma c_{max}, but proportional AUC along with prolonged t_{max} with the initial concentration, $[VZHE\text{-}039]_0$, were observed for VZHE-039, indicating rate-limiting, but ultimately complete dissolution, prior to any HbA binding. The estimated apparent

binding affinity ($1/K_D^{kinetic'}$) for VZHE-039 in WB is 23-fold lower than observed in HbA solution, primarily due to a 300-fold slower apparent k_{on}' (Table 1). On the other hand, HbA-AEH adduct concentrations for 5-HMF in WB decrease after 1.5 hrs - thus providing conclusive evidence of rapid intra-RBC ALDH-mediated metabolism - which resulted in an 8-fold lower apparent binding affinity (K_D' of 3.0 mM) from concentration-dependency study at 1.5 hrs in WB. However, after accounting for first-order metabolism in the WB disposition model, the $K_D^{kinetic'}$ for 5-HMF in WB was quite similar to that in HbA solution; dissociation of 5-HMF from Hb was slow and determined the terminal decline of HbA-AEH adduct in WB (Table 1).

Table 1. Summary for VZHE-039 and 5-HMF

AEH	Binding in HbA Solution			Binding to HbA in WB				Metabolism in HLC	
	$K_D^{kinetic}$	k_{on}	k_{off}	$K_D^{kinetic'}$	k_{on}'	k_{off}'	k_{met}'	$CL_{int}^{in\text{-}vitro}$	K_m
	[mM]	[$mM^{-1}hr^{-1}$]	[hr^{-1}]	[mM]	[$mM^{-1}hr^{-1}$]	[hr^{-1}]	[hr^{-1}]	[µL/min/mg]	[mM]
VZHE-039	**0.10**	61	5.8	**2.3**	0.20	0.46	0	**0**	NA
5-HMF	**0.28**	0.46	0.13	**0.20**	0.56	0.11	2.2	**0.036**	>90

Conclusions: WB disposition of AEH is determined by the kinetics of three concurrent processes, namely (saturable) Hb binding, (non-saturable) ALDH-mediated metabolism in RBC, as well as reversible, first-order PPB/RBC membrane binding. Although the K_D value for VZHE-039 is 3-fold lower than 5-HMF in HbA solution, both compounds exhibit similar apparent K_D' values in WB, albeit due to different mechanisms, namely ALDH-mediated metabolism for 5-HMF and extensive PPB/RBC membrane binding for VZHE-

039 – both processes reducing AEH concentrations at the target site, Hb. Concurrent PPB/RBC membrane binding for lipophilic benzaldehydes, e.g., VZHE-039, also slows down their overall WB HbA adduct formation, but helps sustain them.

Key molecular features of AEH to enhance HbA binding and reduce intra-RBC metabolism have been identified, allowing further rational design of more potent (in WB) drug candidates for further druggability evaluation - with VZHE-039 as the top candidate.

CHAPTER 1

INTRODUCTION

1.1 Sickle Cell Disease (SCD)

1.1.1 Prevalence

Sickle Cell Disease (SCD) is a group of chronic and hereditary blood disorders affecting red blood cells (RBC) with the presence of at least one hemoglobin S (HbS) allele (Ilesanmi, 2010). SCD is caused by a monogenic mutation, where glutamate is replaced by valine (βGlu6 to βVal6) at the amino acid position 6 in the β-chain of HbA to give HbS. It is a multi-organ damage disease with high mortality and morbidity (Piel, Steinberg, & Rees, 2017). In contrast, people with sickle cell trait in which the person only has one abnormal allele of the HbS β chain have very mild symptoms of the disease. As a global public health problem, SCD affects approximately 100,000 Americans, 60,000 Europeans and over 15 million people worldwide (Bender & Hobbs, 2014). SCD is the most common among those with African heritage, and about 1 out of every 365 black or African American births would have the disease. In addition, SCD is one of the most prevalent diseases detected through neonatal blood screening (Lane et al., 2002). About 300,000 infants born with the abnormality are characterized by HbS homozygosity. The number is expected to rise to 400,000 by 2050 (Piel et al., 2017).

Malaria parasite (plasmodium falciparum) spends part of its life cycle in RBC (Bender & Hobbs, 2014; Piel et al., 2017). When malaria parasite is present, the RBCs with defective Hb rupture prematurely to prevent its reproduction. People with HbS

heterozygotes seem to have increased survival from malaria(Bender & Hobbs, 2014). On the other hand, malaria also drives gene selection for red cell disorders including SCD. Therefore, higher frequency of SCD is found in areas associated with malaria, such as tropical regions like Sub-Saharan Africa and the Middle-East(Bender & Hobbs, 2014).

1.1.2 Pathophysiology

HbA exists as solitary units whenever under oxygenated or deoxygenated conditions, whereas HbS molecules aggregate or polymerize under deoxygenated conditions leading to sickling of RBC (Bunn & Forget, 1986). The sickling process of RBC is due to a point mutation of A into T in the codon of the 6th amino acid of the human HBB gene encoding the Hb β-chain, where GAG switches GAG into GTG, resulting in valine replacing glutamate (Bunn & Forget, 1986). In normal Hb (HbA), the negatively charged glutamic enforce the solitary integrity of the Hb molecules. Substitution of glutamic with the hydrophobic valine leads to aggregation or polymerization of the sickle molecules especially at areas of low oxygen pressure (Safo, Ahmed, Ghatge, & Boyiri, 2011).

The hypoxia-driven deoxy-HbS polymerization and the concomitant RBC sickling process is made worse by increased levels of the allosteric effector 2,3-DPG and perhaps sphingosine phosphate in sickle RBCs (W N Poillon, Kim, Labotka, Hicks, & Kark, 1995; William N Poillon & Kim, 1990; Sun et al., 2017, 2016). HbS aggregation is thermodynamically unstable, and more HbS molecules will aggregate until reaching a critical mass, at which point the addition of any other molecules stabilizes the complex,

and finally facilitates the shape change of RBC into dysfunctional sickles or crescent moon morphologies impacting HbS O_2 delivery activity (Piccin et al., 2019). The progression of polymerization, in addition to 2,3-DPG is also influenced by oxygenation, Hb concentration, temperature, pH and saline concentration, etc (W N Poillon et al., 1995; William N Poillon & Kim, 1990; Sun et al., 2017, 2016).

The clustered β-chains along the RBC membrane not only damage cytoskeletal proteins such as band-3, spectrin and ankyrin, but also promote the deposition of IgG, initiate monocyte chemotaxis and lead to early clearance of aged RBC (Piccin et al., 2019). The lifespan of normal RBC is 120-day. However, the lifespan of sickle RBC is no more than 20 days, which is an underlying cause of anemia in people with SCD (Piccin et al., 2019).

Rivera, et al reported endothelin-1 (ET-1) activates Ca^{2+}- dependent K^+ channel (also known as the Gardos channels) (Rivera, 2007). The activation of Gardos channels leads to the loss of hypertonic effluent (composed of KCL or KOH) and alkaline, which further causes the rapid dehydration of RBCs and favors the hypoxia-induced sickling process(Rivera, 2007). Gardos channels play a pivotal role in pathogenesis of SCD because a severe and nearly irreversible dehydration can be resulted from a minimal activation of Gardos channels (Rivera, 2007).

Repeated sickling decreases the elasticity of RBC membrane, preventing the stiff RBC to easily squeeze through blood vessels, leads to vaso-occlusion and circulation impairment, further causing tissue O_2 deprivation and organ damages. Sickling of the RBC also leads to disruption of the stiff RBC membrane, releasing hemolytic products,

such as free Hb, arginase, adenine nucleotides and asymmetric dimethylarginine (Bunn & Forget, 1986). Free Hb in the plasma scavenges nitric oxide (NO) by transforming NO into nitrate, making this important molecule less bioavailable to the vasculature. NO is an important vasodilator to maintain normal vascular tone and inhibit platelet activation. NO depletion leads to vasoconstriction and platelet aggregation (Piccin et al., 2019). In transforming NO to nitrate, Hb is oxidized into methemoglobin, which readily loses heme group, and become unable to bind and transport O_2 (Akinsheye & Klings, 2010). L-arginine is a source of NO and can be converted to NO by endothelial nitric oxide synthase. Patients with SCD tend to be L-arginine deficient due to high levels of arginase in plasma from hemolyzed erythrocytes. The released arginase also reduces arginine level in the blood, further decreasing NO level in circulation and impairing its vasodilation function (Akinsheye & Klings, 2010; Piccin et al., 2019).

In summary, while SCD is a monogenic disease caused by a single pathogenic mutation in normal hemoglobin, its pathophysiology is multifaceted and diverse leading to several clinical manifestations.

1.1.3 Clinical Manifestations

There are four common genotypes of SCD in the United States. Patients who inherit two sickle cell genes (HbSS) have the most severe form of SCD (Bunn & Forget, 1986). Patients who have HbSC genotype SCD inherit a sickle cell gene from one parent, and an abnormal HbC (glutamic acid at the 6th amino acid position replaced by lysine) gene from the other parent. Patients carrying HbSC have a milder form of SCD compared with those carrying HbSS (Bunn & Forget, 1986). There are two different

types of β thalassemia gene, “β^0” or “β^+”. Patients carrying β^0 thalassemia gene have more severe symptoms of SCD than those carrying β^+ thalassemia gene. Similar to patients carrying HbSC, those with HbS-β^+ thalassemia have milder symptoms of SCD (Bunn & Forget, 1986). Patients who have HbAS genotype SCD carry one normal Hb gene from one parent, and a sickle cell gene from the other parent, which is also called sickle cell trait (SCT). Patients who carry SCT live a normal life and have no any symptom of SCD. But there is a chance that they might pass the trait or the disease on to their children (Bunn & Forget, 1986).

SCD symptoms are characterized by chronic hemolytic anemia. Patients might manifest weakness and fatigue. Symptoms of jaundice or cholelithiasis may also be observed (Piel et al., 2017). Patients with SCD have a higher chance for infection (Booth, Inusa, & Obaro, 2010). Normal splenic functions include storing B cells, which produce antibodies, filtering the blood, removing damaged or old RBCs, and helping to clear encapsulated bacteria. However, in patients with SCD, blood flowing to the spleen is impeded because of obstruction by sickle cells compromising its function. In the first few years of life, patients with SCD have loss of function of the spleen (asplenia), resulting in increased susceptibility to infections with encapsulated bacteria, such as pneumococcus, haemophilus influenzae type b and meningococcus serogroup B, etc (Tamouza et al., 2002).

Another remarkable clinical manifestation of patients with SCD is pain, a warning sign that is associated with vaso-occlusive events, acute or chronic complications(Bunn & Forget, 1986). Acute complications of SCD include acute-occlusive crisis, acute anemia, acute splenic sequestration, acute chest syndrome, priapism, acute renal

failure, fever and infection, thrombosis, stroke, hepatobiliary or ocular complications, or multisystem organ failure (Bunn & Forget, 1986). Chronic complications of SCD include chronic pain (greater than 3 months, particularly neuropathic in origin), avascular necrosis, leg ulcers (more common in male and older patients), renal complications (such as proteinuria or renal papillary necrosis), pulmonary complications (such as pulmonary hypertension, obstructive sleep apnea or asthma), ophthalmologic complications, cholecystitis, vitamin D deficiency and fertility, etc (Bunn & Forget, 1986).

1.1.4 Hemoglobin (Hb)

Hb is a polyfunctional protein in RBC. The functions of Hb include O_2 transport, catalytic reaction, nitric oxide metabolism, metabolic reprogramming, pH regulation and maintaining redox balance(Ahmed, Ghatge, & Safo, 2020). The X-ray crystallography structure of Hb was first elucidated by Max Perutz, who won a noble prize for this achievement(Bragg & Perutz, 1952). Hb is an allosteric tetramer protein, composed of two α- and β- globin chains(Ahmed et al., 2020; Bragg & Perutz, 1952). Each globin-chain contains an iron-heme group that is capable of binding to one O_2. Hb functions between two conformational states - the high-affinity R-state, which binds oxygen (oxygenated Hb) and the low-affinity T-state which contains no oxygen (deoxygenated Hb) (Bunn & Forget, 1986). The high-affinity R-state consists of an ensemble of high-O_2 affinity states, including the classical R, RR2, R3, RR3 (Safo et al. 2004; Oder et al. 2016; Ahmed et al., 2020). The O_2 binding to Hb is a cooperative process, where O_2 binding to the hemes destabilize the α1 β2 interface, resulting in a allosteric transition from the T-state to the R-state, facilitating increase binding affinity of oxygen to all

hemes (Ahmed et al., 2020). This cooperative binding allows a more efficient release of O_2 to tissue with a small decrease of partial pressure of O_2.

HbA, normal adult hemoglobin, is found to account for about 90% of total Hb in healthy RBC (Bunn & Forget, 1986). HbA functions normally in sensing metabolic activity and modulating O_2 binding accordingly. However, when abnormal mutation happened within the α1 β2 interface, O_2 binding affinity of Hb is usually altered (Thom, Dickson, Gell, & Weiss, 2013).

1.2 Therapeutic Strategies for SCD

Four medications with different mechanisms have been approved by F.D.A. for the treatment of SCD, including hydroxyurea (HU), voxelotor, crizanlizumab and L-glutamine. Other strategies such as pain management, blood transfusion and infection prevention, etc. are also applied to alleviate the symptoms and improve the outcomes of patients with SCD.

1.2.1 Hydroxyurea (Pharmacological Reactivation of Hemoglobin F (HbF))

HU has been used for the treatment of SCD for over two decades. HU was originally developed as a chemotherapeutic agent for myeloproliferative disorders. HU was later found to be effective for patients with SCD by significantly reducing the frequency of pain episodes, acute chest syndromes, hospitalization and the need for blood transfusion in most cases possibly due to increased fetal Hb (HbF) level (Charache et al., 1995; Cokic et al., 2003).

HbF is composed of two α and two γ subunits and produced from 10 to 12 weeks of gestation by erythroid precursor cells(Bunn & Forget, 1986). HbF is dominant during neonate (about 50% to 95%), but slowly declines through the first six months after birth. HbF (two α and two γ subunits) is replaced by corresponding HbA (two α and two β subunits) by 6 to 12 months after birth. After 12 months, only about 1% HbF remains except for individuals with diseases involving red blood cells. HbA is the dominant Hb present throughout life. Different from the β subunit of HbA, the γ subunit of HbF has either glycine or alanine at position 136. Both of these amino acids are nonpolar and neutral, that make HbF exhibit higher affinity for oxygen compared to HbA (Kaufman & Lappin, 2019).

The levels of HbF increased by HU vary between 10% to 50% in patients with SCD depending on genotype and populations (Cokic et al., 2003; Nader et al., 2018). The cells containing HbF are called F cells. The effects of HbF on SCD symptoms depend on the HbF level in each RBC. HU not only improves the deformability of sickle RBC by increasing the F cells number, decreasing the production and polymerization of HbS, but also increasing the water contents and mean corpuscular volume (MCV) of RBC (Piccin et al., 2019). Cokic et al reported that HbF induced by HU is via NO-dependent activation of soluble guanylyl cyclase (Cokic et al., 2003). The increased release of NO by HU improves the blood flow via vasodilation effect. HU also enhances blood rheology by increasing deformability of RBC and hematocrit. In addition, HU reduces the adhesiveness of circulating cells to endothelium by decreasing phosphatidylserine density on microparticles in RBC, and attenuating neutrophils (Piccin

et al., 2019). HU has been shown to reduce frequency of pain episodes, acute chest syndromes, needs for transfusion and hospitalization (Piccin et al., 2019).

HU is offered to infants 9 months of age and older, children, adolescents and adults with SCD, regardless of the clinical severity based on the clinical study. HU is also considered for patients with HbSC and HbSβ^+ thalassemia with recurrent sickle cell complications (Scott, Hillery, Brown, Misiewicz, & Labotka, 1996; Ware & Aygun, 2009). An initial dose of 10-15 mg/kg/day is used for infants younger than one-year-old with good creatinine clearance (CrCL > 60 mL/min). 20mg/kg/day is used as an initial dose for children one year of age or older with good creatinine clearance (CrCL > 60 mL/min). Adult may start HU on 15 to 20 mg/kg/day. The commercially available dosage forms are capsules, new formulation Siklos and compounded oral suspension. For dosing convenience, the given dose can be rounded off to the nearest 2.5 mg/kg. HU is excreted renally. Individuals with CrCL less than 60 mL/min or end-stage kidney disease exhibit higher HU exposure due to decreased renal clearance. These patients need to be initiate with half of HU starting dose and titrate up with smaller increments. The initial dose is calculated based on weight. The dose is increased approximately every 8 weeks by 5mg/kg daily to a maximal dose of 35 mg/kg/day or 2500 mg daily. The maximal tolerated dose should be maintained if not able to reach 35 mg/kg/day ("Disease-modifying therapies for prevention of vaso-occlusive pain in sickle cell disease. UpToDate, Inc. Accessed June-06," 2020).

The treatment goal is to have HbF level greater than 20%, and HbF levels should be monitored every two or three months. The complete blood count and reticulocyte count should be monitored every four weeks while dose is titrated up. Other lab values

such as platelet, RBC, MCV, HbF quantitative, renal and liver panels are also monitored. The common adverse effects from HU are gastrointestinal upset and darkening of nail beds or skin. Some patients also see symptoms of neuropenia, thrombocytopenia, anemia, hair thinning, teratogenicity and fertility. Bone marrow suppression is the major dose-limiting toxicity for HU(Ware & Aygun, 2009). HU treatment should be stopped if Hb level is less than 8 g/dL off transfusion, or absolute neutrophil count is less than 2000/μL, or platelet count is less than 8000/μL, or target reticulocyte count is less than 80,000 to 100,000/μL. The treatment is restarted at the same dose if recovery occurs within a week or at a lower tolerated dose ("Disease-modifying therapies for prevention of vaso-occlusive pain in sickle cell disease. UpToDate, Inc. Accessed June-06," 2020).

1.2.2 Voxelotor (GBT-440, Anti-Sickling Agent)

Voxelotor (GBT-440) is another anti-sickling drug for the treatment of SCD. Voxelotor is an allosteric modifier of Hb by increasing its O_2 affinity(Han, Saraf, & Gordeuk, 2020). GBT-440 binds to α chain of Hb and shifts the O_2 equilibrium curve (OEC) to the left that increases the affinity of HbS for O_2. This allosteric property prevent polymerization of HbS and leads to inhibition of RBC sickling(Blair, 2020b; Han et al., 2020). Voxelotor has shown to decrease RBC sickling and hemolytic biomarkers in clinical trials, but lack of long-term studies on its prevention of vaso-occlusion and decreasing frequency of pain crises and hospitalizations(Vichinsky et al., 2019). Voxelotor was approved by F.D.A. in November 2019 and indicated for individuals, whose age is equal to or greater than 12 years old with continuous pain episodes resulted from vaso-occlusive events despite appropriately HU dosing, or who cannot

tolerate HU due to severe adverse effects or any other reason(Blair, 2020b). Voxelotor is recommended to be administered as a single oral dose: 1500 mg once daily. Voxelotor can be administered together with HU. As for patients with severe liver impairment, the daily dose of voxelotor is reduced to 1000 mg once daily, since voxelotor is extensively metabolized by CYP3A4 in the liver(Blair, 2020b; Metcalf et al., 2017). Voxelotor is both a substrate and an inhibitor of CYP3A4, and therefore, should be avoided to administer together with CYP3A4 inducers or inhibitors(Blair, 2020b; Metcalf et al., 2017). If voxelotor is concomitantly administered with other CYP3A4 inhibitors such as fluconazole, the daily dose is supposed to be cut to 1000 mg once daily, too. Conversely, the daily dose of voxelotor should be increased if it is simultaneously taken with CYP3A4 inducers up to 2500 mg. Liver function and Hb level should be monitored during voxelotor administration. The common adverse effects from voxelotor include gastrointestinal upset such as nausea, diarrhea and abdominal pain. Rash, hypersensitivity and headache are also observed in some cases(Blair, 2020b; Metcalf et al., 2017).

1.2.3 Crizanlizumab (Anti-Adhesion Agent)

Crizanlizumab is a humanized IgG_2 kappa monoclonal antibody(Ataga et al., 2017). SCD pathophysiology involves adhesive interactions among RBC, endothelial cells and neutrophils facilitating following vaso-occlusive events(Ataga et al., 2017). The activation of endothelial cells recruits neutrophils, and directs them to roll on endothelial selectins, a family of cell adhesion molecules expressed on activated endothelial cells or platelets(Man et al., 2020). The selectins further induce the adhesion

of neutrophils to activated endothelial cells and platelets. Then adherent neutrophils mediate the capture of circulating RBC through a series of signaling transduction reactions (Ley, 2001). Crizanlizumab is a selectin blocker (Ataga et al., 2017; Blair, 2020a; Man et al., 2020). crizanlizumab binds to P-selectin, blocks its interactions with corresponding ligands including P-selectin glycoprotein ligand 1 on the surface of the activated endothelium and platelets, then finally inhibits adhesive interactions between RBC, endothelial cells, platelets and neutrophils (Man et al., 2020). Crizanlizumab was approved by F.D.A. in November 2019. It is recommended to be used for patients 16 years and older with SCD, who have frequent or severe pain episodes derived from vaso-occlusive crisis and unresponsive to L-glutamine, hydroxyurea, or both(Blair, 2020a). Crizanlizumab can also be taken together with hydroxyurea. According to the clinical study, crizanlizumab is recommended to be given at 5 mg/kg by intravenous infusion over 30 minutes once every 2 weeks for 2 doses (at week 0 and week 2), and then followed by 5 mg/kg once every 4 weeks thereafter(Blair, 2020a). The common adverse effects associated with crizanlizumab treatments include infusion site reactions, infusion related reactions, arthralgia or myalgia, abnormal platelet aggregation, headache, pruritis or nausea (Ataga et al., 2017).

1.2.4 L-Glutamine (Modulator of Oxidative Stress)

L-Glutamine is a conditionally essential amino acid and is synthesized in the body. The exact mechanism of L-glutamine in patients with SCD is unknown. As a precursor of nicotinamide adenine dinucleotide, L-glutamine may involve increasing nicotinamide adenine dinucleotide, enhancing availability of reduced glutathione and

improving defense against oxidative stress in RBC (Cox, Hart, Kirkham, & Stotesbury, 2020; Niihara et al., 2014). L-glutamine was approved by F.D.A. in 2017 for SCD children and adults with continuous pain episodes resulting from vaso-occlusive events despite appropriately HU dosing, or who cannot tolerate hydroxyurea due to severe adverse effects or any other reason(Cox et al., 2020; Niihara et al., 2014). L-glutamine can be taken with or without HU. L-glutamine is preferred for patients who can tolerate oral medication and be able to comply with twice-daily regimen. L-glutamine is given based on body weight. If patients with SCD are less than 30 kg, L-glutamine is given 5 g (1 packet) by mouth twice daily; If patients with SCD are between 30 and 65 kg, L-glutamine is given 10 g (2 packets) by mouth twice daily; If patients with SCD are greater than 65 kg, L-glutamine is given 15 g (3 packets) by mouth twice daily. More data is required to demonstrate the long-term efficacy and safety of L-glutamine. L-glutamine is pretty safe and common adverse effects are gastrointestinal side effects and headache(Cox et al., 2020; Niihara et al., 2014).

1.2.5 Pain Management (NSAIDs, Opioids)

For patients with SCD, pain is complicated and impacted by more than just vaso-occlusive events. Firstly, individuals with SCD should minimize or avoid specific pain triggers such as cold temperature, overexertion, dehydration, hormonal changes due to menses and respiratory exposures, for example, smoking- or air pollution-induced asthma exacerbation. Taking care of general health with regular exercises, nutritional food, sleep hygiene and stress reduction also contribute to alleviation of chronic pain in

patients with SCD. It is reported that about a third of patients with SCD self-medicate with cannabinoids to alleviate pains(Roberts et al., 2018).

Pain management is individualized based on the underlying causes, duration, intensity and patients or their clinician's concerns. Corresponding strategies should be applied to cope with underlying varied causes of pain. For example, patients with acute vaso-occlusive pain can be treated with nonsteroidal anti-inflammatory drugs (NSAIDs)(Roberts et al., 2018). Chronic pain associated with SCD may involve hyperalgesia and central sensitization. Some patients may not prefer chronic medications for pain management, however, patients who have severe pain on the majority of days may need daily opioids, such as long-acting oral morphine or oxycodone, etc(Roberts et al., 2018). Opioid treatment is efficacious to alleviate pains in SCD, but it also increases the risk of addiction and adverse effects such as respiratory suppression, gastrointestinal upset, developmental or hormonal changes, etc (Roberts et al., 2018).

As an opioid receptor agonist, N-methyl-D-aspartate (NMDA) receptor antagonist and monoamine re-uptake inhibitor, methadone may have advantages over opioids with less addiction (Roberts et al., 2018). In addition, methadone is effective for patients with neuropathic pain due to NMDA antagonism (Smith & Alsalman, 2013). But methadone increases the risk of arrhythmia such as QT_c interval prolongation (Upadhya et al., 2013). Electrocardiogram should be monitored during methadone treatment. Regular transfusions may be efficacious for individuals with refractory or chronic pain unresponsive to above-mentioned analgesics via lowering the percentage of HbS and preventing following vaso-occlusive events (Piccin et al., 2019; Uwaezuoke et al., 2018).

Disease-modifying medications, such as HU and crizanlizumab, are also beneficial for pain management in patients with SCD (Ataga et al., 2017; Piccin et al., 2019).

1.2.6 Blood Transfusion

Blood transfusion is applied in patients with SCD to lower the amount of HbS to less than 30% in the body (Wahl & Quirolo, 2009). Blood transfusion is given every 3 to 4 weeks for chronic indications, such as patients with severe or recurrent acute chest syndrome or patients with recurrent priapism to debilitate chronic pain, and to reduce risks of stroke, transient ischemic attacks and chronic organ failures (Wahl & Quirolo, 2009). Blood transfusion is also applied in acute conditions such as severe anemia and splenic sequestration. Blood transfusion is not routinely used to prevent pain. But patients with frequent acute or chronic pain episodes despite appropriate disease-modifying treatments may benefit from six months duration of regular blood transfusion (Wahl & Quirolo, 2009). The risk of blood transfusion includes iron overload, alloimmunization, hyperviscosity, viral transmission and volume overload, etc (Wahl & Quirolo, 2009). Iron chelation agents including deferasirox, deferoxamine or deferiprone can be administered to treat iron overload derived from blood transfusion (Wahl & Quirolo, 2009).

1.2.7 Infection Prevention

Patients with SCD have increased susceptibility to infections with encapsulated bacteria and are benefit from updated immunizations with pneumococcal vaccine, Haemophilus Influenzae type b vaccine, meningococcal conjugate vaccine or

meningococcal serogroup B vaccine (Overturf, 1999). Penicillin V potassium (Penicillin VK) should be administered in the first five years of age in those carrying sickle cell HbSS or HBSβ^0 thalassemia (Overturf, 1999; Sobota, Sabharwal, Fonebi, & Steinberg, 2015). Penicillin treatment is usually discontinued at age five to complete vaccination series and to prevent higher rates of penicillin-resistant organisms in older children. Patients with splenectomy or invasive pneumococcal infection may need continuous penicillin prophylaxis beyond age 5 (Overturf, 1999; Sobota et al., 2015). The dosing of penicillin VK is based on age. Infants between 0 to 3 months administer 62.5 mg penicillin VK by mouth, twice daily; children less than 3 years old administer 125 mg penicillin VK by mouth, twice daily; Children between 3 and 5 years old administer 250 mg penicillin VK by mouth, twice daily (Booth et al., 2010; Sobota et al., 2015). Other therapeutic options include amoxicillin 20 mg/kg/day orally or bicillin 600 K units via IM every 4 weeks (Booth et al., 2010; Sobota et al., 2015).

1.3 Allosteric Effectors of Hb (AEH)

1.3.1 Mechanism of Action (MOA) of AEH

Allosteric effectors of Hb (AEH) represents a class of synthetic small molecules with aldehyde as their main functional group. Aldehyde group of AEH reversibly binds to N-terminal of α-chain of Hb via a transiently-covalent imine linkage (Schiff-base HbA-AEH adduct)(Ahmed et al., 2020). Several classes of these aromatic aldehydes bind and stabilize the R-state Hb, increasing the protein affinity for oxygen to which prevent HbS polymerization and concomitantly inhibit RBC sickling(Ahmed et al., 2020). For

example, 5-HMF (a furaldehyde) was under clinical investigation for treatment of SCD, however, terminated at Phase 2 clinical trial due to lack of efficacy presumably by extensive metabolism at target site (Oder, Safo, Abdulmalik, & Kato, 2016). The most predominant metabolites of 5-HMF in human was found to be 5-hydroxymethyl-2-furoic acid (HMFA), an inactive product formed by ALDH enzyme (Obied, 2010; Parikh, 2013). GBT-440 (a benzaldehydes), on the other hand, was successfully made to market for the treatment of SCD(Blair, 2020b).

Besides the primary MOA on increasing O_2-affinity of Hb for 5-HMF and GBT-440, some of the novel synthesized AEH also elicit a second O_2-independent MOA that directly destabilize the polymerization of HbS (Oder, Safo, Abdulmalik, & Kato, 2016; Ahmed 2020). Certain structure feature contributes to this second MOA. An *ortho*-positioned methoxypyridine substitution relatives to the aldehyde group on the benzaldehyde ring allows the compound to make interaction with a surface-located αF-helix that leads to destabilization of the HbS polymers (Oder et al., 2016). The αF-helix is involved in polymer stabilization and SCD patients with a rare mutation αAsn78→αLys78 on the F-helix show significantly fewer sickling episodes with improved clinical phenotype (Burchall & Maxwell, 2010; Rhoda et al., 1983).

1.3.2 Clinical Findings of Voxelotor (GBT-440)

As discussed in the section of therapeutic strategies of SCD, GBT-440 targets on Hb to increase its O_2 binding affinity, resulting in inhibition of HbS polymerization and RBC sickling. GBT-440 belongs to the AEH family. The following physicochemical properties of GBT-440 were collected from Scifinder (Web-based, CAS). GBT-440 is a

small (MW = 337) lipophilic aromatic aldehyde ($LogD_7$ = 4.07) (Figure 1.1). The pKa of GBT-440 is predicted to be 3.46 from the pyridine group and 7.67 from the phenol group. At physiological relevant pH of blood (pH 7.4), majority of GBT-440 are in neutral species. GBT-440 is sparingly soluble in aqueous phase, where the solubility is predicted to be 0.029 mM at pH 7 and 25 °C.

Total of 18 clinical trials of GBT-440 were found on the ClinicalTrail.gov website. 10 complete studies covered the regular Phase I to III studies, as well as special populations including pediatric, renal impairment, hepatic impairment or idiopathic pulmonary fibrosis (IPF) patients ("ClinicalTrials.gov.," 2020). Drug interactions of GBT-440 with caffeine, S-warfarin, omeprazole, or midazolam was also tested among 24 healthy precipitants("ClinicalTrials.gov.," 2020). 2 clinical trials on effect of GBT-440 on hypoxemia in healthy volunteers and IPF patients were terminated ("ClinicalTrials.gov.," 2020). 6 clinical trials are still ongoing, where the majority are faced to pediatric population (3 studies), 1 study on the tolerability of higher dose of GBT-440 (>1500 mg), 1 study on assessment of long-term treatment with GBT-440, and 1 new study on actigraphy improvement with GBT-440 ("ClinicalTrials.gov.," 2020).

1.3.2.1. Clinical Pharmacokinetics (PK)

GBT-440 followed dose-proportional PK in single ascending does SAD and multiple ascending dose (MAD) studies within tested strength (<2800 mg) (Hutchaleelaha et al., 2019). Absorption is rapid with plasma level peaked at around 2 – 4 hrs (median) when dose < 2000 mg (Hutchaleelaha et al., 2019). t_{max} in RBC was observed between 6 – 24 hrs (median) (Hutchaleelaha et al., 2019). AUC_{∞} and c_{max} in

plasma, RBC, and WB (WB) proportionally increased with increasing dose (100 – 2800 mg) (Hutchaleelaha et al., 2019). Plasma and RBC concentrations at SS were proportional to the increasing of dose (300, 600, 900 mg), indicating no auto-induction of enzyme within 118 days. In SCD patients, GBT-440 followed dose-proportional PK as well (500 – 1500 mg) (Hutchaleelaha et al., 2019). Inter-subject variability (%CV) for AUC_{∞} and c_{max} was below 22% for healthy volunteers receiving dose < 1000 mg, but between 22% - 36% with 2000 and 2800 mg(Hutchaleelaha et al., 2019). In SCD patients, %CV were below 28% in WB, but slightly higher in plasma (~35%)(*Multi-Discipline Review of Voxelotor*, 2019). Dissolution may explain the larger variability at higher dose and delayed t_{max} (7 hrs) at 2800 mg(Hutchaleelaha et al., 2019). Low-fat breakfast showed no significant effect on GBT-440 absorption, where a high-fat meal increased AUC with 42% and c_{max} with 45%(Hutchaleelaha et al., 2019; *Multi-Discipline Review of Voxelotor*, 2019). GBT-440 is recommended to be taken with or without food according to the F.D.A. label.

Steady-state was achieved at 15 days in healthy volunteers and the exposure was accumulated 6-fold approximately(Hutchaleelaha et al., 2019). In SCD patients, steady-state was reached by day 8 and around 3-fold accumulation was observed(*Multi-Discipline Review of Voxelotor*, 2019). The dosing interval was the same as once daily across studies. The terminal decline in plasma, WB, and RBC are parallel. The terminal half-life in healthy volunteers was around 61 – 85 hrs, while in SCD patients was shorter with approximately 36 hrs, which probably due to low Hb level of SCD patients(Hutchaleelaha et al., 2019). The long terminal half-life suggests once-daily dosing regimen.

GBT-440 was highly bound to plasma protein (99.8%) in a dose-independent manner(*Multi-Discipline Review of Voxelotor*, 2019). RBC/plasma ratio calculated by AUC_{∞} were reported to range from 67:1 to 111:1 from phase I study(Hutchaleelaha et al., 2019). Though PPB is high, it is expected to be low affinity and high capacity, while Hb binding of GBT-440 is expected to be high affinity and low capacity (saturable binding). This High Hb binding affinity is believed to drive GBT-440 into RBC, resulting in a high RBC/plasma ratio. In SCD patients, blood-to-plasma ratio was reported as 15-17 from the multi-disciplines review report of F.D.A.. The primary research data on how the blood-to-plasma ratio was calculated is not available, which may help to explain the large discrepancy on RBC partitioning of GBT-440 between healthy volunteers and patients. Low Hb level in SCD patients may contribute to the lower RBC partitioning. Regardless, the WB disposition of GBT-440 is toward RBC rather than stay in plasma.

In the mass balance study with a single dose of 400 mg GBT-440, 63% was recovered in feces including 33% as the parent compound form, indicating GBT-440 was not well absorbed in gut or eliminate through biliary excretion(*Multi-Discipline Review of Voxelotor*, 2019). 35% (metabolites and parent compound) was recovered in urine, where only 0.08% excreted unchanged, indicating renal elimination for parent compound is negligible and the majority of GBT-440 was metabolized before excretion via kidney(*Multi-Discipline Review of Voxelotor*, 2019). Absolute oral bioavailability was not tested, however, from the results of its mass balance study, where majority of the drug was excreted unchanged in feces and only 0.08% unchanged in urine, oral bioavailability of GBT-440 is predicted to be low to moderate.

GBT-440 is metabolized primarily by CYP450, UGT, and SULT enzymes. When GBT-440 was co-administrated with CYP3A4 inhibitor, midazolam to healthy volunteers, the exposure was increased by around 75%(*Multi-Discipline Review of Voxelotor*, 2019). A PBPK model based on *in-vitro* metabolism and ADME studies predicted an increase of exposure by 73% - 100% with concomitant administration of fluconazole (moderate CYP3A/CYP2C9, strong CYP2C19)(*Multi-Discipline Review of Voxelotor*, 2019). Daily dose of GBT-440 is recommended to be reduced to 1000 mg when co-administrated with strong CYP3A4 inhibitor or fluconazole(*Multi-Discipline Review of Voxelotor*, 2019).

Part of results on GBT440 on pediatric population was published in an abstract in a meeting of European hematology association at 2018. 6 children received single dose of 600 mg GBT-440 capsule, and 25 adolescents received 900 mg daily for up to 24 weeks(Washington et al., 2018). WB and plasma concentration were collected up to 15 days after single dose and 24 weeks for multiple dose administration. Authors applied a two-compartmental PK model for data analysis, and concluded as similar PK exposure among adolescents and adults (Washington et al., 2018). Authors also mentioned higher PK exposure was observed in children than adolescents(Washington et al., 2018). F.D.A. approved the use of GBT-440 for adolescent at the same dose regimen as adult (1500 mg QD). The original data supported this dosing regimen in adolescents has not been published yet. Regarding children, no dosing regimen was recommended from F.D.A., but an ongoing clinical trial on children may provide essential information for the approval of the use of GBT-440 in children.

The clinical results on 16 renal impairment subjects (900 mg) are consistent to the findings in mass balance study, that the renal elimination of GBT-440 is a minor

pathway. The geometric mean of AUC_{0-24} and c_{max} in WB with renal impairment were 80% and 84% compared to healthy volunteers(Blair, 2020b; *Multi-Discipline Review of Voxelotor*, 2019). AUC_{0-24} and c_{max} in plasma with severe renal impairment was 60% and 56% compared to healthy volunteers(*Multi-Discipline Review of Voxelotor*, 2019). The lower exposure of GBT-440 in severe renal impairment subjects may due to the lower albumin level in plasma, which increased the unbound fraction of GBT-440 for hepatic metabolism. Anemia caused by severe renal impairment may also further increase the free GBT-440 from Hb binding for hepatic metabolism. No dose adjustment is required for GBT-440 from F.D.A. for subjects with severe renal impairment.

GBT-440 was studied in mild (Child-Pugh A, n = 7), moderate (Child-Pugh B, n = 7) and severe (Child-Pugh C, n = 7) hepatic impairment subjects, as well as normal subjects (n = 7)(Han et al., 2020). The geometric mean ratio of the dose normalized AUC_{∞} for mild, moderate or severe hepatic impairment group to normal group were 1.14, 1.15, and 1.90 respectively(*Multi-Discipline Review of Voxelotor*, 2019). F.D.A. recommended no dose adjustment for mild and moderate hepatic impairment, but reduced to 1000 mg of GBT-440 for severe hepatic impairment patients.

1.3.2.2. Clinical Pharmacodynamics (PD)

In the Phase I/II study (Clinical trial: GBT440-001), the primary PD endpoints at steady-state were p_{50} and p_{20} shift (the pO_2 at 50% and 20% of Hb saturated with O_2) and the percentage modified Hb derived from oxygen-equilibrium curve(Howard et al., 2019; Hutchaleelaha et al., 2019). The secondary PD measurements were changes in

bilirubin, lactate dehydrogenase, reticulocyte counts, which were biomarkers of hemolysis. GBT-440 showed dose-dependent p_{50} and p_{20} decrease, indicating enhanced O_2 binding affinity of Hb(Howard et al., 2019; Hutchaleelaha et al., 2019). Additionally, all hemolysis biomarkers also showed does-dependent decrease(Howard et al., 2019; Hutchaleelaha et al., 2019). The incidences of adverse events (AEs) were mild to moderate and were comparable among three arms (300, 600, 900 mg). 900 mg was selected for Phase III study, and a higher dose 1500 mg was designed intended to achieve higher efficacy.

In the Phase III study (Clinical trial: GBT440-031), the primary PD endpoints were the proportion of patients achieving the change of Hb level ≥ 1 g/dL from week 24 to baseline(Vichinsky et al., 2019). 59% of the patients (n =74) with 900 mg achieved the primary Hb response, while 38% in 900 mg (n = 79) and 9% in placebo (n = 76), regardless of HU use or anemia severity at baseline(Vichinsky et al., 2019). The adjusted mean changes in Hb level from week 24 to baseline was 1.1 g/dL, 0.6 g/dL, and -0.1 g/dL for 1500 mg, 900 mg of GBT-440 and placebo, respectively(Vichinsky et al., 2019). Literature indicated an increase of Hb level is associated to decrease of multiorgan failure and death(Vichinsky et al., 2019). Actual effect of GBT-440 on morbidity and mortality among patients were not evaluated, however, a long-term follow-up studies are planned next(Vichinsky et al., 2019). GBT-440 reduced in incidences of hemolysis, indicated by the significantly decreased of bilirubin level and increased of the percentage of reticulocytes in 1500 mg group from week 24 to baseline(Vichinsky et al., 2019). Lactate dehydrogenase level and reticulocyte count also showed numerically but no significant decrease in 1500 mg group(Vichinsky et al.,

2019). The incidences of acute vaso-occlusive crises were not significantly difference among three groups, where the percentages of participants who received blood transfusions during clinical trials are similar among treatment and placebo groups(Vichinsky et al., 2019). Long-term effect of GBT-440 on frequency of SCD related complications including vaso-occlusive were planned for a Phase III extensive clinical trial (NCT035573882)("ClinicalTrials.gov.," 2020). In summary, GBT-440 showed a rapid directly pharmacological effect on increasing Hb level and decreasing hemolysis within 2 weeks and sustain to 24 weeks. The long-term effect of GBT-440 on improvement of vaso-occlusive crises and other SCD related complications are needed. The percentage of participants who reported serious AEs were low and similar among treatment and placebo groups(Vichinsky et al., 2019). To maximize the therapeutic effect with safety permission, 1500 mg daily was recommended by F.D.A..

1.4 Relevant Metabolic Enzymes

1.4.1 Aldehyde Dehydrogenase (ALDH)

Aldehydes are highly reactive electrophilic compounds, involved in many physiological and therapeutic effects, as well as cytotoxic, genotoxic, and mutagenic or carcinogenic problems(Vasillou, Pappa, & Estey, 2004). Aldehydes are primarily detoxified through phase I enzymatic reactions. One of the most important pathways is through oxidative metabolism by ALDH.

In ALDH superfamily, sixteen genes have been identified, among which the class 1 (ALDH-1) and class 2 (ALDH-2) are most abundantly expressed and well-studied(Yoshida, Rzhetsky, Hsu, & Chang, 1998). Both ALDH-1 and ALDH-2 are homotetramers (Liu et al., 1997). ALDH-1 is mainly located in cytosol, and widely expressed in various tissue including liver and RBC (Vasillou et al., 2004). ALDH-2 is a mitochondrial enzyme, and widely expressed in various tissue with highest levels found in liver (Vasillou et al., 2004). AEH with the functional aldehyde group is expected to subject to ALDH-1 metabolism on the RBC target site. ALDH-1 in both RBC and human liver cytosol (HLC) share similar physical, chemical, and kinetic properties. HLC is selected as the biomatrix to screen ALDH-mediated metabolism for AEH(Ryzlak & Pietruszko, 1987). ALDH mentioned in this research specifically referred to ALDH-1.

The oxidation of aldehyde to the corresponding carboxylic acid by ALDH requires the presence of cofactor nicotinamide adenine dinucleotide (NAD^+)(Liu et al., 1997). *In-vitro* study showed that ALDH can oxidize a broad spectrum of both aliphatic and aromatic aldehydes with different binding affinities (K_m)(Vasillou et al., 2004). This

cytosolic enzyme shows high binding affinity on retinal (K_m < 0.1 μM) and acetaldehyde (K_m < 100 μM), two prototypical substrates of ALDH(Vasillou et al., 2004). Binding affinity of ALDH of aromatic aldehydes are vary for substrate with different structures(Marchitti, Brocker, Stagos, & Vasiliou, 2008; Vasillou et al., 2004).

1.4.2 Other Metabolic Enzymes for Aldehydes

As discussed earlier, AEH may subject to ALDH-mediated metabolism, and HLC is selected as the biomatrix for the study. A typical method to characterize ALDH activity on a substrate is to measure NADH, the reduced form of the cofactor NAD^+(Liu et al., 1997; Marchitti et al., 2008; Vasillou et al., 2004). In HLC, other oxidative and reductive enzymes may also react with aldehydes with or without co-factor NAD^+, including aldehyde oxidase (AO) and alcohol dehydrogenase (ADH)(Marchitti et al., 2008).

AO is a molybdenum cofactor-containing soluble enzyme, located in liver and other tissues, but not in RBC(Marchitti et al., 2008). AO catalyzes the oxidation of a broad substrate with low-specificity, including aromatic azaheterocycles and various aldehydes, such as benzaldehyde, retinal, pyridoxal, and vanillin (Wroczyński & Wierzchowski, 2000). AO has several cofactor binding sites, including iron-sulfur protein (2Fe-2S clusters), flavin adenine dinucleotide (FAD), and molybdopterin cofactor (MoCo)(Parikh, 2013). The reaction involves converting electron accepter (O_2 or electron accepters) and water molecules (H_2O) to hydrogen peroxide (H_2O_2), while an aldehyde is converted to carboxylic acid("Uniport.org. Accessed June-01," 2020). *In-vitro* study showed the K_m of AO on benzaldehyde to be 5 μM and 45 μM in the presence of 2,6-dichlorophenol indophenol and ferricyanide as electron acceptors,

respectively(Foti et al., 2016). In HLC system, without addition of electron acceptor, the oxidation of AO on aromatic aldehydes may have limited influence on characterization of ALDH-mediated metabolism for AEH.

ADH is a dimeric-enzyme that catalyze the interconversion of alcohols and their corresponding aldehydes(Obied, 2010). There are seven different ADH isozymes in human, where three belongs to class I (ADH-1), one to class II (ADH-2), one to class III (ADH-3), one to class IV (ADH-7) and one to class V (ADH-6)("Uniport.org. Accessed June-01," 2020). ADH-1 and ADH-2 are cytosolic enzyme primarily expressed in liver, while ADH-3 is present in liver and other tissues(Obied, 2010). ADH can metabolize primary, secondary, and tertiary alcohols that are primarily aliphatic and to a lesser degree of cyclic(Obied, 2010). Ethanol is a known substrate of ADH with K_m of low millimolar range (0.05 – 4 mM for class 1, and 30 mM for class II, IV, V)(Obied, 2010). Benzaldehyde is not a substrate to ADH, while the alcohol group on furan ring (e.g. 5-HMF) has been reported to be metabolized by ADH(Obied, 2010). *In-vitro* studies showed that in the presence of the ADH inhibitor, i.e., methylpyrazine, the oxidation of 5-HMF was reduced in HLC(Obied, 2010). Co-factor NAD^+ is required for oxidation of alcohols and NADH is required for reduction of aldehydes(Jelski, Zalewski, & Szmitkowski, 2008). ADH is present in HLC but not in RBC, which may complex the extrapolation of ALDH-mediated metabolism of AEH in HLC to RBC.

Other Non-CYP450 enzymes may involve in aldehyde metabolism, including aldo-keto reductase (AKR) and short chain dehydrogenase/reductase (SDR)(Marchitti et al., 2008). AKR is present in HLC and lysosome, but need NADPH as cofactor to reduce aldehydes("Uniport.org. Accessed June-01," 2020). SDR catalyzes the reduction

of retinal in presence of NADPH(“Uniport.org. Accessed June-01,” 2020). Therefore, these enzymes will not affect the characterization of ALDH-mediated metabolism of AEH in HLC through measurement of NADH.

1.4.3 Cytochrome P450 (CYP450)

A broad spectrum of substrates can be catalyzed by CYP450 (Manikandan & Nagini, 2017). Many aromatic drugs covering wide therapeutic area have been approved to be substrates of CYP450, such as anti-virus (Darunavir, CYP3A4), anti-histamine (Meclizine, CYP2D6), anesthetic (Ropivacaine, CYP1A2, CYP2B6, CYP3A4) drugs(“Drugbank.ca. Accessed June-07,” 2020). However, the specificity of CYP450 on aromatic aldehydes has not been systemically studied. AEH, as xenobiotic aromatic aldehyde, may become substrates of CYP450 in liver, where CYP450 may serve as important elimination pathway for AEH, but may also decrease oral bioavailability from first-past metabolism. AEH may also be inhibitor or inducer of CYP450, which will influence the elimination of other drugs that are mainly eliminated through CYP450.

Human CYP450 are membrane-bound enzyme system found on endoplasmic reticulum (ER) and mitochondrion of cells that play a pivotal role in detoxification of xenobiotics, cellular metabolism and homeostasis(Manikandan & Nagini, 2017). CYP450 are hemoproteins with 400-500 amino acid residues(Manikandan & Nagini, 2017). The typical monooxygenation reaction of CYP-450 is via incorporation of one oxygen into substrate (Scheme 1.1) (Manikandan & Nagini, 2017).

$$\mathbf{RH + O_2 + 2e^- + 2H^+ \rightarrow ROH + H_2O} \qquad \text{----} \qquad \textbf{Scheme 1.1}$$

Energy is required in this reaction supplied by the transfer of electrons from NADPH through FAD (Manikandan & Nagini, 2017). CYP450 are widely expressed in various tissue, mainly in liver. The classification of CYP450 based on major substrate class and the functions of CYP450 gene families are listed in table 1.1 and 1.2 (Manikandan & Nagini, 2017).

Some CYP450 families can be inhibited by various xenobiotics, which is essential in therapeutic area since CYP450 are the major enzymes in metabolism of many drugs. The inhibition can be classified as reversible and irreversible (mechanism-based) inhibitions. Competitive inhibitor reversibly binds to the same binding site as other substrate, which decreases the apparent binding affinity, characterized by K_m' of the substrate but does not influence the maximum rate of metabolism (v_{max}'). Non-competitive inhibitor reversibly binds to allosteric site of enzyme, which reduces the v_{max}' but has the same K_m' as no inhibitor presence. Uncompetitive inhibitor reversibly binds to enzyme-substrate complex, which decreases the v_{max}' and increases K_m'. Mechanism-based inhibitor covalently binds to enzyme, which reduces the amount of active enzyme to other substrate resulting in reduced v_{max}'. For the market drugs acting as CYP450 inhibitors, most are competitive inhibitors, which means, the elimination of the victim drug is reduced in presence of these inhibitor (perpetrator drugs), a lower dose of victim drug is needed to prevent toxic accumulation of drug in body("FDA.gov/drugs/drug-interactions-labeling [online]. Accessed June-07," 2020). Some prototypical CYP450 substrates serve as probes to test inhibitors in drug-drug interaction studies, for example, midazolam (CYP3A4), warfarin (CYP2C9), omeprazole (CYP2C19), and caffeine (CYP1A2), metoprolol (CYP2D6), and rosiglitazone

(CYP2C8)(“FDA.gov/drugs/drug-interactions-labeling [online]. Accessed June-07,” 2020).

Some CYP450 can also be induced by drugs through transcription factors, such as aryl hydrocarbon receptor (AhR) for CYP1A1, CYP1A2, and CYP1B1, pregnane nuclear receptor (PXR) for CYP3A, constitutive androstane receptor (CAR) for CYP2B(Manikandan & Nagini, 2017). Unlike inhibition effect that can be seen rapidly after inhibitor is onboard, induction of enzyme is much slower through modification of gene, followed by the level change of mRNA and the production of CYP450 enzymes. When CYP450 is induced, the corresponding substrate concentration is reduced, in order to achieve the same therapeutic effect, a larger dose of victim drug is needed to achieve the same desirable drug level on target site.

Table 1.1. Classification of CYP450 based on major substrate class.

Class of Substrates	CYP450 Enzymes
Sterols	1B1, 7A1, 7B1, 8B1, 11A1, 11B1, 11B2, 17A1, 19A1, 21A2, 27A1, 39A1, 46A1, 51A1
Xenobiotics	1A1, 1A2, 2A6, 2A13, 2B6, 2C8, 2C9, 2C18, 2C19, 2D6, 2E1, 2F1, 3A4, 3A5, 3A7
Fatty acids	2J2, 4A11, 4B1, 4F12
Eicosanoids	4F2, 4F3, 4F8, 5A1, 8A1
Vitamins	2R1, 24A1, 26A1, 26B1, 26C1, 27B1
Unknown	2A7, 2S1, 2U1, 2W1, 3A43, 4A22, 4F11, 4F22, 4V2, 4X1, 4Z1, 20A1, 27C1

Table 1.2. Functions of CYP450 gene families.

CYP450 Family	Functions
CYP1-4	Biotransformation of xenobiotics, chemicals and drugs
CYPs 5 and 8	Thromboxane and prostacyclin biosynthesis
CYPs 11, 17, 19, and 21	Hydroxylations required for the biosynthesis of bile acids, activated vitamin D3, and cholesterol
CYP26	Hydroxylation of retinoic acid

CHAPTER 2

HYPOTHESES, SPECIFIC AIMS, AND SIGNICANCE

2.1. Hypotheses

Allosteric effectors of hemoglobin (AEH) represent a class of synthetic aromatic aldehydes for the development of therapeutic use in Sickle Cell Disease (SCD). AEH have been shown *in-vitro* and *in-vivo* to bind to Hb in a transiently-covalent manner, increasing oxygen binding affinity of Hb and decreasing hypoxia-induced sickle Hb (HbS) polymerization(Oder et al., 2016). The main objectives of this research are 1). To understand the primary mechanism of action (MOA) of the AEHs, by fully characterizing concentration- and time-dependent profiles of selected AEH binding to Hb. Compounds with large structural and functional diversity were selected for structure-activity relationship (SAR) study. 2). To investigate their ALDH susceptibility; and 3). To integrate the underlying disposition mechanisms of WB (WB) using quantitative kinetic models. Therefore, the hypotheses of this research are as follows:

1) AEH exhibit concentration- and time-dependent binding to Hb. Due to the absence of metabolic enzymes in HbA solution, all AEH are expected to achieve steady-state and sustain Hb-AEH adduct level in HbA solution. Specific structural modifications of AEH affect their Hb binding affinity and binding kinetics.
2) Since the primary mechanism of action (MOA) involves aldehyde functional group of AEH and ALDH is known to be present in red blood cell (RBC), AEH

can undergo ALDH-medicated metabolism. Specific structural modifications of AEH can reduce ALDH-medicated metabolism at target site (RBC).

3) Since human liver cytosol (HLC) and RBC share the same isoform of ALDH-1 enzyme. *In-vitro* metabolic findings in HLC are expected to be translatable to *in-vitro* RBC metabolism for AEH.
4) AEH bind to Hb in a concentration- and time-dependent manner in WB. Several processes including plasma protein binding (PPB), red blood cell membrane binding/crossing, ALDH-mediated metabolism in RBC, may affect their WB binding kinetics and decrease apparent binding affinity in WB.
5) AEH with no evidence of *in-vitro* ALDH-mediated metabolism can achieve steady-state and sustain Hb-AEH adduct levels in WB. Whereas AEH that undergoes *in-vitro* ALDH-mediated metabolism, the Hb-AEH adduct levels in WB will decrease after a peak and steady-state cannot be achieved.

2.2. Specific Aims

To address the objectives and hypotheses listed in section 2.1, the following specific aims are proposed:

<u>Specific Aim 1</u>: Characterize, assess and compare concentration- and time-dependent Hb binding of AEHs in HbA solution.

1) Develop and validate a universal LC-UV assay method to quantitate Hb-AEH adduct in HbA solution.
2) Investigate *in-vitro* time- and SS concentration-dependent Hb binding of selected AEH in HbA solution with optimized experimental conditions.

3) Develop quantitative kinetic and SS models to fit experimental data and obtain relevant parameters. Characterize and compare the HbA binding profiles among different AEH, and select AEH with high HbA binding affinity and fast binding kinetic for further testing in WB.
4) Conduct SAR studies on Hb binding affinity and binding kinetics of AEH to provide information on molecular design for future drug development.

Specific Aim 2: Characterize, assess and compare *in-vitro* metabolism of AEH in human liver cytosol (HLC)

1) Verify ALDH-enzyme activity in HLC using the prototypical substate, acetaldehyde. Monitor the UV/Vis absorption interference of AEH on measurement of co-factor of NADH formation.
2) Characterize *in-vitro* metabolism of AEH in HLC, assess and compare ALDH-mediated metabolism among selected AEH.
3) Select AEH that are resistant to the ALDH-mediated metabolism in HLC for further testing in WB disposition studies.

Specific Aim 3: Characterize the *in-vitro* WB disposition of the selected AEH.

1) Develop and validate a universal LC-UV assay method to quantitate Hb-AEH adduct in WB.
2) Develop and validate a LC-UV assay method to quantitate the selected AEH in plasma.
3) Characterize *in-vitro* WB disposition of selected AEH and compare to its binding in HbA solution.

4) Characterize and compare Hb-AEH adduct binding profiles of selected AEH with 5-HMF in WB.
5) Develop quantitative PK/PD model to characterize HbA-AEH adduct binding kinetics and to integrate the underlying WB disposition mechanisms of selected AEH.

2.3. Significance

SCD is characterized primarily by a chronic, severe hemolytic anemia, leading to vascular occlusion, tissue infection, painful “crises” and, eventually, and chronic organ damage(Piel et al., 2017). Both life-quality and life-span are extensively affected by this chronic disease. On the average, life expectancy of SCD patients is reduced by about 30 years(Bunn & Forget, 1986). Based on a 2017 review, approximately 100,000 people live with SCD in the United States, and 300,000 babies are born with SCD per year worldwide(Piel et al., 2017).

Common clinical management includes administration of analgesics and blood transfusions for symptom relief. Four F.D.A.-approved drug treatment options are available for SCD, including hydroxyurea, voxelotor (GBT-440), crizanlizumab and L-glutamine. Noticeably, voxelotor is an AEH that targets Hb and prevents hypoxia-induced HbS polymerization and RBC sickling by increasing O_2 binding affinity of Hb (Vichinsky et al., 2019). Nonetheless, F.D.A. approval of voxelotor for SCD was based on significantly increased Hb levels and reduced hemolysis in patients, considered to be clinically relevant, rather than pertinent long-term clinical outcomes(*Multi-Discipline Review of Voxelotor*, 2019; Vichinsky et al., 2019). Moreover, as the first approved therapy

targeting the Hb in SCD, Voxelotor is very costly. Global Blood, the company discovered voxelotor, set a list price of $10,417 a month for the drug. To give health provider multiple choices of AEH, and reduce the current high cost of the only approved AEH, and aid in future development of potentially more effective AEH drug candidates with better PK/PD properties, several *in-vitro* studies on screening novel synthetic AEH were conducted in this research.

AEH has been studied over 30 years. Prior to voxelotor clinical trials, the VCU lead compound, 5-HMF successfully passed Phase I study, but failed at Phase II due to poor PK properties. Our group has discovered a new class of novel AEH with the same MOA of O_2-dependent anti-sickling activity as 5-HMF and voxelotor. Some of these compounds exhibit an additional mechanism of anti-sickling activity by directly destabilizing HbS polymerization. This novel oxygen-independent anti-sickling MOA is due to the compounds interacting with the surface-located F-helix (Abdlumalik, **D67**, 920–928 (2011)). Crystal structures of these novel AEH have been published to explain their MOA on atomic level (Oder et al., 2016; Pagare et al., 2018). Despite these studies, no systematic studies have been performed on their *in-vitro* time- and SS concentration-dependent binding with the primary target Hb, as well as their *in-vitro* ALDH-mediated metabolism. This is the first study to fully characterize and understand kinetic binding of AEH to Hb, and discover the underlying SAR, which is beneficial for guiding future molecular design. It is also essential to assess the role of ALDH-enzyme to *in-vitro* metabolism of selected AEH, which when combined with the Hb binding study can provide early screening for selecting promising AEH candidates for further development. In this research, we use experimentally and quantitatively modeling approach to

understand AEH primary binding to Hb, metabolic stability in HLC and the disposition and biological activities in WB from healthy human volunteers.

CHAPTER 3

IN-VITRO SS CONCENTRATION- AND TIME-DEPENDENCY OF HBA-AEH ADDUCT FORMATION IN HBA SOLUTION

3.1 Introduction

As discussed in Chapter 1 of the introduction section, AEH bind "transiently covalently" via Schiff-base reaction with α globin chains of Hb in RBC that formed Hb-AEH adduct to increase O_2 - affinity of Hb, decrease polymerization of HbS and inhibit RBC sickling. The Schiff-base reaction has been reported to be a concentration- and time-dependent binding based on the previous studies with 5-HMF (Obied, 2010; Parikh, 2013). 5-HMF binding to Hb in HbA and HbS solutions has been studied using an HPLC-UV/Vis ultrafiltration assay to determine free 5-HMF concentration, which decreased in a concentration- and time-dependent manner in Hb solution (Obied, 2010; Parikh, 2013). Endogenous moiety, e.g. glucose, has also been reported to bind to Hb via Schiff-base reaction in a concentration- and time-dependent manner (Ge & Lee, 1997). The formed Schiff-base further undergoes Amadori rearrangement to form $HbA1_C$, which is used widely in clinic as a surrogate endpoint and diagnose for diabetes. Unlike 5-HMF, where dissociation from Hb is slower than association to Hb, glucose is found to be 1,000 times slower in associating to Hb than dissociating, followed by Amadori rearrangement (Ge & Lee, 1997; Parikh, 2013).

Isolated HbA solution instead of HbS is normally the matrix used for characterizing AEH binding to Hb because of easy accessibility. HbS differs from

normal HbA by only a single base substitution (mutation) of the (polar) β6-glutamic acid by the neutral amino acid, valine (Bunn & Forget, 1986). The overall fold of both HbA and HbS structures are identical with only minor localized structural differences at the βVal6 mutation site (Safo et al., 2011). AEH is known to bind to the N-terminal Val1 nitrogen on α-subunits of the Hb molecule, which is identical in HbA and HbS. It is expected therefore that the binding kinetics of AEH to HbA and HbS are similar. Previous results on 5-HMF support this hypothesis, where the estimated binding affinities are almost identical (K_D^{HbS} = 0.13 mM (17%); K_D^{HbA}= 0.18 mM (4%)) with only slight intrinsic kinetic differences between HbA and HbS solution (k_{on} = 0.27 ± 0.03% and 0.83 ± 0.13% $mM^{-1}hr^{-1}$, respectively, and k_{off}= 0.05 ± 0.01% and 0.1 ± 0.04% hr^{-1}, respectively).

Various analytical methods has been reported for 5-HMF quantification in both non-biological and biological matrices (Abdulmalik et al., 2005; Driffield et al., 2005; Menez et al., 1984; Michail et al., 2007; Obied, 2010; Standefer & Eaton, 1983). More recently, LC-MS/MS was reported for quantification of 5-HMF in biological matrices, with the advantages of improved detection limit, not having to deal with absorption interference compared to UV detection, and identification of multiple interest of analytes in complex system (Hardt-Stremayr et al., 2012; Lin et al., 2008; Zhang et al., 2012). However, besides the high cost involved in LC-MS system, it also requires more tedious sample preparation processes.

In this study, we aimed to characterize the binding kinetics of AEH to Hb, either via quantification of AEH or Hb / Hb-AEH adduct. Since Hb solution is a relatively clean matrix with little UV/Vis absorption interference after ultrafiltration process, our previous

lab members developed an HPLC-UV/Vis assay method on 5-HMF (reference assay method). This involves, first reacting 5-HMF with Hb and passing through a filter with a cutoff 10 kD, and then determining free 5-HMF concentration using with a C_{18} column. Unfortunately, this ultrafiltration method is not applicable to compounds with high non-specific membrane binding on filter, including lipophilic AEH, e.g. INN-312, a benzaldehyde (Parikh, 2013). Unlike 5-HMF (cLogP = - 0.1), most of the AEH selected in this research are lipophilic compounds (cLogP =1.3 - 3.5) that are expected to highly bind to the filer membrane. Therefore, the previous reference assay method is not suitable for novel selected lipophilic AEH, necessitating the development of a new analytical method.

A novel “universal" assay method was designed that allows measurement of Hb-AEH adduct of chemically different AEH, rather than individual AEH molecule, thus allowing its use across a series of AEH (furaldehydes and benzaldehydes). This method involves a weak cation-exchange HPLC-UV/Vis assay to separate HbA-AEH adduct from free Hb. Similar analytical methods have been used to readily separate and quantify various Hb from RBC lysates, as well as for qualitative screening of Hb variants, with the benefits of high efficiency and little sample preparation time (Kutlar, Kutlar, Wilson, Headlee, & Huisman, 1984; Ou, C.-N., & Rognerud, 1997; Ou, Buffone, & Reimer, 1983). Cation-exchange HPLC has also been used for kinetic analysis of glycated Hb, aspirin-acetylated Hb and acetaldehyde Hb-adducts (Itala, Seppa, Turpeinen, & Sillanaukee, 1995; Turpeinen, Stenman, & Roine, 1989). The separation of Hb variants and Hb-adducts is based on their different isoelectric point (pI), as well as the different pH and ion concentrations of mobile phases. In our assay, AEH modified

Hb (Schiff-base Hb-AEH Adduct) decrease the pI of Hb, i.e. becomes more anionic than the free Hb, which allows the separation from free Hb (Adducts, Zaugg, Walder, & Klotz, 1977).

A library of ten structurally different AEH (5-HMF, 2,5-DMF, vanillin, TD-8, TD-9, TD-7, INN-310, PP-14, VZHE-039, and GBT-440, Figure 3.1) were selected for their HbA binding kinetic characterization, based on their varying *in-vitro* functional and anti-sickling effects. WB obtained from SCD patients were incubated with each AEH separately for 2 hrs, where the % Hb-AEH adduct formation and % sickling inhibition were measured (Abdulmalik, 2018). All tested AEH (n = 8) showed concentration-dependent HbS adduct formation (Figure 3.2). Three AEH (VZHE-039, PP-14, and INN-310) were chosen for their potently modifying HbS (100% HbS-AEH adduct) at 2 mM (Pagare et al., 2018). Three isomers (TD-7, TD-8, TD-9) were chosen because of their different HbS binding profiles(Deshpande et al., 2018), which may due to different primary target (Hb) binding affinity and/or binding kinetics, as well as ALDH-mediated metabolism that reduced AEH concentrations in RBC. Vanillin, the parent compound of the eight chosen benzaldehydes, was included as negative control. GBT-440 (voxelotor), currently approved for the treatment of SCD was chosen as the positive clinical reference (Han et al., 2020; *Multi-Discipline Review of Voxelotor*, 2019). Two furaldehydes, i.e., 5-HMF and 2,5-DMF were included to cover VCU lead compound and enlarge structural variability for SAR study (Xu et al., 2017).

The functional/biological results described above for the 10 selected in WB were lack of kinetic binding information. In addition, the WB environment cannot distinguish the underlying mechanisms that result in different Hb binding profiles, which include Hb

binding kinetic, ALDH-mediated metabolism, PPB, and/or RBC membrane binding/partitioning. This chapter is aimed to study AEH binding to the primary target, i.e., Hb, to characterize their binding kinetics. SS concentration-dependency studies were designed to estimate the primary binding affinity and capacity, as well as time-dependency studies for characterization of kinetic reactions via the estimation of the corresponding rate constants and equilibrium half-lives.

Figure 3.1. Structure of selected AEH.

5-HMF

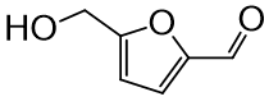

2,5-DMF

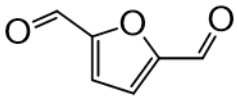

Vanillin

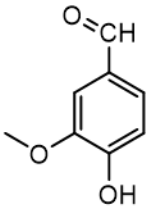

TD-7

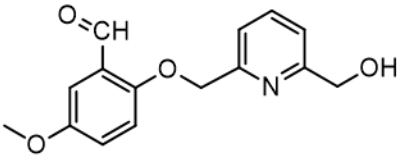

TD-8

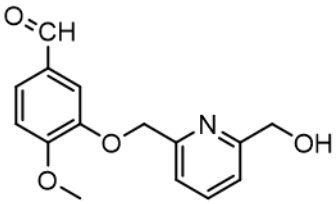

TD-9

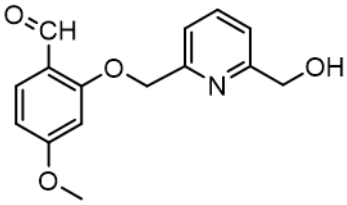

PP-14

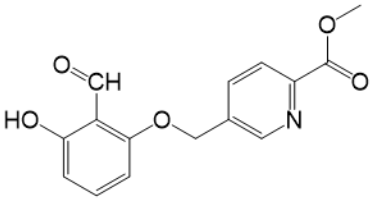

INN-310

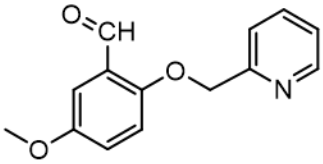

VZHE-039

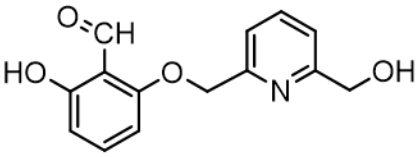

GBT-440

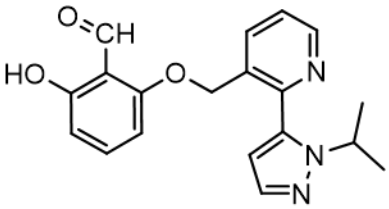

Figure 3.2. AEH selection: *in-vitro* concentration-dependency of HbS-AEH adduct formation in SCD WB at 2 hrs. Smooth lines connected the experimental data (symbols) for visual inspection.

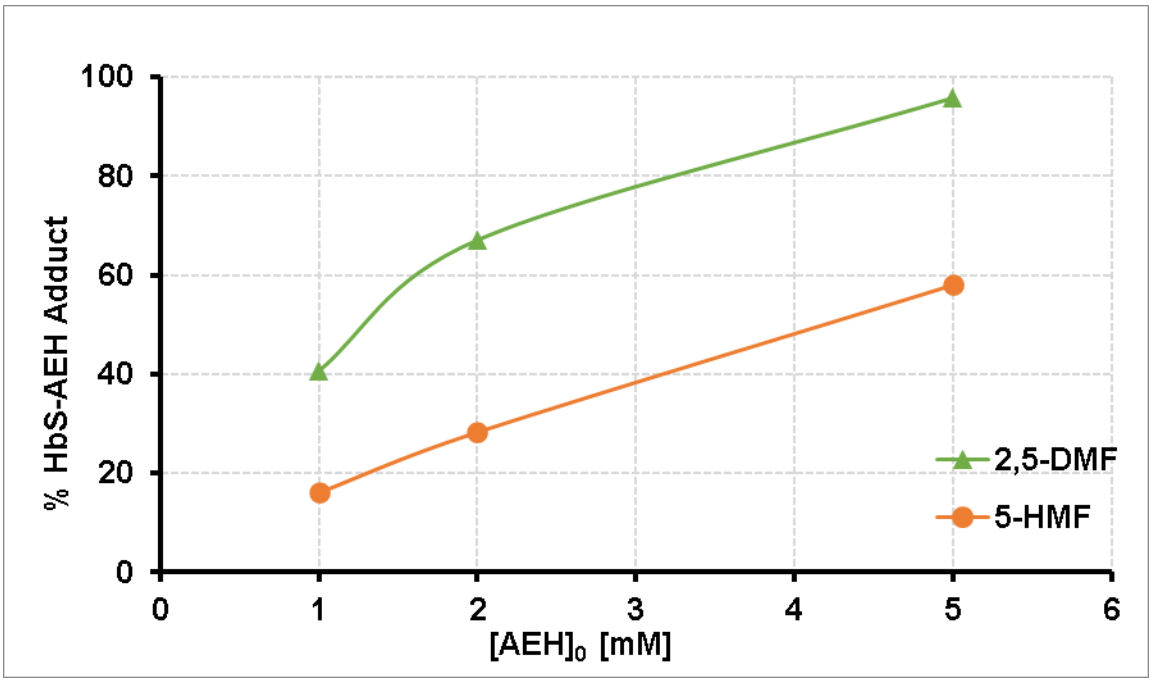

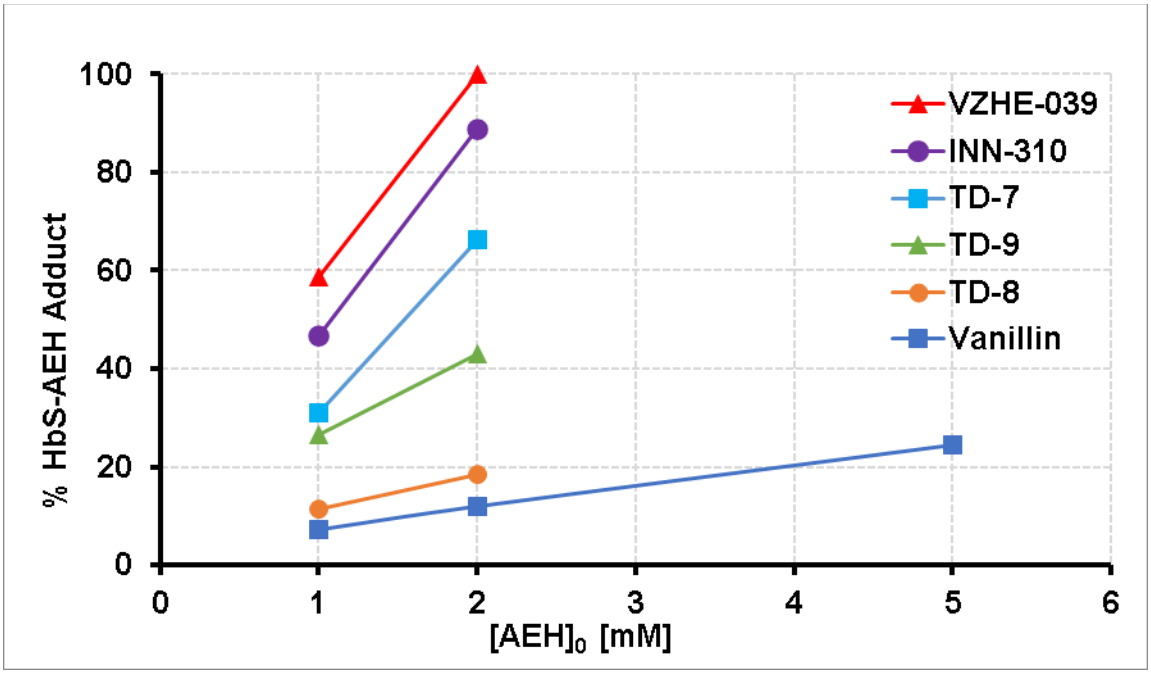

3.2 Methods

3.2.1 Materials and Reagents

1. NERL® high purity water (Fisher Scientific, Nazareth, PA)
2. Bis-tris (Sigma-Aldrich, St.Louis, MO) (209.24 g/mol)
3. Potassium cyanide (Sigma-Aldrich, St.Louis, MO) (KCN, 65.12 g/mol)
4. Sodium chloride (Sigma-Aldrich, St.Louis, MO) (NaCl, 58.44 g/mol)
5. HbA solution (isolated and concentrated by Dr. Martin Safo's lab, Department of Medicinal Chemistry, VCU) (12.60 g/dL)
6. AFSC Hemo Control (Cat. No. 5331) (Helena laboratories, Beaumont, TX)
7. Methanol, HPLC grade (Burdick and Jackson, Morristown, NJ)
8. Hydrochloric acid, ACS 37% (Sigma-Aldrich, Milwaukee, WI) (HCl ,36.46 g/mol)
9. Sodium cyanoborohydride (sigma-aldrich, St.Louis, MO) ($NaBH_3CN$, 62.84 g/mol)
10. Sodium borohydride (sigma-aldrich, St.Louis, MO) ($NaBH_4$, 37.84 g/mol)
11. 5-Hydroxymethyl-2-furfural (5-HMF) (Sigma, St. Louis, MO) (126.11 g/mol)
12. 2,5-Furandicarboxaldehyde (2,5-DMF) (Sigma-Aldrich, Milwaukee, WI) (124.09 g/mol)
13. TD-7 (provided by Dr. Martin Safo, Dr. Yan Zhang, Department of Medicinal Chemistry, VCU) (273 g/mol)
14. TD-8 (provided by Dr. Martin Safo, Dr. Yan Zhang, Department of Medicinal Chemistry, VCU) (273 g/mol)

15. TD-9 (provided by Dr. Martin Safo, Dr. Yan Zhang, Department of Medicinal Chemistry, VCU) (273 g/mol)
16. INN-310 (provided by Dr. Martin Safo, Dr. Yan Zhang, Department of Medicinal Chemistry, VCU) (243 g/mol)
17. VZHE-039 (provided by Dr. Martin Safo, Dr. Yan Zhang, Department of Medicinal Chemistry, VCU) (259 g/mol)
18. Vanillin ReagentPlus® 99% (Sigma, St. Louis, MO) (152.15 g/mol)
19. PP-14 (provided by Dr. Martin Safo, Dr. Yan Zhang, Department of Medicinal Chemistry, VCU) (287 g/mol)
20. GBT-440 (Voxelotor, 337.37 g/mol) (MedChemExpress, NJ)
21. Dimethyl sulfoxide (DMSO), ≥ 99.9%, A.C.S. Reagent (Sigma-Aldrich, Milwaukee, WI) (78.13 g/mol)
22. 0.5M EDTA.2Na, pH 8.0 (Quality Biological, Gaithersburg, MD)

3.2.2 Equipment

1. 96-well deep plate (Thermo Scientific, Nazareth, PA)
2. Incubator (Thermo Fisher Scientific Inc., Pittsburgh PA)
3. ABL800 FLEX blood gas analyzer (Radiometer America, Inc., Westlake, OH)
4. HPLC Water 2695 (Waters, Milford, MA)
5. Photodiode array detector 2996 (Waters, Milford, MA)
6. Poly CAT^{A} weak cation-exchange column, 30 mm x 4.6 mm (Poly^{LC}, Inc., Columbia, MD)
7. Supelco® Pre-column Filter 0.2 µm (Sigma-Aldrich, St.Louis, MO)
8. Durapore® membrane filter, 0.22 µm (Sigma-Aldrich, St.Louis, MO)
9. 9 mm autosampler Insert (VWR, West Chester, PA)
10. 9 mm autosampler Insert (Thermo Fisher Scientific Inc., Pittsburgh PA)
11. 9 mm autosampler vail (Waters, Milford, MA)
12. 9 mm autosampler vail cap (Thermo Fisher Scientific Inc., Pittsburgh PA)
13. Vacuum filtration apparatus (assembled, department of MedChem, VCU)
14. Empower 2 software (Waters, Milford, MA)
15. Scientist®, version 3.0 (Micromath Software)
16. pH Meter (Fisher Scientific, Pittsburgh, PA)
17. Vortex (Vortex-Genie, VWR, West Chester, PA).
18. Balance (Fisher Scientific A 250, Pittsburgh, PA).
19. 0.5-5 mL Finnpipette (Thermo Scientific, Waltham, MA).
20. 30 – 300 µL multichannel pipette (Fisher Scientific, Hanover Park, IL)

21. 3-25 µL positive displacement pipette and corresponding pipette tips (Rainin Instruments, Oakland, CA).
22. 10-100 µL and 100-1000 µL VWR pipettes and corresponding pipette tips (VWR, West Chester, PA).

3.2.3 Preparation of Solutions

1. HbA solution

Concentrations of purified isolated human HbA solution were determined by using automated blood gas analyzer (Radiometer America, Inc., Westlake, OH). HbA stock solution was then diluted with HPLC grade water to achieve the designed experimental nominal concentrations (0.2 or 0.1 mM).

2. $NaBH_3CN$ and $NaBH_4$ solution (stopping solution)

10 mg $NaBH_3CN$ was dissolved into 3 mL of water to make 50 mM $NaBH_3CN$ solution. 10 mg of $NaBH_4$ was dissolved into 5 mL of water to make 50 mM $NaBH_4$ solution. $NaBH_3CN/NaBH_4$ mixture (1:1 v/v) stock solution was freshly made every day to stop the Schiff-base reaction and reduce unreacted aldehydes for kinetic measurement of HbA-AEH adduct (Deshpande et al., 2018). 50 μL was added to each sample collection tube and kept on ice ready for use.

3. AEH solution

AEH was dissolved in DMSO to make 100 mM stock solution. Different volume of stock solution was added to 96-well plate to achieve designed final initial nominal concentration of AEH ($[AEH]_0$) in the 96-well. Necessary pilot studies for some AEH were performed to determine $[AEH]_0$ range for definitive studies. Final concentrations of DMSO in 96-well were equal or less than 2%.

4. Mobile phases

Buffer A (20 mM Bis-Tris, 2 mM KCN, pH 6.5) and buffer B (20 mM Bis-Tris,2 mM KCN, 200 mM NaCl, pH 6.6) were prepared with HPLC grade water, and adjusted pH with HCl. 8.37 g Bis-Tris, 0.26 g KCN were dissolved in 2000 mL water to make Buffer A. 8.37 g Bis-Tris, 0.26 g KCN, and 23.38 g NaCl were dissolved in 2000 mL water to make Buffer B. Both mobile phases were filtered through a membrane filter (0.22 μm) under vacuum.

3.2.4 Sample Preparation and Experimental Design

3.2.4.1 Sample Preparation

For each AEH, varying $[AEH]_0$ were added to HbA solution (0.2 mM or 0.1 mM) in a 96-well plate and incubated at 37 ºC along with mild shaking. After AEH addition, aliquots were taken at different time intervals until SS achieved. $NaBH_3CN/NaBH_4$ was added to and well mixed with aliquots (V:V = 1:1) to terminate the Schiff-base reaction, fixate the Hb-adduct and reduce the free reactive aldehydes from the mixture (Deshpande et al., 2018). Samples were immediately frozen and kept at -80 ºC. For HPLC analysis, samples were thawed on ice, well mixed and then transferred to HPLC vails. Samples were kept at 4 ºC during HPLC analysis.

3.2.4.2 Pilot Experimental Design for SS Concentration- and Time-Dependency of HbA-AEH Adduct Formation in HbA Solution

Pilot studies were performed to optimize $[AEH]_0$ range and sampling schedule for definitive studies, as well as to provide information of initial parameter estimates for SS concentration- and time-dependency modeling. Two SS concentration-dependent models, which are hyperbolic and sigmoidal B_{max}-model were compared based on their goodness-of-fit for 5-HMF, TD-7 and VZHE-039.

Concentrations and sampling schedule for each AEH were designed either from visual inspection of the previous *in-vitro* SCD WB binding studies of AEH (Figure 3.2), the known HbA binding kinetics of other AEH, or literatures. For example, 12% of HbS-AEH adduct was observed when 2 mM of $[vanillin]_0$ incubated with WB from SCD

patients for 2 hrs (Figure 3.2). When compared among tested AEH, vanillin appeared to behave more like a less potent and a slow kinetic AEH, like 5-HMF (28% HbS modification). Therefore, 0.44 – 5.8 mM of vanillin were studied up to 27 hrs based on the study design of 5-HMF (Parikh, 2013).

In-vitro studies showed that 1 mM and 2 mM of $[VZHE\text{-}039]_0$ resulted in 60% and 100% of HbS modification in WB, respectively (Figure 3.2). Concentration- and time-dependency binding suggested that VZHE-039 may be similar to TD-7, with fast and potent Hb binding (Deshpande et al., 2018). Therefore, a concentration range of 0.01 mM to 1 mM was chosen for VZHE-039, and aliquots were collected every 6 mins at early time points to capture its fast kinetics at earlier reaction time, followed by every half to one hour till 3.5 hrs.

Due to the lack of *in-vitro* Hb binding data on GBT-440, a large concentration range of 0.1 – 12.5 mM was designed with few aliquots collection (0.03, 0.5, 1, 3 hrs).

3.2.4.3 Definitive Experimental Design for SS Concentration- and Time-Dependency of HbA-AEH adduct Formation in HbA Solution

Based on the pilot studies, preliminary data, literatures and rational designs (Deshpande et al., 2018; Parikh, 2013), the final $[AEH]_0$ range and sampling schedule were designed to cover the full SS concentration- and time-dependent HbA binding profiles of AEH (Table 3.1).

For example, free concentrations of 5-HMF in presence of HbA has been found to decline and approached equilibrium within 24-30 hrs, with a binding affinity of 0.25 mM (Parikh, 2013). Therefore, 5-HMF was designed to cover concentration range from

0.06 to 4 mM with aliquots collection up to 24 hrs. 2,5-DMF, another furaldehyde, showed enhanced *in-vitro* apparent binding affinity than 5-HMF in WB (Figure 3.2); therefore, lower concentrations (0.025, 0.05, 0.1 mM) were designed compared to 5-HMF.

Since 100% HbA modification was not achieved with 5.8 mM of vanillin from pilot study, higher $[\text{vanillin}]_0$ up to 20 mM (about 10-fold higher than the estimated K_D = 1.7 mM from its pilot study) was designed in the definitive study.

TD-7, TD-8, and TD-9 are isomers, however major difference in their ability to induce Hb-AEH adduct formation in SCD blood have been reported (Figure 3.1) (Deshpande et al., 2018). At 2 mM, TD-7 showed 66% HbS modification, whereas TD-8 and TD-9 only showed 18% and 43%, respectively, in WB. Therefore, more condense sampling were scheduled up to 5 hrs for TD-7 and covered lower $[\text{TD-7}]_0$. In contrast, aliquots were collected up to 24 and 27 hrs for TD-8 and TD-9, respectively and higher $[\text{TD-8}]_0$ and $[\text{TD-9}]_0$ (2 and 4 mM) were studied. *In-vitro* HbS binding kinetics of INN-310 in WB was more like TD-7 than other AEH; therefore, similar concentration and time-dependency study were designed for both compounds (Table 3.1) (Deshpande et al., 2018).

In-vitro studies showed that 1 mM and 2 mM of PP-14 resulted in 44.4% and 90.8% of inhibition of cell sickling, respectively (Safo et al., 2019). PP-14 may behave more like fast and potent binding compound, such as TD-7. Therefore, concentration range of 0.02 mM to 2 mM were chosen, and aliquots were collected up to 4 hrs, according to the experimental design of TD-7.

Unlike other AEH where their kinetic profiles can be characterized with 0.2 mM HbA, VZHE-039 achieved SS fast (< 6 mins). Therefore, 0.1 mM of HbA was used for VZHE-039 in definitive study to slow down the overall kinetics. Condense sampling schedule (every 3 mins) was designed in order to capture the kinetics at early reaction time to optimize parameter estimates.

According to the pilot study of GBT-440, SS was observed to be achieved almost instantaneously. High GBT-440 concentrations show possible secondary reactions with evidence of new peaks observed on chromatogram after long incubation time, as well as a decrease of the primary HbA-adduct concentration after 2 mins. Therefore, the primary HbA-AEH adduct was assumed to achieve SS by 2 mins. Since the kinetic study is not achievable under the current experimental method, only the SS concentration-dependency definitive study was designed. According to its pilot study, lower $[\text{GBT-440}]_0$ (below K_D: 0.02, 0.04, 0.06, 0.08 mM) were designed in the definitive study.

Table 3.1. Definitive experimental design for SS concentration- and time-dependency of HbA-AEH adduct formation in HbA solution.

AEH	$[AEH]_0$	Time Point	$[HbA]_0$
	[mM]	[hr]	[mM]
5-HMF	0.063, 0.13, 0.25, 0.5, 1, 2, 4	0.03, 0.3, 0.6, 1, 3, 5, 7, 23, 24	0.2
2,5-DMF	0.025, 0.05, 0.1, 0.25, 0.5, 1, 2, 4, 8	0.1, 0.2, 0.5, 1, 2, 4, 6, 24, 25	0.2
Vanillin	0.44, 0.74, 1.5, 2, 3, 3.5, 4.4, 5, 6, 7, 11, 21	0.05, 0.5, 1, 2, 3, 4.5, 8.5, 27	0.2
TD-8	0.1, 0.2, 0.4, 1, 2, 4	0.05, 0.5, 1, 2, 4, 6, 24	0.2
TD-9	0.1, 0.2, 0.4, 1, 2, 4	0.05, 0.5, 1, 4.5, 5, 6, 24, 27	0.2
TD-7	0.025, 0.05, 0.1, 0.2, 0.4, 0.8, 1.6	0.1, 0.2, 0.3, 0.4, 0.5, 0.6, 0.8, 1, 1.1, 2.1, 5.1	0.2
PP-14	0.05, 0.1, 0.2, 0.25, 0.3, 0.4, 0.5, 0.6, 1, 2	0.025, 0.1, 0.15, 0.2, 0.25, 0.35, 0.45, 0.55, 0.65, 1, 4	0.2
INN-310	0.027, 0.046, 0.09, 0.11, 0.18, 0.36, 0.57, 1, 2, 3, 5	0.03, 0.1, 0.2, 0.3, 0.4, 1, 1.5, 2, 4, 6	0.2
VZHE-039	0.026, 0.04, 0.06, 0.083, 0.12, 0.25, 0.3, 0.4	0.025, 0.05, 0.1, 0.15, 0.2, 0.25, 0.3, 0.35, 0.4	0.1
GBT-440	0.02, 0.04, 0.06, 0.08, 0.1, 0.12, 0.14, 0.16, 0.2, 0.4, 0.5, 0.65, 0.8, 0.9, 1, 1.7, 3.3, 6.5, 12.5	0.03	0.2

3.2.5 HPLC-UV/Vis Conditions

HbA and HbA-AEH adduct concentrations were quantitated by HPLC-UV/vis with a weak cation-exchange column (PolyCAT[A], 30 mm x 4.6 mm) and a detection wavelength of 410 nm. A precolumn filter (Supelco®, 2.0 µm) was used to protect column. A linear gradient wash was applied with buffer A (20 mM Bis-Tris, 2 mM KCN, pH 6.5) and buffer B (20 mM Bis-Tris,2 mM KCN, 200 mM NaCl, pH 6.6) over 20 minutes with flow rate of 1.5 mL/min (Table 3.2).

Table 3.2. HPLC conditions for HbA and HbA-AEH adduct quantification in HbA solution.

LC System	Waters 2695 separation model	
Detector	Waters 2996 PDA	
Analytical Column	Poly CAT[A] weak cation-exchange column, 30 mm x 4.6 mm	
Pre-column	Supelco® Pre-column Filter 0.2 µm	
Detection Wavelength	410 nm	
Autosampler Temperature	4 ºC	
Flow Rate	1.5 mL/min	
Injection Volume	10 µL	
Mobile Phases	A (20 mM Bis-Tris, 2 mM KCN, pH 6.5)	B (20 mM Bis-Tris, 2 mM KCN, 200 mM NaCl, pH 6.6)
0 min	100	0
10 min	60	40
15 min	0	100
16 min	100	0
20 min	100	0

3.2.6 Partial Validation of HPLC-UV/Vis Assay Method

3.2.6.1 Selectivity and Representative Chromatograms

Assay selectivity was assessed with water/stopping solution (V:V = 1:1) in presence of 2%DMSO as control. A mixture of Hb variants, including HbF, HbA, HbS, HbC (Helena Laboratories, Beaumont, TX) was qualitatively assessed in order to confirm the separation of Hb according to their different isoelectric point (pI). The separation of HbA-AEH adduct and HbA mixture were monitored for all AEH.

3.2.6.2 UV Spectra of HbA and HbA-AEH Adduct

A 3D capture from (200 nm to 600 nm) was set up on a PDA detector to compare the UV spectrum properties of HbA and HbA-AEH adduct. Detection wavelength was optimized for HbA and HbA-AEH adduct quantification. Molar absorptivity (extinction coefficient ε) of HbA and HbA-AEH adduct at the detection wavelength (410 nm) were compared using Lambert-Beer's law (Equation 3.1), in order to determine if HbA calibration curve can be used for the quantification of HbA-AEH adduct.

$$\Delta A = \varepsilon * l * \Delta C \qquad \text{----} \qquad \textit{Equation 3.1}$$

ΔA: change of absorbance measured by PDA detector

ε: experimental molar extinction coefficient of HbA, HbA-AEH adduct

l: pathlength that automatically corrected by Empower 2 software

ΔC: change of HbA, HbA-AEH adduct concentration

3.2.6.3 Linearity

Three HbA calibration curves (0.003 - 0.4 mM) were prepared in water and followed by a 2-fold dilution with stopping solution in presence of 2%DMSO for the assay validation. The peak area was used for quantification. Linearity was assessed using linear regression with 1/y weighting factor applied in order to cover large $[AEH]_0$ range (133-fold). Sensitivity (slope), accuracy (DNF = (Predicted concentration – Nominal concentration) / Nominal concentration) and precision (RSD = SD / Mean) were evaluated. eLOQ was estimated as the lowest observed nominal concentration which has acceptable of %DFN and %RSD, corrected by the dilution factor. Concentrations below eLOQ were not included in the data set.

3.2.6.4 Mass Balance

Mass balance was assessed by adding HbA-AEH adduct and HbA concentrations quantified from HbA calibration curves, and compared to the $[HbA]_0$.

3.2.6.5 Comparison to the Reference Assay Method using 5-HMF

In order to further validate this “universal” assay method, the SS concentration-dependency study data of 5-HMF collected from the previous validated reference assay method were revisited and remodeled using a Sigmoidal B_{max}-model (Parikh, 2013). Binding affinity (K_D) was estimated using calculated bound 5-HMF molar concentrations against $[5\text{-HMF}]_0$ in the reference assay method, and compared to the K_D estimated using HbA-AEH adduct molar concentrations against $[5\text{-HMF}]_0$ in the “universal” assay method.

3.2.7 Data Analysis and Modeling

3.2.7.1. Data Analysis

The HbA-AEH adduct peak well separated from free HbA peak for all tested AEH (Figure 3.3 – 3.5 in Section 3.3.1.1). Peak area was consistently integrated using Gaussian skim method, since the separation between HbA-AEH adduct and HbA peak at low $[AEH]_0$ did not allow valley-to-valley integration. HbA-AEH adduct peak area was corrected from the baseline measurement by subtraction from the peak area at the same retention time in absence of AEH (control sample). HbA-AEH adduct and HbA exhibited the same molar absorptivity at 410 nm (Figure 3.6 in Section 3.3.1.2). Since no reference chemical compound for Hb-AEH adduct is available, HbA calibration curve was used for HbA-AEH adduct quantification.

Experimental data obtained at SS were used in concentration-dependent modeling to determine binding affinity. For each AEH, equilibrium time was observed from time-dependent HbA binding, where HbA-AEH adduct concentration stopped increasing and remained the same with time. HbA-AEH adduct concentrations above eLOQ (0.006 mM) were all included in the data set, except special cases listed below which violated the assumptions of models (Section 3.2.7.2 and 3.2.7.3). 1). HbA-AEH adduct concentrations decrease after SS. In SS concentration-dependency study, 2,5-DMF showed a major mass balance lost at high $[2,5\text{-DMF}]_0$; therefore, data were excluded when $[2,5\text{-DMF}]_0 > 0.5$ mM, where the HbA-AEH adduct concentrations decreased. 2). For kinetic studies, sub-set data were used for parameter estimation for

5-HMF, 2,5-DMF, vanillin, and PP-14, which excluded the data showed the loss of HbA-AEH adduct along time.

The AEH SS concentration- and time-dependent data were modeled by a Sigmoidal-B_{max} model and a simple 1:1 saturable binding model (simple kinetic binding model), respectively, described in the following sections 3.2.7.2 and 3.2.7.3.

3.2.7.2. Modeling of SS Concentration-Dependency of HbA-AEH Adduct Formation and HbA Loss

The SS (at equilibrium) concentration-dependency HbA-AEH adduct data of 5-HMF, TD-7 and VZHE-039 were firstly modeled using the saturable hyperbolic model (Equation 3.2) according to the previous study on 5-HMF (Parikh, 2013).

$$[\boldsymbol{HbA - AEH\ adduct}]_{\infty} = \frac{\boldsymbol{B_{max}} * [\boldsymbol{AEH}]_{\boldsymbol{0}}}{\boldsymbol{K_D} + [\boldsymbol{AEH}]_{\boldsymbol{0}}} \qquad \textbf{---- Equation 3.2}$$

B_{max}: Maximal AEH-HbA adduct formed/AEH bound

K_D: Equilibrium dissociation constant

$[HbA\text{-}AEH\ adduct]_{\infty}$: HbA-AEH adduct concentration at SS

$[AEH]_0$: Nominal initial concentration of AEH

Scientist® (version 3.0) was used for nonlinear-regression. Initial estimates of B_{max} and K_D were obtained from the visual inspection of the experimental data. Final

parameters were optimized based on the goodness-of-fit of model determined by r^2, residuals, sum of squared observations, model selection criterion, and precision of parameter estimation (COV). 1/y weighted factor was applied to cover the large $[AEH]_0$ range.

Due to imprecision of the parameter estimates for novel AEH (large COV of K_D estimates for TD-7 (28%) and VZHE-039 (43%)), a simple sigmoidal B_{max}-model was applied by introducing a Hill coefficient (n) to account for the potential cooperative binding of AEH (Equation 3.3). Accordingly, a reversed sigmoidal B_{max}-model was applied to fit SS HbA concentrations (Equation 3.4).

$$[\boldsymbol{HbA - AEH\ adduct}]_\infty = \frac{\boldsymbol{B_{max}} * [\boldsymbol{AEH}]_0{}^{\boldsymbol{n}}}{\boldsymbol{K_D}^{\boldsymbol{n}} + [\boldsymbol{AEH}]_0{}^{\boldsymbol{n}}} \qquad \textbf{---- Equation 3.3}$$

$$[\boldsymbol{HbA - AEH\ adduct}]_\infty = \boldsymbol{B_{max}} - \frac{\boldsymbol{B_{max}} * [\boldsymbol{AEH}]_0{}^{\boldsymbol{n}}}{\boldsymbol{K_D}^{\boldsymbol{n}} + [\boldsymbol{AEH}]_0{}^{\boldsymbol{n}}} \qquad \textbf{---- Equation 3.4}$$

Goodness-of-fit from both hyperbolic and sigmoidal models were compared for all three tested AEH (5-HMF, TD-7 and VZHE-039), which covered both furaldehydes and benzaldehydes, as well as less, medium and potent binding affinities. The sigmoidal model provided better parameter estimates with improved r^2 and COV. Therefore, for other AEH, SS concentration-dependent experimental data were fit by sigmoidal model only.

3.2.7.3. Modeling of Time-dependency of HbA-AEH Adduct Formation

A simple kinetic binding model was established based on the MOA of AEH (Scheme 3.1). Association of AEH to Hb is characterized by a second-order rate constant, k_{on}, while dissociation of the Hb adduct is described by a first-order rate constant, k_{off}.

$$\textbf{AEH + HbA} \underset{k_{off}}{\overset{k_{on}}{\rightleftharpoons}} \textbf{HbA-AEH adduct} \quad \text{----------} \textbf{ Scheme 3.1}$$

Assumptions built in this simple kinetic binding model are: 1). one AEH molecule reversibly binds to one HbA molecule (1:1); 2). HbA-AEH adduct is the primary and the only modified Hb formed in the system, where no parallel/sequential reactions happened. 3). AEH, HbA and HbA-AEH adduct are stable in the sample system within incubation time.

The rate of change in HbA-AEH adduct, AEH concentrations at any time, “t” was described by the differential equations listed below (Equations 3.5), where [AEH], [HbA], and [HbA-AEH adduct] are concentrations of unbound AEH, unmodified HbA, and HbA-AEH adduct at time t, respectively.

$$\frac{d[HbA - AEH\ adduct]}{dt} = (k_{on} * [AEH] * [HbA]) - \left(k_{off} * [HbA - AEH\ adduct]\right)$$

$$\frac{d[AEH]}{dt} = \left(k_{off} * [HbA - AEH\ adduct]\right) - (k_{on} * [AEH] * [HbA])$$

----- Equations 3.5

HbA are present in the mixture as either free HbA or HbA-AEH adduct form (Equation 3.6).

$$[\boldsymbol{HbA}] = [\boldsymbol{HbA}]_{\mathbf{0}} - [\boldsymbol{HbA - AEH\ adduct}] \qquad \textbf{-----} \quad \textbf{\textit{Equation 3.6}}$$

Initial conditions were fixed (listed below), where $[AEH]_0$, $[HbA]_0$, and $[HbA\text{-}AEH\ adduct]_0$ are concentrations of unbound AEH, free HbA, and HbA-AEH adduct at time 0, respectively.

$$[\mathbf{HbA}]_{\mathbf{0}} = \mathbf{0.2\ mM\ (or\ 0.1\ mM\ for\ VZHE - 039)}$$

$$[\mathbf{AEH}]_{\mathbf{0}} = \mathbf{Nominal\ concentration\ \ of\ AEH, at\ time\ 0}$$

$$[\mathbf{HbA - AEH\ adduct}]_{\mathbf{0}} = \mathbf{0}$$

Scientist® (version 3.0) was used for nonlinear-regression. Initial estimates were obtained from pilot studies or rational design of the definitive studies. Final parameters were optimized based on the goodness-of-fit determined by r^2, residuals, sum of squared observations, model selection criterion, precision of parameter estimation (COV), and correlation matrix. 1/y weighted factor was applied to cover a large $[AEH]_0$ range.

To help interpret the primary model parameters (k_{on} and k_{off}), the following secondary model parameters were calculated as shown below (Equations 3.7):

$$\boldsymbol{K_D = \frac{k_{off}}{k_{on}}}$$

$$\boldsymbol{k^{ass} = k_{on} * [HbA]_0}$$

$$\boldsymbol{k^{diss} = k_{off}}$$

$$\boldsymbol{k^{eq} = k^{ass} + k^{diss}}$$ ---- ***Equations 3.7***

The dissociation equilibrium constant, K_D, was used as a measure of AEH affinity for Hb, while the (first-order) association (k^{ass}), dissociation (k^{diss}) and equilibrium rate constants allow the calculation of half-lives ($t_{1/2}$ = ln 2 / k) for these processes - assuming first-order conditions (k^{eq}), i.e., $[AEH]_0$ are lower than K_D. Finally, k^{ass} and k^{eq} depend on $[HbA]_0$, which are quite diluted in our HbA binding experiments (0.2 or 0.1 mM to slow down kinetic reactions), and were therefore extrapolated to the physiological HbA concentrations (2.0 mM) in WB described in Chapter 5.

3.2.7.4. Sensitivity Analysis for the Simple Kinetic Binding Model

In order to better understand the simple kinetic binding model, sensitivity analyses were performed to provide information for the experimental design and initial parameter estimates. Initial estimates on k_{on} (0.25 hr^{-1}*mM^{-1}), k_{off} (0.05 hr^{-1}), and $[HbA]_0$ (0.125mM) were obtained from the previous studies for 5-HMF (Parikh, 2013). Four

scenarios were designed by changing $[HbA]_0$ (0.025mM to 0.625 mM, 25-fold), k_{off} (0.01 hr^{-1} to 0.25 hr^{-1} , 25-fold), k_{on} (0.05 $hr^{-1}*mM^{-1}$ to 1.25 hr-1*mM-1, 25-fold), or proportionally changing on k_{off} and k_{on} (0.01 hr-1 /0.05 $hr^{-1}*mM^{-1}$ to 0.25 hr^{-1} / 1.25 $hr^{-1}*mM^{-1}$, 25-fold). Model sensitivity analyses were performed to assess how the change of k_{on}, k_{off}, and $[HbA]_0$ affected the overall time-dependent and SS concentration-dependent binding for AEH, characterized by $t_{1/2}^{eq}$, K_D, as well as HbA-AEH adduct concentrations at equilibrium ([HbA-AEH adduct] $_\infty$). Fold-change calculated by dividing the largest number by the smallest value obtained using parameter values from upper limit (UL) and lower limit (LL). If results from UL were smaller than results from LL, the fold-change is expressed as a negative number.

3.3 Results

3.3.1. Partial Validation of HPLC-UV/Vis Assay Method

3.3.1.1. Selectivity and Representative Chromatograms

A chromatogram of water/stopping solution in the presence of 2% DMSO showed no peak (Figure B.3.1 in Appendix B), while 0.1 mM HbA showed a single peak (Figure 3.3). Hb variants separated from each other, eluted in the order of HbF (pI = 6.90), HbA (pI = 6.95), HbS (pI = 7.09) and HbC (pI = 7.40) (Figure B.3.2 in Appendix B) (Bunn & Forget, 1986). AEH binding to Hb is expected to decrease the pI of protein, which allows its separation from free Hb. For each tested AEH, regardless of their different physicochemical properties (e.g., cLogP of 5-HMF = -0.1, TD-7 = 1.3), HbA-AEH adduct peak was separated and eluted prior to the HbA peak on chromatogram (Figure 3.4 – 3.6, other representative chromatogram listed in Appendix B Figure B.3.3 – B.3.10).

3.3.1.2. UV Spectra of HbA and HbA-AEH Adduct

HbA and HbA-AEH adduct show similar UV/Vis spectra (Figure 3.7). λ was determined as 410 nm, which is close to λ_{max} and is consistent with the λ used in the previous studies (Deshpande et al., 2018). The estimated extinction coefficients at 410 nm were 2.9 and 2.8 $AU*mM^{-1}cm^{-1}$, for HbA and HbA-AEH adduct, respectively. Therefore, using HbA calibration for HbA-AEH adduct quantification is scientifically reasonable.

Figure 3.3. Representative chromatogram of 0.003 mM HbA solution.

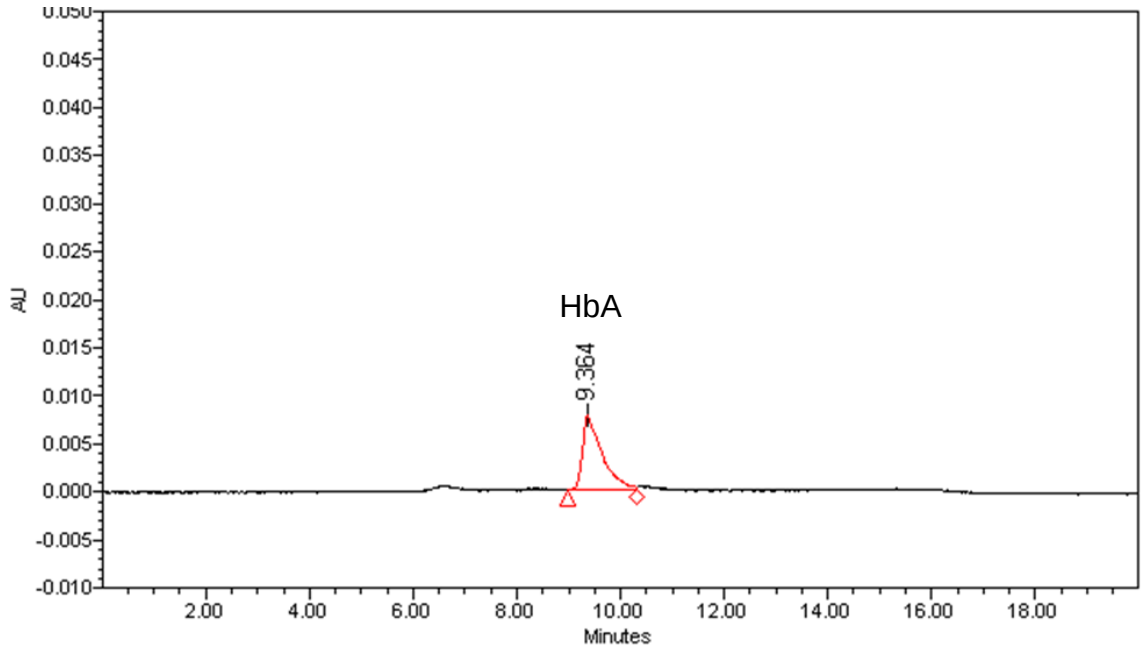

Figure 3.4. Representative chromatogram of HbA-AEH adduct and HbA separation for 0.25 mM of 5-HMF in HbA solution (0.2 mM) at 3 hrs.

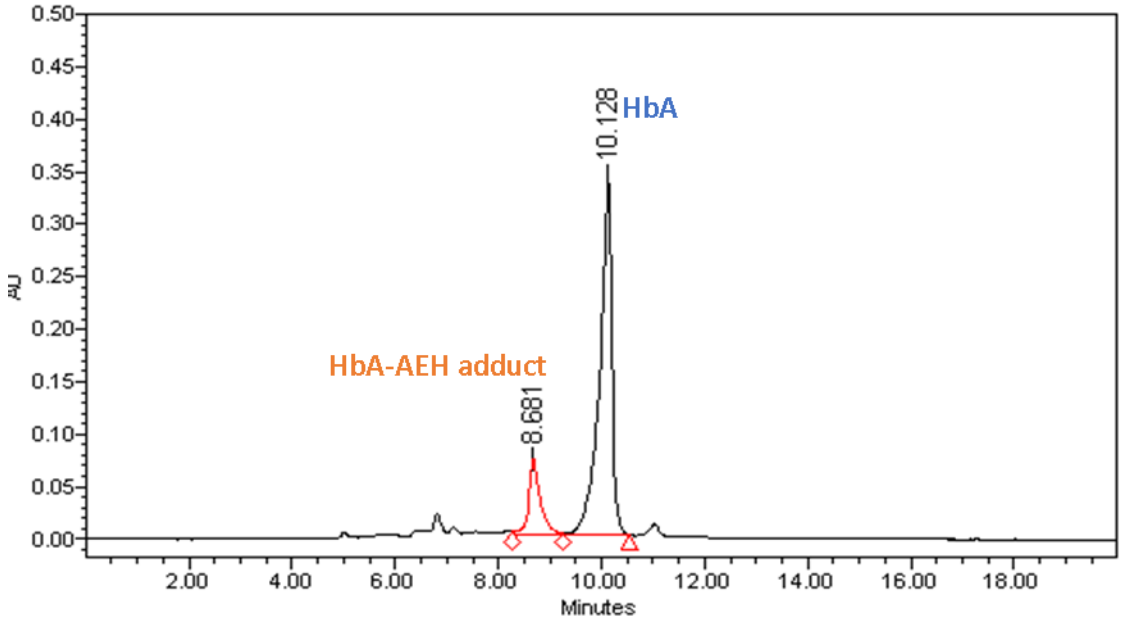

Figure 3.5. Representative chromatogram of HbA-AEH adduct and HbA separation for 8 mM of 5-HMF in HbA solution (0.2 mM) at 8 hrs.

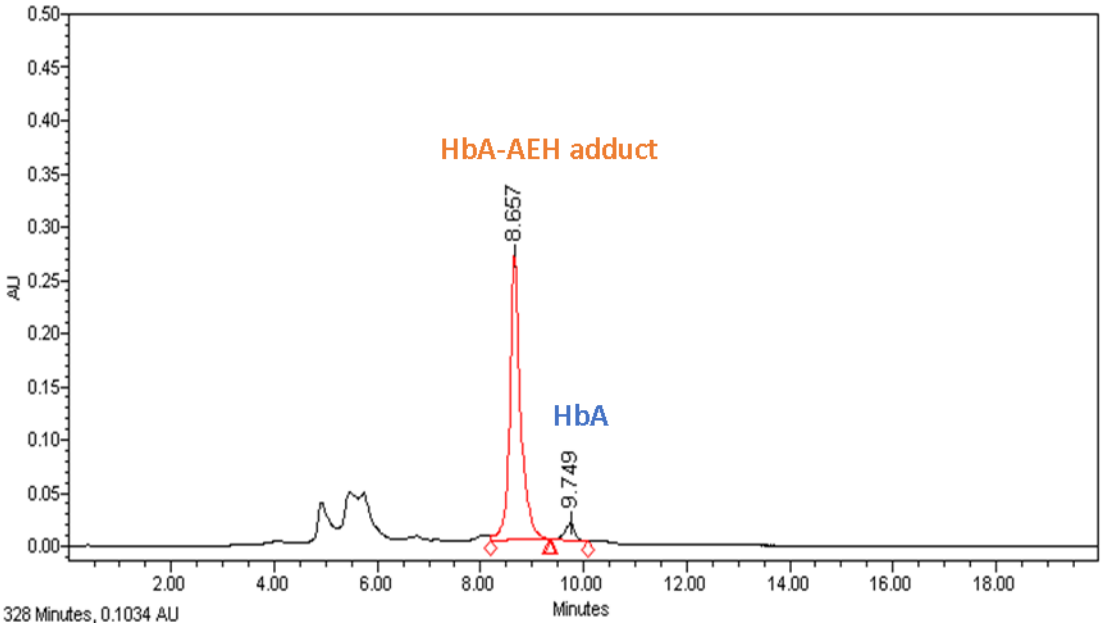

Figure 3.6. Representative chromatogram of HbA-AEH adduct and HbA separation for 0.2 mM of TD-7 in HbA solution (0.2 mM) at 0.8 hr.

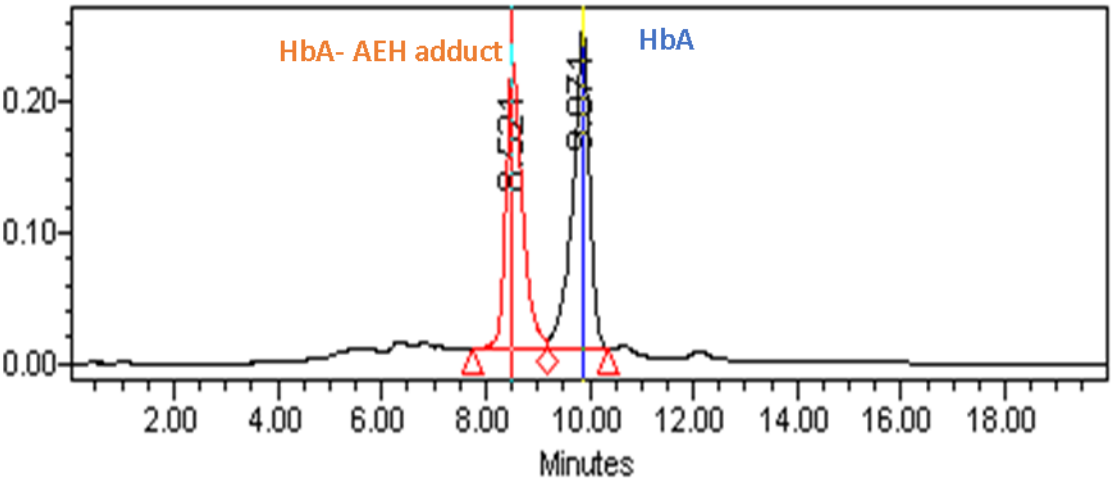

Figure 3.7. Representative UV spectra (λ = 200 – 600 nm) of HbA-AEH adduct and HbA for 0.2 mM of TD-7 in HbA solution (0.2 mM) at 0.8 hr.

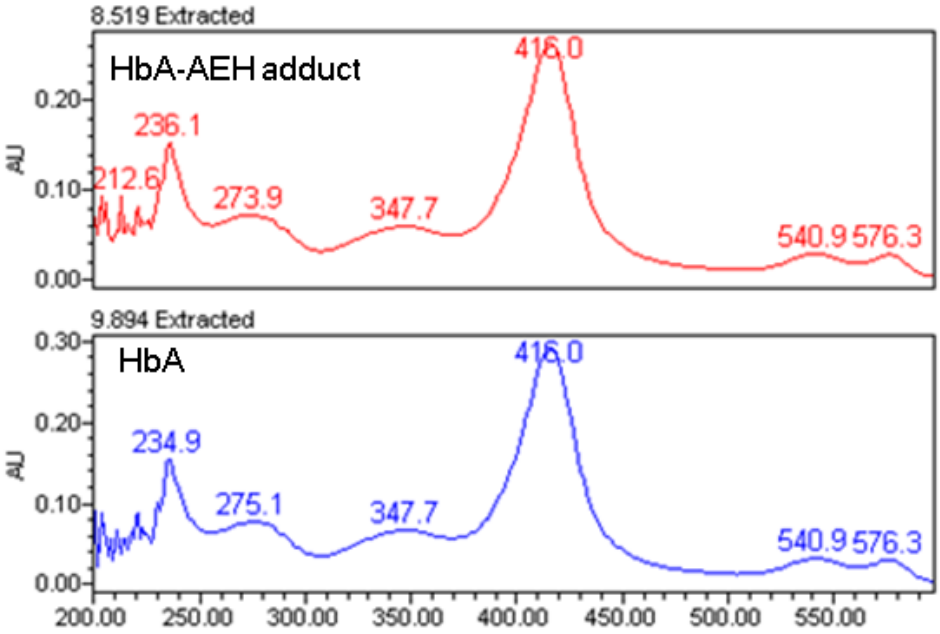

3.3.1.3. Linearity

HbA calibration curves (0.0015 – 0.2 mM) were linear (1/y weighted) with r^2 of 0.999 and slope of 1.1 * 10^8 (Figure 3.8). 0.0015 mM showed acceptable precision (%RSD = 6%) and accuracy (%DFN = 9%). After corrected by the 2-fold dilution factor, eLOQ for HbA and HbA-AEH adduct quantification in HbA solution is 0.003 mM. Overall, HbA calibration curves (n = 3) showed acceptable precision (%RSD of 4%-15%) and accuracy (%DFN of -20% to 4.5%).

Figure 3.8. Representative calibration curve of HbA in water/stopping solution (V:V = 1:1) in presence of 2%DMSO. 1/y weighted linear regression (line) was fit to the experimental data (symbols). Data are as mean ± SD (n = 3).

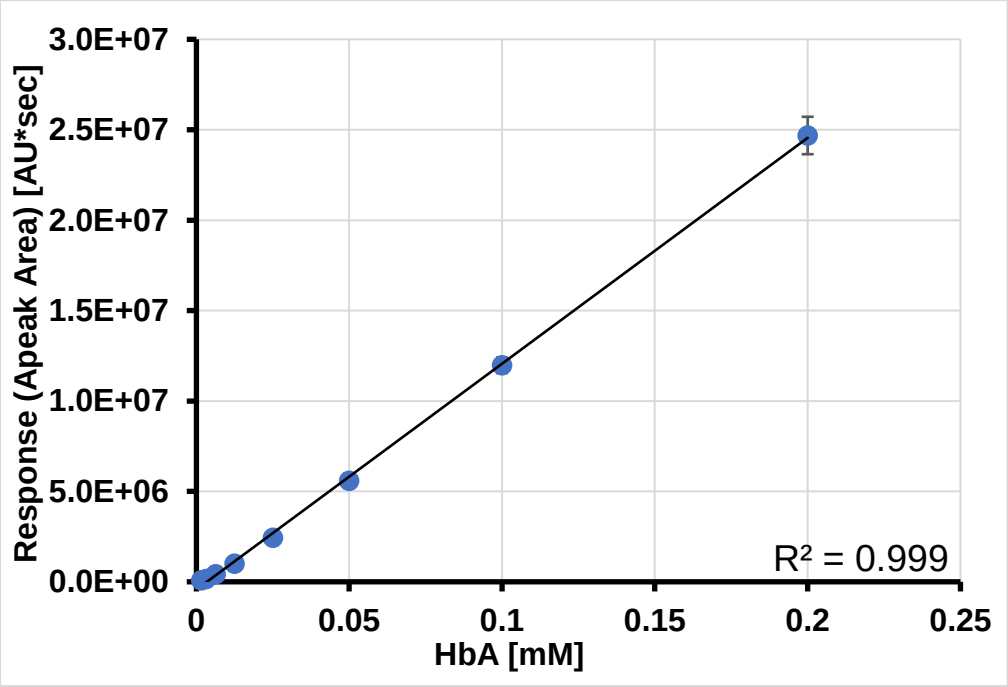

3.3.1.4. Mass Balance

At SS, free HbA concentrations decreased as $[AEH]_0$ increased, concurrently HbA-AEH adduct concentrations increased as more of free AEH were able to bind to and saturate the HbA binding sites (Figure 3.9 – 3.10). For most AEH, HbA concentrations decreased to zero at the saturable condition, except GBT-440, where 50% of free HbA still remained (Figure 3.9 – 3.10). Mass balance (i.e., HbA + HbA-AEH adduct relative to $[HbA]_0$) for all tested AEH were above 83% except for high $[AEH]_0$. There is a trend of the loss of mass balance at high $[AEH]_0$ and/or long incubation times (Figure 3.9, and Figure B.3.11 – B.3.18 in Appendix B). Two extreme examples are vanillin and 2,5-DMF, where vanillin only achieved a maximum of 70% HbA modification, and 2,5-DMF showed almost completely lost mass balance (9%) at 8 mM for 24 hrs reaction time (Figure B.3.11 – B.3.19 in Appendix B). Some AEH, namely 5-HMF, 2,5-DMF, vanillin, PP-14, and GBT-440 showed additional peaks eluted prior to HbA-AEH adduct peak especially at high $[AEH]_0$ and/or long reaction time - indicating additional parallel/sequential reactions.

In the SS concentration-dependency study, binding affinity was estimated based on the primary HbA-AEH adduct concentrations quantified by HbA calibration curves. The mass balance lost at high $[AEH]_0$ were incorporated by B_{max} estimation. In kinetic studies, selected data were included for parameter estimation, where the loss of HbA-AEH adduct along time were excluded. Though some mass balance were lost at high $[AEH]_0$, for the research purposes of this study, this assay method is still valid for characterizing SS concentration- and time-dependent profiles of the primary HbA-AEH adduct.

Figure 3.9. Mass balance assessment for VZHE-039 in HbA solution for 0.4 hr. The sigmoidal B_{max}-model and the reverse sigmoidal B_{max}-model (lines) were fit with for HbA-AEH adduct and HbA (symbols), respectively. Linear regression (dashed line) was fit for visual inspection of mass balance (HbA-AEH adduct + HbA).

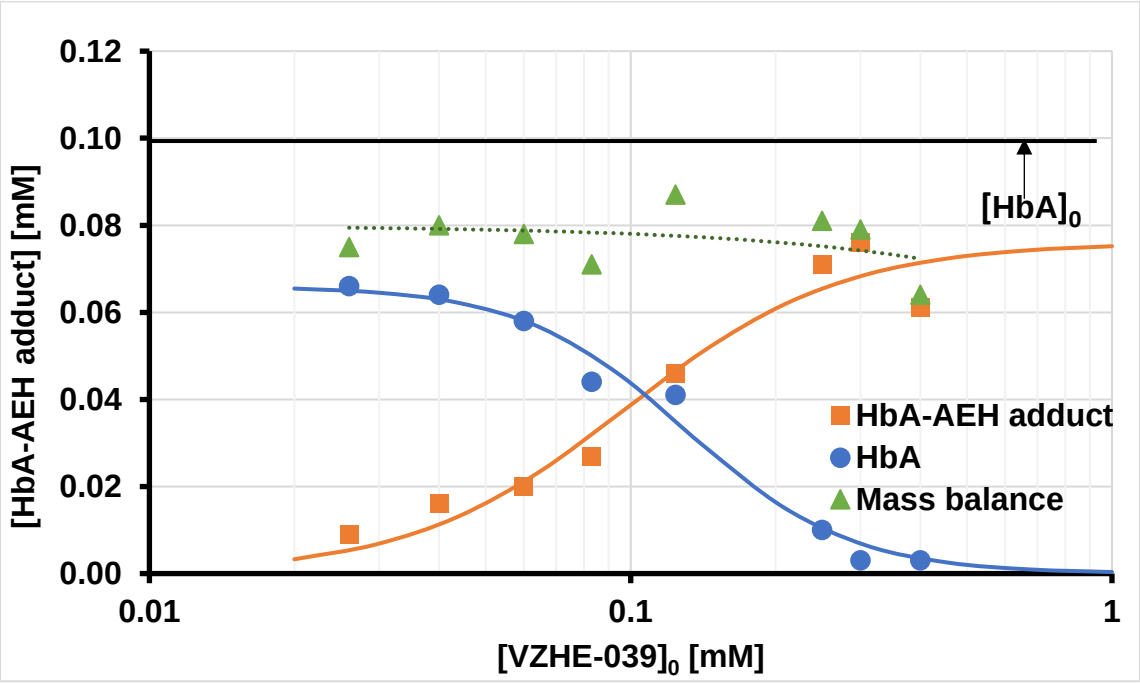

Figure 3.10. Mass balance assessment for GBT-440 in HbA solution for 0.03 hr. The sigmoidal B_{max}-model and the reverse sigmoidal B_{max}-model (lines) were fit with for HbA-AEH adduct and HbA (symbols), respectively. Linear regression (dashed line) was fit for visual inspection of mass balance (HbA-AEH adduct + HbA).

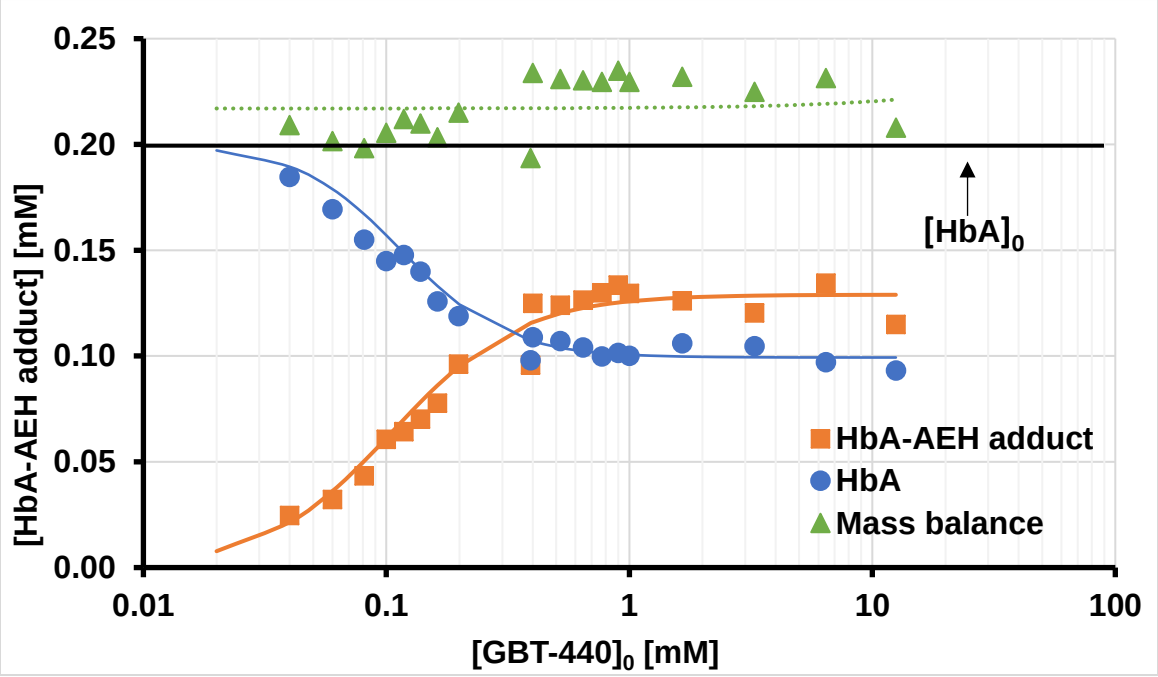

3.3.1.5. Comparison to the Previous Reference Assay Method using 5-HMF

The binding estimates obtained from both the previous reference assay and the current "universal" assay method using the same Sigmoidal B_{max}-model are statistically the same (Table 3.3), validating the prospective use of the current "universal" assay method.

Table 3.3. Comparison of the final parameter estimates of SS concentration-dependency of HbA-AEH adduct formation for 5-HMF by the sigmoidal B_{max}-model, using two different HPLC-UV/Vis assay methods. Data were presented as PE estimate with (COV).

	Reference Method	**"Universal" Method**
r^2	0.994	0.998
B_{max} / HbA_0	0.74 (10%)	1.0 (6%)
K_D	**0.28** (17%)	**0.37** (16%)
n	1.7 (20%)	1.1 (10%)

3.3.2. Sensitivity Analysis for the Simple Kinetic Binding Model

HbA solution provides an environment that is absent of any metabolic AEH degradation, allowing that equilibrium (SS) of AEH binding to HbA is achieved. Both association and dissociation rate determine the time it takes to achieve SS. The association rate is driven by both AEH and HbA concentrations, as well as the second-order association rate constant (k_{on}). When AEH concentrations are lower than K_D, $[HbA]_0$ multiplied by k_{on} is the apparent first-order association rate constant as since Hb concentrations remain close to $[HbA]_0$. The dissociation rate is driven by Hb-AEH adduct concentration and the first-order dissociation rate constant (k_{off}). The overall equilibration rate depends on both association and dissociation rates; under first-order condition, i.e., AEH concentrations below K_D, the equilibration rate is the sum of apparent first-order association rate constant ($k_{on}*[HbA]_0$) and first-order dissociation rate constant, k_{off}.

Therefore, when AEH is below K_D, increasing $[HbA]_0$, k_{on}, or k_{off} resulted in shorter equilibrium half-lives ($t_{1/2}^{eq}$) (Figure 3.11 – 13). Compared to the change of k_{on} and $[HbA]_0$, $t_{1/2}^{eq}$ is more sensitive to the change k_{off} (Table 3.4). When both k_{on} and k_{off} increase, $t_{1/2}^{eq}$ also is shortened inverse-proportionally (Table 3.4). However, when AEH concentrations exceed K_D, the association rate is sped up by the higher concentration of AEH. Therefore, $t_{1/2}^{eq}$ remains the same with increasing $[HbA]_0$ and k_{on}. Since k_{off} is a first-order rate constant, which is not affected by AEH concentrations, $t_{1/2}^{eq}$ remains sensitive to the change of k_{off} (Table 3.4).

Once the reaction achieves equilibrium, the HbA-AEH adduct$_\infty$ at a given $[AEH]_0$ and $[HbA]_0$ is determined are by both k_{on} and k_{off}. Larger k_{on} and/or smaller k_{off} results in

larger HbA-AEH adduct$_\infty$ (Figure 3.15 – 16). The maximum of HbA-AEH adduct$_\infty$ (B_{max}) achieved depends on the initially available concentration of HbA ($[HbA]_0$) in the system. Therefore, increasing $[HbA]_0$ leads to higher HbA-AEH adduct$_\infty$, while K_D remains the same (Figure 3.14). On the other hand, the change of k_{on} and k_{off} do not affect B_{max}, but move K_D into different directions (Figure 3.15 - 16). Larger k_{off} values result in larger K_D (i.e., lower binding affinity), while larger k_{on} values result in smaller K_D (i.e., higher binding affinity). When k_{on} and k_{off} are changed the same, K_D remains the same (Figure 3.17).

In summary, $t_{1/2}^{eq}$ (= $\ln(2)/(k_{on}*[HbA]_0)$), HbA-AEH adduct$_\infty$ or B_{max} (= $[HbA]_0*[AEH]_0/((k_{off}/k_{on})+[AEH]_0)$), K_D (=k_{on}/k_{off}) are determined by both k_{on} and k_{off} together. With our current experimental design, where serial HbA-AEH adduct concentrations were measured until SS, and k_{on} and k_{off} estimated from the simple binding model, their final estimates are expected and were indeed found to be highly correlated. To help reduce this correlation, $[AEH]_0$ were selected, based on pilot experiments, to cover a concentration range about 10-fold below and above the expected K_D. In addition, the serial sampling schedule was designed to cover both the ascending portion and the SS plateau of the time-dependent HbA-AEH adduct curve. The entire time-dependency HbA-AEH adduct dataset (or subset) across $[AEH]_0$ were used to fit by the simple kinetic binding model to obtain estimates for the primary model parameters, k_{on} and k_{off}.

Table 3.4. Assessment of outcome metrics from sensitivity analysis for the simple kinetic binding model. Data are presented as fold-change calculated by dividing the largest number by the smallest value obtained using parameter values from upper limit (UL) and lower limit (LL). If results from UL were smaller than results from LL, the fold-change is expressed as a negative number.

$AEH_0 : K_D = 1 : 10$				
	Fold-change	B_{max}	$t_{1/2}^{eq}$	K_D
$[HbA]_0$	25	25	-3	0
k_{on}	25	0	-3	-25
k_{off}	25	0	-6	25
k_{on} / k_{off}	25	0	-25	0
$AEH_0 : K_D = 50 : 1$				
	Fold-change	B_{max}	$t_{1/2}^{eq}$	K_D
$[HbA]_0$	25	25	0	0
k_{on}	25	0	0	-25
k_{off}	25	0	-13	25
k_{on} / k_{off}	25	0	25	0

Figure 3.11. Simulation of time-dependent HbA-AEH adduct formation using the simple kinetic binding model by changing $[HbA]_0$ (25-fold). ($[AEH]_0$ = 0.13 mM, K_D = 0.2 mM)

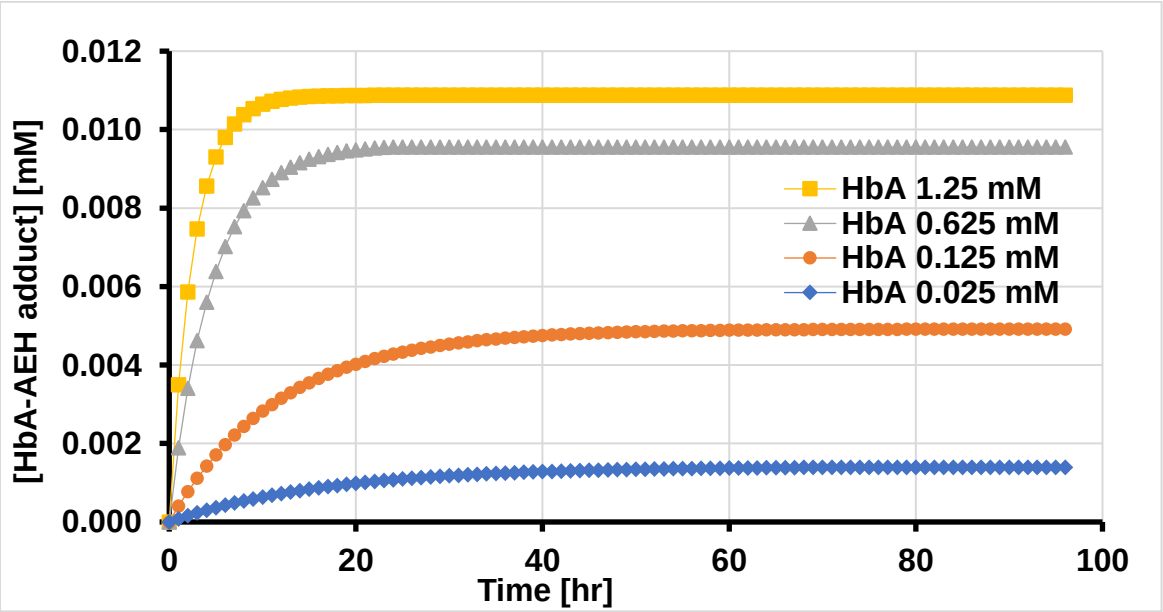

Figure 3.12. Simulation of time-dependent HbA-AEH adduct formation using the simple kinetic binding model by changing k_{on} (25-fold). ($[AEH]_0$: K_D = 1:10)

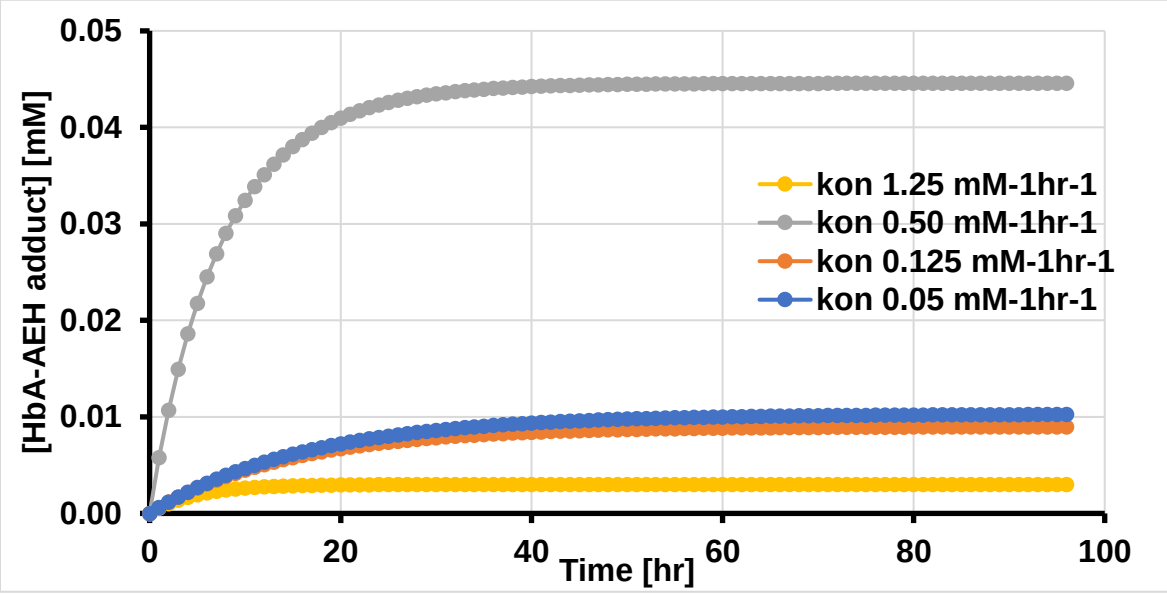

Figure 3.13. Simulation of time-dependent HbA-AEH adduct formation using the simple kinetic binding model by changing k_{off} (25-fold). ($[AEH]_0$ = 0.02 mM)

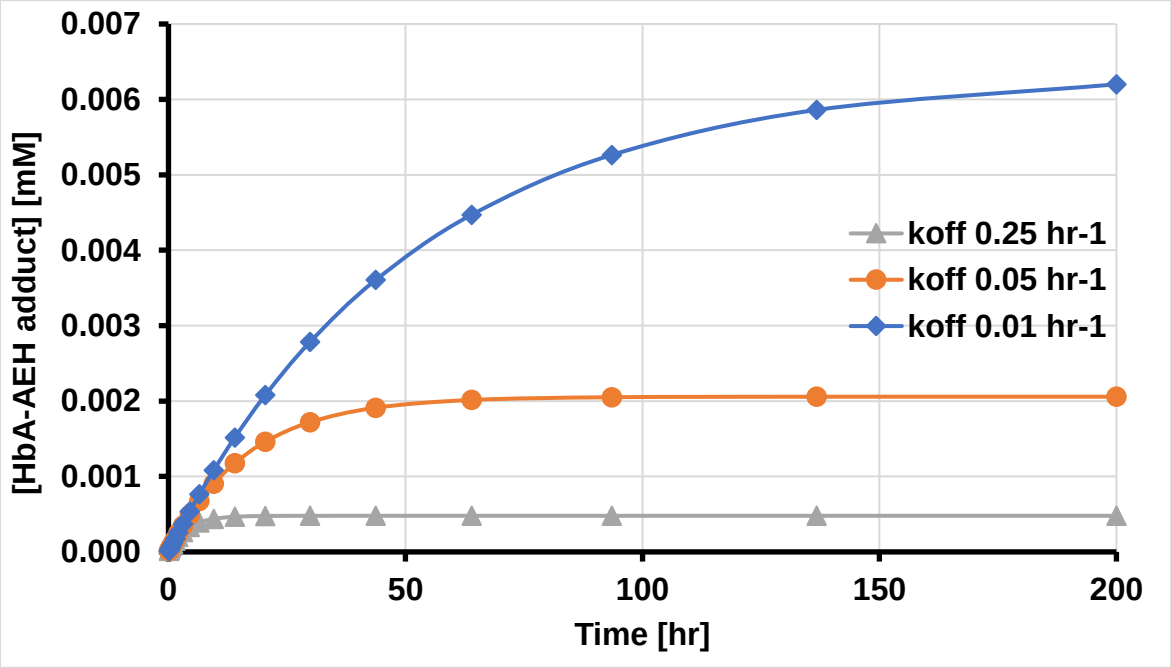

Figure 3.14. Simulation of SS concentration-dependency of HbA-AEH adduct formation using the simple kinetic binding model by changing $[HbA]_0$ (25-fold).

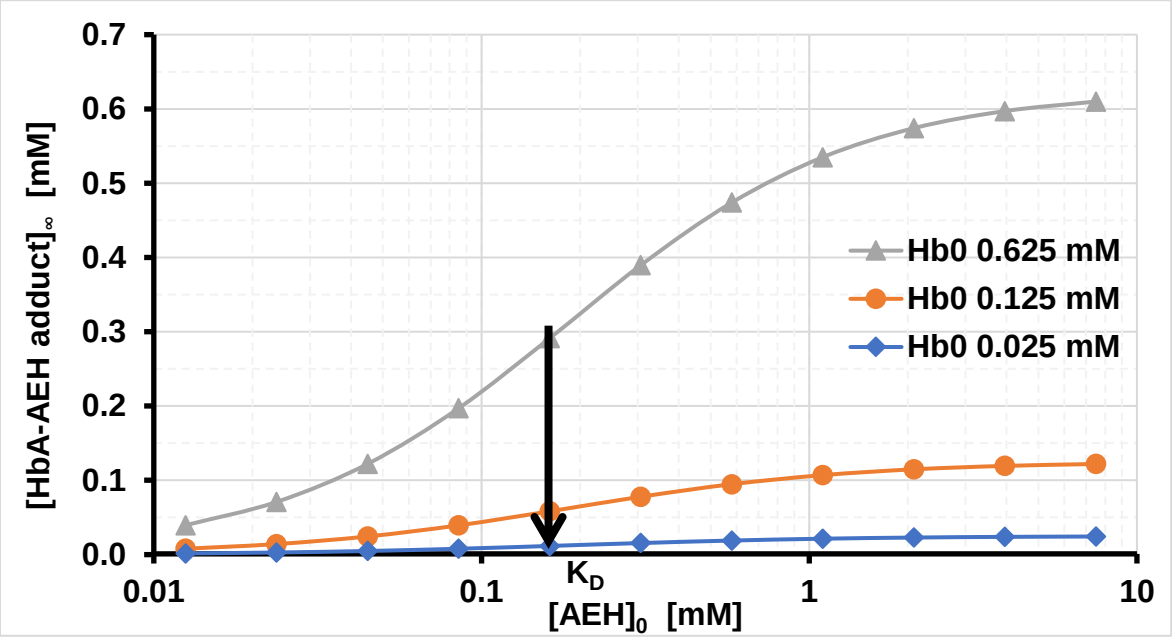

Figure 3.15. Simulation of SS concentration-dependency of HbA-AEH adduct formation using the simple kinetic binding model by changing k_{on} (25-fold).

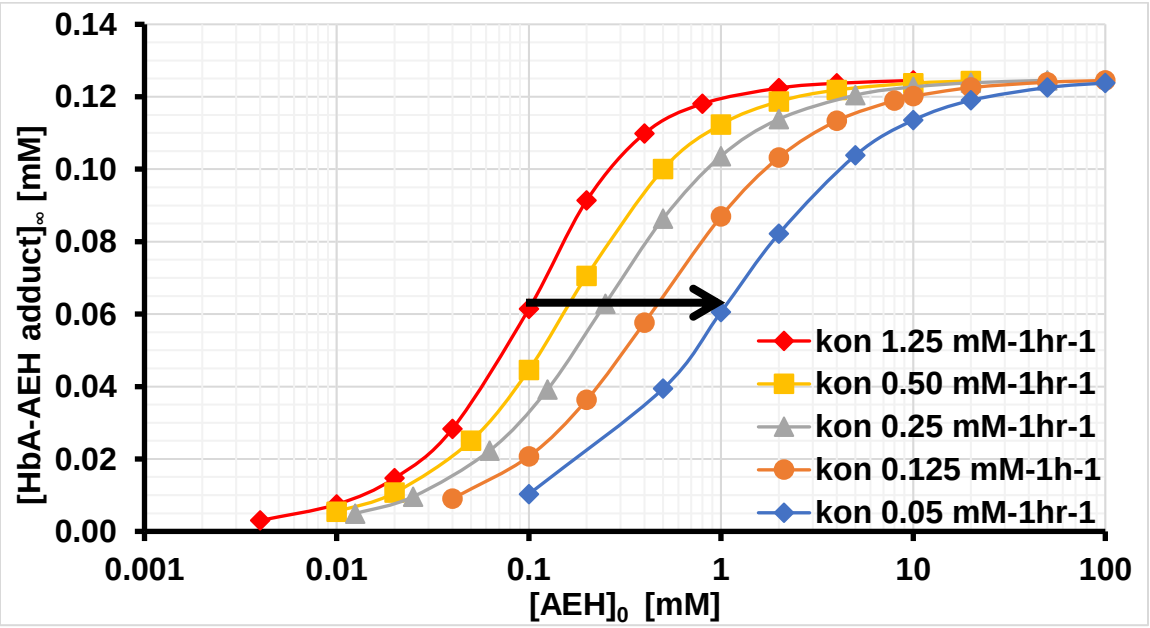

Figure 3.16. Simulation of SS concentration-dependency of HbA-AEH adduct formation using the simple kinetic binding model by changing k_{off} (25-fold).

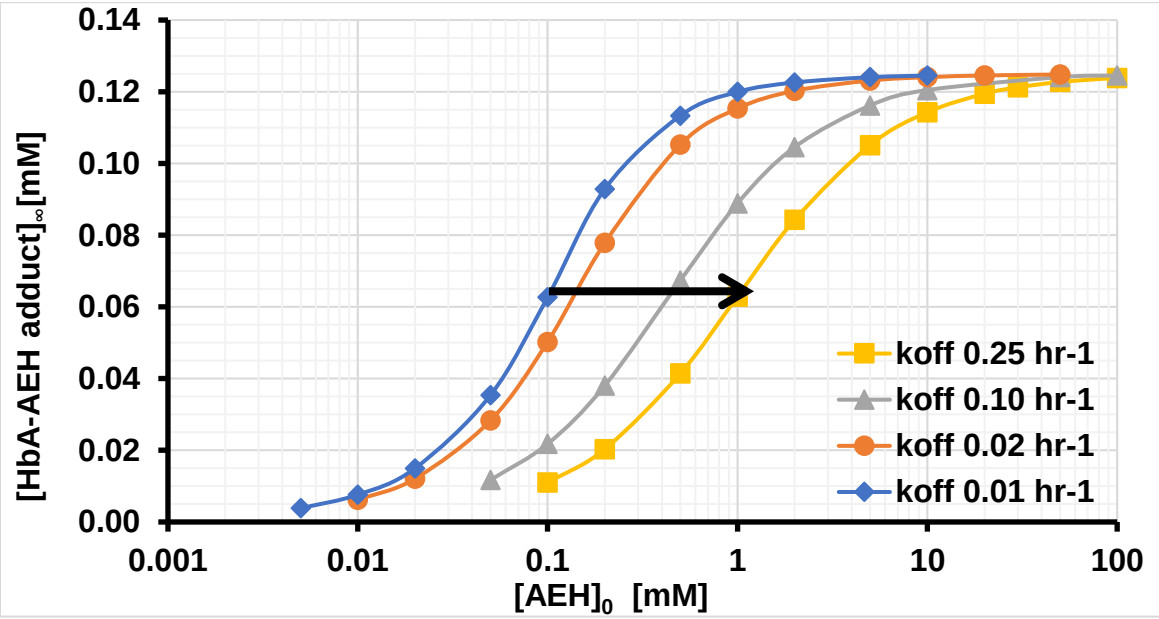

Figure 3.17. Simulation of SS concentration-dependency of HbA-AEH adduct formation using the simple kinetic binding model by changing k_{off} and k_{on} simultaneously (25-fold).

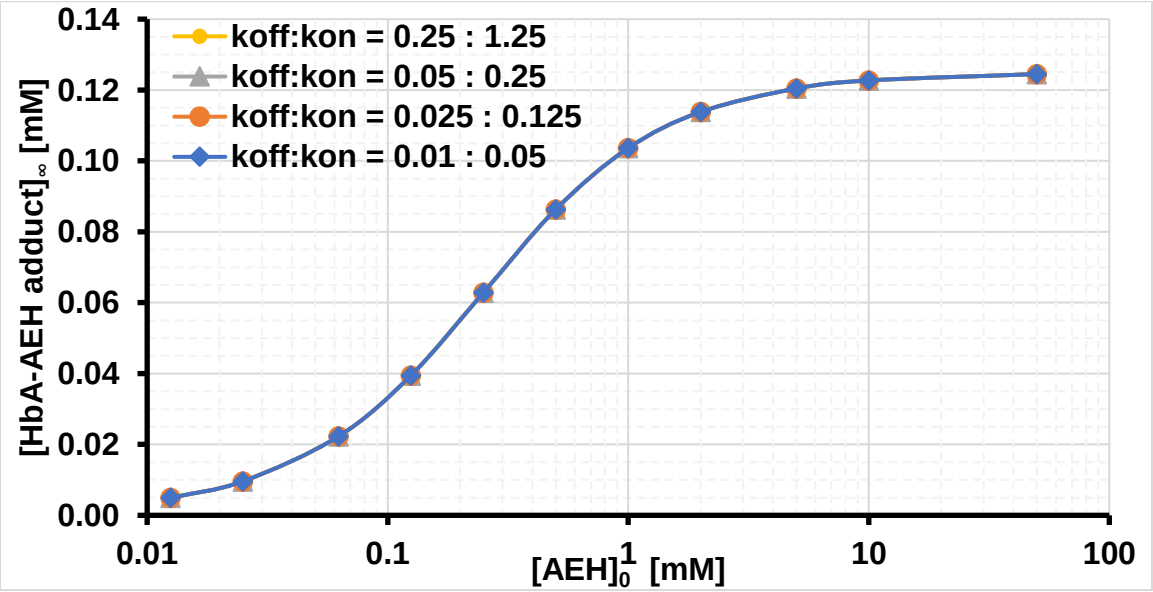

3.3.3. Pilot Study of SS Concentration- and Time-Dependency of HbA-AEH Adduct in Formation HbA Solution

The hyperbolic-B_{max}-model was used from previous study for 5-HMF by fitting the calculated bound 5-HMF against free 5-HMF concentrations in HbA solution mixture (Parikh, 2013). This hyperbolic model was also chosen to fit the HbA-AEH adduct concentration against nominal AEH concentrations for 5-HMF, TD-7 and VZHE-039 first. However, the hyperbolic B_{max}-model resulted in large imprecision (large COV) on point estimates, especially for TD-7 and VZHE-039 (Table 3.5). Steeper slopes were observed for VZHE-039 and TD-7 than for 5-HMF. Therefore, another parameter, i.e., Hill coefficient (n), was introduced to account for the potential cooperative binding of AEH to Hb molecules. The sigmoidal B_{max}-model fitted the experimental better with more precise point estimates and better r^2 for all three tested AEH (Table 3.5). Therefore, sigmoidal B_{max}-model was used to fit SS concentration-dependency studies for all selected AEH in definitive studies.

Table 3.5. Comparison of the final parameter estimates of SS concentration-dependency of HbA-AEH adduct formation for 5-HMF, TD-7, and VZHE-039, using the sigmoidal B_{max}-model and hyperbolic B_{max}-model. Data are presented as PE with (COV).

	5-HMF		TD-7		VZHE-039	
	Sigmoidal	**Hyperbolic**	**Sigmoidal**	**Hyperbolic**	**Sigmoidal**	**Hyperbolic**
r^2	**0.998**	**0.988**	**0.997**	**0.989**	**0.980**	**0.974**
B_{max}/ HbA_0	1.0 (6%)	1.1 (7%)	0.085 (5%)	1.4 (11%)	0.085 (18%)	1.1 (16%)
K_D	0.37 (16%)	0.58 (23%)	0.19 (10%)	0.38 (28%)	0.17 (37%)	0.24 (43%)
n	1.1 (10%)	1.0	1.8 (15%)	1.0	1.5 (39%)	1.0

Though the pilot study design for VZHE-039 using 0.2 mM HbA solution does not use optimized experimental conditions, it still provided useful information for the initial parameter estimates (K_D = 0.17 (37%) mM; k_{on} = 22 (14%) hr^{-1} mM^{-1}, and k_{off} = 3.0 (18%) hr^{-1}) for definitive study. VZHE-039 achieved SS in presence of 0.2 mM of $[HbA]_0$ within the first time point (6 mins), indicating that the originally designed experimental conditions missed most of the ascending portion of the reaction kinetics (Figure 3.18). According to the nature of a bimolecular reaction, their association rate depends on k_{on}, $[HbA]_0$ and $[AEH]_0$ concentrations. Since we aimed to cover both low and high concentration of AEH around the K_D, decreasing $[VZHE\text{-}039]_0$ to prolong the kinetic reaction time is not an optimal experimental design (Figure 3.18). Rather, lowering $[HbA]_0$ to 0.1 mM was chosen for the definitive study to slow down the overall reaction kinetics.

Figure 3.18. Pilot study of SS concentration- and time-dependency of HbA-AEH adduct formation for VZHE-039 in HbA solution (0.2 mM). The hyperbolic B_{max}-model and sigmoidal B_{max}-model (lines) were fit to the SS concentration-dependency of HbA-AEH adduct (symbols), while the simple kinetic binding model for the time-dependency.

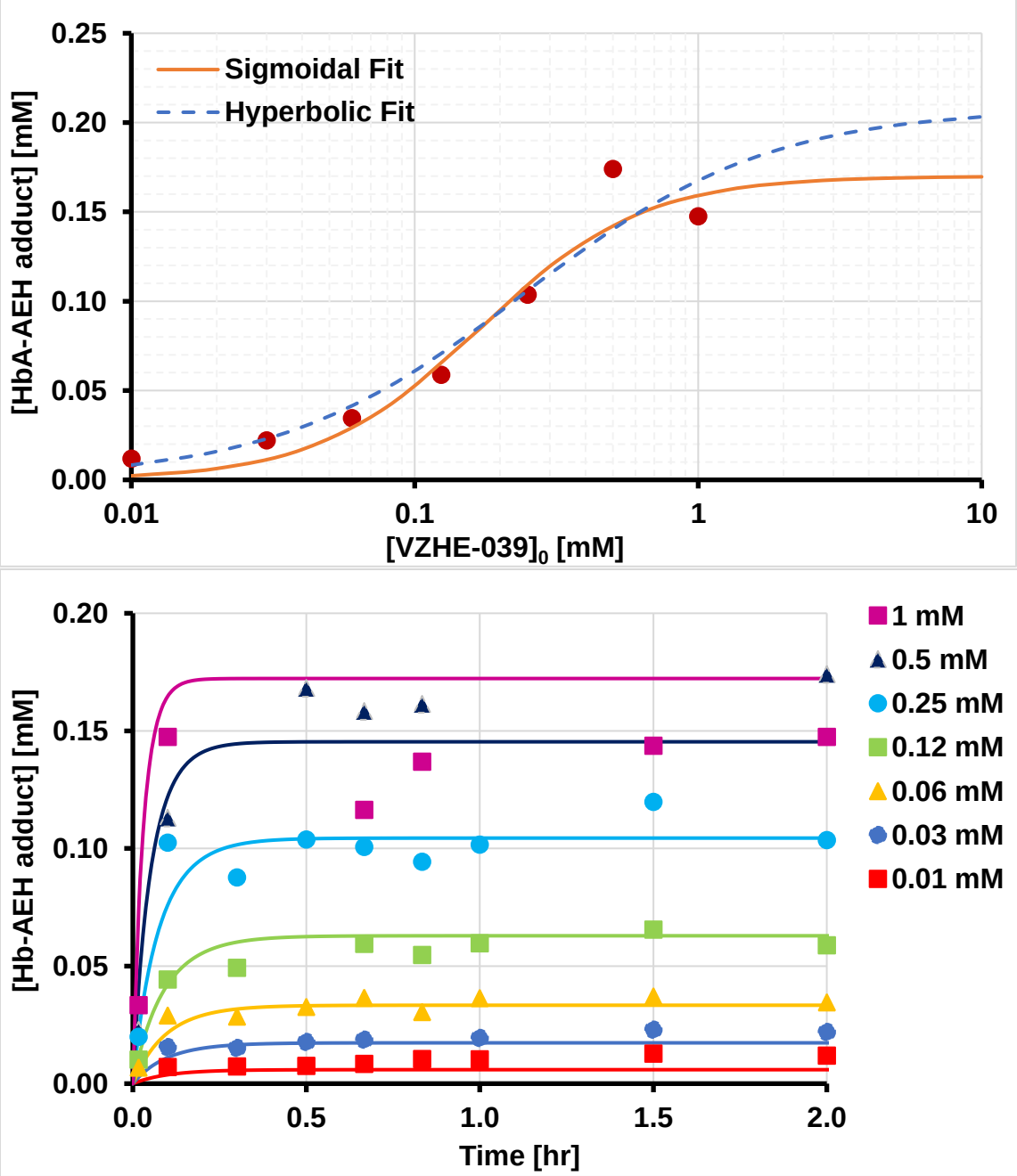

The initial concentrations selected for vanillin ($[vanillin]_0$) successfully covered the low and ascending portion of the sigmoidal curve, but may miss the plateau (Figure 3.19). Higher $[vanillin]_0$ (>5.8 mM) were designed for definitive study to capture the saturation portion to estimate B_{max} more precisely. The sigmoidal B_{max} -model fits the data well with acceptable goodness-of-fit ($r^2 = 0.999$). Point estimates for K_D, B_{max} and n were 2.2 mM (COV = 8%), 0.16 (5%) mM, 1.4 (7%), respectively, and were used as initial parameter estimates for the definitive study. The time-dependency experimental design captured both the ascending and plateau phase of the kinetic curves (Figure 3.19). The simple kinetic binding model fitted the data well with acceptable goodness-of-fit ($r^2 = 0.963$). Point estimates for k_{on} and k_{off} were 0.19 (12%) $hr^{-1}mM^{-1}$, and 0.43 (17%) hr^{-1}, respectively, and were used as initial parameter estimates for the definitive study.

Figure 3.19. Pilot study of SS concentration- and time-dependency of HbA-AEH adduct formation for vanillin in HbA solution (0.2 mM). The sigmoidal B_{max}-model and the simple kinetic binding model (lines) were fit to the SS concentration- and time-dependency of HbA-AEH adduct (symbols), respectively.

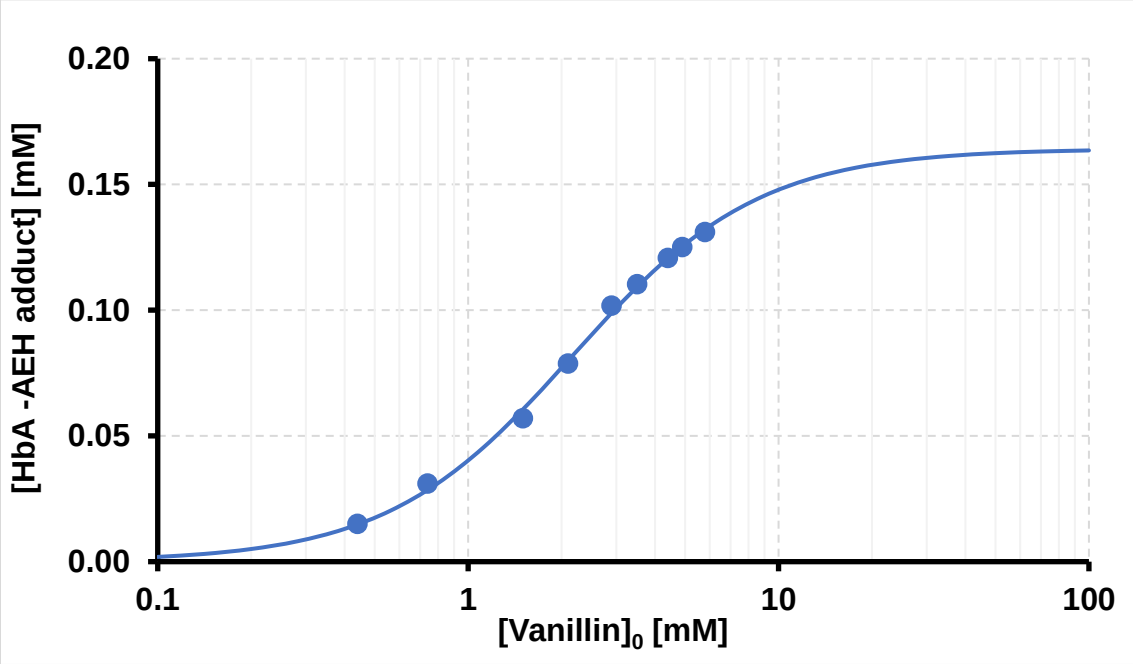

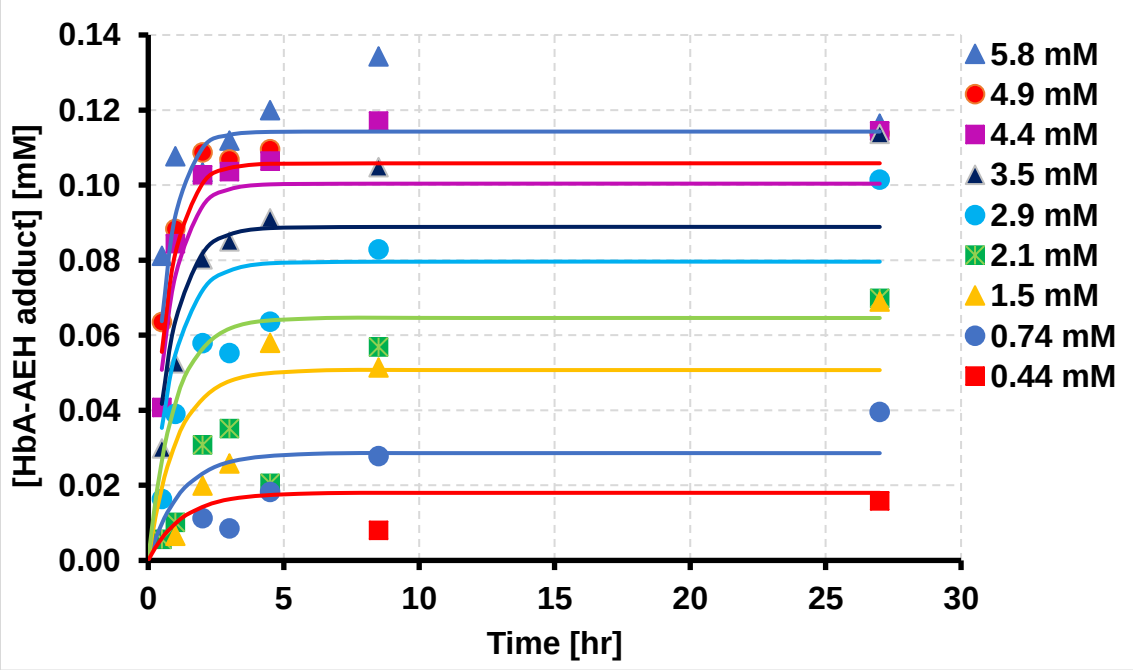

The initial concentrations selected for GBT-440 ($[GBT\text{-}440]_0$) covered the plateau and the sigmoidal portion of SS concentration-dependency curve, but missed the $[GBT\text{-}440]_0$ below K_D (Figure 3.20). Lower $[GBT\text{-}440]_0$ (< 0.1 mM) were added for definitive study to capture the low and ascending portions of the curve and better estimate n. The sigmoidal B_{max} -model fitted the data well with acceptable goodness-of-fit ($r^2 = 0.998$). Point estimates for K_D, B_{max} and n were 0.10 mM (COV = 5%), 0.13 (2%) mM, 3.6 (27%), respectively, and were used as initial parameter estimates for the definitive study. In time-dependency study, HbA-AEH adduct concentrations decreased after 2 mins for most of GBT-440 concentrations, indicating the binding kinetics was too fast for full quantitative characterization under these experimental conditions (Figure 3.20).

Figure 3.20. Pilot study of SS concentration- and time-dependency of HbA-AEH adduct formation for GBT-440 in HbA solution (0.2 mM). The sigmoidal B_{max}-model (line) was fit to the SS concentration- dependency of HbA-AEH adduct (symbols), and smooth dashed lines to connect time- dependency of HbA-AEH adduct.

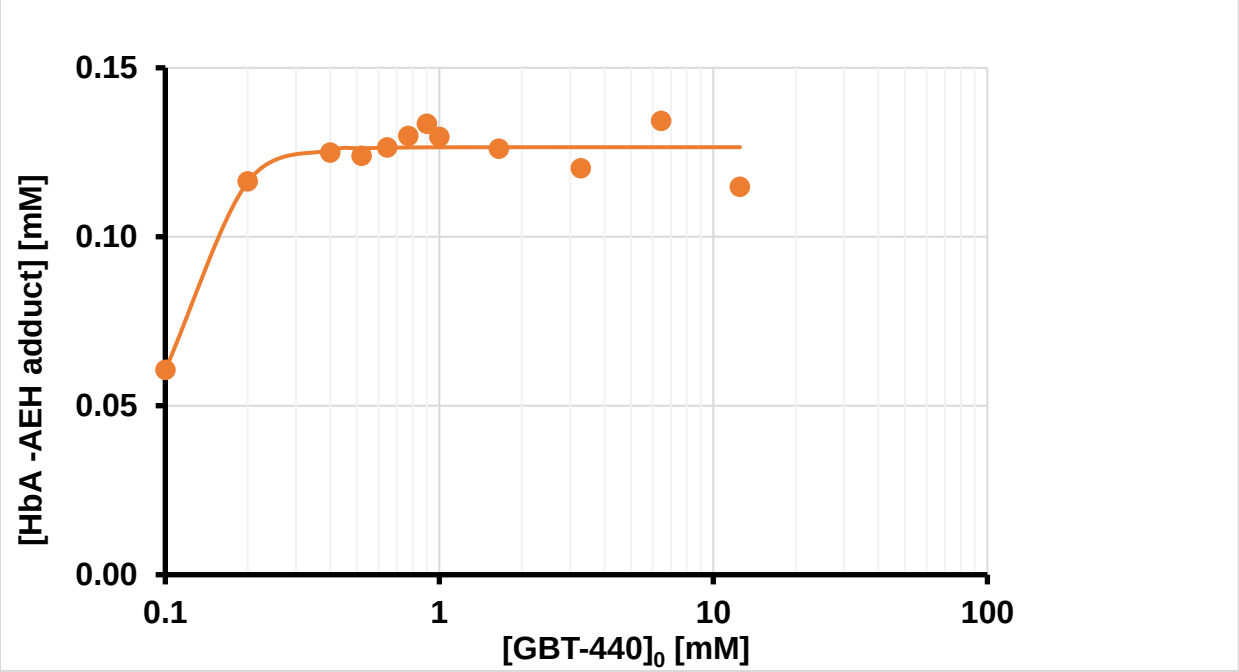

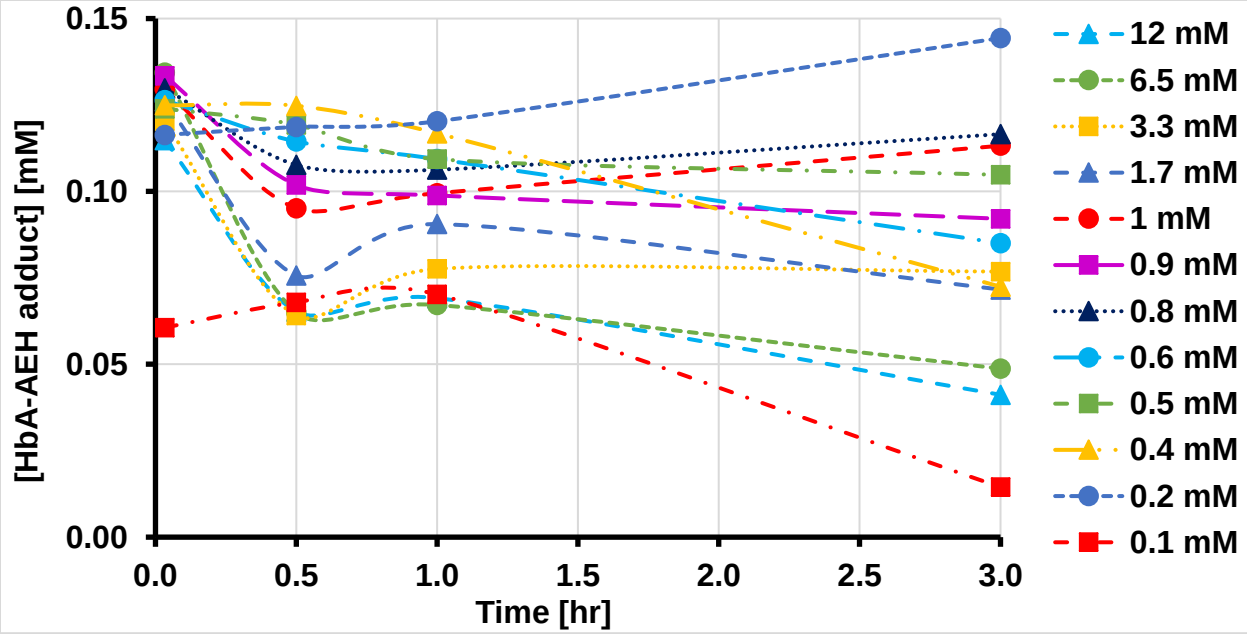

3.3.4. Definitive Study of SS Concentration- and Time-Dependency of HbA-AEH Adduct Formation in HbA Solution

3.3.4.1 Definitive Study of SS Concentration-Dependency of HbA-AEH Adduct Formation in HbA solution

All AEH showed the expected saturable concentration-dependent HbA binding, where HbA-AEH adduct concentrations ultimately achieved SS under the experimental conditions - except 2,5-DMF (Figure 3.21). The entire $[HbA]_0$ was modified by AEH, resulting in saturation, except for GBT-440, where only about 50% HbA were modified to the HbA adduct and the remaining 50% were not. B_{max}/HbA_0 values were close to 1, except for vanillin, INN-310 and GBT-440 (Table 3.6). Consistently positive values for n in SS binding indicate allosteric effects, supported by X-ray crystallography studies, where two AEH molecules (e.g., TD-7) were observed binding to the N-terminal Val1 of each of the α-globin chain (Deshpande et al., 2018).

Figure 3.21. Definitive study of SS concentration-dependency of HbA-AEH adduct formation for the selected AEH in HbA solution (0.2 mM). The sigmoidal B_{max}-model (lines) was fit to the experimental data (symbols).

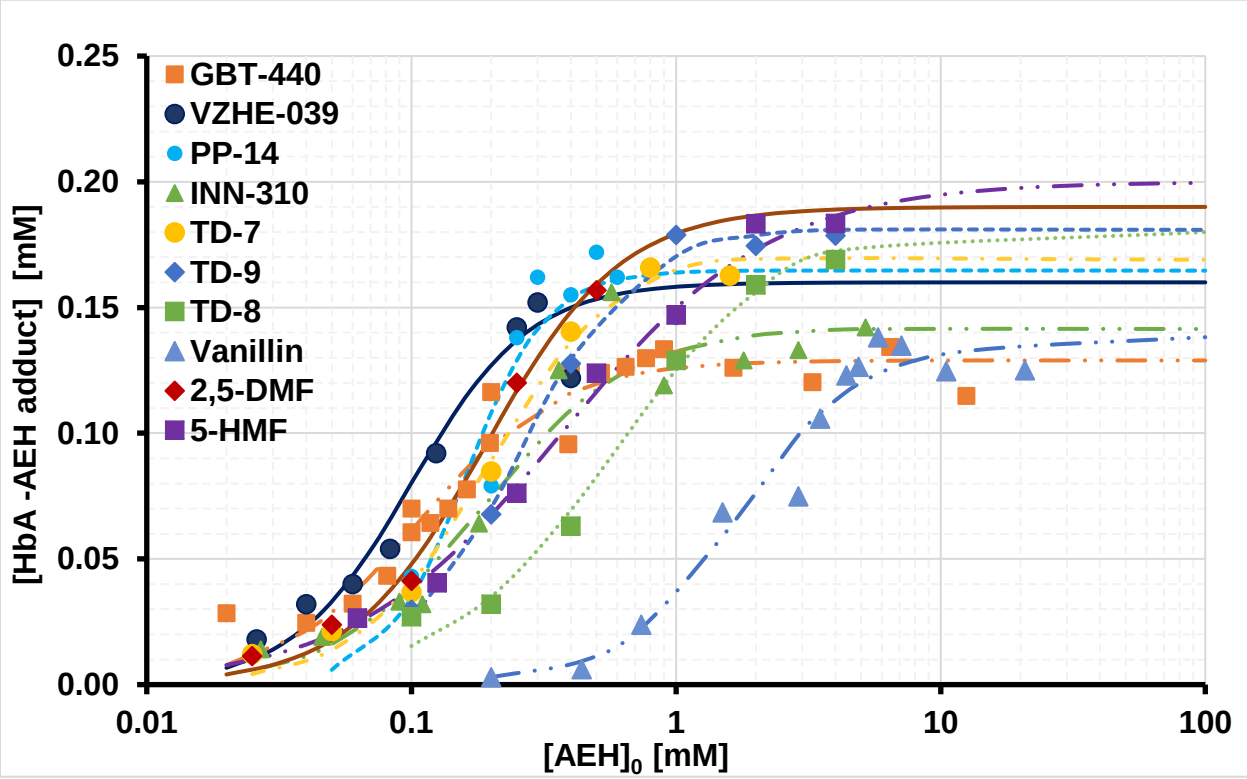

Table 3.6. Final parameter estimates of SS concentration-dependency of HbA-AEH adduct formation in HbA solution using sigmoidal B_{max}-model. Data are presented as PE with (COV).

	r^2	B_{max} /HbA_0	K_D [mM]	n
5-HMF	0.998	1.0 (6%)	**0.37** (16%)	1.1 (10%)
2,5-DMF	0.997	1.0 (15%)	**0.19** (25%)	1.7(21%)
Vanillin	0.990	0.70 (7%)	**1.7** (16%)	1.9 (24%)
TD-8	0.997	0.90 (8%)	**0.58** (19%)	1.4(17%)
TD-9	0.999	0.90 (3%)	**0.25** (7%)	2.0 (12%)
TD-7	0.997	0.85 (5%)	**0.19** (10%)	1.8 (15%)
INN-310	0.976	0.70 (8%)	**0.19** (21%)	2.4 (20%)
PP-14	0.988	0.80 (6%)	**0.16** (13%)	2.8 (30%)
VZHE-039	0.986	0.80 (14%)	**0.10** (24%)	1.9 (34%)
GBT-440	0.991	0.65 (3%)	**0.11** (9%)	1.6 (16%)

Compared to 5-HMF (VCU lead compound), 2,5-DMF showed a 2-fold enhanced binding affinity (smaller K_D), possibly due to its additional aldehyde group on the furan ring (Figure 3.22). Compared to the parent compound, vanillin, all benzaldehyde derivatives exhibited enhanced HbA binding affinity, indicating that the additional pyridinyl-methoxy side chain increases HbA binding affinity/interactions, as supported by X-ray crystallography findings (Figure 3.21)(Deshpande et al., 2018). In addition, the positions of methoxy group and/or the pyridinyl-methoxy group on the benzene ring determine K_D (TD-7<TD-9<TD-8) (Figure 3.23).

Figure 3.22. Definitive study of SS concentration-dependency of HbA-AEH adduct formation for 5-HMF and 2,5-DMF in HbA solution (0.2 mM). The sigmoidal B_{max}-model (lines) was fit to the experimental data (symbols).

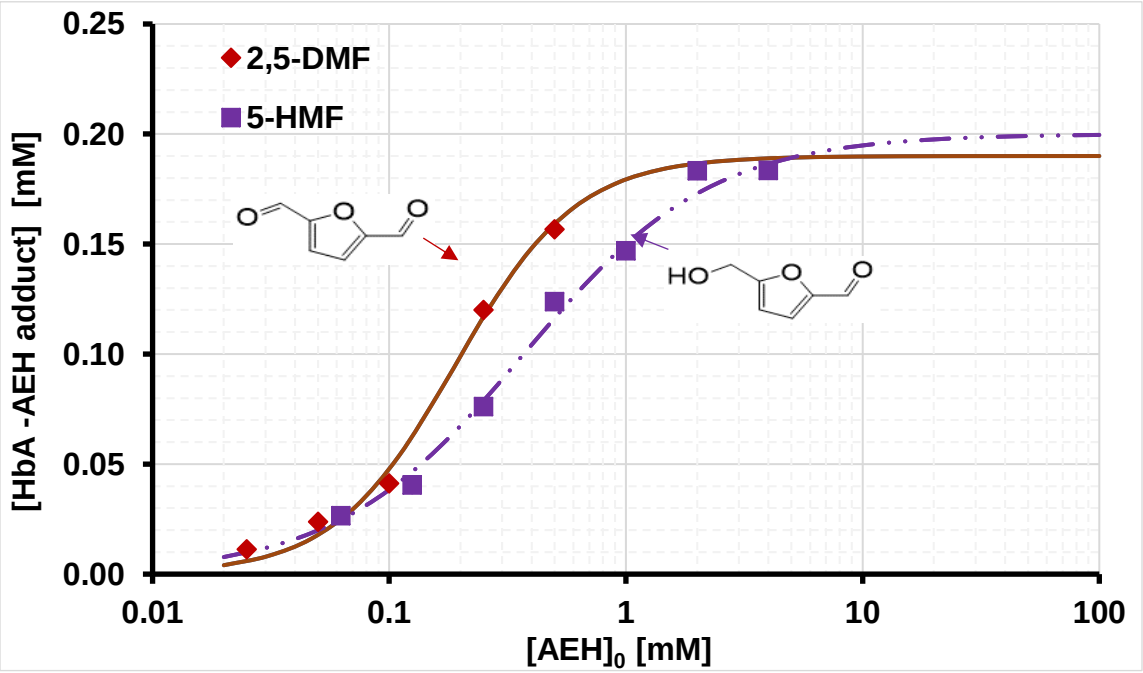

Figure 3.23. Definitive study of SS concentration-dependency of HbA -AEH adduct formation for TD isomers, as well as 5-HMF and vanillin in HbA solution. The sigmoidal B_{max}-model (lines) was fit to the experimental data (symbols).

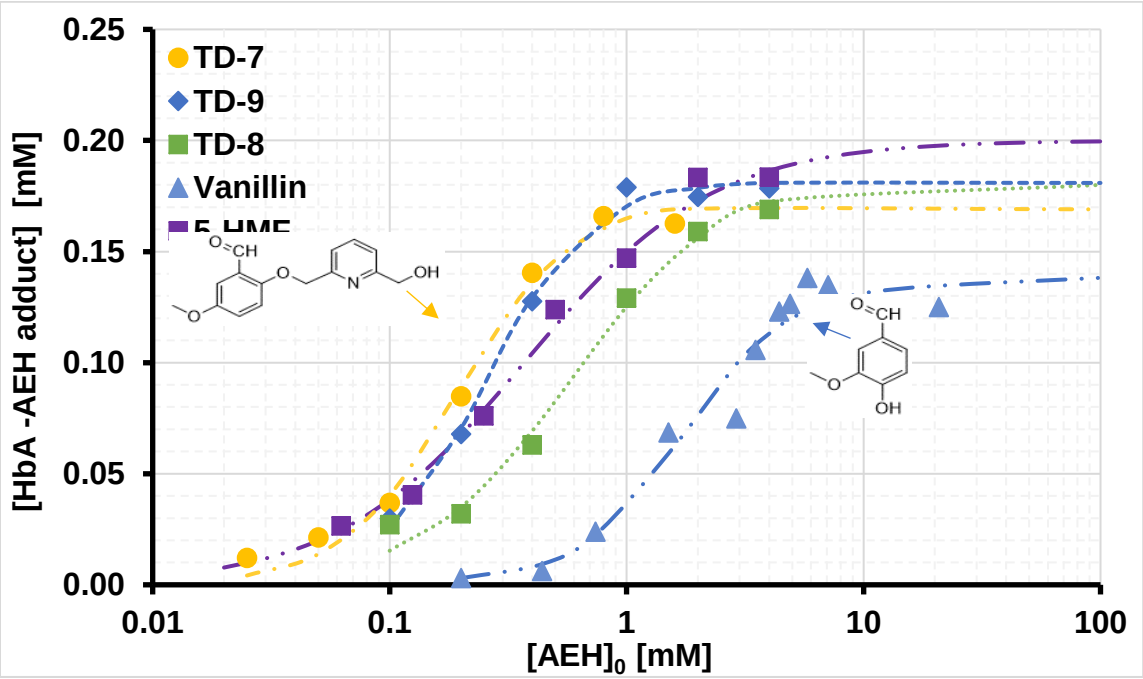

Similar to 2,5-DMF and TD-7, a group of AEH showed enhanced binding affinity over 5-HMF as well, namely, INN-310, PP-14, VZHE-039, and GBT-440 (Figure 3.24). INN-310 share the same *meta*-positioned methoxy group on benzene ring as in TD-7, where the only difference is the hydroxy group on pyridine ring, which resulted in identical binding affinity estimates (K_D = 0.19 mM). PP-14, VZHE-039 and GBT-440 shared the same *ortho*-positioned-hydroxy group on benzene ring and exhibited high HbA binding affinity (K_D = 0.16 mM, 0.10 mM and 0.11 mM, respectively).

Figure 3.24. Definitive study of SS concentration-dependency of HbA -AEH adduct formation for high affinity AEH, as well as 5-HMF and Vanillin in HbA solution. The sigmoidal B_{max}-model (lines) was fit to the experimental data (symbols).

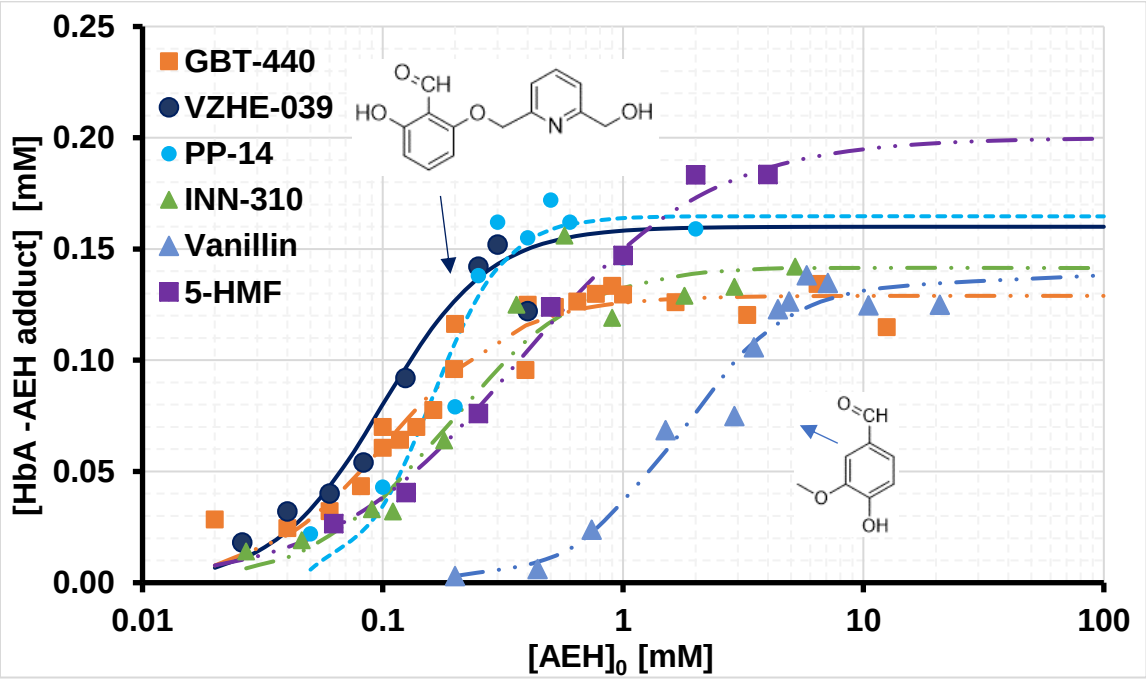

3.3.4.2 Definitive Study of Time-dependency of HbA-AEH adduct Formation in HbA Solution

All AEH showed time-dependent HbA-AEH adduct formation under designed experimental conditions (Figure 3.25 – 3.27). Increasing initial AEH concentrations ($[AEH]_0$) led to a more rapid achievement of HbA adduct equilibrium, as well as increased HbA-AEH $adduct_\infty$ concentrations - as expected from the sensitivity analysis discussed in section 3.3.2. The simple kinetic binding model adequately described the observed data across a wide range of AEH_0 concentrations and time points (Figure 3.25 – 3.27, Table 3.7) and resulted in similar K_D estimates compared to the K_D obtained from SS concentration-dependency studies using Sigmoidal B_{max}-model (Table 3.8).

Table 3.7. Final parameter estimates of time -dependency of HbA-AEH adduct formation in HbA solution, using the simple kinetic binding model. Data are presented as PE with (COV).

	r^2	k_{on} [$mM^{-1}*hr^{-1}$]	k_{off} [hr^{-1}]	K_D [mM]	$t_{1/2}^{eq}$ [hr]
5-HMF	0.934	**0.46** (11%)	**0.13** (25%)	0.28	3.1
2,5-DMF	0.980	**0.54** (6%)	**0.065** (14%)	0.12	4.5
Vanillin	0.956	**0.16** (13%)	**0.69** (16%)	4.3	0.96
TD-8	0.935	**0.18** (10%)	**0.10** (26%)	0.55	5.0
TD-9	0.979	**0.76** (8%)	**0.18** (15%)	0.23	2.1
TD-7	0.992	**9.8** (5%)	**1.5** (9%)	0.15	0.20
PP-14	0.958	**16** (12%)	**2.2** (19%)	0.14	0.13
INN310	0.897	**5.0** (11%)	**0.70** (25%)	0.14	0.41
VZHE-039	0.983	**61** (9%)	**5.8** (13%)	0.10	0.058

Table 3.8. Comparison of the final K_D and $K_D^{kinetic}$ estimates from SS concentration- and time-dependency of HbA-AEH adduct formation in HbA solution, using sigmoidal B_{max}-model and simple kinetic binding model, respectively. Data are presented as PE with (COV).

	K_D [mM]	$K_D^{Kinetic}$ [mM]
5-HMF	**0.37** (16%)	**0.28** (36%)
2,5-DMF	**0.19** (25%)	**0.12** (20%)
Vanillin	**1.7** (16%)	**4.3** (29%)
TD-8	**0.58** (19%)	**0.55** (36%)
TD-9	**0.25** (7%)	**0.23** (23%)
TD-7	**0.19** (10%)	**0.15** (14%)
INN-310	**0.19** (21%)	**0.14** (31%)
PP-14	**0.16** (13%)	**0.10** (36%)
VZHE-39	**0.10** (24%)	**0.10** (22%)
GBT-440	**0.11** (9%)	NA

The tested AEH achieved equilibrium on different time scales (Figure 3.25 – 3.27). At low $[AEH]_0$ - assuming first-order conditions - 5-HMF, TD-8, and TD-9 equilibrated slowly with HbA, in 12 – 20 hrs, with an equilibrations half-life of 3.1, 5.0, 2.1 hrs, respectively (Figure 3.25). The slow equilibration rates were caused by their small k_{on} and k_{off} rate constants (Table 3.7). TD-7, being an isomer with TD-8 and TD-9, exhibited significantly more rapid equilibration in less than 1 hr due to its large k_{on} and k_{off} values (Figure 3.26). The three TD isomers differ by either the position of the methoxy moiety or the methoxypyridine moiety on the benzene ring (Figure 3.1). TD-7 has a *meta*-located methoxy group relative to the aldehyde, while TD-9 has the methoxy group located at the *para* position on the benzene ring. TD-8 differs from TD-9 by the position of the methoxypyridine moiety, which is located *para* and *ortho* to the aldehyde moiety, respectively. These structural differences appear to determine their binding kinetics to HbA. VZHE-039, which is structurally similar to TD-7, but with an *ortho*-positioned hydroxyl group instead of *meta*-positioned methoxy group relative to the aldehyde moiety, showed the fastest binding kinetics, achieving equilibrium in less than half an hour (Figure 3.27). PP-14 and INN-310, which showed slightly lower binding affinity (large K_D) than VZHE-039, exhibited slower overall binding kinetics than VZHE-039. GBT-440, on the other hand, showed the same binding affinity as VZHE-039 in the SS concentration-dependency study, but very fast reaction kinetics which could not be characterized under current experimental conditions.

Figure 3.25. Definitive study of time-dependency of HbA-AEH adduct formation for 5-HMF in HbA solution (0.2 mM). The simple kinetic model (lines) was fit to the experimental data (symbols).

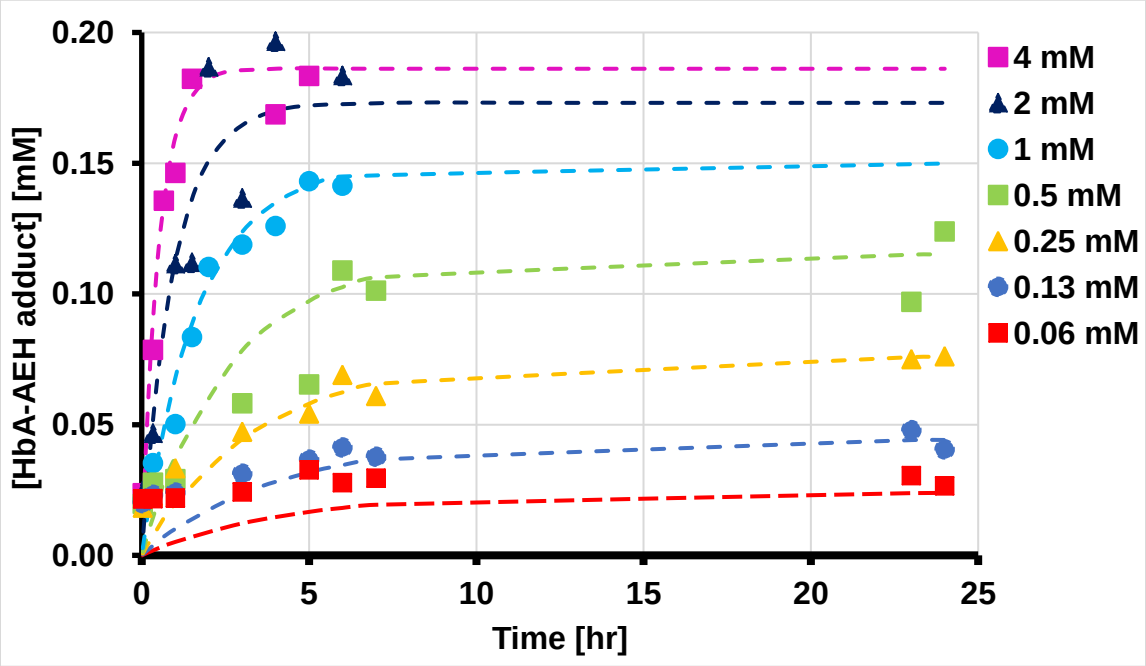

Figure 3.26. Definitive study of time-dependency of HbA-AEH adduct formation for TD-7 in HbA solution (0.2 mM). The simple kinetic model (lines) was fit to the experimental data (symbols).

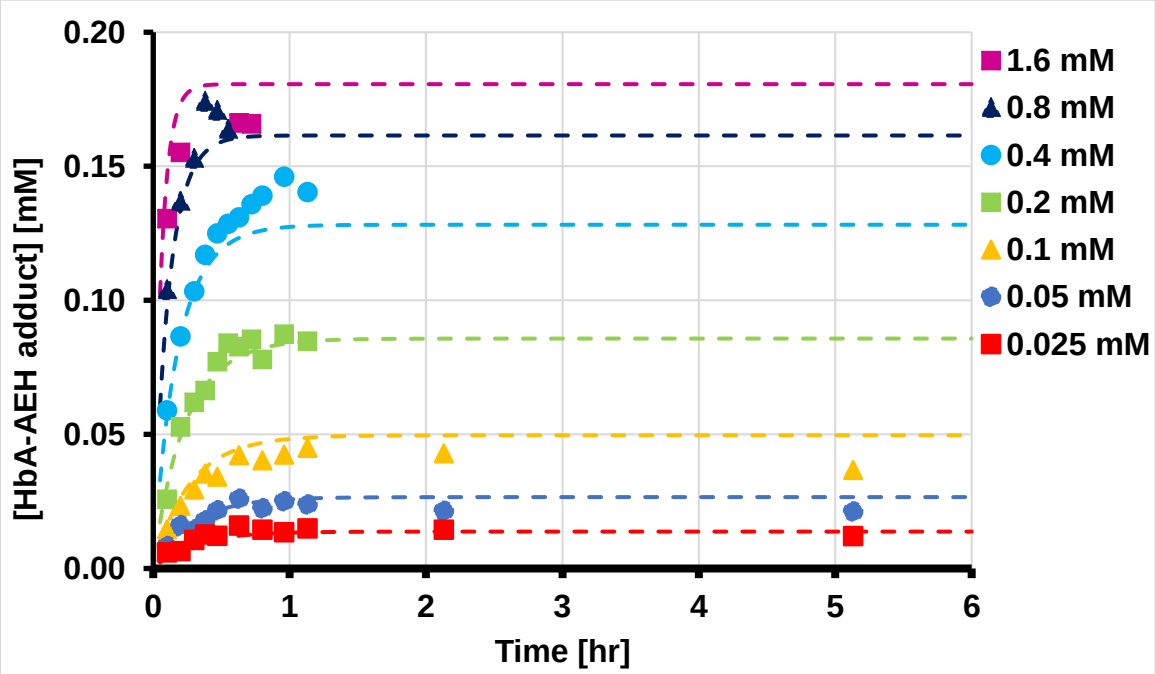

Figure 3.27. Definitive study of time-dependency of HbA-AEH adduct formation for VZHE-039 in HbA solution (0.1 mM). The simple kinetic model (lines) was fit to the experimental data (symbols).

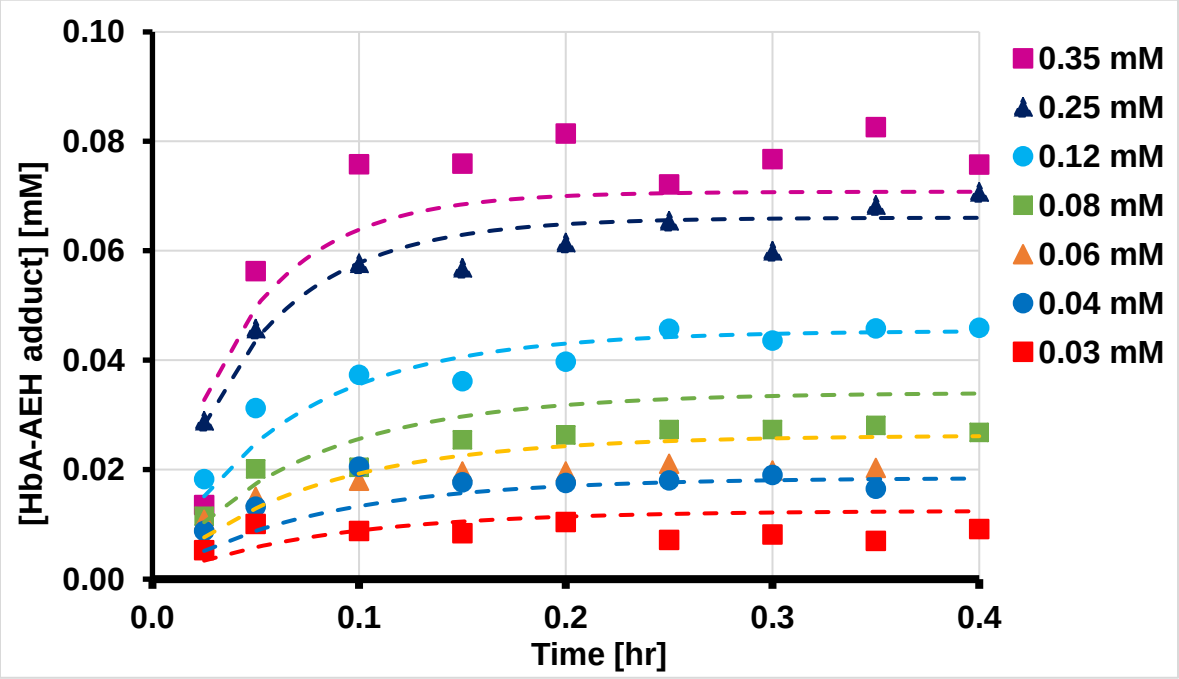

Vanillin - without a bulky side-chain available for supplemental HbA interactions besides the Schiff base binding - exhibits a small k_{on} and relatively large k_{off}, resulting in poor HbA affinity (K_D) (Table 3.7). Compared to the parent compound, vanillin, the addition of a methoxy-pyridine side chain to the benzene ring, in general, leads to a (desirable) increase of k_{on}. However, TD-7, PP-14 and VZHE-039 also show, to a lesser extent, an (undesirable) increase of k_{off} (Table 3.7).

All AEH across furaldehydes and benzaldehydes, except vanillin and 2,5 - DMF, showed a strong correlation (r = 0.993, n=7) between their k_{on} and k_{off} values (Figure 3.28). The two furaldehydes, 2,5-DMF and 5-HMFdiffers from each by the former having an additional aldehyde moiety at the 2-position. The two exhibited similar k_{on} values, but 2,5-DMF has a 2-fold smaller k_{off} relative to 5-HMF. The previously discussed SS concentration-dependency studies showed that most of the studied AEHs (except GBT-440, vanillin, 2,5-DMF) achieved more than 80% of HbA modification at full HbA saturation. However, vanillin and 2,5-DMF showed a significant loss of mass balance, especially at high $[AEH]_0$ (Figure B.3.11 – 2.12 in Appendix B); along with the observed additional peaks on chromatograms for both vanillin and 2,5-DMF, this indicates other parallel/sequential reactions may happen beyond the primary HbA-AEH adduct formation. These might explain why vanillin and 2,5-DMF are outliners in the coloration of k_{on} and k_{off}.

The strong correlation between k_{on} and k_{off} with most of the AEHs indicates that the current molecular design strategy did enhance interaction with Hb (as intended), but also enhanced dissociation from Hb, albeit inadvertently. This strong correlation also indicates proportional changes of k_{on} and k_{off} in the same direction, resulting in a less

than 5-fold improvement of K_D from the top candidate VZHE-039, relative to the previous lead compound (5-HMF). However, the overall Hb binding kinetics of VZHE-039 is more rapid than 5-HMF, as reflected by a more than 50-fold shorter $t_{1/2}^{eq}$ under the current experimental conditions, due to the increase of both k_{on} and k_{off}.

Figure 3.28. Log-log correlation of k_{on} and k_{off} for AEH. A power equation (dashed line) was fit to the experimental data (blue circle symbols), except for two outliners (orange triangle symbols), i.e., 2,5-DMF and vanillin.

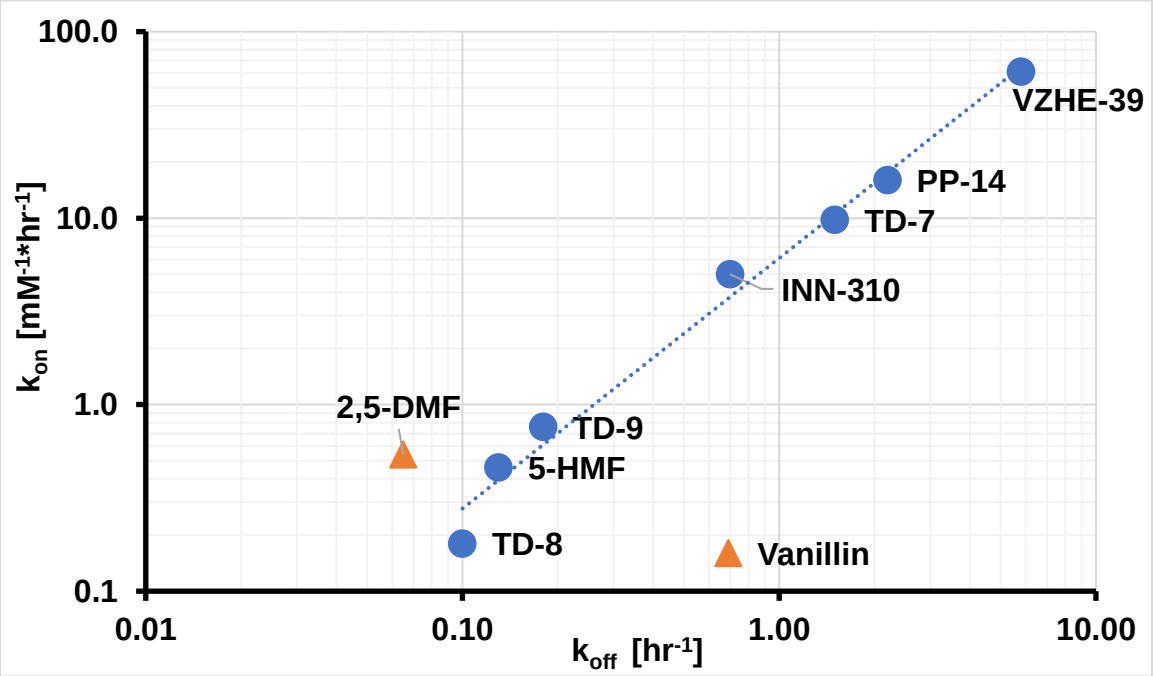

3.4 Discussion and Conclusions

Previous X-ray crystallography studies showed that two AEH molecules (e.g., TD-7) bind to each α-chain of Hb molecule (2:1 stoichiometry) (Deshpande et al., 2018). In our SS concentration-dependency studies, a sigmoidal B_{max}-model was applied to incorporate the possibility of cooperative binding by Hill coefficient, n. All AEH resulted in n >1, which matched the 2:1 binding phenomenon observed in X-ray crystallography studies.

In the SS concentration-dependency studies, major losses of mass balance were observed at saturable conditions with long incubation times for some AEH, namely 2,5-DMF, vanillin, and GBT-440. Unidentified new peaks were also observed, eluting at an earlier time on the chromatograms for all three AEH, which indicates that besides the primary HbA-AEH adduct formation, other "unidentified Hb adducts (UHbA-adducts)" are formed in Hb mixtures. Since the increase of HbA-adducts parallels the decrease of the primary HbA-AEH adduct, a sequential conversion of primary HbA-AEH adduct to UHbA-adducts may occur.

A similar process, glycation may provide some hints, where glucose first reversibly binds to Hb via Schiff-base reaction, followed by irreversible rearrangement to form $HbA1_C$ (Ge & Lee, 1997). However, the loss of the primary HbA-AEH adduct may also be due to parallel conversion from free Hb directly to HbA-adducts. For example, GBT-440 is also believed to bind to β-chain of Hb when high $[GBT\text{-}440]_0$ is present in Hb solution (Abdulmalik, 2018). Binding to other sides of Hb may change the conformation of Hb in different way, which further decrease pI of UHbA-adducts protein (early elution)

compared to the free HbA and the primary HbA-AEH adduct. 2,5-DMF and vanillin are also the outliners in the coloration relationship of k_{on} and k_{off}, where the potential UHbA-adducts may play a role.

For the time-dependency studies, a simple kinetic binding model (1:1 binding) was used because of its good model selection criteria, indicating an acceptable fit of the experimental data, resulting in reliable final point estimates for k_{on} and k_{off} (Table 3.7 in Section 3.4.4.2). The different assumptions on AEH to Hb binding ratio between SS concentration- and time- dependent models resulted in slightly different final estimates for K_D (Table 4.8 in Section 3.4.4.2). However, after accounting for the coefficient of variance (COV%), i.e., imprecision, of the final estimates, these differences between K_D and $K_D^{kinetic}$ estimates are considered negligible - indirectly confirming the proper use of both models for Hb binding affinity and binding kinetic characterization.

The crystal structures of some AEH in complex with liganded Hb have been elucidated, which can provide some insight into the differences in the binding affinity of the AEHs to Hb. Consistent with TD-7 showing the lowest K_D (highest binding affinity) among the three isomers, TD-7 (0.19 mM), TD-8 (0.58 mM) and TD-9 (0.25 mM), the electron density of bound TD-8 and TD-9 was found to be very weak and sparse compared to TD-7, suggesting weaker interactions of TD-8 and TD-9 with Hb than TD-7 (Deshpande et al., 2018). INN-310 (SAJ-310) also showed strong binding density like TD-7; however, it appears to make more interactions with Hb than TD-7, explaining a slightly higher affinity to HbA of INN-310 (0.14 mM) than TD-7 (0.19 mM).

TD-7 and VZHE-039 share the same methylhydroxyl group on the pyridine ring. However, TD-7 differs from VZHE-039, with the former having a *meta*-positioned

methoxy group while the latter has an *ortho*-hydroxyl group. The methylhydroxyl group on the pyridine ring is expected to make interactions with the surface-located αF-helix to directly weaken polymer interactions. The F-helix is implicated in polymer stabilization through hydrogen-bonding interactions with other polymer strands (Cretegny & Edelstein, 1993). Consistent with this idea, natural mutations, e.g. αAsn78→Lys (Hb Stanleyville) that abrogate these interactions, lead to increased solubility/less "sickling" of deoxy HbS hetero tetramers, mitigating the severity of SCD (Cretegny & Edelstein, 1993). Interestingly, while the methylhydroxyl of VZHE-039 makes the predicted interactions with the F-helix that of TD-7 does not; rather rotating away from the F-helix (Ahmed et al., 2020). This unique F-helix interaction may help explain why VZHE-039 binds with the highest affinity among the benzaldehydes (Ahmed et al., 2020). Consistently, VZHE-039 showed the lowest K_D (0.1 mM), i.e., VZHE-039 < INN-310 <TD-7 < TD-9 < TD-8 < vanillin. We also note that VZHE-039 interactions with αF-helix has resulted in a secondary O_2-independent anti-sickling activity in addition to the primary O_2-dependent anti-sickling activity, which may show clinical benefits over other aromatic aldehydes (Ahmed et al., 2020; Oder et al., 2016; Pagare et al., 2018).

A difference between our novel AEH and the SCD-approved GBT-440 with respect to their HbA binding is their binding ratio to Hb molecules: GBT-440 binds to the HbA molecule with 1:1 ratio, as suggested by X-ray studies where its bulky pyrazole substituent precluded a second molecule to bind to the opposite α-chain of Hb tetramer; this is in contrast with the observed 2:1 stoichiometry for other AEH. In SS concentration-dependency studies with GBT-440, 50% natural HbA remains unmodified under saturable conditions, whereas for all other AEH, all the entire initial HbA was

modified to form the HbA-AEH adduct (although, as discussed above, a few AEH showed evidence of incomplete mass balance and unknown chromatography peaks, suggesting other, as yet-unknown HBA adducts

The “universal” HPLC-UV/Vis assay method used to quantitate HbA-AEH adduct employed indirect validation by HbA (rather than HbA-AEH adduct) calibration curves, where the tetrameric structure of HbA were measured. Our novel AEH bind to both sides of α-chains of Hb, leading to 100% HbA tetramer modification. On the other hand, for GBT-440, because only one side of α-chain is bound, but the other side remains in its unbound natural form, i.e., only 50% of HbA tetramer is modified

k_{on} and k_{off} are highly correlated among most of novel AEH, which indicates the current molecular design strategy led to enhanced association, by design, but also enhance dissociation, albeit unintentionally. Several reasons may explain the undesirable increasing of k_{off}, 1). The stability of side chains of AEH binding with HbA; 2). The electric density of imine carbon and nitrogen that affect hydrolysis process of Schiff-base; 3). The kinetic feature of Schiff-base reaction.

For example, to explain the kinetic difference between 5-HMF and TD-7 (k_{on} = 0.46 and 9.8 $hr^{-1}mM^{-1}$, k_{off} = 0.13 and 1.5 hr^{-1}, respectively), crystal structures were compared. A pair of 5-HMF or TD-7 molecules form Schiff-base interactions with the N-terminal αVal1 nitrogen of the two α-subunits in a symmetry-related fashion (Ahmed et al., 2020). The additional interactions for 5-HMF involves a strong and intricate network of water-mediated and direct hydrogen bonds (Ahmed et al., 2020). On the other hand, in TD-7, the additional interactions to the proteins are predominantly hydrophobic and

weak hydrogen bonds, which may be unstable in water environment to facilitate the dissociation of AEH from Hb (Ahmed et al., 2020).

The Schiff-base hydrolysis reaction of the HbA-AEH adduct may be facilitated with the increasing electropositive and electronegative nature of the imine carbon and nitrogen, respectively (Scheme 3.2). A computational approach using Mulliken charge analysis (Software: Gaussian 09) was applied to calculate the electric density of Schiff-base formed by AEH. Compared to INN-310 and TD-7, the intramolecular hydrogen bond of PP-14 and VZHE-039 increased the electronegativity of the nitrogen atom (-0.37 for INN-310 and TD-7, -0.54 for PP-14 and VZHE-039) and the electropositivity of the carbon atom (0.071 for INN-310 and TD-7, 0.198 for PP-14 and VZHE-039) of the Schiff-base, which is favorable for the decomposition of the Schiff base ($k_{off:}$ VZHE-039 > PP-14 > TD-7 > INN-310) (Abdulmalik, 2018).

The reversible “transient covalent” Schiff-base reaction involves intermediates (Kallen, 1971). The kinetic features between the formation and hydrolysis of Schiff-base may be determined by any of steps shown in Scheme 3.2. k_{off} used in our kinetic model is an overall rate constant that includes all the steps of Schiff-base hydrolysis and is ultimately determined by the rate-limiting part in the Schiff-base hydrolysis reaction steps. To explain the overall increasing of k_{off} for tested AEH and design novel AEH with smaller k_{off}, further research on kinetic profile of Schiff-base hydrolysis may be helpful.

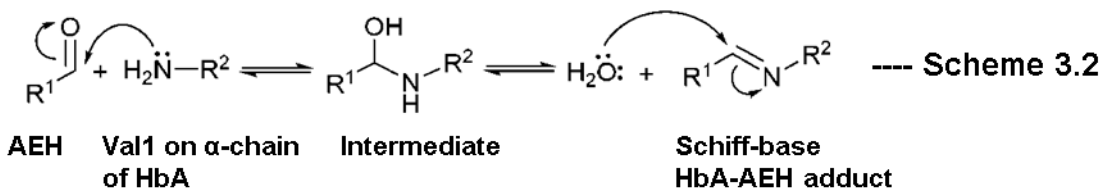

---- Scheme 3.2

In summary, we report for the first time the validation and application of a weak cation-exchange HPLC-UV/Vis assay (Universal Method) for ten diverse anti-sickling aromatic aldehydes, which provided insight into the binding kinetics of aromatic aldehydes interactions with HbA. Key molecular features to enhance Hb binding have been identified, allowing rational design of potentially more effective drug candidates for druggability evaluation. A top candidate, namely VZHE-039, is selected based on its fastest binding kinetics among tested AEH and the most potent binding affinity that comparable to the clinical reference, GBT-440.

In addition to its rapid and high-affinity HbA binding, VZHE-039 has a secondary O_2-independent anti-sickling MOA, which may provide clinical advantages. However, one of the major potential drawbacks of aromatic aldehydes is their potentially poor PK properties due to extensive and rapid metabolic oxidation of the aldehyde moiety into the corresponding inactive functional metabolites by ALDH, which is abundantly present in RBC, their site of action. Therefore, the stability of novel AEH in presence of ALDH enzyme is discussed in the next Chapter 4.

CHAPTER 4

IN-VITRO METABOLISM OF AEH IN HUMAN LIVER CYTOSOL (HLC)

4.1. Introduction

In-vitro metabolic studies are common approach to identify relative essential metabolic pathways at early stages of drug development. Compared to *in-vivo* approach, *in-vitro* metabolic study has the advantages of cost- and time-effectiveness, easy experimental procedures, protection of experimental animals, and avoiding the problem of inter-species differences. Several enzyme systems are commonly used in studying *in-vitro* metabolism, including recombinant enzymes, sub-cellular fractions, hepatocytes, and tissue slides (Ekins, Ring, Grace, Mcrobie-belle, & Wrighton, 2001). Depending on the relative metabolic pathways of research interests, choosing the correct *in-vitro* enzyme system is essential. For example, since human liver is the major elimination organ for most small molecule drugs, and nearly 80% such therapeutic drugs are metabolized by CYP450 enzymes, microsome becomes the most widely used for *in-vitro* metabolism studies(Manikandan & Nagini, 2017). Microsome contains enzymes on endoplasmic reticulum, such as CYP450 enzymes, flavin-monooxygenases, glucuronosyltransferases, monoamine oxidase (Jia & Lliu, 2007). However, as an artificial sub-cellular fraction, microsome often faces the problem of capacity limitations (Foster et al., 2010). The use of recombined enzyme is good for studying a specific enzyme isoform but limited by its deficiency of extrapolation to *in-vivo* clearance. Human liver cytosol (HLC) contains soluble metabolic enzymes, including sulfotransferases, methyltransferase, aldehyde dehydrogenase (ALDH), aldehyde oxidase, alcohol

dehydrogenase (ADH) and so on (Jia & Lliu, 2007). Human liver S9 is the supernatant fraction obtained from liver homogenate by centrifuging at 9000 g for 20 minutes in a suitable medium, which contain both microsomal and cytosolic fractions that are commonly used to study sulfation, methylation, glucuronidation. Like other sub-cellular enzyme systems, HLS9 shares the same limitation of the lack of intact cell structure that accounts for cell membrane permeability and co-factors. Hepatocytes and liver slices are the *in-vitro* systems that most closely mimic *in-vivo* metabolism, including the intact cell environment and necessary co-factors that account for potential of hydrolysis, oxidation, reduction, and glucuronidation (Jia & Lliu, 2007). Some major drawbacks for use of hepatocyte and liver slices are stability problem of the enzymatic activities, cell viability, and labor extensive (Jia & Lliu, 2007). None of *in-vitro* enzyme system is thus prefect but a system matched to the research interests provides the most needed information.

ALDH is a primary enzyme that oxidizes varying endogenous and exogenous aldehydes to carboxylic acids using the co-factor NAD^+. Human ALDH enzymes are involved in essential detoxified pathways and widely expressed in various tissues (Mezey, Rawles, Rhodes, & Potter, 1987; O'Brien, Siraki, & Shangari, 2005). Substrate specificity of ALDH is broad, covering a large variety of aldehydes, such as retinal, acetaldehyde, aromatic and aliphatic aldehydes (O'Brien et al., 2005). Previous *in-vitro* and *in-vivo* studies showed that some allosteric effectors of Hb (AEH) exhibit anti-sickling activities, e.g. furaldehydes (example is 5-HMF) and benzaldehydes (INN-312), but are subjected to ALDH – mediated metabolism, rendering these molecules less desirable for development to treat sickle cell disease (SCD) (Obied, 2010; Parikh, 2013).

Novel synthetic AEH selected in this research are benzaldehydes that structurally share similar aromatic and pyridine ring with the previously studied anti-sickling benzaldehydes, i.e., INN-compounds. Like the INN compounds, these compounds, are also suspected to undergo ALDH-mediated metabolism. Liver is the major organ for detoxification of aldehydes by the most abundant metabolizing enzyme ALDH (O'Brien et al., 2005). Both cytosolic ALDH-1 and mitochondrial ALDH-2, two major isoforms of ALDH are expressed in liver (O'Brien et al., 2005). ALDH-1 is also expressed in RBC, and was found to have similar physical, chemical, and kinetic properties as the ALDH-1 in HLC (Mezey et al., 1987). ALDH-1 in both RBC and HLC show high affinity for aldehydes, low affinity to cofactor NAD^+, and is strongly inhibited by disulfiram (Inoue, Nishimukai, & Yamasawa, 1979). In order to study the potential stability of AEH in presence of ALDH, HLC is chosen as the enzyme matrix to screen their metabolic efficiency.

UV/Vis spectrophotometry is a commonly used analytical method for metabolic reactions, which has the advantages of low-cost, easy-sample preparation, and time-effectiveness. To characterize metabolic reactions, several approaches are being used, including monitoring the depletion of substrate, the formation of product or co-factor consumption. Depending on the physicochemical properties of substrate and product, consumption of co-factor may be used to monitor enzyme activities. For example, if both the substrate and product share similar UV spectrum features and no detection wavelength can be optimized to separate product from substrate, monitoring the co-factor consumption can be a good alternative way if substrate and product have limited interference at the detection wavelength of co-factor. To better conduct *in-vitro*

metabolic reactions using sub-cellular system like HLC, the concentration of corresponding co-factor (e.g. ALDH enzyme with NAD^+ as the cofactor) need to be optimized. Enough concentration of co-factor is needed to be added into system to avoid the early completion of the metabolic reaction due to the deficiency of co-factor.

A typical metabolic model to quantitatively characterize enzyme activity is Michaelis-Menten (MM) kinetics (Equation 4.2). Initial reaction rate (v_i) is obtained as the slope from concentration (products or cofactor) -time dependent progress curve. When [S] << k_m, v_i is proportional to the increase of substrate concentrations (apparent first-order kinetics). When [S] >>k_m, v_i becomes independent of substrate concentrations due to the saturation of metabolic enzyme (apparent zero order kinetics). Intrinsic clearance (CL_{int}) describes the ability of the organ to remove drug in the absence of flow limitations and binding to cells or proteins in the blood. CL_{int} can be estimated from the ratio of maximum reaction rate to binding affinity (v_{max} / K_m), which is equal to the slope of the apparent first-order kinetics (when [S] << k_m). CL_{int} is commonly used to compare the enzyme specificity to substrates. The larger the CL_{int} is, the more efficient is the enzyme to clearing this specific substrate, in absence of other factors, including PPB and blood flow. It is also useful to allow extrapolation of *in-vitro* data to *in-vivo* metabolism.

AEH, characterized by aromatic aldehyde may be subject to ALDH-mediated metabolic degradation in red blood cells (RBC), limiting their duration of action. The main objective of this chapter is to screen their ALDH susceptibility in early developing phase. a UV/Vis spectrophotometric assay method was used to assess the oxidation of 5-HMF, 2,5-DMF, TD isomers, INN-310, and VZHE-039 in HLC by monitoring the

reduction of the cofactor (NAD^+) of ALDH. Their metabolic kinetic properties to ALDH enzyme were then characterized by MM kinetics or a linear apparent first-order kinetics. Structure features that protect the aldehyde group of AEH from ALDH enzyme metabolism were also discussed.

4.2. Methods

4.2.1. Materials and Reagents

1. Tris-HCl buffer 1 M, pH 7.5 (Fisher Scientific, Pittsburgh, PA).
2. Tris Base (Sigma, St. Louis, MO) (121 g/mol)
3. Co-factor - β-Nicotinamide adenine dinucleotide hydrate (NAD^+) from yeast (Sigma, St.Louis, MO) (663 g/mol)
4. β-Nicotinamide adenine dinucleotide, reduced dipotassium salt (NADH) (Sigma, St.Louis, MO) (742 g/mol)
5. Ethanol 200 proof, 99.5% (Sigma-Aldrich, Milwaukee, WI) (46 g/mol)
6. Acetaldehyde, ACS 99% (Sigma-Aldrich, Milwaukee, WI) (44 g/mol)
7. HCl, ACS 37% (Sigma-Aldrich, Milwaukee, WI) (36 g/mol)
8. 5-Hydroxymethyl-2-furfural (5-HMF) (Sigma, St. Louis, MO) (126 g/mol)
9. 2,5-Furandicarboxaldehyde (2,5-DMF) (Sigma-Aldrich, Milwaukee, WI) (124 g/mol)
10. TD-7-HCl (provided by Dr. Martin Safo, Department of Medicinal Chemistry, VCU) (309 g/mol)
11. TD-8-HCl (provided by Dr. Martin Safo, Department of Medicinal Chemistry, VCU) (309 g/mol)
12. TD-9-HCl (provided by Dr. Martin Safo, Department of Medicinal Chemistry, VCU) (309 g/mol)
13. INN-310 (provided by Dr. Martin Safo, Department of Medicinal Chemistry, VCU) (243 g/mol)

14. VZHE-039-HCl (provided by Dr. Martin Safo, Department of Medicinal Chemistry, VCU) (331 g/mol)
15. Vanillin ReagentPlus® 99% (Sigma, St. Louis, MO) (152 g/mol)
16. Dimethyl sulfoxide (DMSO), ≥ 99.9%, A.C.S. Reagent (Sigma-Aldrich, Milwaukee, WI) (78 g/mol)
17. Human Liver cytosol, 10 mg protein/mL, mixed gender, pool size 50 (XenoTech, Lenexa, KS)

4.2.2. Equipment

1. Synergy™ 2 multi-mode microplate reader (BioTek, Winooski, VT).
2. Greiner® UV-Star 96-well plate (Sigma, St.Louis, MO)
3. Falcon® assay plate, 96-well plate (VWR, West Chester, PA).
4. SciFinder® (CAS software, 2010).
5. MarvinSketch, version 17.9 (ChemAxon software, 2017)
6. Scientist®, version 3.0 (Micromath Softwar)
7. pH Meter (Fisher Scientific, Pittsburgh, PA)
8. Vortex (Vortex-Genie, VWR, West Chester, PA).
9. Balance (Fisher Scientific A 250, Pittsburgh, PA).
10. 0.5-5 mL Finnpipette (Thermo Scientific, Waltham, MA).
11. 30 – 300 µL multichannel pipette (Fisher Scientific, Hanover Park, IL)
12. 3-25 µL positive displacement pipette and corresponding pipette tips (Rainin Instruments, Oakland, CA).
13. 10-100 µL and 100-1000 µL VWR pipettes and corresponding pipette tips (VWR, West Chester, PA).

4.2.3. Sample Preparation and Experimental Design

1. 0.5 M Tris-HCl, pH 7.5

   60.57 g of Tris Base was dissolved in 800 mL sterile deionized (DI) water, and the pH adjusted to 7.5 with HCl with stirring. The Tris-HCl solution was then made up to 1000 mL with sterile DI water and filtered with sterile-filter.

2. NAD^+ solution

   11.2 mM stock solution was freshly made every day for oxidative metabolism experiments. 22.3 mg NAD^+ was dissolved in 3 mL of 0.5 M Tris-HCl buffer (pH 7.5). 25 µL of 11.2 mM stock solution was added to each well of 96-reaction plate to obtain a final in-well concentration of 1.4 mM (200 µL).

3. NADH solution

   3.2 mM stock solution was freshly made every day for reductive metabolism experiments. 11.9 mg NAD^+ was dissolved in 5 mL of 0.5 M Tris-HCl buffer (pH 7.5). 25 µL of 3.2 mM stock solution was added to each well of 96-reaction plate to obtain a final in-well concentration of 0.4 mM (200 µL).

4. Human liver cytosol (HLC) solution

   1.6 mg/mL stock solution was made with 160 µL of 10 mg/mL. HLC added to 840 µL of Tris buffer on ice. 25 µL was transferred to each well of 96-reaction plate to obtain a final in-well concentration of 0.2 mg/mL (200 µL).

5. 0.5% DMSO in Tris buffer

   0.5 mL DMSO was added to 100 mL of Tris buffer. The co-factor NAD^+ and NADH, and the HLC solutions were prepared with 0.5% DMSO in Tris buffer.

6. Substrate solution

Most AEH (5-HMF, 2,5-DMF; salt form of TD-7, TD-8, TD-9 and VZHE-039) were dissolved in Tris buffer with no co-solvent present. INN-310, which is insoluble in Tris buffer, was then dissolved with 0.5% DMSO as co-solvent. The concentration range for acetaldehyde and ethanol were selected based on previously reported K_m values to cover the full MM kinetics (Parikh, 2013). For 5-HMF, concentrations were studied up to 90 mM, which was approached to the UV/Vis detection limit (3 AU). For other novel AEH (2,5-DMF, TDs, INN-310, VZHE-039), concentrations were studied up to the solubility limit (Table 4.2). Solubility of AEH was estimated from their UV/Vis absorption at λ_{max}, when absorption value was observed to deviate from the Lambert-Beer's law.

4.2.4. UV/Vis Spectrophotometric (Warburg) Measurement Procedure

Enzymatic reaction in HLC was characterized spectrophotometrically by monitoring by the formation or depletion of co-factor (NADH) at 340 nm (λ_{max}) using a Synergy® 2 Multi-Mode Microplate reader. The absorbance of NADH was then converted to the corresponding concentrations using Lamber-Beer's law (Equation 4.1), followed by in-well volume (200 µL) correction to obtain the amount generated or depleted during oxidative metabolism or reductive metabolism.

$$\Delta A = \varepsilon * l * \Delta C \quad \text{----------} \quad \textit{Equation 4.1}$$

ΔA: change of absorbance measured by the microplate reader

ε: experimental molar extinction coefficient of NADH at 340 nm

l: pathlength of the solution in well

ΔC: change of NADH concentration

The baseline absorbance at 340 nm from each AEH were captured in the micro-well in the absence of HLC. The change of absorbance was corrected from the baseline AEH interference to reflect NADH formation or depletion.

4.2.5. Validation of ALDH and ADH Activity in HLC

Prototypical substrates of ALDH and ADH, i.e., acetaldehyde and ethanol respectively, were used to verify enzyme activities for each batch of HLC. Varying substrates concentrations were selected based on previous studies to capture full MM kinetics (Parikh, 2013). Kinetic parameters (K_m, v_{max}, and $CL_{int}^{in\text{-}vitro}$) were estimated using a modified MM model and compared with literature reported values, to verify the enzyme activities of HLC for the AEH metabolism studies.

4.2.6. Optimization of Experimental Conditions

The concentrations of enzyme, co-factor and substrate determine the overall metabolic rate. To capture proper metabolic profile for kinetic parameter estimates within the reasonable reaction time frame, 0.2 mg/mL HLC and 1.4 mM NDA^+ were selected based on previous studies for oxidative metabolism of AEH (Parikh, 2013). 0.4 mM of NADH was used for reductive metabolism studies of AEH, which was optimized based on calibration curve and the UV/Vis detection limit.

The concentration range of each substrate (AEH) was optimized according to the solubility and baseline interference of AEH. Before conducting the metabolism studies in HLC, UV spectrum properties (200 – 500 nm) of AEH were characterized first to estimate their interference at the detection wavelength (340 nm) and to determine their solubility in Tris buffer. Maximum absorbance wavelength (λ_{max}) and the corresponding extinction coefficient (ε) were estimated. Solubility of AEH was assessed by observed their absorption deviation from Lambert-Beer' law at λ_{max}. ε^{340nm} of AEH was characterized to assess their interference to NADH absorption.

Since INN-310 is insoluble in Tris buffer, DMSO was used as a co-solvent. The inhibition effect of DMSO to ALDH enzyme was studied using acetaldehyde with 2% or 0.5% DMSO. We finally chose 0.5% over 2% DMSO, since 2% DMSO completely abolished ALDH enzyme activities in HLC.

The interference of two types of plates, i.e., Greiner® UV-Star 96-well plate and Falcon® assay plate. ε^{340nm} of NADH, kinetic parameters estimated from oxidative metabolism of acetaldehyde and ethanol in HLC were compared to assess the potential interference of the plates.

4.2.7. Oxidative and Reductive Metabolism of AEH in HLC

A mixture of co-factor (1.4 mM NAD^+ for AEH oxidative metabolism and 0.4 mM NADH for reductive metabolism) and varying concentrations of AEH substrate were added to a 96-well plate and allowed to equilibrate for 15 mins at 37 °C. The metabolic reaction was initiated by addition of 0.2 mg /mL HLC. All concentrations listed above are final concentrations in well. Enzymatic reaction was measured by monitoring NADH spectrophotometrically at 340 nm (λ_{max}) with constant slow plate shaking. Each experimental run was performed in triplicates.

Progress curve of NADH formation (oxidative reaction) or depletion (reductive reaction) were captured over 10 mins. Initial reaction rates (v_i) were estimated as the initial linear slope from NADH progress curve, which are the zero-order rates of metabolism for the respective substrate concentrations. The v_i values were then plotted against initial substrate concentrations ($[AEH]_0$) to assess enzyme kinetics. Michaelis-Menten (MM) curves were fitted by a modified MM model (Equation 4.2). Non-linear

regression approach (Scientist® software, version 3.0) was used to estimate kinetic parameters. Goodness-of-fit was assessed by r^2, residuals, correlation matrix, and coefficient of variant (COV) of parameters.

$$\boldsymbol{v = v_0 + \frac{v_{max} * [S]}{K_m + [S]}} \qquad \text{----} \qquad \textbf{\textit{Equation 4.2}}$$

v: initial metabolic reaction rate

v_0: baseline enzymatic activity (in absence of exogenous substrate)

v_{max}: maximal rate of metabolism

K_m: MM affinity constant

S: initial substrate concentration

In-vitro metabolic efficiency, also known as intrinsic clearance ($CL_{int}^{in\text{-}vitro}$) was calculated based on the primary kinetic parameters (Equation 4.3) estimated from MM curve. For AEH, where only first-order enzyme kinetics were observed, $CL_{int}^{in\text{-}vitro}$ was estimated as the slope from the non-saturable enzyme reaction phase.

$$\boldsymbol{CL_{int}^{in-vitro} = \frac{v_{max}}{K_m}} \qquad \text{----} \qquad \textbf{\textit{Equation 4.3}}$$

4.3. Results

4.3.1. Calibration of UV/Vis Spectrophotometer

Since AEH and its corresponding carboxylic acid share similar UV spectrum properties, the formation of the reduced form of co-factor (NADH) was monitored over time instead of the product (carboxylic acid) or substrate (AEH). In this enzymatic reaction, when one molar of substate is converted to product, concurrently, one molar of co-factor (NAD^+) is reduced to NADH. Therefore, by monitoring the formation of NADH, the oxidative metabolism of AEH can be characterized. Vice versa, by monitoring the depletion of NADH, the reductive metabolism can be characterized.

The Lambert-Beer's law is used to convert UV/Vis absorbance of NADH to molar concentrations (Equation 4.1). Literature reported the extinction coefficient of NADH at 340 nm (ε^{NADH}) is 6.22 $mM^{-1}cm^{-1}$, while NAD^+ with a significantly less absorbance (ε^{NAD} = 0.04 $mM^{-1}cm^{-1}$) (Horecker & Kornberg, 1948; Inoue et al., 1979). In order to determine the experimental molar absorptivity of NADH, calibration curves of NADH (0.01 – 0.5 mM) were characterized at 340 nm. A 1/y weighted linear regression was applied to put more weighting on lower concentrations, which is the testing concentration range of the NADH used in the experimental set up for AEH metabolism studies. Lambert-Beer's law was used to estimate ε^{NADH} as the slope of the calibration curve. All tested NADH calibration curves were comparable using the two different 96-well plates (Greiner® UV-Star and Falcon® assay plate), where ε^{NADH} ranged from 4.99 to 5.31 $mM^{-1}cm^{-1}$ (Figure 4.1). The experimental molar absorptivity values (4.99 - 5.31 $mM^{-1}cm^{-1}$) were slightly lower than the literature reported values (6.22 $mM^{-1}cm^{-1}$) (Horecker & Kornberg, 1948;

Inoue et al., 1979), likely due to differences in experimental conditions and/or procedures. For example, the literature reported value was obtained by using a DU quartz spectrophotometer and 1.0 cm cells with Corex D windows, while we used the Synergy™ 2 multi-mode microplate reader and 96-well plates (Horecker & Kornberg, 1948).

Figure 4.1. Representative calibration curve of NADH at λ of 340 nm.

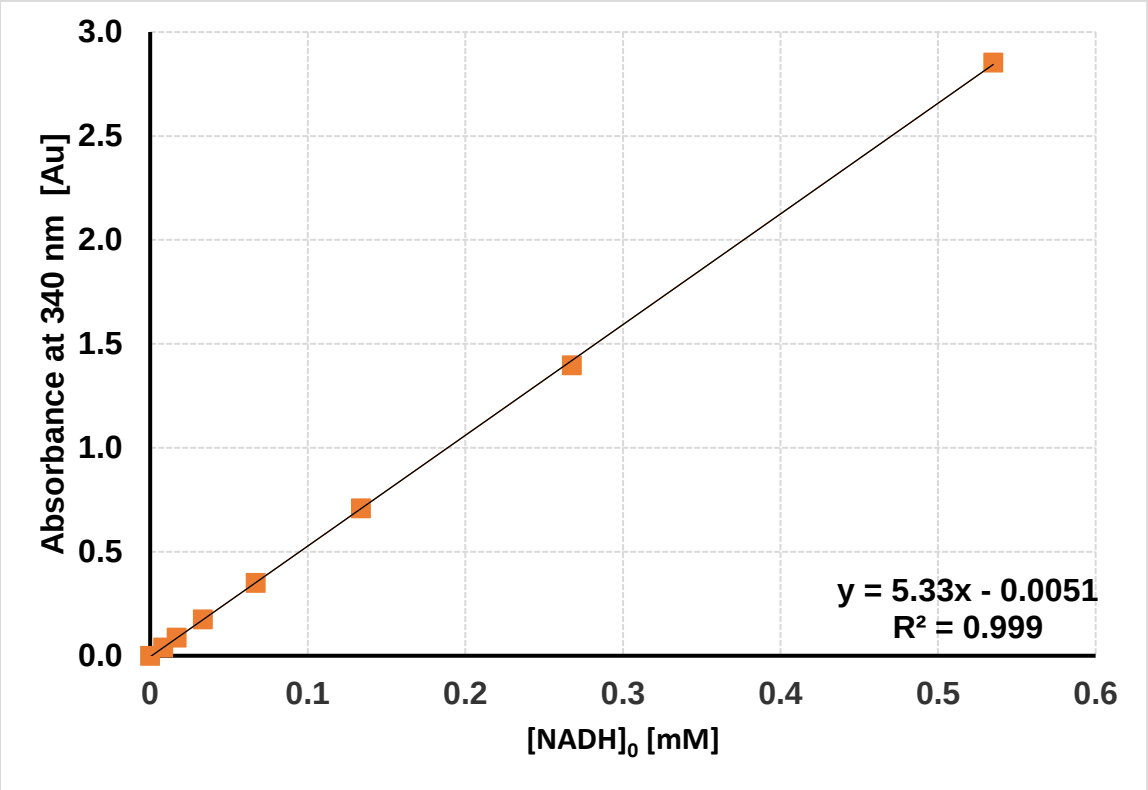

4.3.2. Selectivity of Assay Technique

Since the absorbance of NADH was used to monitor the enzymatic reaction, assay selectivity at 340 nm was studied to assess other potential interfering factors, including the 96-well plate, Tris buffer, NAD^+ and AEH. Empty plates show no notable absorption at 340 nm. As mentioned in section 4.3.1, both two type of plates show comparable ε^{NADH} at 340 nm, i.e., Greiner® UV-Star (5.16, 5.33 $mM^{-1}cm^{-1}$) and Falcon® assay plate (4.99 $mM^{-1}cm^{-1}$). Tris buffer shows no absorption at 340 nm. 1.4 mM NAD^+ shows some baseline absorbance. Among the 7 tested AEH (5-HMF, 2,5-DMF, TD-7, TD-8, TD-9, INN-310, VZHE-039), molar absorptivity of NAD^+ ranged from 0.1 to 0.2 mM^{-1} cm^{-1}, which was considered as low interference compared to NADH (ε^{NADH} = 4.99 - 5.33 $mM^{-1}cm^{-1}$).

The majority of the interference at 340 nm came from the benzaldehydes (Table 4.1). Vanillin, the parent compound of the benzaldehydes showed more than 3-fold higher molar absorptivity (16.9 $mM^{-1}cm^{-1}$) than NADH at 340 nm. Therefore, its oxidative metabolic reaction in HLC could not be characterized by monitoring co-factor using this UV/Vis spectrophotometric assay. All other benzaldehydes, structurally characterized with an additional pyridine ring, showed 4 to 8-fold lower molar absorptivity than NADH at 340 nm, allowing co-factor to be monitored for the characterization of the enzymatic reactions after baseline correction. The two furaldehydes, namely 5-HMF and 2,5-DMF, showed 300-fold and 50-fold lower molar absorptivity than NADH at 340 nm (Table 4.1).

Table 4.1. Molar absorptivity of AEH at λ of 340 nm.

	Extinction Coefficient [$mM^{-1}cm^{-1}$]
5-HMF	0.017
2,5 - DMF	0.10
Vanillin	16.9
TD-7	1.0
TD-8	0.71
TD-9	1.2
VZHE-039	1.1
INN-310	1.5
NADH	4.99 - 5.31

4.3.3. Optimization of Experimental Conditions

All batches of HLC showed baseline metabolic rate (v_0), probably due to the existence of endogenous substances. v_0 were similar among all oxidative or reductive metabolism studies (Table 4.2, Table 4.3), indicating experimental runs were carried out under similar experimental conditions. The capacity of enzyme (v_{max}) depends on the total amount of enzyme in system (E_{tot}) and the catalytic activity (k_{cat}). Increased concentrations of enzyme result in higher $v_{max,}$ but also v_0, which may lead to saturation of detection limit. Due to the reasons listed above and results from previous studies, 0.2 mg/mL of HLC was chosen for all test AEH (Parikh, 2013).

Some of the selected AEH have solubility issues in Tris buffer. One of solution to this problem was to use solubilizing agent, for example DMSO. However, DMSO has been known to inhibit ADH and ALDH enzyme activities (Obied, 2010; Parikh, 2013). 2% DMSO showed completely inhibition of ALDH enzyme activity to acetaldehyde. 0.5% DMSO resulted in 30% decrease on v_{max} and 50% decrease on CL_{int} of acetaldehyde, compared to enzyme with no DMSO (Figure 4.2). 0.5% DMSO was eventually determined to be optimal for studying one of the AEH, namely INN-310. We used an alternate solution to increase the solubility of other AEH by derivatizing the free acids of the following AEH (TD-7, TD-8, TD-9 and VZHE-039) into their corresponding HCl salt forms (provided by Dr.Zhang and Dr.Safo's labs) for metabolism studies in HLC.

The oxidative metabolism of AEH is facilitated by co-factor, i.e. NAD^+, where reductive metabolism of AEH is facilitated by its reduced form NADH. Concentration of co-factor influence overall enzymatic reactions. An inadequate co-factor would result in rapid completion of reactions due to exhaustion of co-factor supply. However, high

concentration of co-factor, especially NADH, would increase the baseline interference and even saturate detection limit. Therefore, based on preliminary data and previous studies, 1.4 mM of NAD^+ and 0.5 mM of NADH were chosen for oxidative and reductive metabolic studies, respectively (Parikh, 2013).

Substrate concentration ranges of the acetaldehyde and ethanol were optimized according to the literature reported K_m. In order to characterize the full MM profiles and estimate relative parameters (v_{max}, K_m), concentrations of acetaldehyde and ethanol were chosen to cover at least 10-fold lower and higher than their K_m (Table 4.2). Concentration ranges for tested AEH were limited due to different reasons. For most AEH, upper limits were due to the solubility issues, therefore only low millimolar concentrations of AEH were used in oxidative and reductive metabolism studies in HLC (Table 4.2). For 5-HMF, concentrations were studied up to 90 mM, where it approached to the saturation of detection limit (3 AU) due to baseline absorption of 5-HMF.

4.3.4. Validation of ALDH and ADH Activity

Acetaldehyde was used as substrate to verify ALDH activity for each batch of HLC. Because of the presence of the methyl alcohol, 5-HMF is also expected to subject to ADH, therefore ADH activity was also verified by using ethanol as substrate (Figure 4.3). The studied concentrations of acetaldehyde and ethanol covered both first-order and zero-order enzyme kinetics. Plateau of MM curves were achieved. K_m of acetaldehyde obtained from two different plates (0.012 mM, 0.016 mM) and v_{max} (1.4 mM, 1.0 mM) were slightly different but comparable between two batches of HLC, indicating metabolic results obtained using these two batches of HLC can be compared

and interpreted among different AEH. Experimental K_m value of acetaldehyde is smaller but still comparable (0.014 mM) to literature reported value (0.03 – 0.10 mM) (Vasiliou, Pappa, & Petersen, 2000). Similarly, ADH enzyme activity between two batches are comparable (K_m = 1.4 mM, 1.9 mM; v_{max} = 2.5 mM, 1.9 mM), and are similar to literature reported value (5 mM) (Bosron & Li, 1986).

Figure 4.2. Concentration-dependent oxidative metabolism of acetaldehyde in HLC with/without 0.5%DMSO. The modified MM model (lines) was fit to the experimental data (symbols). Data are presented as mean ± SD (n=3).

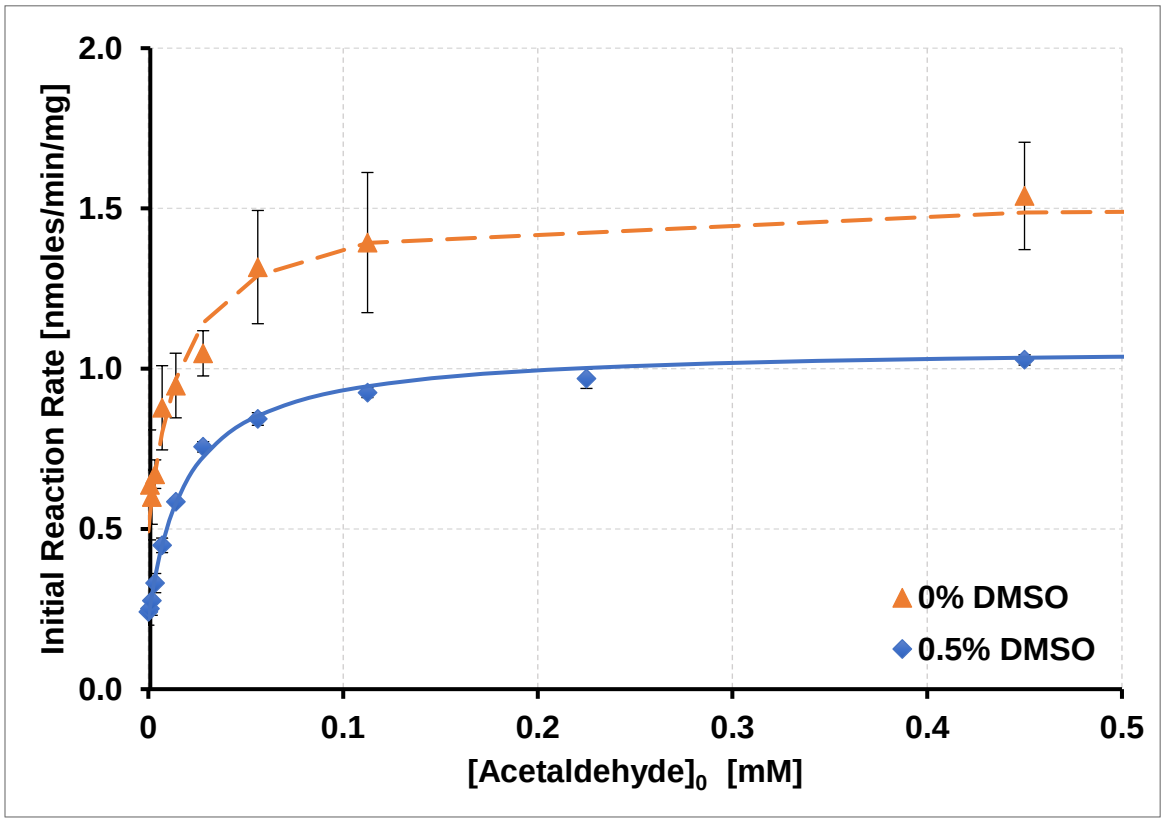

Figure 4.3. Concentration-dependent oxidative metabolism of ethanol in HLC. The modified MM model (line) was fit to the experimental data (symbols). Data are presented as mean ± SD (n=3).

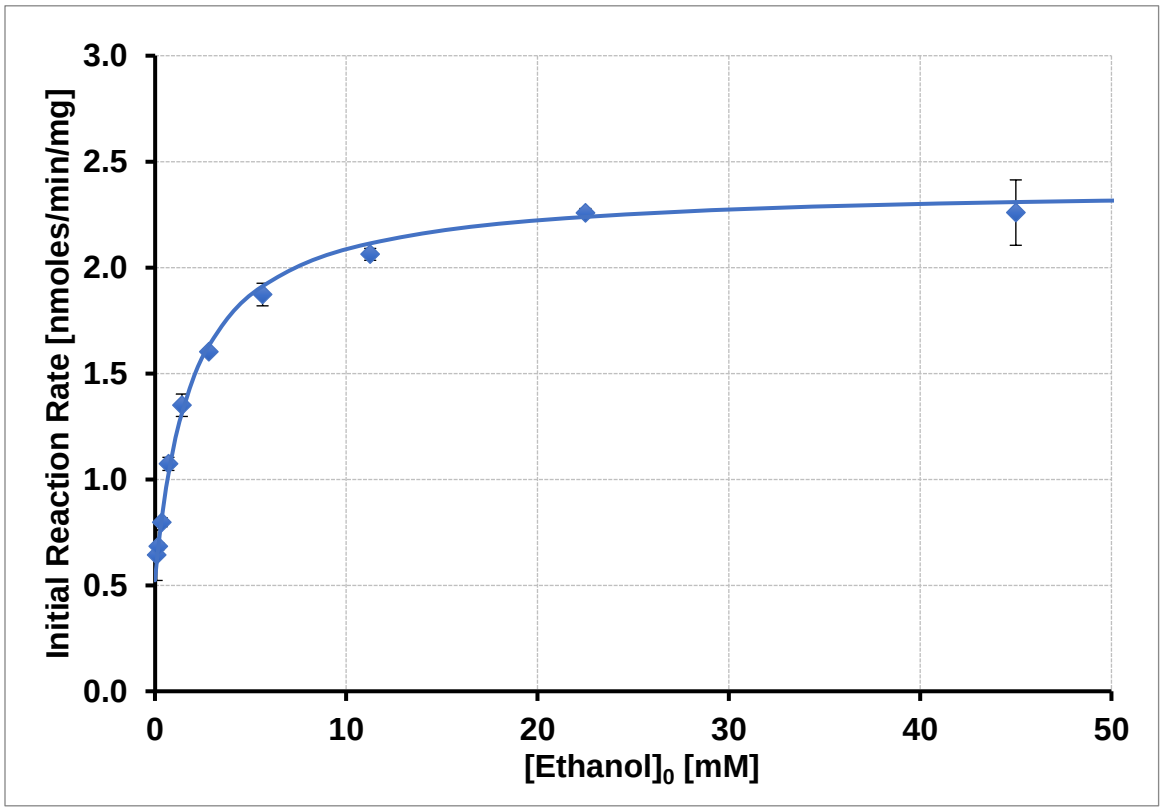

4.3.5. Oxidative Metabolism of AEH in HLC

For each experimental run, the baseline absorbance of each AEH at 340 nm in the well were comparable to the ε obtained during method validation procedure, indicating that AEH were well dissolved and achieved the designed concentrations in well.

None of the tested AEH showed saturable metabolism in HLC. 5-HMF, TD-7 and INN-310 showed first-order enzymatic reactions with K_m and v_{max} in millimolar range (Table 4.2, Figure 4.4, Figure 4.5). Compared to acetaldehyde, which has K_m in micromolar range and v_{max} in low millimolar range, 5-HMF, TD-7 and INN-310 are considered as low affinity but high capacity substrates to ALDH, resulting in low *in-vitro* intrinsic clearance ($CL_{int}^{in\text{-}vitro}$). Though there is an additional aldehyde group that replaces the methyl hydroxy group of 5HMF on the furan ring, the initial reaction rates (v_i) of 2,5-DMF only fluctuated around baseline v_0, indicating no net oxidative metabolism evidence at the studied concentration range.

TD-7 and INN-310 showed higher $CL_{int}^{in\text{-}vitro}$ than 5-HMF in HLC. Among the TD isomers, TD-8 and TD-9, structurally featured with para-methoxy group instead of meta-methoxy group in TD-7, showed no net oxidative metabolism in HLC. Compared to TD-7, the only structurally difference for VZHE-039 is the ortho-hydroxy group that protects aldehyde/AEH from ALDH enzymatic degradation (Figure 4.5). Structurally, the only difference between TD-7 and INN-310 is the methyl-hydroxy group on pyridine ring in TD-7. Due to solubility issue, INN-310 was tested in presence of 0.5% DMSO. Even this low DMSO concentration decreased ALDH enzyme activities in HLC by 50%, INN-310 still showed faster $CL_{int}^{in\text{-}vitro}$ than TD-7.

Figure 4.4. Concentration-dependent oxidative metabolism of 5-HMF in HLC. The linear regression (line) was fit to the experimental data (symbols). Data are presented as mean ± SD (n=3).

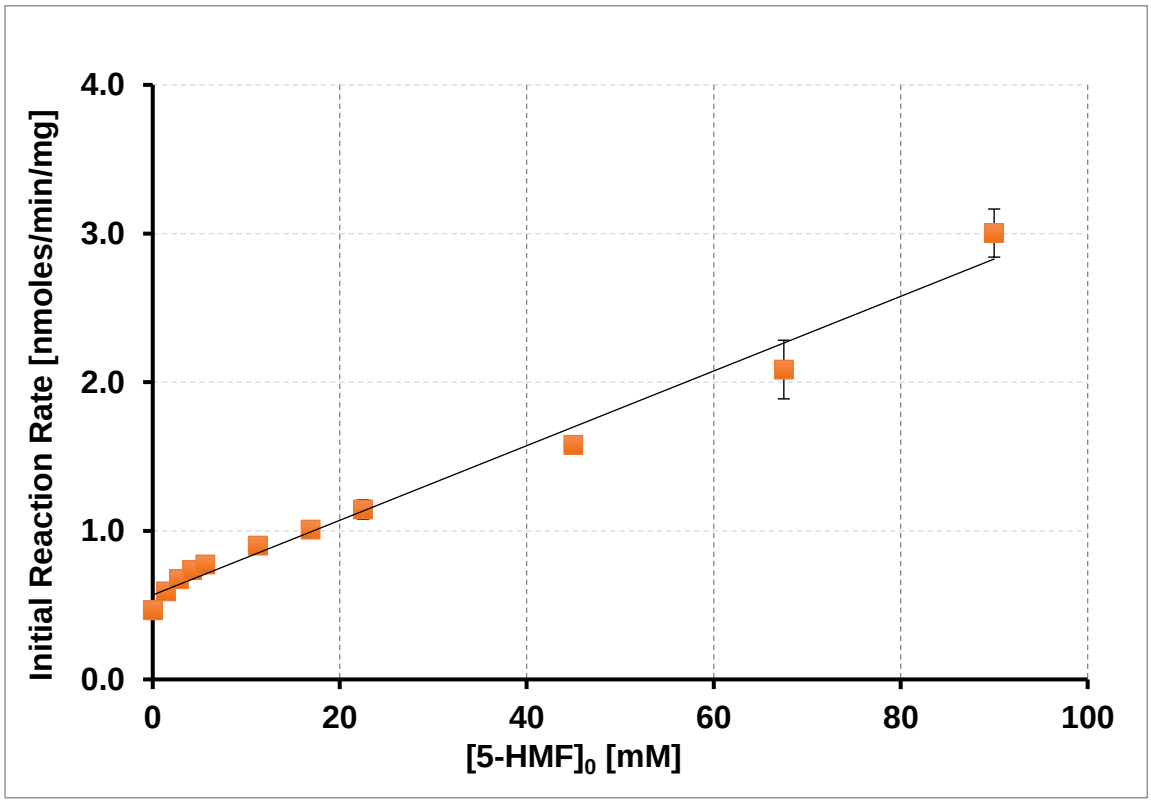

Figure 4.5. Concentration-dependent oxidative metabolism of TD-7 and VZHE-039 in HLC. The linear regression (line) was fit to the experimental data (symbols). Data are presented as mean ± SD (n=3).

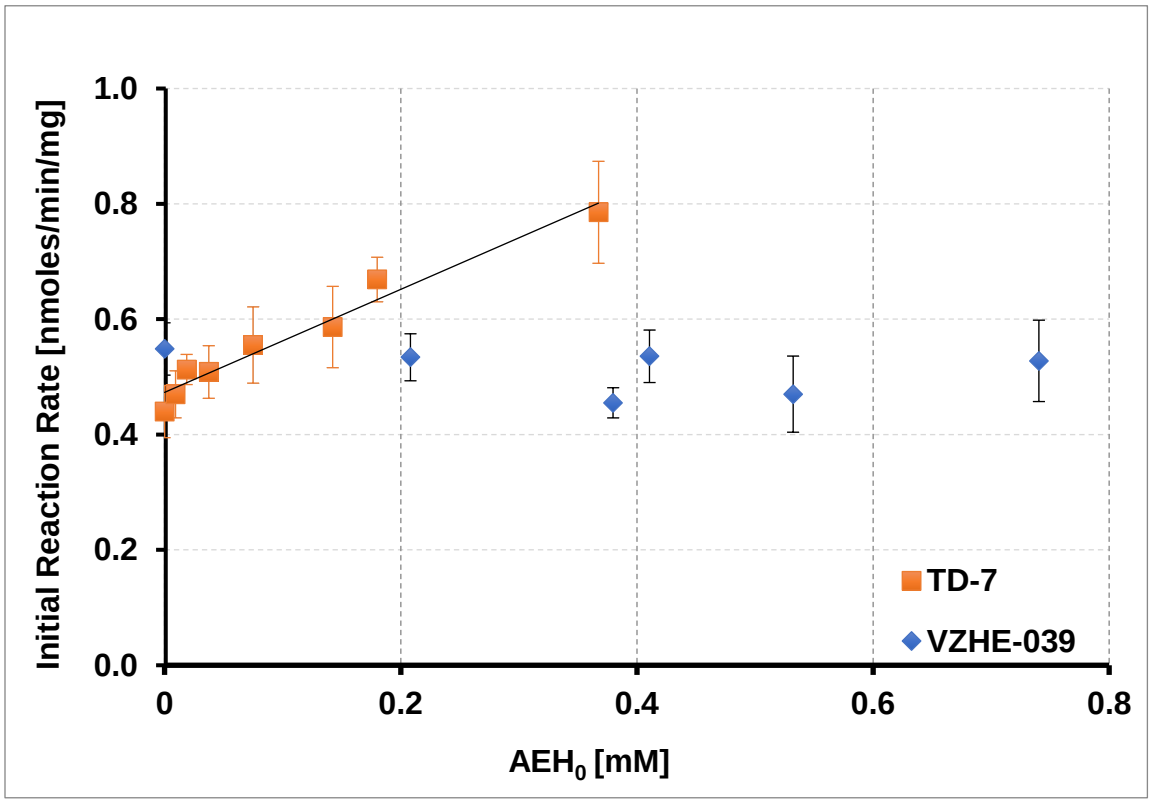

Table 4.2. Final parameter estimates of oxidative metabolism of AEH as well as acetaldehyde and ethanol (prototypical substrates of ALDH and ADH enzyme) in HLC, using linear regression for AEH and modified MM model. Data are presented as the mean from two separate experiment runs (except INN-310 and acetaldehyde in 0.5% DMSO with only one experiment run), where each experiment run as triplicates (n=3).

Substrate	$[AEH]_0$ [mM]	K_m [mM]	v_{max} [nmoles/ min/mg]	$CL_{int}^{in\text{-}vitro}$ [µL/min/mg protein]	v_0 [nmoles/min/ mg]
5-HMF	1.4 - 90	>90	>90	0.036	0.5
2,5-DMF	0.003 - 3	NA	NA	NA	0.5
TD-8	0.02 – 0.6	NA	NA	NA	0.7
TD-9	0.004 – 0.3	NA	NA	NA	0.6
TD-7	0.01 – 0.5	> 0.53	>0.53	0.88	0.5
VZHE-039	0.02 – 1.2	NA	NA	NA	0.4
INN-310 (0.5%DMSO)	0.0003 – 0.3	> 0.30	>0.30	1.6	0.3
Acetaldehyde (0.5% DSMO)	0.001 – 0.9	0.019	0.85	44	0.2
Acetaldehyde	0.001 – 0.9	0.014	1.2	89	0.4
Ethanol	0.09 – 90	1.7	2.2	1.4	0.5

4.3.6. Reductive Metabolism of AEH in HLC

Both 5-HMF and 2,5-DMF (furaldehydes) showed saturable reductive metabolism in HLC (Figure 4.6). A modified MM model were used to fit the experimental data (Equation 4.2 in section 4.2.7). Initial estimates were based on the visual inspection of experimental data. For 5-HMF, initial estimates were v_0 = 2.5 nmoles/min/mg, v_{max} = 3 nmoles/min/mg, and K_m = 1.5 mM. For 2,5-DMF, initial estimates were v_0 = 2.5 nmoles/min/mg, v_{max} = 16 nmoles/min/mg, and K_m = 1.0 mM. Final estimates were listed in table 4.3. 5-HMF achieved plateau and showed more than 5-fold smaller enzyme capacity (v_{max}) than 2,5-DMF. Both of compounds showed similar affinity. However, 2,5-DMF with an additional aldehyde group on the furan ring (replaces the methyl hydroxyl group on 5-HMF) shows higher intrinsic clearance ($CL_{int}^{in\text{-}vitro}$) due to its larger v_{max}. Unlike furaldehydes, none of tested benzaldehydes (n =5) showed reductive metabolism in HLC.

Figure 4.6. Concentration-dependent reductive metabolism of 5-HMF and 2,5-DMF in HLC. The modified MM model (lines) were fit to the experimental data (symbols). Data are presented as mean ± SD (n=3).

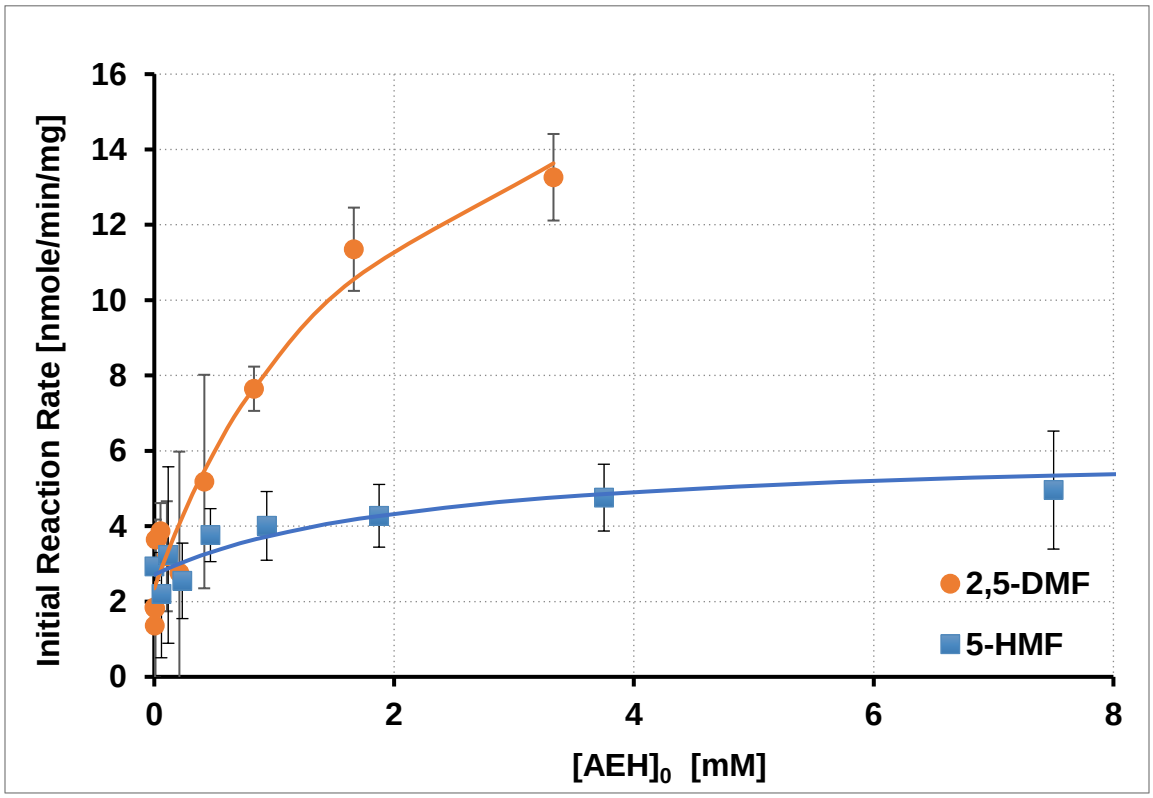

Table 4.3. Final parameter estimates of reductive metabolism of AEH in HLC, using the modified MM model. Data are presented as PE with (COV) (n = 3).

Substrate	$[AEH]_0$ [mM]	K_m [mM]	v_{max} [nmoles/min/mg]	$CL_{int}^{in\text{-}vitro}$ [µL/min/mg protein]	v_0 [nmoles/min/mg]
5-HMF	0.06- 60	2.2 (40%)	3.4 (9%)	1.5 (49%)	2.7 (8%)
2,5-DMF	0.003 - 3	2.0 (47%)	18.1 (22%)	9.0 (69%)	2.3 (16%)
TD-8	0.02 – 0.6	No evidence			1.4
TD-9	0.004 – 0.3	No evidence			1.8
TD-7	0.001 – 0.5	No evidence			1.3
VZHE-039	0.02 – 1.2	No evidence			1.5
INN-310 (0.5%DMSO)	0.0003 – 0.3	No evidence			0.3

4.4. Discussion and Conclusions

The purpose of this part of research was to study the ALDH susceptibility of selected AEH (5-HMF, 2,5-DMF, TD-7, TD-8, TD-9, INN-310, and VZHE-039). By using a UV/Vis spectrophotometer assay method, their ALDH-mediated oxidation was successfully characterized in HLC. Key structure features that protect the aldehyde group from ALDH metabolism were identified. In addition, their reductive metabolism was also studied to understand their possible complication to the interpretation of ALDH-mediated oxidation results in HLC.

5-HMF showed net oxidative metabolism in HLC. The methylhydroxyl group on the furan ring was also expected to undergo alcohol dehydrogenase (ADH)-mediated metabolism in HLC as well. Previous studies showed that in the presence of the ALDH and ADH enzymes inhibitor (i.e., 17.4 μM disulfiram), maximum inhibition of 59.9 % oxidative metabolism of 5-HMF in HLC was observed (Obied, 2010). When 273 μM of methylpyrazine, inhibitor of ADH, was added in HLC, maximum inhibition of oxidative metabolism for 5-HMF in HLC was 33.6% (Obied, 2010). These observations indicate that both ADH-mediated and ALDH-mediated metabolisms of 5-HMF occur in HLC.

5-HMF also undergoes reductive metabolism in HLC by consuming NADH that competes with the oxidative metabolism (Scheme 4.1.a). Therefore, $CL_{int}^{in\text{-}vitro}$ of ALDH-mediated oxidative metabolism is expected to be underestimated in HLC. A possible responsible enzyme for this reductive reaction is ADH. Literature suggested that ADH is able to reduce aldehyde back to alcohol (Jelski et al., 2008). The influence from ADH-mediated oxidative and reductive metabolism complicates the extrapolation from *in-vitro*

HLC results to intra-RBC metabolism, since ADH enzyme is absent in RBC. In addition, lack of the information of ALDH enzyme concentration in RBC, $CL_{int}^{in\text{-}vitro}$ obtained from HLC cannot be quantitatively extrapolated into RBC. Though many factors listed above hindered the quantitative extrapolation for 5-HMF, qualitatively, 5-HMF is expected to be metabolized by ALDH enzyme in RBC. This is also supported by the previous *in-vitro* studies, where ALDH-oxidation of 5-HMF was observed in diluted human RBC(Obied, 2010).

5-HMF showed a first-order oxidative metabolism in HLC, because the studied substrate concentrations were lower than K_m (> 90 mM). The dosing regimen of 5-HMF in phase II clinical trial was 1000 mg (4 times a day)("ClinicalTrials.gov.," 2020). Assuming a body fluid of 250 mL, the nominal concentration of a single dose (1000 mg) administration for 5-HMF would be 32 mM (MW = 126 g/mole), which is lower than K_m. A non-saturable ALDH metabolism in RBC is expected for 5-HMF under physiological relevant concentrations.

2,5-DMF with an additional aldehyde group that replaces the methyl hydroxy group of 5HMF showed no net oxidative metabolism. However, all previously and currently studied furaldehydes (n = 5) showed reductive metabolism evidences in HLC(Wohlford, Safo, & Venitz, 2015). One possible reason could be the ADH-mediated reductive metabolism balanced out the ALDH-mediated oxidative metabolism in HLC (Scheme 4.1.b). Though 2,5-DMF showed no net oxidative metabolism in HLC, it might show ALDH-mediated metabolism in RBC, because of the missing ADH-mediated reductive metabolism pathway in RBC.

The competing reductive metabolism in HLC complicated the interpretation of the ALDH-mediated oxidative metabolism for 5-HMF and 2,5-DMF, which also applies to other previously studied furaldehydes studied by previously, namely 5-MMF, 5-EMF, and 5-PMF(Wohlford et al., 2015). Unlike the furaldehydes, the benzaldehydes (TD-7, TD-8, TD-9, INN-310, and VZHE-039) did not show evidence of reductive metabolism in HLC, indicating the furan ring is more susceptible to reductive enzymes than benzene ring, presumably and primarily due to ADH enzyme.

RBC and HLC share the same isoform of ALDH enzyme (ALDH-1)(Mezey et al., 1987). Reductive metabolism in HLC does not apply to the studied benzaldehydes. Therefore, a benzaldehyde with no *in-vitro* oxidative metabolism evidence in HLC are predicted to be resistance to intra-RBC metabolism as well.

Scheme 4.1. Proposed metabolic schemes of 5-HMF (a) and 2,5-DMF (b) in HLC.

a.

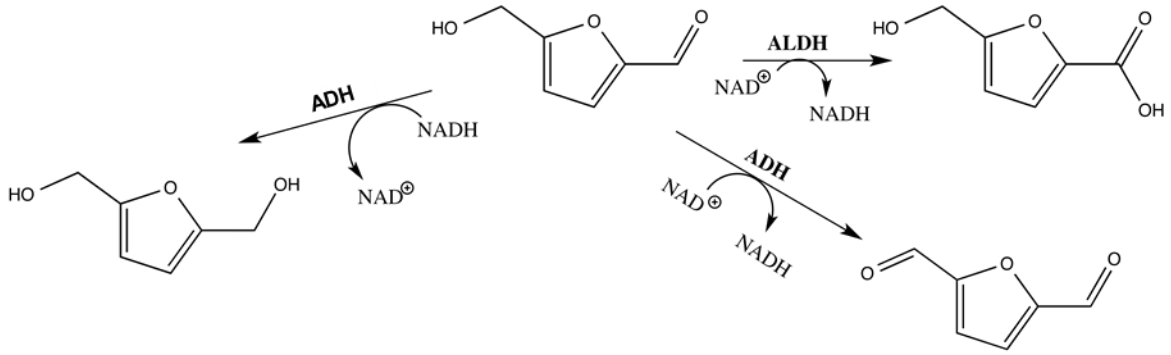

b.

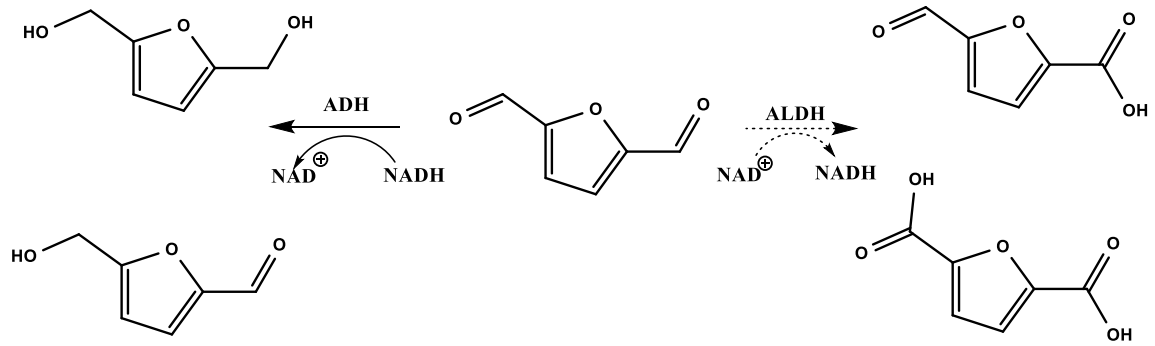

By comparing the oxidative metabolism among the different benzaldehydes in HLC, it became obvious that certain structural features seem to protect AEH from ALDH enzymatic degradation (Figure 4.7). Meta-methoxy group (in TD-7 and INN-310) favors ALDH-mediated oxidative metabolism, while para-methoxy group (in TD-8 and TD-9) show no oxidative metabolism in HLC. Methoxy group is an electron-donating group that will affect the overall electric density of aromatic ring ("Reactions of Arenes.Electrophilic Aromatic Subsitution [online]. Accessed June-10," 2020). Meta-positioned methoxy may increase the electropositive nature of the carbon atom and electronegative of oxygen atom of the aldehyde group, which would favor conversion of the aldehyde moiety to the corresponding carboxylic acid by ALDH enzyme. It is also possible that para-methoxy group unlike meta-methoxy group sterically prevent the AEH from optimally binding to the ALDH. TD-7 and INN-310 are expected to undergo intra-RBC metabolism in WB, while TD-8 and TD-9 are not. Time-dependent Hb modification studies in WB are consistent with this conclusion, where TD-7 and INN-310 showed modified Hb level to decrease after 2 hrs, while TD-8 and TD-9 sustained for at least 12 hrs (Pagare et al., 2018). VZHE-039 is structurally similar to TD-7 but the former has a hydroxyl group ortho to the aldehyde, while the latter has a methoxy group meta to the aldehyde. The presence of the hydroxyl group led to VZHE-039 resistance to ALDH enzyme. The ortho-hydroxy forms an intra-hydrogen bond with the aldehyde group to protect the aldehyde from ALDH enzymatic degradation. Therefore, TD-8, TD-9 and VZHE-039 with certain unique structural features on the benzene ring are able to protect the aldehyde group from ALDH-mediated oxidative metabolism in HLC, which are expected to be resistance to intra-RBC metabolism in WB as well.

Figure 4.7 .SAR of oxidative metabolism in HLC for the selected benzaldehydes.

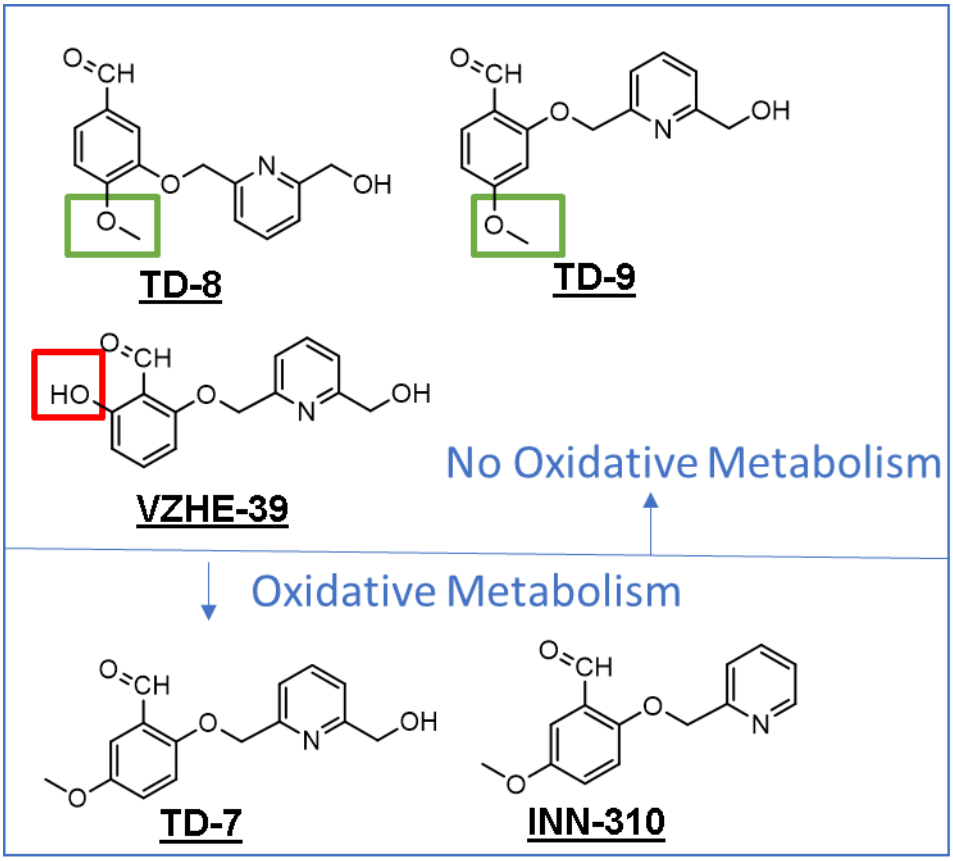

GBT-440 (Voxelotor, Oxbryta®), structurally characterized with an ortho-hydroxy group like VZHE-039, is predicted to be resistance to ALDH-mediated metabolism in RBC. Phase I clinical studies showed that with 1000 mg single-oral dose (powder in capsule), GBT-440 concentration in RBC peaked with a median of 14 hrs and showed a terminal half-life of 50 hrs over 600 hrs measurements among 6 healthy volunteers (Hutchaleelaha et al., 2019). This slow RBC clearance supports our hypothesis of GBT-440 resistance to ALDH-mediated metabolism in RBC. Clinical studies showed that GBT-440 primarily undergoes hepatic clearance metabolized by CYP-3A4, with minor contribution from CYP-2C19, CYP2B6 and CYP-2C9, and it also undergoes phase-2 conjugation by UGT and SULT (*Multi-Discipline Review of Voxelotor*, 2019). GBT-440 is also a CYP-3A4 inhibitor, supported by clinical DDI studies(*Multi-Discipline Review of Voxelotor*, 2019). GBT-440 is expected to be low extraction ratio drug due to its highly PPB (99.8%, does-independent)(*Multi-Discipline Review of Voxelotor*, 2019), which is a favorable PK property to prolong its circulating time in body.

Similar to GBT-440 (cLogP = 3.5), VZHE-039 also shows high *in-vitro* PPB (98% at 5 μM), presumably due to its lipophilicity (cLogP =1.8) (Safo, 2019), and therefore is expected to be a low extraction ratio substrate in liver as well. VZHE-039 does not show obvious *in-vitro* inhibition to CYP-3A4, CYP-2C9 and CYP-2C19 enzymes (IC_{50} > 100 μM), with some inhibition to CPY1A2 (4.7 μM) and CYP2B6 (41.4 μM) (Safo, 2019). Our *in-vitro* HLC study suggested VZHE-039 is resistant to ALDH-mediated metabolism, and therefore, is expected to sustain in RBC (target site). These *in-vitro* metabolic and PPB results suggesting VZHE-039 may have favorable PK properties for the further drug development.

In summary, this study provides fundamental structure-activity-relationship for AEH, including furaldehydes and benzaldehydes with respect to their ALDH-mediated metabolism in HLC. Since HLC and RBC express the same isoform of ALDH (ALDH-1), this HLC approach allows rational design of potential improved candidates with resistance to intra-RBC metabolism. This approach can be used as a critical tool to screen drug candidates for SCD therapy at early development stage with benefits of lower cost, lower risk and higher efficiency than *in-vivo* approaches. Among the tested AEH, key molecular features that protect the aldehyde moiety from intra-RBC metabolism have been identified, namely the ortho-hydroxy group by forming intra molecular hydrogen bond and potentially para-methoxy group by enhancing electropositivity of the carbon atom in aldehyde group or increase steric hindrance. VZHE-039, TD-8 and TD-9 are selected as good candidates from the prospective of their resistance to ALDH-mediated metabolism.

CHAPTER 5

IN-VITRO DISPOSITION OF VZHE-039 AND 5-HMF IN WB

5.1 Introduction

This chapter addresses the specific aim 3: To integrate the underlying disposition mechanisms of WB (WB) using quantitative kinetic models for VZHE-039 and 5-HMF.

WB (WB) is the target “tissue” for allosteric effectors of Hb (AEH), where they bind to Hb RBC) to elicit their anti-sickling effect. In the WB environment, other processes may facilitate or hinder AEH penetrating into RBC and/or binding to Hb. These processes include ALDH-mediated metabolism in RBC, metabolism in plasma, plasma protein binding (PPB) and RBC membrane binding/crossing (Scheme 5.1). Therefore, their apparent binding affinity and binding kinetics of AEH to Hb in WB may be different to their Hb binding properties in Hb solution.

Scheme 5.1. WB disposition of AEH

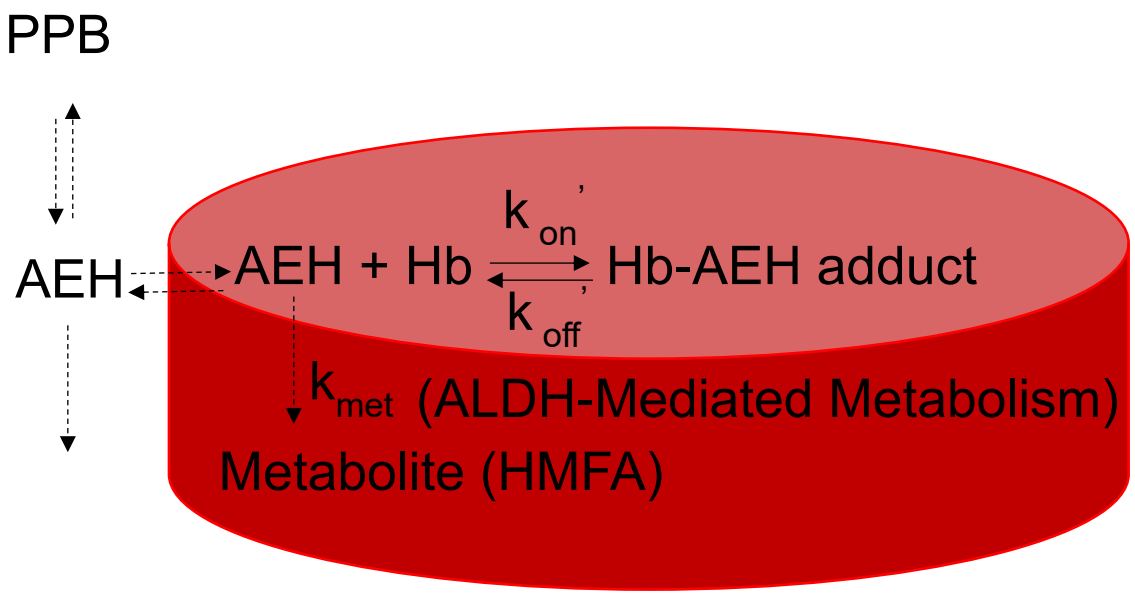

As discussed in Chapter 3 and 4, the HbA binding kinetic properties and *in-vitro* ALDH-mediated metabolism of selected AEH have been characterized. Among the studied AEH, 5-HMF and VZHE-039 were chosen to further study their disposition in WB, based on their HbA binding properties and ALDH-mediated metabolism. 5-HMF is our previous lead compound with moderate anti-sickling potency, which underwent phase II clinical study until terminated due to apparent lack of efficacy in SCD. VZHE-039, which is more potent than 5-HMF in inhibiting RBC sickling, is currently one of our top candidates, and undergoing preclinical studies for the treatment of SCD. 5-HMF behaves as a slow Hb binder ($t_{1/2}^{eq}$ = 3.1 hrs) with relatively low affinity to Hb (K_D = 0.37 mM) in Hb solution, and undergoes significant ALDH-mediated oxidative metabolism in human liver cytosol (HLC). VZHE-039, on the other hand, exhibits faster Hb binding ($t_{1/2}^{eq}$ = 0.058 hrs) and high affinity to Hb (K_D = 0.10 mM), and is resistant to *in-vitro* ALDH-mediated oxidative metabolism. The physicochemical properties of these two compounds are also quite different: While 5-HMF is hydrophilic (cLogP = -0.1), VZHE-039 is lipophilic (cLogP = 1.8).

Previous studies had shown that the *in-vitro* plasma clearance ($CL_{plasma}^{in\text{-}vitro}$) of 5-HMF in WB was high, but decreased with increasing $[5\text{-HMF}]_0$ (2 – 5 mM)(Parikh, 2013). Two processes may be responsible for this non-linear behavior, namely saturable Hb binding and/or saturable ALDH-mediated metabolism in RBC. *In-vitro* HLC studies showed that 5-HMF – relative to acetaldehyde - behaves as a low affinity (K_m >90 mM) and high-capacity (v_{max} > 90 nmoles/min/mg) substrate for ALDH (Chapter 4). At the studied concentrations in WB, 5-HMF was expected to show first-order ALDH-mediated metabolism in RBC. Therefore, saturable Hb binding was speculated to cause

the saturable clearance of 5-HMF in plasma. However, the lack of a validated generic analytical assay method on quantification of Hb-AEH adduct prevented the testing of this hypothesis in the original study (Parikh, 2013). In this chapter, we directly quantitate Hb-AEH adduct in WB to further characterize the disposition of 5-HMF.

In this previous WB study, the p_{50}-shift (pO_2 at 50% oxygen saturation), i.e. the change of oxygen binding affinity of Hb, was used to indirectly characterize Hb binding properties of AEH, as it was assumed to reflect concentrations of HbA-5HMF adduct (Parikh, 2013). Kinetic profiles were characterized not directly from 5-HMF, Hb, or HbA-AEH adduct concentrations in RBC, but indirectly based on plasma concentration (c_p) of 5-HMF and the corresponding p_{50}-shift in WB which is the downstream effect of HbA-AEH adduct(Parikh, 2013). In this research, a generic “universal” analytical assay method allows direct characterization of the primary HbA binding profile of AEH by measuring HbA-AEH adduct concentrations.

The objective in this chapter is to determine *in-vitro* disposition of 5-HMF and VZHE-039 in WB. To fulfill this objective under specific aim 3, the following research tasks were carried out: 1). Quantitate the HbA-AEH adduct concentrations for 5-HMF and VZHE-039 using a cation-exchange HPLC/UV assay method. 2). Apply non-compartmental analysis (NCA) to estimate AUC from HbA-AEH adduct concentration – time profile. 3). Develop quantitative models to adequately fit the experimental data (HbA-AEH adduct concentrations) and to fully characterize their concentration and time-dependent Hb binding properties. 4). Compare the Hb binding properties of VZHE-039 and 5-HMF in WB and to their binding properties in isolated HbA solution. 5) Quantitate the plasma concentration of VZHE-039 using a reversed-phase HPLC/UV assay. 6)

Apply NCA to estimate relevant PK parameters for VZHE-039, assess dose-proportionality and compare with the plasma disposition of 5-HMF from previous studies.

7). Integrate the available experimental and literature information to analyze the underlying mechanism of WB disposition for VZHE-039 and 5-HMF.

5.2 Methods

5.2.1. Materials and Reagents

1. NERL® high purity water (Fisher Scientific, Nazareth, PA)
2. Bis-tris (Sigma-Aldrich, St.Louis, MO) (209.24 g/mol)
3. Potassium cyanide (Sigma-Aldrich, St.Louis, MO) (KCN, 65.12 g/mol)
4. Sodium chloride (Sigma-Aldrich, St.Louis, MO) (NaCl, 58.44 g/mol)
5. HbA solution (purified by Dr. Martin Safo's lab, Department of Medicinal Chemistry, VCU) (12.60 g/dL)
6. Formic acid (Sigma-Aldrich, St.Louis, MO) (46.03 g/mol)
7. Methanol, HPLC grade (Burdick and Jackson, Morristown, NJ)
8. Hydrochloric acid, ACS 37% (Sigma-Aldrich, Milwaukee, WI) (HCl ,36.46 g/mol)
9. Sodium cyanoborohydride (sigma-aldrich, St.Louis, MO) ($NaBH_3CN$, 62.84 g/mol)
10. Sodium borohydride (sigma-aldrich, St.Louis, MO) ($NaBH_4$, 37.84 g/mol)
11. 5-Hydroxymethyl-2-furfural (5-HMF) (Sigma, St. Louis, MO) (126.11 g/mol)
12. VZHE-039 (provided by Dr. Martin Safo, Dr. Yan Zhang, Department of Medicinal Chemistry, VCU) (259 g/mol)
13. Dimethyl sulfoxide (DMSO), ≥ 99.9%, A.C.S. Reagent (Sigma-Aldrich, Milwaukee, WI) (78.13 g/mol)
14. 0.5M EDTA.2Na, pH 8.0 (Quality Biological, Gaithersburg, MD)
15. Acetonitrile (Fisher Scientific, Nazareth, PA)

5.2.2. Equipment

1. 96-well deep plate (Thermo Scientific, Nazareth, PA)
2. Incubator (Thermo Fisher Scientific Inc., Pittsburgh PA)
3. ABL800 FLEX blood gas analyzer (Radiometer America, Brea, CA)
4. HPLC Water 2695 (Waters, Milford, MA)
5. Photodiode array detector 2996 (Waters, Milford, MA)
6. Poly CAT^{A} weak cation-exchange column, 30 mm x 4.6 mm (Poly^{LC}, Inc., Columbia, MD)
7. BDS HYPERSIL C18 column, 50 mm x 4.6 mm (Thermo Scientific, Nazareth, PA);
8. Supelco® pre-column Filter 0.2 µm (Sigma-Aldrich, St.Louis, MO)
9. Durapore® membrane filter, 0.22 µm (Sigma-Aldrich, St.Louis, MO)
10. 9 mm autosampler Insert (VWR, West Chester, PA)
11. 9 mm autosampler Insert (Thermo Fisher Scientific Inc., Pittsburgh PA)
12. 9 mm autosampler vail (Waters, Milford, MA)
13. 9 mm autosampler vail cap (Thermo Fisher Scientific Inc., Pittsburgh PA)
14. Vacuum filtration apparatus (assembled, department of MedChem, VCU)
15. Empower 2 software (Waters, Milford, MA)
16. Scientist®, version 3.0 (Micromath Software)
17. pH Meter (Fisher Scientific, Pittsburgh, PA)
18. Vortex (Vortex-Genie, VWR, West Chester, PA)
19. Balance (Fisher Scientific A 250, Pittsburgh, PA)
20. Micro centrifuge (USA Scientific, Ocala, FL)

21. Centrifuge 5804R (Eppendorf, Hauppauge, NY)
22. Thermo Sorvall Legend Micro 17 centrifuge (Thermo Scientific, Waltham, MA)
23. 0.5-5 mL Finnpipette (Thermo Scientific, Waltham, MA)
24. 30 – 300 µL multichannel pipette (Fisher Scientific, Hanover Park, IL)
25. 3-25 µL positive displacement pipette and corresponding pipette tips (Rainin Instruments, Oakland, CA).
26. 10-100 µL and 100-1000 µL VWR pipettes and corresponding pipette tips (VWR, West Chester, PA).

5.2.3. Preparation of Solutions

1. <u>$NaBH_3CN$ and $NaBH_4$ solution (stopping solution)</u>

10 mg $NaBH_3CN$ was dissolved into 3 mL of water to make 50 mM $NaBH_3CN$ solution. 10 mg of $NaBH_4$ was dissolved into 5 mL of water to make 50 mM $NaBH_4$ solution. $NaBH_3CN/NaBH_4$ mixture (1:1 v/v) stock solution was freshly made every day for the experiments. The mixture was used to stop the Schiff-base reaction between the AEH and Hb, and also to reduce unreacted aldehydes for kinetic measurement of HbA-AEH adduct at specific time points (Deshpande et al., 2018).

2. <u>VZHE-039 and 5-HMF stock solution</u>

VZHE-039 or 5-HMF was dissolved in DMSO to make 100 mM stock solution. Different volume of stock solution was added to 96-well plate to achieve designed final initial nominal concentration of VZHE-039 or 5-HMF in the 96-well (see section 5.2.1 for concentration range). Final concentration of DMSO in 96-well was kept equal or less than 2%.

3. <u>Mobile phases for VZHE-039 quantification in plasma</u>

Aqueous phase was made using HPLC grade water with 0.1% FA. Organic phase was made using ACN with 0.1%FA.

4. <u>Mobile phases for HbA-AEH adduct quantification in WB</u>

Buffer A (20 mM Bis-Tris, 2 mM KCN, pH 6.5) and buffer B (20 mM Bis-Tris,2 mM KCN, 200 mM NaCl, pH 6.6) were made using HPLC grade water, and adjusted pH with HCl. 8.37 g Bis-Tris, 0.26 g KCN were dissolved in 2000 mL water to make Buffer

A. 8.37 g Bis-Tris, 0.26 g KCN, and 23.38 g NaCl were dissolved in 2000 mL water to make Buffer B. The mobile phases were filtered through membrane filter (0.22 μm) under vacuum.

5. VZHE-039 calibration curve in net solution

Net solution was prepared with water and ACN (V:V = 1:1). Spike VZHE-039 solution to net solution to achieve final concentration of 0.004 – 8 mM and injected 50 μL into HPLC.

6. VZHE-039 calibration curve in plasma

Plasma was prepared from WB donated by healthy volunteer. WB was centrifuged at 3000 rpm for 8 mins to collect top plasma layer. Different volume of VZHE-039 stock solution was added into blank plasma sample to achieve a final concentration range of 0.004 – 8 mM. In order to deproteinize plasma proteins, 200 μL ACN (with 0.1%FA) was added to each plasma sample with VZHE-039 spiked (50 μL). Samples were well mixed, and left at 4°C for 30 mins for protein precipitation. Then samples were centrifuged at 13,000 rpm for 20 min. The top layer (supernatant) was collected and transferred to HLPC tube, which 50 μL was injected for HPLC analysis.

7. HbA calibration curve in water

Hb was purified from discarded normal blood samples using standard procedures(Safo & Abraham, 2003). Concentration of isolated HbA solution was measured using automated blood gas analyzer (Radiometer America, Inc., Westlake, OH), followed by dilution with HPLC grade water to the designed concentration range (0.0005 – 0.5 mM) of calibration curve.

5.2.4. Experimental Design

5.2.4.1. HbA-AEH Adduct Quantification in WB

Normal WB was collected from adult donors at the Virginia Commonwealth University after informed consent, in accordance with regulations of the IRB for Protection of Human Subjects. WB was used within 48 hrs to ensure the integrity of blood components including the enzyme activities. %Hct was measured by blood gas analyzer (Radiometer America, Inc., Westlake, OH) (45%Hct, 2.3 mM HbA for VZHE-039; 38%Hct, 2.0 mM HbA for 5-HMF). Varying initial concentrations of VZHE-039 or 5-HMF were added to 2.25 mL WB in a 96-well plate and incubated at 37 ºC with mild shaking. After compound addition, 30 µL aliquots were taken at different time points until 24 hrs. 150 µL (6-fold dilution) $NaBH_3CN/NaBH_4$ was added to and well mixed with each aliquot to terminate the Schiff-base reaction and to hemolyze WB(Deshpande et al., 2018). Aliquots were immediately frozen and kept at -80 ºC. HbA-AEH adduct was measured in WB hemolysate instead of RBC to avoid additional Schiff-base reaction time during plasma separation process. For HPLC analysis, aliquots were thawed on ice, and centrifuged at 6000 rpm for 10 mins to separate HbA solution with cell membrane. 10 µL of top supernatant was injected for HPLC analysis at 4 ºC.

For VZHE-039, three pilot studies were performed to finalize experimental condition for definitive studies. The first pilot study was designed to determine proper dilution factor to quantify HbA-AEH adduct and HbA for HPLC analysis. According to the kinetic binding profile (K_D = 0.1 mM, $t_{1/2}^{eq}$ = 0.058 hrs) of VZHE-039 in isolated HbA solution, 0.03, 0.1, and 2 mM initial concentrations were prepared. 30 µL aliquot was

taken at 0.05, 0.5, and 1 hrs and mixed with 120 µL (5-fold dilution) $NaBH_3CN/NaBH_4$. After thawing (from -80ºC) aliquots were further diluted to 15-fold and 25-fold relative to the original WB concentrations. The second and third pilot studies were designed to determine concentration and time points for definitive studies. Initial concentrations of 0.25, 0.4, 0.5, 0.8, 1. 1.6, 2 mM were chosen and aliquots were taken at 0.1, 0.5, 1, 1.5, 2, 5.5, 6.5, and 20 hrs for pilot 2 study. However due to the bad performance of analytical column, HbA-AEH adduct peak did not adequately separate from natural HbA peak for pilot 2 studies. For pilot 3 study, due to limitation by available WB volume, initial concentrations of 0.4, 0.5, 1, 2, 4, 8 mM were chosen and aliquots were taken at 0, 2.5, and 17 hrs. For definitive study, 0.3, 0.5, 0.9, 1.4, 2.0, 2.7, 4.2, 7.8 mM of VZHE-039 were studied with aliquots taken at 0.1, 0.5, 1, 1.5, 2, 2.5, 3, 5, 8, 12, 15, and 24hrs.

For 5-HMF, one definitive study was performed. The initial concentrations (0.5, 1, 2, 3, 5 mM) were selected based on previous study (Parikh, 2013). Aliquots were taken at 0.1, 0.5, 1, 1.5, 2, 4, 8, 10, 12, 14, and 24 hrs, which is similar to the sampling schedule of VZHE-039 in order to compare their kinetic profiles.

5.2.4.2. VZHE-039 Quantification in Plasma

In the definitive study of VZHE-039, while preparing WB hemolysate, 150µL aliquots were taken at the same time point and centrifuged at 6000 rpm for 3 mins to separate plasma from RBC. 50 µL of top plasma was then collected and frozen at -80 ºC. After plasma sample thaw on ice, 200 µL of ACN (with 0.1%FA) was added to plasma to deproteinize plasma proteins. Samples were well mixed, and left at 4°C for 30

mins for protein precipitation. Then samples were centrifuged at 13,000 rpm for 20 min. Top clear supernatant was collected and 50 µL was injected for HPLC analysis.

5.2.5. HPLC-UV/Vis Conditions

5.2.5.1. HbA-AEH Adduct Quantification in WB

HbA and HbA-AEH adduct concentrations were quantitated by the same HPLC/UV assay method as for Hb quantification in isolated HbA solution, using a weak cation-exchange column (PolyCAT[A], 30 mm x 4.6 mm) and a detection wavelength of 410 nm. A precolumn filter (Supelco®, 2.0 µm) was used to protect column. A linear gradient wash was applied with buffer A (20 mM Bis-Tris, 2 mM KCN, pH 6.5) and buffer B (20 mM Bis-Tris,2 mM KCN, 200 mM NaCl, pH 6.6) over 20 minutes with flow rate of 1.5 mL/min (Table 5.1).

5.2.5.2. VZHE-039 Quantification in Plasma

Total VZHE-039 concentrations (free + PPB bound) were quantitated by a reversed-phase HPLC-UV/Vis assay, using a C_{18} column (Thermo, 50 mm x 4.6 mm) and a detection wavelength of 310 nm. A precolumn filter (Supelco®, 2.0 µm) was used to protect column. A linear gradient wash was applied with an aqueous phase (water, 0.1%FA) and organic phase (ACN, 0.1%FA) over 10 minutes with flow rate of 1.5 mL/min (Table 5.2).

Table 5.1. HPLC conditions for HbA and HbA-AEH adduct quantification in WB.

LC System	Waters 2695 separation model	
Detector	Waters 2996 PDA	
Analytical Column	Poly CAT[A] weak cation-exchange column, 30 mm x 4.6 mm	
Pre-column	Supelco® Pre-column Filter 0.2 µm	
Detection Wavelength	410 nm	
Autosampler Temperature	4 ºC	
Flow Rate	1.5 mL/min	
Injection Volume	10 µL	
Mobile Phases	A (20 mM Bis-Tris, 2 mM KCN, pH 6.5)	B (20 mM Bis-Tris, 2 mM KCN, 200 mM NaCl, pH 6.6)
0 min	100	0
10 min	60	40
15 min	0	100
16 min	100	0
20 min	100	0

Table 5.2. HPLC conditions for VZHE-039 quantification in plasma.

LC System	Waters 2695 separation model	
Detector	Waters 2996 PDA	
Analytical Column	Thermo BDS HYPERSIL C18 column, 50 mm x 4.6 mm	
Pre-column	Supelco® Pre-column Filter 0.2 µm	
Detection Wavelength	310 nm	
Autosampler Temperature	4 ºC	
Flow Rate	1.5 mL/min	
Injection Volume	50 µL	
Mobile Phases	Aqueous phase (water, 0.1%FA)	Organic phase (ACN, 0.1%FA)
0 min	90	10
1 min	90	10
5 min	10	90
6 min	10	90
7 min	90	10
10 min	90	10

5.2.6. Partial Validation of HPLC-UV/Vis Assay Methods

5.2.6.1 HbA-AEH Adduct Quantification in WB

Selectivity was assessed by comparing blank WB hemolysate and WB with AEH added, i.e. comparing peaks of natural HbA and AEH-AEH adduct. HbA calibration curves (n = 2) were prepared for each definitive study of VZHE-039 and 5-HMF. HbA concentrations ranged from 0.00125 – 0.325 mM, and 0.0005 – 0.5 mM. The peak area was used for quantification. Linearity was assessed using linear regression with 1/y weighting factor. Sensitivity, accuracy, and precision were evaluated. eLOQ was estimated as the lowest observed nominal concentration which has acceptable of %DFN and %RSD, and multiplied by dilution-factor (6-fold) of WB hemolysate. Concentrations below eLOQ were not included in the data set.

Mass balance was assessed by adding HbA-AEH adduct and HbA concentrations quantified from HbA calibration curve and corrected with dilution factor (6-fold), and compared to the initial nominal concentration of HbA in blank WB.

5.2.6.2 VZHE-039 Quantification in Plasma

Selectivity was assessed by comparing blank plasma and plasma spiked with VZHE-039. Calibration curves (n=3) of VZHE-039 (0.004 - 8 mM) were prepared in net solution water/ACN (V:V = 1:1) and plasma. The peak area was used for quantification. Concentrations below eLOQ were not included in the data set. Linearity was assessed using linear regression with 1/y weighting factor. Sensitivity, accuracy, and precision

were evaluated. eLOQ was estimated as the lowest observed nominal concentration which has acceptable of precision, accuracy and absolute recovery.

Absolute recovery was assessed by comparing HPLC response of VZHE-039 calibration curves in net solution and VZHE-039 spike in plasma (Equation 5.1). Experimental amount on column for VZHE-039 in plasma was estimated by using VZHE-039 calibration curve in net solution. Calculated amount on column was determined by nominal concentration multiplied by injection volume (50 µL) and corrected from dilution factor (5-fold). Absolute recovery value within 80% - 120% range is acceptable.

$$\boldsymbol{Absolute\ Recovery} = \frac{\boldsymbol{Experimental\ amount\ on\ column}}{\boldsymbol{Calculated\ amount\ on\ column}} * \mathbf{100}\%$$

----- ***Equation 5.1***

5.2.7. Data Analysis and Modeling

5.2.7.1 Non-compartmental analysis (NCA) of c_p -t and HbA-AEH adduct – t profiles for VZHE-039 and 5-HMF

The NCA approach was used to characterize the c_p -t profile of VZHE-039 and HbA-AEH adduct – t profiles for VZHE-039 and 5-HMF in WB, where the relevant exposure metrics were estimated. NCA does not have compartmental model-based assumptions, but it assumes a terminal log-linear portion sufficient for estimation of the extrapolated area based on the terminal slope.

Area under the curve (AUC_{trap}) was calculated by the linear trapezoidal method (Equations 5.2).

$$\boldsymbol{AUC_{trap}} = \sum_{i=1}^{n} \frac{c_i + c_{i+1}}{2} * (t_{i+1} - t_i)$$

$$\boldsymbol{AUC_{extrap}} = \frac{c_n}{\lambda}$$

$$\boldsymbol{AUC_{total}} = \boldsymbol{AUC_{trap}} + \boldsymbol{AUC_{extrap}}$$

---- ***Equations 5.2***

The extrapolated area (AUC_{extrap}) after the last measured concentration (c_n) was calculated by using terminal slope from log-transformed c_p -t or HbA-AEH adduct – t profiles. Traditionally, AUC_{extrap} should be less than 20% of the total area, in order to

adequately estimate the AUC_{total} based on the available experimental measurements. In this research, c_p and HbA-AEH adduct were monitored until 24 hrs only, limited by the stability of *in-vitro* WB environment. Visual inspection on c_p-t showed that VZHE-039 concentrations decreased slowly after the peaks, while its HbA-AEH adduct levels were sustained in WB. Therefore, only AUC_{trap} was used for VZHE-039. For 5-HMF, HbA-AEH adduct concentrations decreased below eLOQ after 4 hrs for the lowest $[5\text{-HMF}]_0$ (0.5 mM). In order to compare AUC fairly across $[5\text{-HMF}]_0$, AUC_{trap} was calculated up to 4 hrs.

The highest observed plasma concentration (c_{max}) and the time it achieved peak concentration (t_{max}) were determined by visual inspection from c_p-t profile. *In-vitro* plasma clearance ($CL_{plasma}^{in\text{-}vitro}$) was estimated from initial dose ($[\text{VZHE-039}]_0$*0.6 mL plasma volume) and AUC_{trap} (Equation 5.3).

$$\boldsymbol{CL_{plasma}^{in-vitro} = \frac{Dose}{AUC_{trap}}} \qquad \textbf{---- Equation 5.3}$$

Dose-proportionality for VZHE-039 and 5-HMF were assessed by plotting AUC_{trap}, c_{max}, or $CL_{plasma}^{in\text{-}vitro}$ against $[\text{VZHE-039}]_0$ or $[5\text{-HMF}]_0$ on linear scale and fitted with a power equation ($y = a*X^b$). The estimate for the exponent (b) from the power equation - representing the slope after log-log transformation - was then compared to 1. If the exponent is equal to or close to 1, exposure metrics increase proportionally with increasing $[\text{VZHE-039}]_0$ or $[5\text{-HMF}]_0$. When the exponent is less than 1, it represents

less than proportional (infra-proportional) kinetics. Vice versa, when the exponent is larger than 1, it represents more than proportional (super-proportional) kinetics.

5.2.7.2 Modeling of SS Concentration-Dependency of HbA-AEH Adduct Profiles for VZHE-039 and 5-HMF

For concentration-dependency studies, the same sigmodal B_{max}-model and reverse sigmodal B_{max}-model used for binding studies in HbA solution (Chapter 3) were applied to fit HbA-AEH adduct and HbA concentrations in WB, respectively.

HbA-AEH adduct level of VZHE-039 in WB were sustained within 24 hrs, so that K_D' for VZHE-039 was estimated at equilibrium (24 hrs). For 5-HMF, because of the irreversible ALDH-mediated metabolism in RBC, equilibrium could not be achieved. K_D' of 5-HMF was estimated at peak (1.5 hrs).

5.2.7.3 Modeling of Time-Dependency of HbA-AEH Adduct Profiles for VZHE-039

Due to dissolution rate-limitations of VZHE-039 in WB, three modeling approaches were applied for the time-dependency studies. 1). Simple kinetic binding model fit of entire dataset to serve as a reference for the other two models; 2). Simple kinetic binding model fit with a subset, including HbA-AEH adduct concentrations only for low $[\text{VZHE-039}]_0$, where dissolution may be assumed instantaneous; 3). Simple dissolution kinetic binding model, incorporating a zero-order input rate constant into WB (k_0) to account for the dissolution step, and fit to the entire dataset.

Modeling approaches 1 and 2 were based on the same simple kinetic binding model previously discussed in detail under section of 3.2.7.3 in Chapter 3 (Scheme 5.2),

$$\text{AEH + HbA} \underset{k_{off}'}{\overset{k_{on}'}{\rightleftharpoons}} \text{HbA-AEH adduct} \quad \text{---------- Scheme 5.2}$$

In WB kinetic model, k_{on}' and k_{off}' represent the apparent association and dissociation rate constants, respectively, which may be affected by PPB, RBC membrane binding/partitioning compared to the fundamental k_{on} and k_{off} in HbA solution.

1) Modeling approach 1: The entire dataset including 0.3 – 7.8 mM of $[\text{VZHE-039}]_0$ was used.
2) Modeling approach 2: Subset including only 0.3, 0.4, 0.9 mM of $[\text{VZHE-039}]_0$ was used. $[\text{VZHE-039}]_0$ above 0.9 mM were excluded since c_p peaked after time zero and t_{max} was found to increase with increasing $[\text{VZHE-039}]_0$, presumably due to decreased dissolution rates/times with increasing $[\text{VZHE-039}]_0$.
3) Modeling approach 3: Initial slopes of c_p -t and HbA-AEH adduct – t profiles appeared to be linear and parallel across higher $[\text{VZHE-039}]_0$. A zero-order dissolution process is assumed to be responsible for the delayed c_{max}, as well as the slowing down of the formation of HbA-AEH adduct in WB. Therefore, a zero-order rate constant k_0 was introduced to the simple binding kinetic binding model in WB (Scheme 5.3). In this model, VZHE-039 was assumed to directly dissolve into RBC, in order to simplify the overall model and minimize the possibility of overparameterization. The entire dataset including 0.3 – 7.8 mM of $[\text{VZHE-039}]_0$ was used.

$$\text{AEH}_0 \xrightarrow{k_0} \text{AEH + HbA} \underset{k_{off}'}{\overset{k_{on}'}{\rightleftharpoons}} \text{HbA-AEH adduct} \quad \text{---------- Scheme 5.3}$$

Due to dissolution limitations, VZHE-039 is assumed to dissolve in WB via a zero-order input rate. The time it takes for VZHE-039 to dissolve from time zero up to the time when all VZHE-039 fully dissolved in WB is defined as dissolution time (TE), which increases with increasing $[\text{VZHE-039}]_0$. After TE, VZHE-039 is completely dissolved and the input rate becomes 0. TE is determined by k_0 and $[\text{VZHE-039}]_0$, namely, TE = $[\text{VZHE-39}]_0/k_0$ where smaller k_0 and/or higher $[\text{VZHE-039}]_0$ results in longer TE. Equations used for modeling are listed below,

$$\boldsymbol{When\ t < TE,\ CRATE = k_0\ ;\ When\ t > TE,\ CRATE = 0}$$ ---- ***Equations 5.4***

$$\frac{\boldsymbol{d[HbA - AEH\ adduct]}}{\boldsymbol{dt}} = \boldsymbol{CRATE + (k_{on}{}' * [AEH]_t * [Hb]_t) - \left(k_{off}{}' * [HbA - AEH\ adduct]_t\right)}$$

$$\frac{\boldsymbol{d[AEH]}}{\boldsymbol{dt}} = \boldsymbol{\left(k_{off}{}' * [HbA - AEH\ adduct]_t\right) - (k_{on}{}' * [AEH]_t * [HbA]_t)}$$

---- ***Equations 5.5***

$$\boldsymbol{[HbA]_t = [HbA]_0 - [HbA - AEH\ adduct]_t}$$ ---- ***Equations 5.6***

Initial conditions:

$$\mathbf{[AEH]_0 = 0}$$

$$\mathbf{[HbA - AEH\ adduct]_0 = 0}$$

Scientist® (version 3.0) was used for nonlinear-regression. Initial estimates of k_{on}' (61 $mM^{-1}hr^{-1}$) and k_{off}' (5.8 hr^{-1}) for modeling approach 1 were obtained from the binding study of VHZE-039 in HbA solution (Chapter 3). For modeling approach 2, initial estimates of k_{on}' (0.085 $mM^{-1}hr^{-1}$) and k_{off}' (0.17 hr^{-1}) were based on the modeling approach 1. For modeling approach 3, initial estimates of k_{on}' (0.16 $mM^{-1}hr^{-1}$) and k_{off}' (0.31 hr^{-1}) were based on the modeling approach 2. Initial estimate of k_0 was obtained as the slope from c_p-t profile of VZHE-039, corrected by the WB volume in well (0.75 mL). Final parameters were optimized based on goodness-of-fit determined by r^2, residuals, coefficient of variation (COV), and correlation matrix, and compared among different modeling approaches.

To help interpret the apparent primary model parameters (k_{on}', k_{off}' and k_0) and assess the rate limiting step in the WB environment, the following secondary model parameters were calculated as shown below (Equations 5.7):

$$\boldsymbol{K_D{}' = \frac{k_{off}{}'}{k_{on}{}'}}$$

$$\boldsymbol{k^{ass\prime} = k_{on}{}' * [HbA]_0}$$

$$\boldsymbol{k^{diss\prime} = k_{off}{}'}$$

$$\boldsymbol{t_{1/2}{}^{eq} = \frac{ln2}{k^{ass\prime} + k^{diss\prime}}}$$

---- ***Equations 5.7***

Assuming first-order association ($k^{ass'}$), and dissociation ($k^{diss'}$), half-lives ($t_{1/2}$ = ln 2 / k) were calculated to assess the rate limiting step for these processes.

5.2.7.4 Modeling of Time-dependency of HbA-AEH Adduct Profiles for 5-HMF

5.2.7.4.1 Simple metabolism kinetic binding model

The concentrations of HbA-AEH adduct for 5-HMF in WB were observed to peak at 1.5 hr, and decreased below eLOQ after 24hrs across all $[5\text{-HMF}]_0$. Along with the evidence of *in-vitro* oxidative metabolism of 5-HMF in HLC, a first-order metabolism rate constant, i.e., k_{met}', were introduced to the previously simple kinetic binding model (discussed in Chapter 3) to account for ALDH-mediated metabolism in RBC. Since the studied concentration of 5-HMF in WB (0.5 – 5 mM) is much lower than the K_m of 5-HMF (>90 mM) in HLC, the metabolism in RBC was assumed to follow first-order reaction rate. Time-dependent profile was fit by the simple metabolism kinetic binding model (Scheme 5.4),

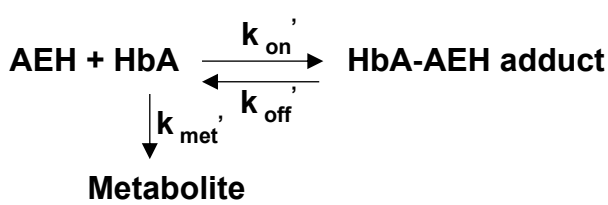

---- **Scheme 5.4**

The following equations were used for modeling,

$$\frac{d[HbA - AEH\ adduct]}{dt}$$

$$= (k_{on}' * [AEH] * [HbA]) - \left(k_{off}' * [HbA - AEH\ adduct]\right) - (k_{met}' * [AEH])$$

$$\frac{d[AEH]}{dt} = \left(k_{off}{}' * [HbA - AEH\ adduct]\right) - (k_{on}{}' * [AEH] * [HbA])$$

$$\frac{d[Metabolite]}{dt} = (k_{met}{}' * [AEH])$$

---- ***Equations 5.8***

$$[HbA] = [HbA]_0 - [HbA - AEH\ adduct]$$ **----** ***Equation 5.9***

Initial conditions:

$$[\mathbf{AEH}]_0 = \mathbf{Initial\ concentration}\ of\ 5 - HMF$$

$$[\mathbf{HbA - AEH\ adduct}]_0 = 0$$

$$[\mathbf{Metabolite}]_0 = 0$$

Scientist® (version 3.0) was used for nonlinear-regression. Initial estimates of k_{on}' (0.46 $mM^{-1}hr^{-1}$) and k_{off}' (0.13^1hr^{-1}) were obtained from the binding study of 5-HMF in HbA solution (Chapter 3). Due to the lack of experimental references for k_{met}', two initial estimates were tested, including 0.3 hr^{-1} obtained from the previous studies (Parikh, 2013) and a 10-fold larger value 3 hr^{-1}. Final parameters were optimized based on goodness-of-fit determined by r^2, residuals, COV, and correlation matrix.

To help interpret the apparent primary model parameters (k_{on}', k_{off}', and k_{met}') and assess the rate-limiting step in WB environment, secondary model parameters (K_D', $k^{ass'}$, $k^{diss'}$, $t_{1/2}$) were calculated. Assuming first-order association ($k^{ass'}$), dissociation ($k^{diss'}$),

and metabolism ($k_{met'}$) rate constants, half-lives ($t_{1/2}$ = ln 2 / k) were calculated to assess the rate limiting step for these processes. $k^{ass'}$ depends on the initial HbA concentrations ($[HbA]_0$), which were quite diluted in the HbA binding experiments (0.2 or 0.1 mM, discussed in Chapter 3), but was speeded up by $[HbA]_0$ (2.0 – 2.3 mM, within the physiological range) in WB study.

5.2.7.4.2 Post hoc sensitivity analyses of simple metabolism kinetic binding model

k_{on} and k_{off} estimates for 5-HMF in HbA solution discussed in Chapter 3 can be used as a reference for WB kinetic profile. However, $CL_{int}^{in\text{-}vitro}$ estimated in HLC (Chapter 4) cannot quantitatively be related to k_{met}' in kinetic model due to the lack of information of ALDH enzyme concentrations in RBC. Besides, the COV of k_{met}' is 48% from the final WB kinetic model, which is larger than the generally accepted cut-off value of 30%, indicating less confidence in the point estimate for k_{met}'. Goodness-of-fit results of WB kinetic model for 5-HMF showed a highly correlation between k_{on}' and k_{off}' (0.946), which increased the difficulties of independently estimating each of the three model parameters with the available experimental data. In order to better assess the reliability for k_{met}' estimated from WB kinetic model, *post-hoc* sensitivity analyses were performed based on the final point estimates.

2 mM initial concentration of 5-HMF is used for all simulations, which is higher than K_D' (0.2 mM). Since the HbA binding is a nonlinear process, different initial 5-HMF concentrations will result in a nonlinear fold-change for the corresponding exposure metrics. But the overall model sensitivity trend for k_{on}', k_{off}', and k_{met}' should be the same. The initial HbA concertation is fixed to 2 mM, which is the experimental value from WB (38% Hct). k_{on}', k_{off}', or k_{met}' (scenario 1, 2, and 3) were increased or decreased 4-fold

relative to their final point estimate, leading to a 16-fold total change from upper limit (UL) to lower limit (LL) (Table 5.3). This 16-fold change was chosen to assess the change of exposure metrics under physiological relevant range.

The change of the primary HbA-AEH adduct were assessed, using the metrics of AUC_{∞}^{adduct}, $t_{1/2}^{terminal}$, t_{max}, c_{max}. The change of 5-HMF exposures in RBC was also assessed, using the metrics of $AUC_{\infty}^{5\text{-}HMF}$ and $t_{1/2}^{terminal}$. To plot the 24 hrs profiles of exposure metrics in both linear and log scale, 0.01 to 24 hrs were simulated using 20 time points with log scale interval to get smooth lines. Terminal half-lives were determined from the terminal log-linear slope from 24 hr simulation. AUC_{∞} was obtained by simulation from 0.01 to 1000 hrs with 2 time points to ensure the completion of reaction. t_{max} and c_{max} were determined by visual inspection from simulations of 1 to 3 hrs with 100 time points with linear scale interval (every 0.03 hr). The fold-change was calculated by dividing the largest number by the smallest value obtained using parameter values from upper limit (UL) and lower limit (LL). If results from UL were smaller than results from LL, the fold-change is expressed as a negative number. A cut-off of 4-fold change was set to determine if a parameter is sensitive to the change of exposure metrics (16-fold change).

Non-compartmental analysis (NCA) was applied to estimate experimental $AUC_{0.5\text{-}14hr}$, c_{max}, t_{max} and $t_{1/2}^{terminal}$ at 2 mM of $[5\text{-HMF}]_0$ and compared to the simulation results from the final point estimate, to validate the simple metabolism kinetic binding model. AUC from 0.5 to 14 hrs were chosen instead of 24 hrs because HbA-AEH adduct concentrations were above eLOQ after 14 hrs.

Table 5.3. *Post hoc* sensitivity analyses for the simple metabolism kinetic binding model of 5-HMF.

		Point Estimate (PE)	Lower Limit (LL)	Upper Limit (UL)	Fold Change (FC)	K_D [mM]			
						LL	PE	UL	FC
k_{on}'	[$mM^{-1}hr^{-1}$]	0.56	0.14	2.2	***16***	0.79	0.20	0.05	***16***
k_{off}'	[hr^{-1}]	0.11	0.028	0.44	***16***	0.05	0.20	0.79	***16***
k_{met}	[hr^{-1}]	2.2	0.55	8.8	***16***	0.20	0.20	0.20	***1.0***

5.3 Results

5.3.1 Partial Validation of HPLC-UV/Vis Assay Methods

5.3.1.1 HbA-AEH Adduct Quantification in WB

5.3.1.1.1 Selectivity and Representative Chromatograms

The chromatogram for blank WB sample (6-fold diluted) showed a single peak at similar retention time (11 – 11.5 mins) with isolated HbA solution (Figure 5.1). The HbA-AEH adduct peak was well separated and eluted prior to HbA peak (Figure 5.2 – 5.4). For 5-HMF, the HbA-AEH adduct peak was increased at early incubation time, and then decreased along with an increasing of natural HbA peak with longer incubation time.

Figure 5.1. Representative chromatograms for blank WB sample (a) and 0.125 mM of HbA solution (b).

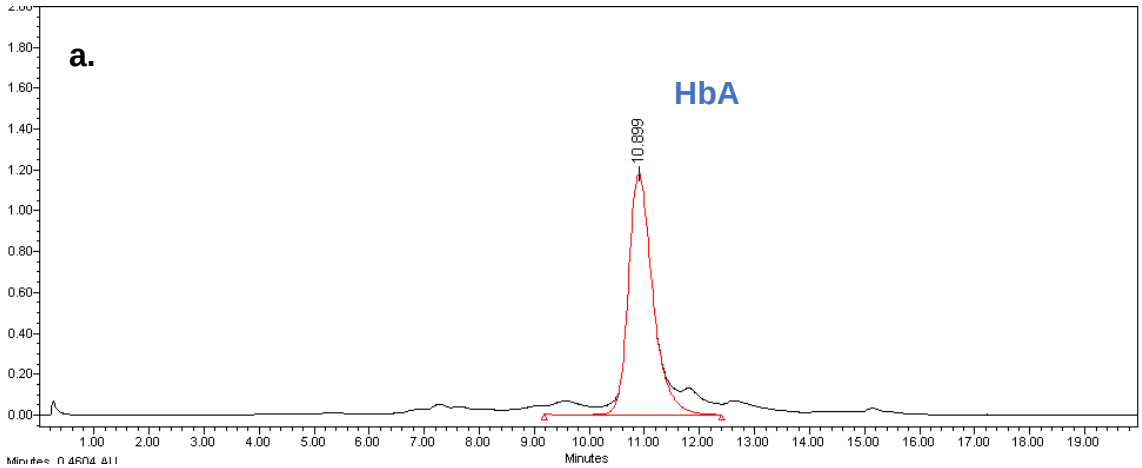

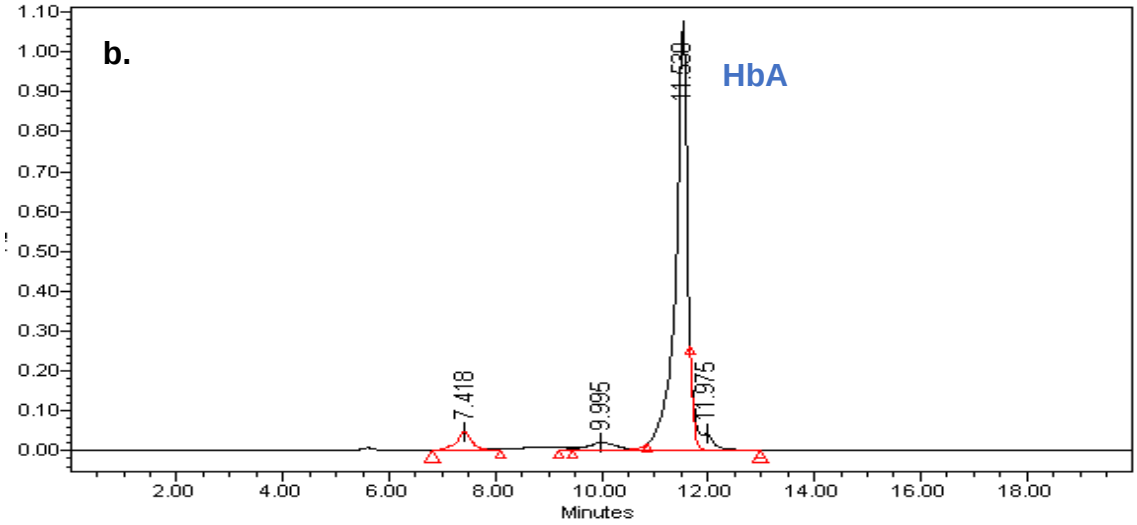

Figure 5.2. Representative chromatogram of HbA-AEH adduct and HbA separation for 0.3 mM of VZHE-039 in WB at 15 hrs.

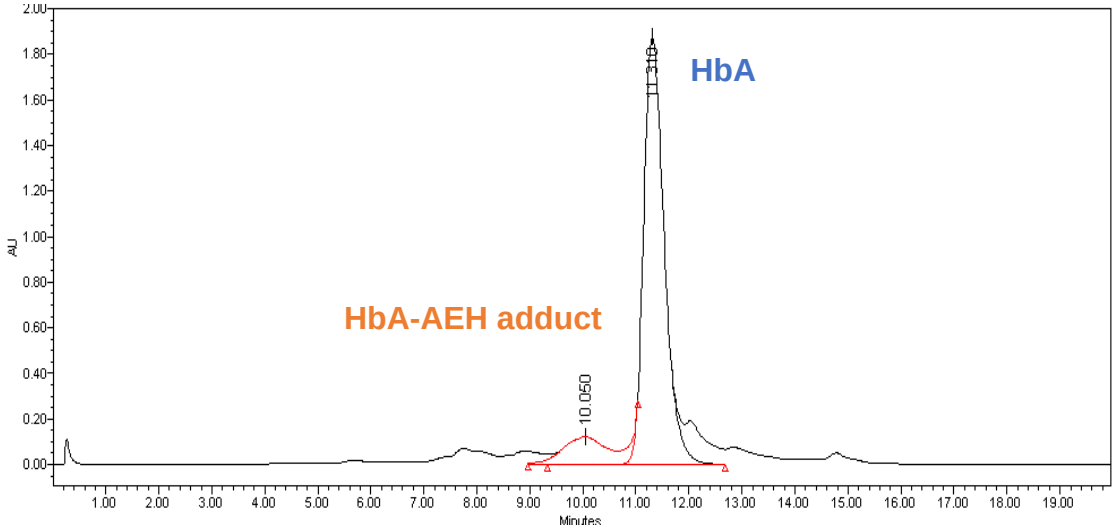

Figure 5.3. Representative chromatogram of HbA-AEH adduct and HbA separation for 2 mM of 5-HMF in WB at 2 hrs.

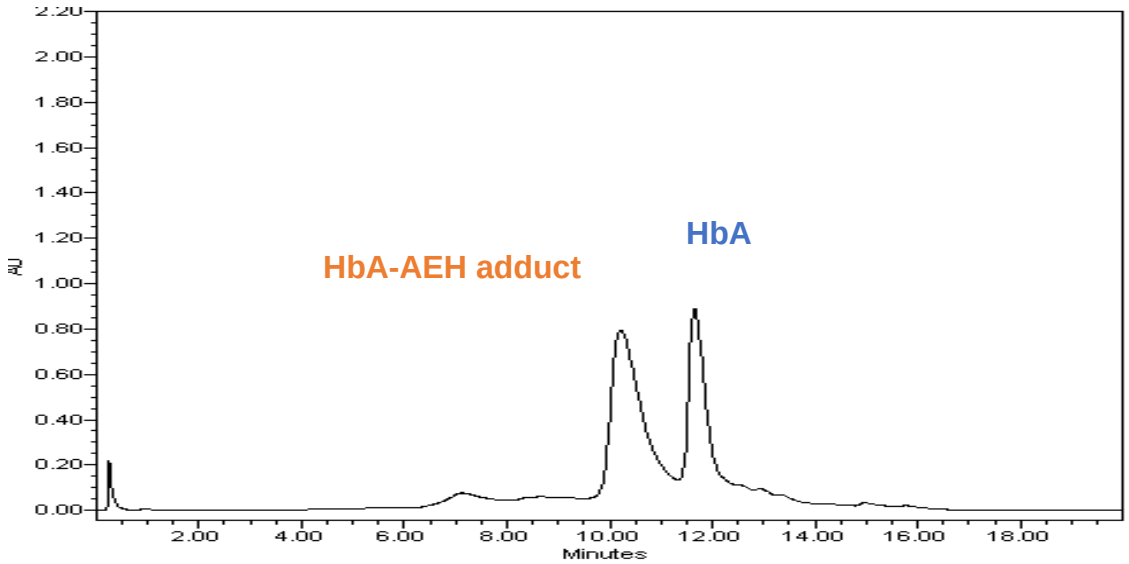

Figure 5.4. Representative chromatogram of HbA-AEH adduct and HbA separation for 2 mM of 5-HMF in WB at 14 hrs.

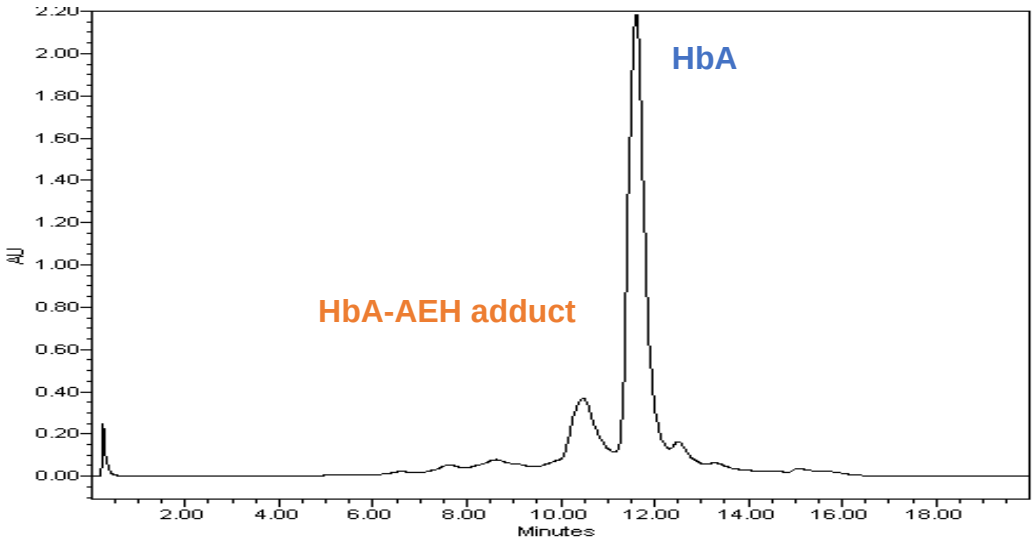

5.3.1.1.2 Linearity, Precision and Accuracy

HbA calibration curves (n=2) were run every time before testing samples. All calibration curves (0.00125 – 0.325 mM or 0.0005 – 0.5 mM) were linear (1/y weighted) with r^2 of 0.993 – 0.994 and slope of $1.07 * 10^8$ and $1.24 * 10^8$ (Figure 5.5). 0.0005 mM HbA showed acceptable precision (%RSD = 2%) and accuracy (%DFN = -4.4%). After corrected by the 6-fold dilution factor, eLOQ for HbA and HbA-AEH adduct quantification is 0.003 mM. Overall, the HbA calibration curves showed acceptable precision (%RSD of 0%-5%) and accuracy (%DFN of -9% to 16%).

Figure 5.5. Representative calibration curve of HbA in water/stopping solution (V:V = 1:5). 1/y weighted linear regression (line) was fit to the experimental data (symbols). Date were presented as mean ± SD (n = 2).

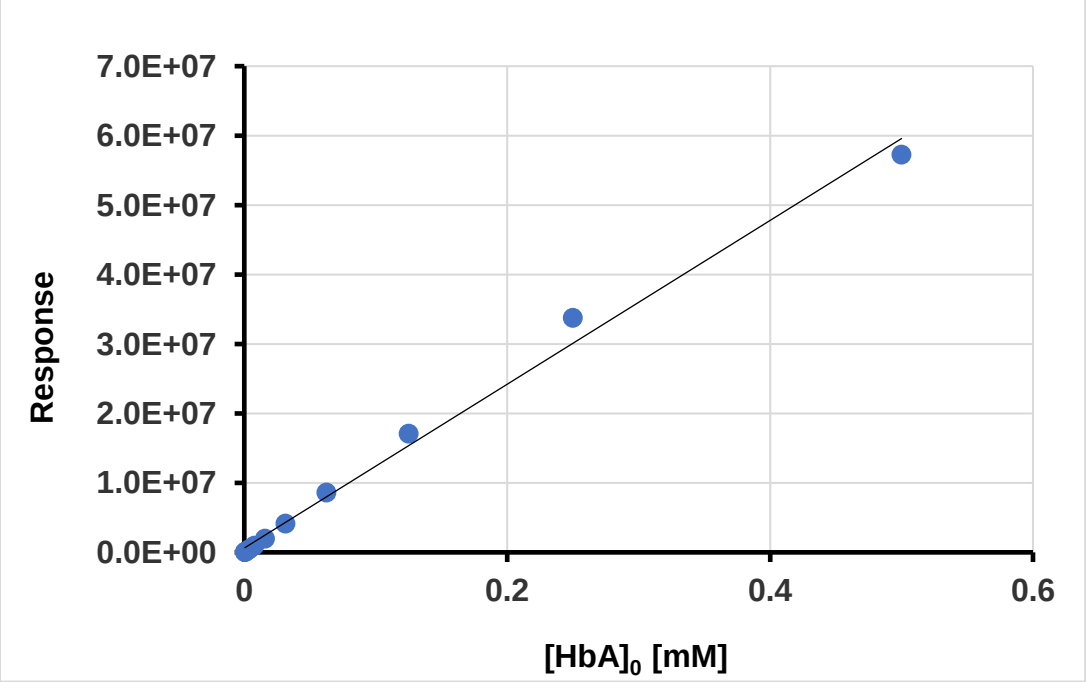

5.3.1.1.3 Mass Balance

With increasing $[VZHE\text{-}039]_0$, more of free HbA were modified by AEH, reflected by a decrease in HbA concentration and corresponding increase in HbA-AEH adduct concentration in the SS concentration-dependency study (Figure 5.6 – 5.7). For $[VZHE\text{-}039]_0$, 0.3 -7.8 mM is a proper range that covered both low and high concentrations relative to K_D. At $[VZHE\text{-}039]_0$ of less than 4.2 mM, mass balance is acceptable (91% - 120%) across tested $[VZHE\text{-}039]_0$. HbA concentrations decreased to zero at 7.8 mM of $[VZHE\text{-}039]_0$, but only 63% converted to HbA-AEH adduct, resulting in 37% loss of mass balance. This trend in the loss of mass balance at high $[VZHE\text{-}039]_0$ and long incubation times was previously observed when VZHE-039 was incubated in HbA solution (discussed in Chapter 3).

For 5-HMF, mass balance was 79% at 0.5 mM of $[5\text{-}HMF]_0$ caused by an unexpectedly lower HbA concentration, speculatively due to dilution error for that single sample (Figure 5.7). For all other studied $[5\text{-}HMF]_0$, mass balance was within 100% – 109% range.

Figure 5.6. Mass balance assessment for VZHE-039 in WB for 24 hrs. The sigmoidal B_{max}-model and the reverse sigmoidal B_{max}-model (lines) were fit with for HbA-AEH adduct and HbA (symbols), respectively. Linear regression (dashed line) was fit for visual inspection of mass balance (HbA-AEH adduct + HbA).

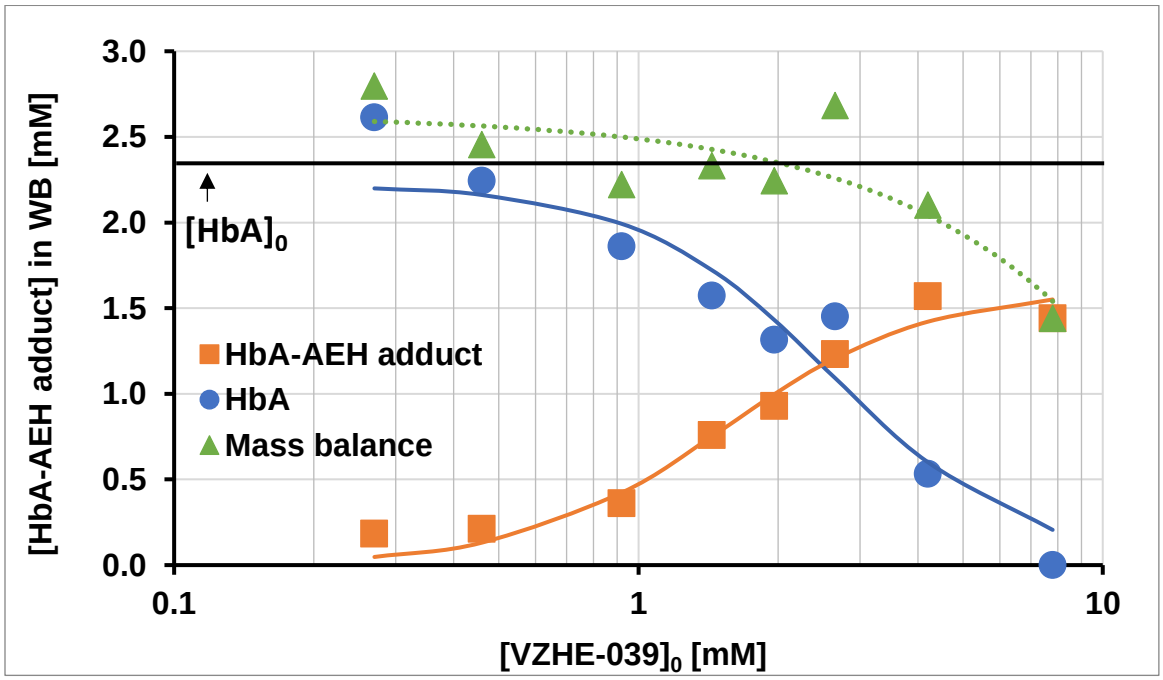

Figure 5.7. Mass balance assessment for 5-HMF in WB for 24 hrs. The sigmoidal B_{max}-model and the reverse sigmoidal B_{max}-model (lines) were fit with for HbA-AEH adduct and HbA (symbols), respectively. Linear regression (dashed line) was fit for visual inspection of mass balance (HbA-AEH adduct + HbA).

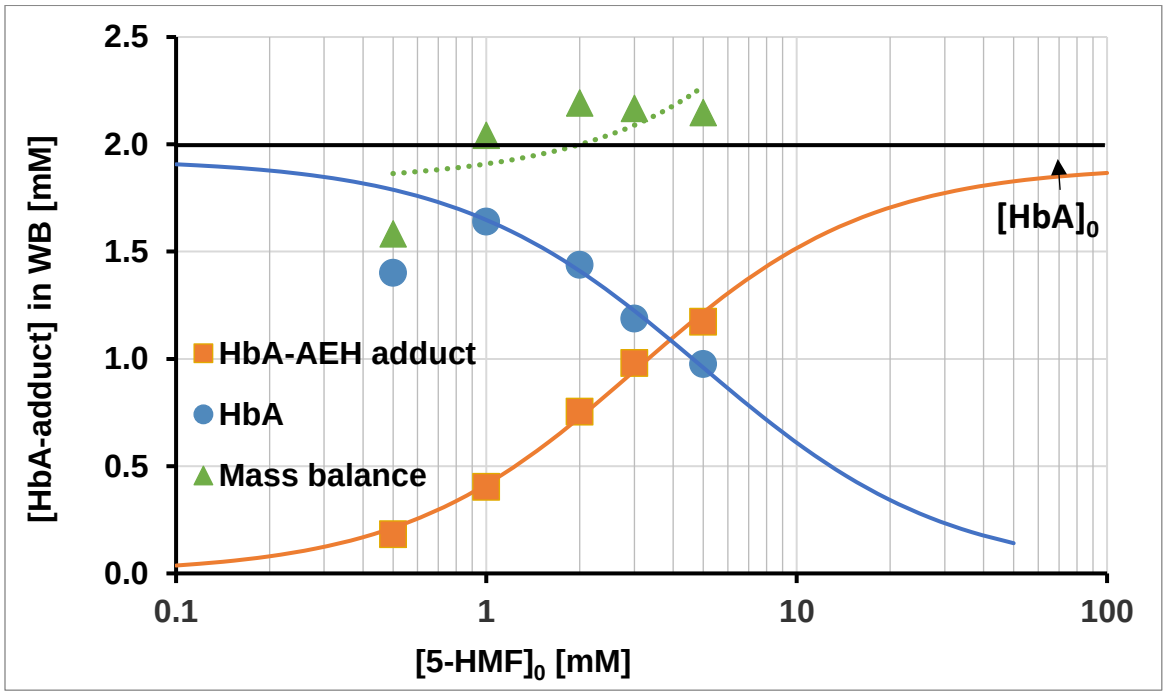

5.3.1.2 VZHE-039 Quantification in Plasma

All chromatograms showed the same retention time (3.3 min) for VZHE-039 in neat solution and plasma (Figure 5.8). VZHE-039 peak was absent in blank neat solution and blank plasma sample (Figure 5.8). Precision is acceptable (<20%) for all measured concentrations in neat solution and plasma (Table 5.3 -5.4). Accuracy of low concentrations has been significantly improved by 1/y weighted factor. Therefore, all calibration curves were fitted with linear regression using 1/y weighting factor to put more strength on the lower concentration points in order to properly cover the large concentration range. Overall, %DNF was within -6% - 20% range. Concentrations below 0.004 mM showed no detectable peak at 3.3 min. Calibration curves in both neat solution and plasma statistically showed the same slope, $5.65 * 10^6$ (Figure 5.9). At the lowest concentration (0.004 mM), a o145% absolute recovery was observed due to its below the detection limit. After excluded the 0.004 mM concentration point, all other concentrations show acceptable absolute recovery (90 – 116%). 0.008 mM is the eLOQ with acceptable precision, accuracy and absolute recovery.

Figure 5.8. Representative chromatograms for blank and 2 mM of [VZHE-039]$_0$ in neat solution (Water:ACN = 1:1) and plasma.

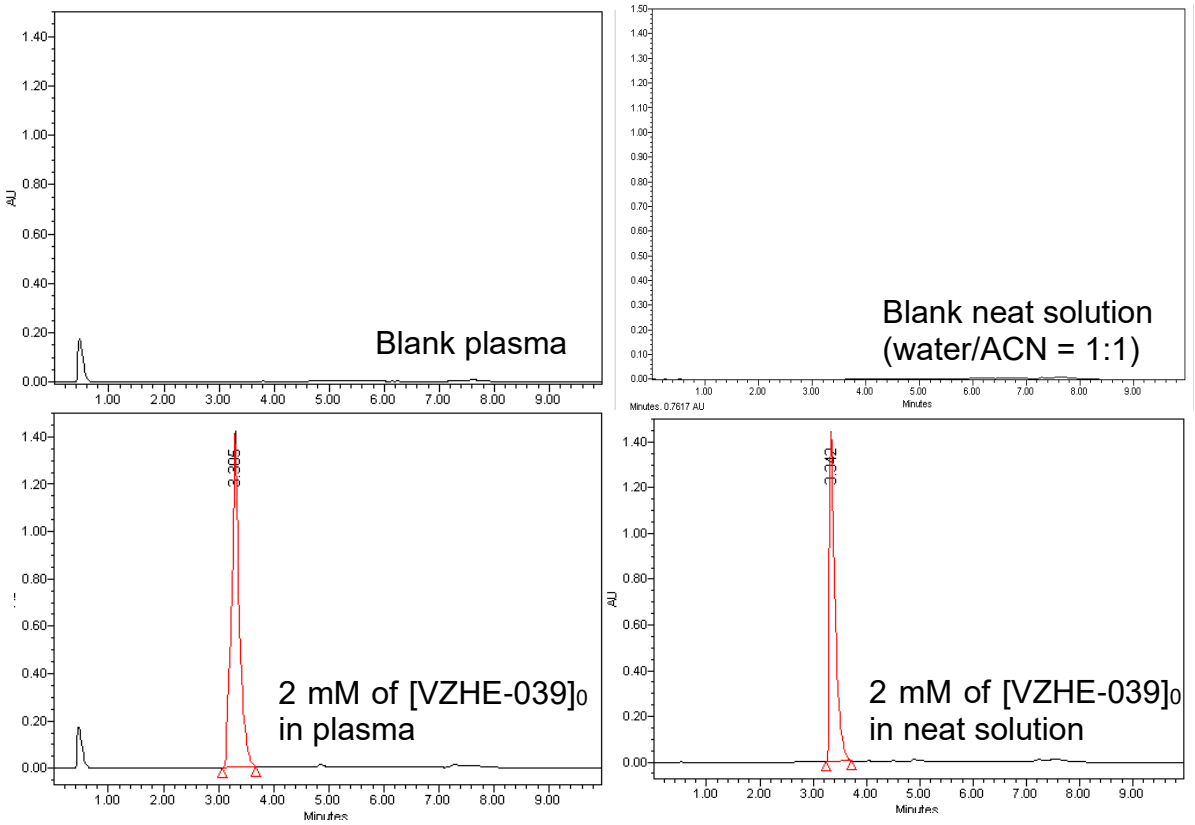

Figure 5.9. Representative calibration curves of VZHE-039 in neat solution and plasma. 1/y weighted linear regression (lines) were fit to the experimental data (symbols). Data are presented as mean ± SD (n = 3).

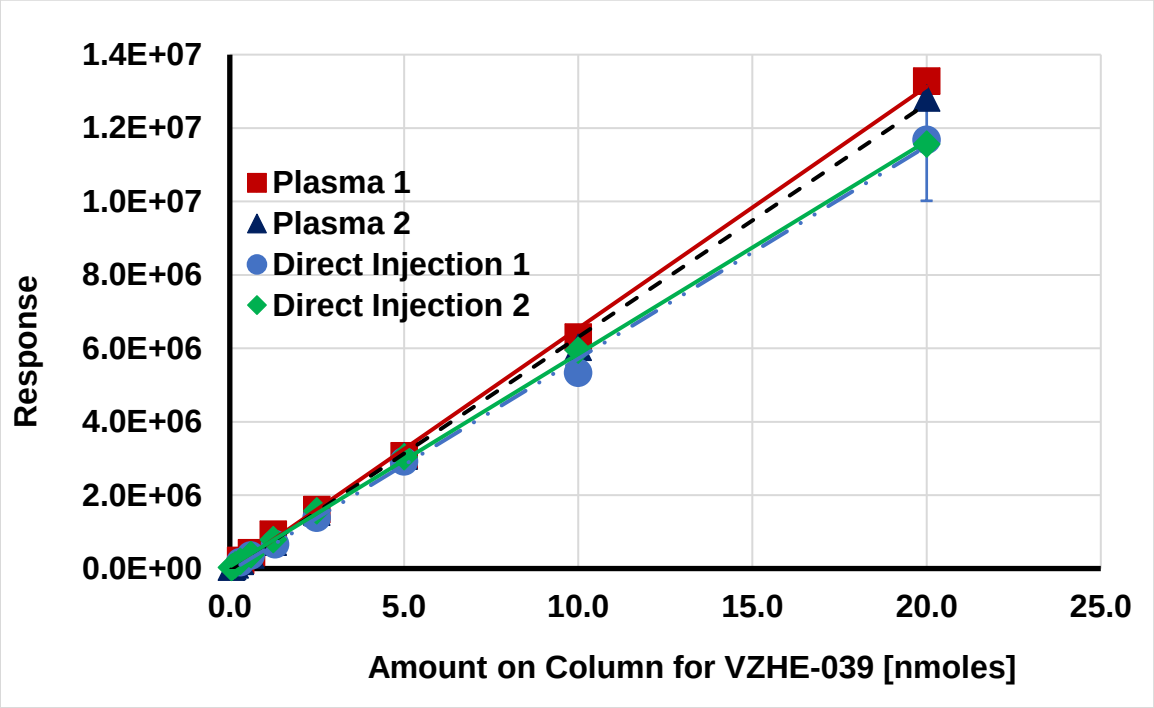

Table 5.4. Linearity, precision, and accuracy assessment for VZHE-039 in net solution (Water:ACN = 1:1) (n = 3).

$[VZHE\text{-}039]_0$ mM	Response n=3	RSD n=3	DFN unweighted	DFN 1/y weighted	Calculated Amount on Column nmoles
0.004	28422	18%	NA	-9%	0.04
0.008	48518	6%	NA	-12%	0.08
0.015	95296	4%	-51%	0%	0.15
0.03	192616	6%	-20%	5%	0.3
0.06	380776	7%	-6%	5%	0.6
0.13	786180	7%	1%	5%	1.25
0.25	1574212	8%	5%	6%	2.5
0.5	3047747	7%	3%	3%	5
1	5945746	6%	2%	1%	10
2	11561330	7%	-1%	-2%	20
4	23925389	5%	4%	4%	40
8	43478466	12%	-3%	-2%	80

Table 5.5. Linearity, precision, accuracy and absolute recovery assessment for VZHE-039 in plasma (n = 3).

[VZHE-039]$_0$ mM	Response n=3	RSD n=3	DFN unweighted	DFN 1/y weighted
0.004	34975	2%	NA	20%
0.008	55575	5%	-94%	1%
0.015	99053	5%	-50%	-6%
0.03	197153	9%	-17%	3%
0.06	368570	6%	-9%	-3%
0.13	718654	9%	-4%	-5%
0.25	1537149	8%	2%	-2%
0.5	3060126	6%	4%	-2%
1	6022667	6%	3%	-3%
2	12816151	7%	10%	3%
4	24627156	4%	11%	8%
8	42363177	1%	-3%	-7%

[VZHE-039]$_0$ mM	Calculated Amount on Column nmoles	Experimental Amount on Column nmoles	Absolute Recovery
0.004	0.04	0.06	**145%***
0.008	0.08	0.09	**116%**
0.015	0.15	0.17	**111%**
0.03	0.3	0.33	**111%**
0.06	0.6	0.62	**104%**
0.13	1.25	1.21	**97%**
0.25	2.5	2.6	**104%**
0.5	5	5.18	**104%**
1	10	10.19	**102%**
2	20	21.68	**108%**
4	40	41.67	**108%**
8	80	71.68	**90%**

5.3.2 WB disposition of VZHE-039

5.3.2.1 NCA Analysis of c_p – t Profile

The c_p of VZHE-039 peaked after t_0 for high $[VZHE\text{-}039]_0$ (>0.9 mM). On a log-linear scale of c_p - t profile, c_p declined with parallel terminal slopes across all $[VZHE\text{-}039]_0$ studied (Figure 5.10).

Table 5.9 summarizes the relevant exposure metrics for c_p-t profiles, estimated by NCA. The $t_{1/2}^{terminal}$ was similar across $[VZHE\text{-}039]_0$, except for 7.8 mM where c_p showed no obvious decline at 24 hrs. AUC_{trap} increased proportionally with increasing $[VZHE\text{-}039]_0$ (Figure 5.11), indicating the extent of VZHE-039 dissolution in WB at 24 hrs is proportional to $[VZHE\text{-}039]_0$, i.e., ultimately ALL VZHE-039 is dissolved However, with increasing $[VZHE\text{-}039]_0$, c_{max} increased infra-proportionally and t_{max} was prolonger, indicating the rate of dissolution slowed down the overall kinetics of VZHE-039 in plasma, especially for high $[VZHE\text{-}039]_0$. This dissolution rate limitation was also reflected by a constant c_0 for high $[VZHE\text{-}039]_0$ (Table 5.6).

In summary, the *in-vitro* disposition of VZHE-039 in plasma and, by extension, in WB before reaching RBCs was impacted by its slow dissolution (despite DMSO 2%) due to its physicochemical properties. However, ultimately, all of VZHE-039]0 was dissolved. Plasma clearance of VZHE-039 was found to be slow (0.0005 mL/min/12mL plasma) and was independent of $[VZHE\text{-}039]_0$, i.e., consistent with reverse first-order removal from plasma into RBC (see below).

Figure 5.10. c_p-t profiles (linear and log-scale) for VZHE-039. Smooth lines connected experimental data (symbols) for visual inspection.

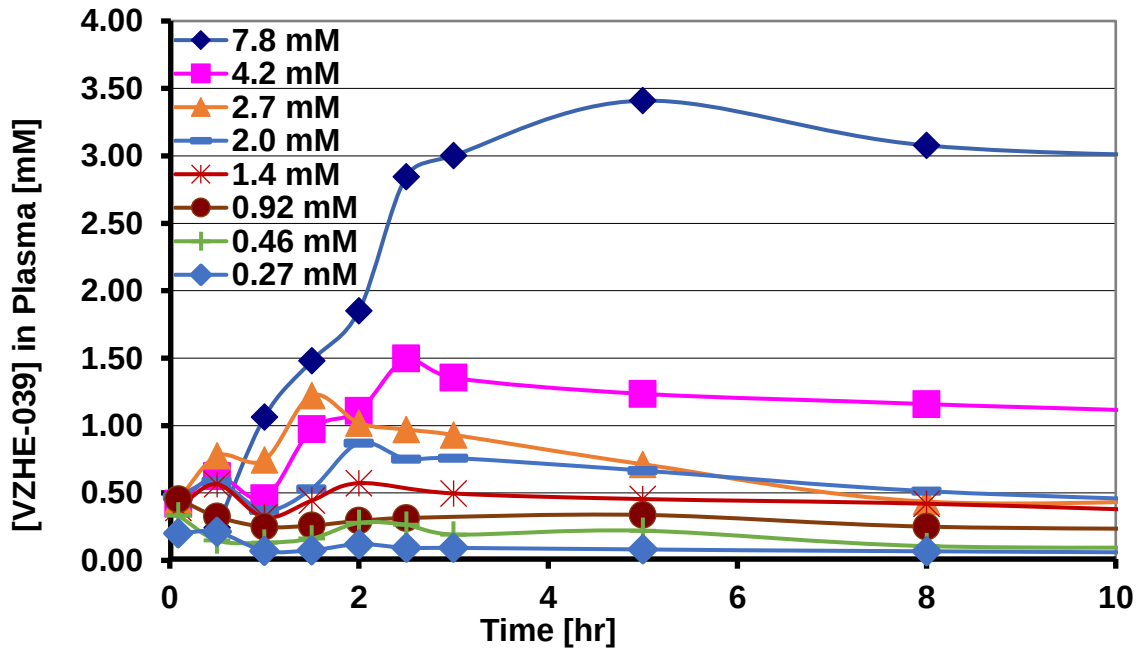

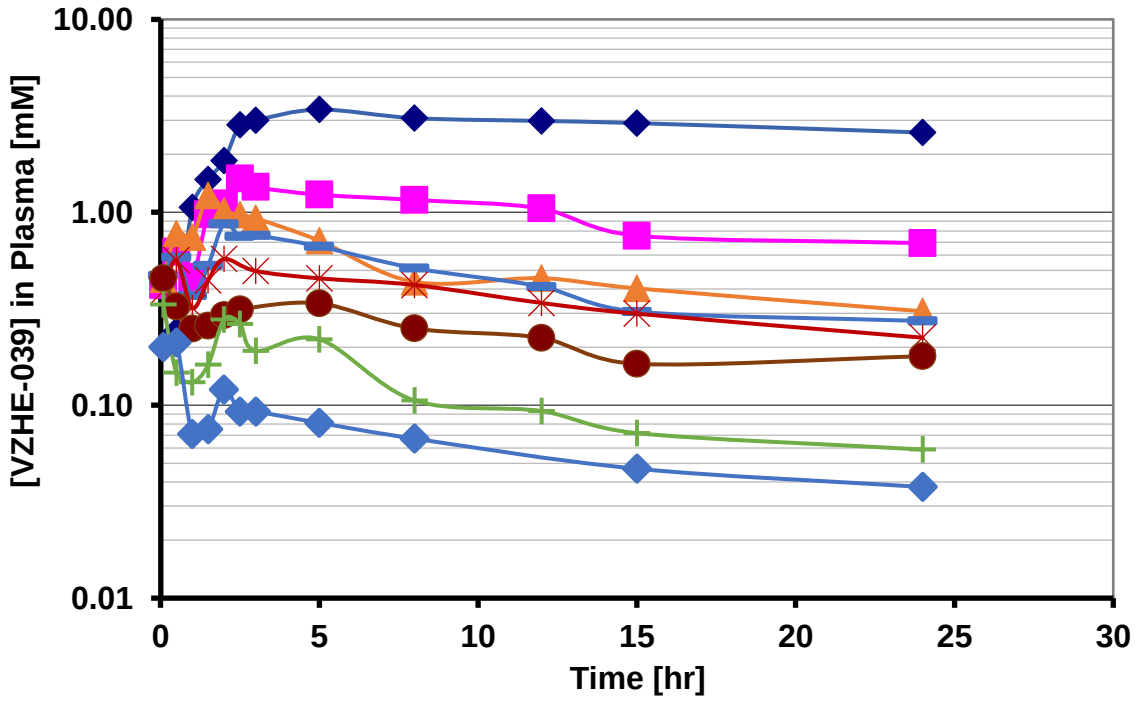

Figure 5.11. Dose-proportionality assessment for VZHE-039 in plasma. A power equation (dashed line) was fit to the experimental data (symbols).

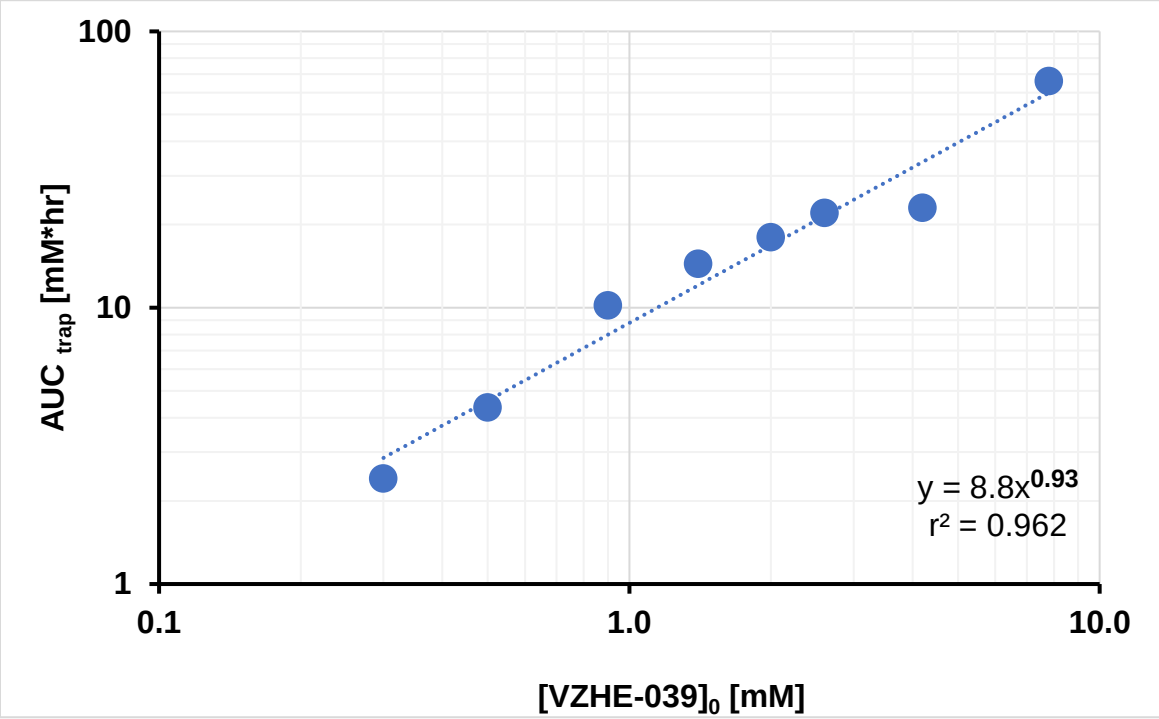

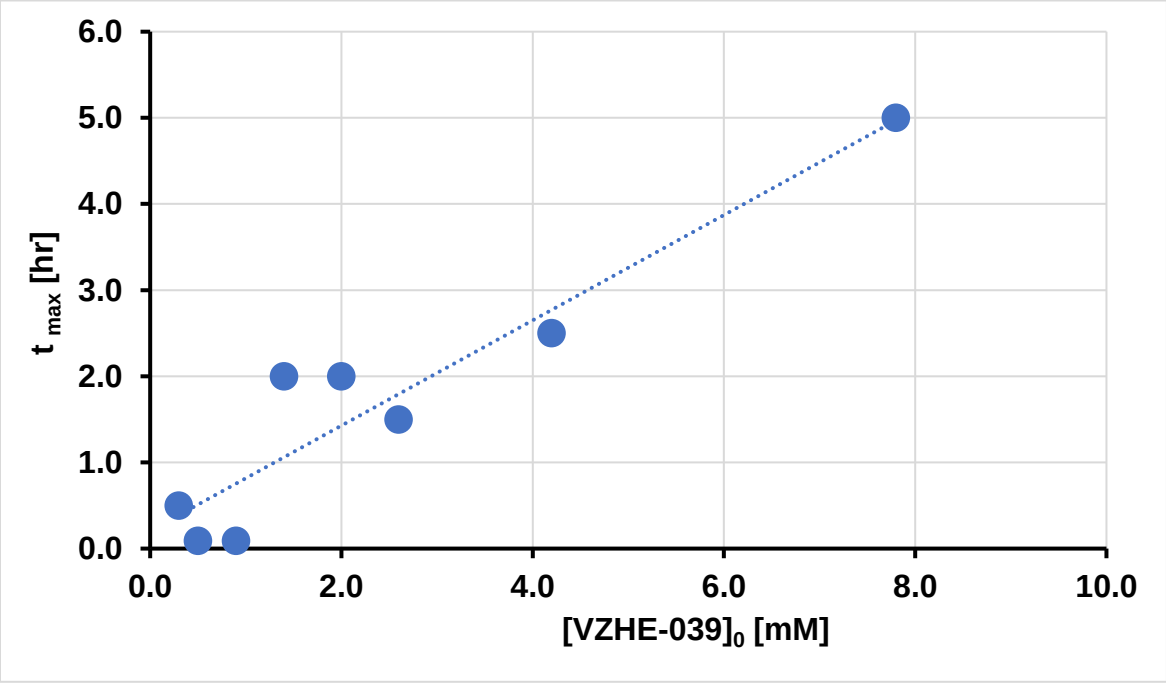

Table 5.6. Final parameters estimated from NCA analysis for VZHE-039 in plasma.

$[VZHE\text{-}39]_0$ [mM]	c_0 [mM]	c_{max} [mM]	AUC_{trap} [mM*hr]	$CL_{plasma}^{in\text{-}vitro}$ mL/min/12 mL plasma	t_{max} [hr]	$t_{1/2}^{terminal}$ [hr]
7.8	0	3.4	66	0.0047	5.0	NA
4.2	0.42	1.5	23	0.0073	2.5	21
2.6	0.45	1.2	22	0.0047	1.5	21
2.0	0.47	0.90	18	0.0044	2.0	18
1.4	0.39	0.60	14	0.0040	2.0	18
0.9	0.45	0.45	10	0.0036	0.09	22
0.5	0.33	0.33	4	0.0050	0.09	19
0.3	0.20	0.20	2	0.0060	0.09	16

5.3.2.2 SS Concentration- and Time- Dependency of HbA-AEH Adduct Formation in WB

In the pilot 1 study, no adduct peak was observed for 0.03 and 0.1 mM of VZHE-039_0 incubated with WB for 1 hr, indicating that the apparent K_D in WB maybe larger than K_D (0.1 mM) in HbA solution. Higher $[VZHE\text{-}039]_0$ were needed for the definitive studies. A HbA-AEH adduct peak was observed for 2 mM VZHE-039 incubated in WB for 1 hr, and the peak height is about one-third of unmodified HbA peak. Both HbA and HbA-AEH adduct peaks were within concentration range (0.006 – 0.5 mM) of calibration curves with 5-fold dilution factor. For 25-fold dilution factor, HbA-AEH adduct was further diluted below eLOQ. To better quantitate HbA-AEH adduct when $[VZHE\text{-}039]_0$ is below K_D', 5-fold dilution was therefore deemed to be a better dilution factor than 25-fold.

$[VZHE\text{-}039]_0$ range and sampling time for the definitive study were optimized according to pilot 2 and 3 studies. Although we were not able to adequately separate the HbA-AEH adduct peak because of performance problem of the analytical column, the trend of HbA-AEH adduct formation provided useful information. VZHE-039 showed time-dependent binding in WB but was slower in binding to Hb when compared to HbA solution. The sampling time used in pilot 2 study seems to give an optimal schedule. The concentration range in pilot 3 study covered the saturable binding condition, where HbA peak decreased below eLOQ with 8 mM of VZHE-039_0 incubated in WB for 17 hrs. In definitive studies, 0.3 – 7.8 mM of VZHE-039_0 was incubated in WB and aliquots were collected till 24 hrs.

5.3.2.2.1 NCA Analysis of HbA-AEH Adduct – t Profile

HbA-AEH adduct concentrations increased from time zero, achieved equilibrium and were sustained over 24 hrs, for all $[VZHE\text{-}039]_0$ studied in WB (Figure 5.12). AUC for HbA-AEH adduct ($AUC_{0\text{-}24}^{adduct}$) was then calculated by the trapezoidal rule to estimate the extent of Hb-AEH adduct formed in RBC over 24 hrs and were used to assess dose-proportionality. At a physiological relevant $[VZHE\text{-}039]_0$ range (0.3 – 7.8 mM), $AUC_{0\text{-}24}^{adduct}$ increased less than proportional, as described by an exponent of 0.79 from the power equation fit (Figure 5.13). This is a conclusive evidence of saturable HbA binding, consistent with VZHE-039 being a high-affinity and low-capacity binder to HbA (see below).

Figure 5.12. Time-dependency of HbA-AEH adduct formation for VZHE-039 in WB. Smooth lines connected the experimental data for visual inspection.

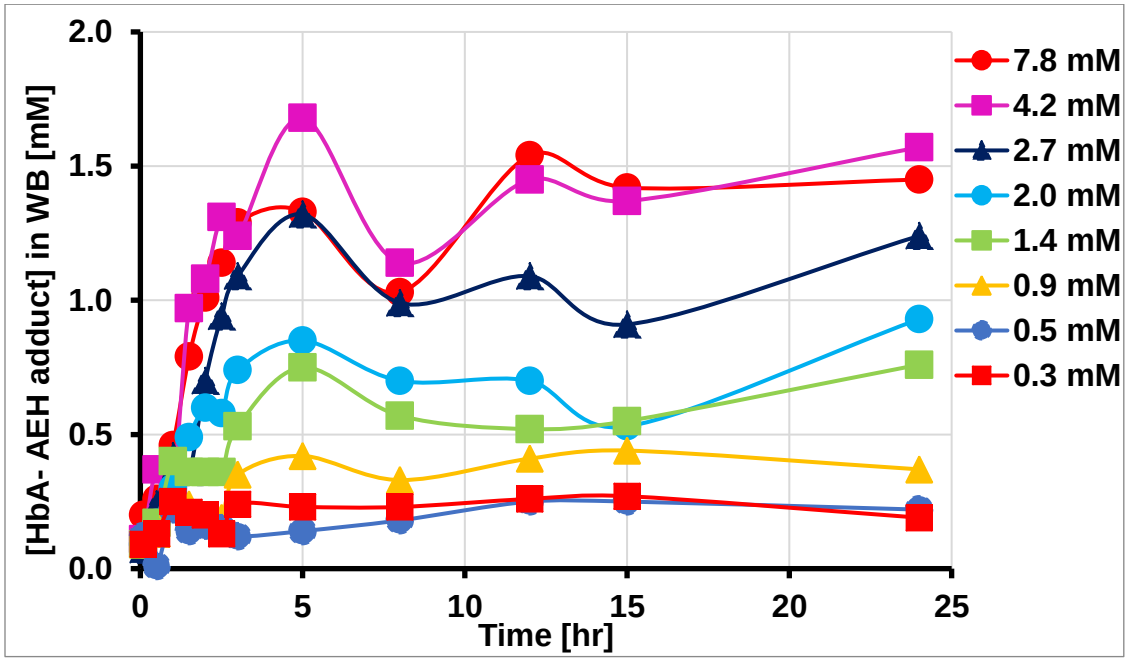

Figure 5.13. Dose-proportionality assessment for HbA-AEH adduct of VZHE-039 in WB. A power equation (dashed line) was fit to the experimental data (symbols).

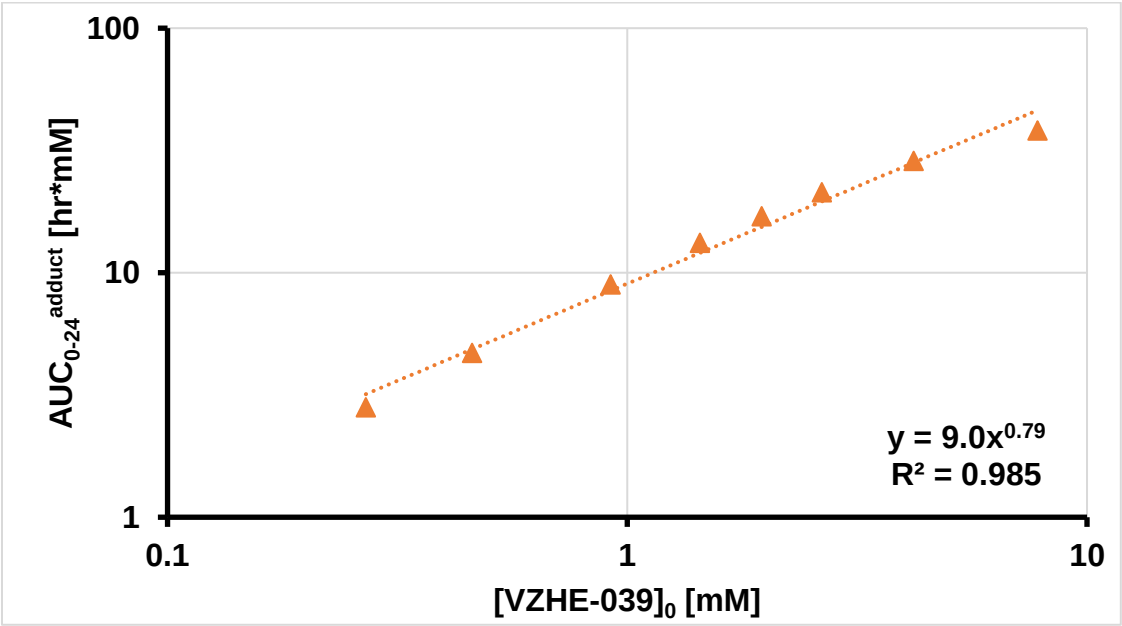

5.3.2.2.2 SS Concentration-Dependency of HbA-AEH Adduct Formation in WB

Concentration-dependency HbA-AEH adduct profile was characterized at equilibrium (24 hrs). The sigmoidal B_{max}-model fitted the concentration-dependent experimental well with an r^2 value of 0.989. the Hill coefficient (n = 2.0 (22%)) was similar to “n” (1.9 (34%)) estimated from in HbA solution. However, the apparent binding affinity (K_D' = 1.5 (13%) mM) was 15-fold lower than the K_D' (0.1 (24%) mM) in HbA solution. Since VZHE-039 is resistant to ALDH-mediated metabolism in HLC (as discussed in Chapter 4), and the HbA-AEH adduct concentrations were sustained in WB until 24 hrs, there is no evidence of intra-RBC metabolism. The lower apparent binding affinity in WB reflects the high PPB (94%) of VZHE-039 and likely RBC membrane binding due to its lipophilicity (cLogP = 1.76) (Abdulmalik, 2018).

Figure 5.14. SS concentration-dependency of HbA-AEH adduct formation for VZHE-039 in WB and the extrapolation (dashed line) using the final PE from the sigmoidal B_{max}-model in HbA solution. The sigmoidal B_{max}-model (solid line) was fit to experimental data (symbols) in WB.

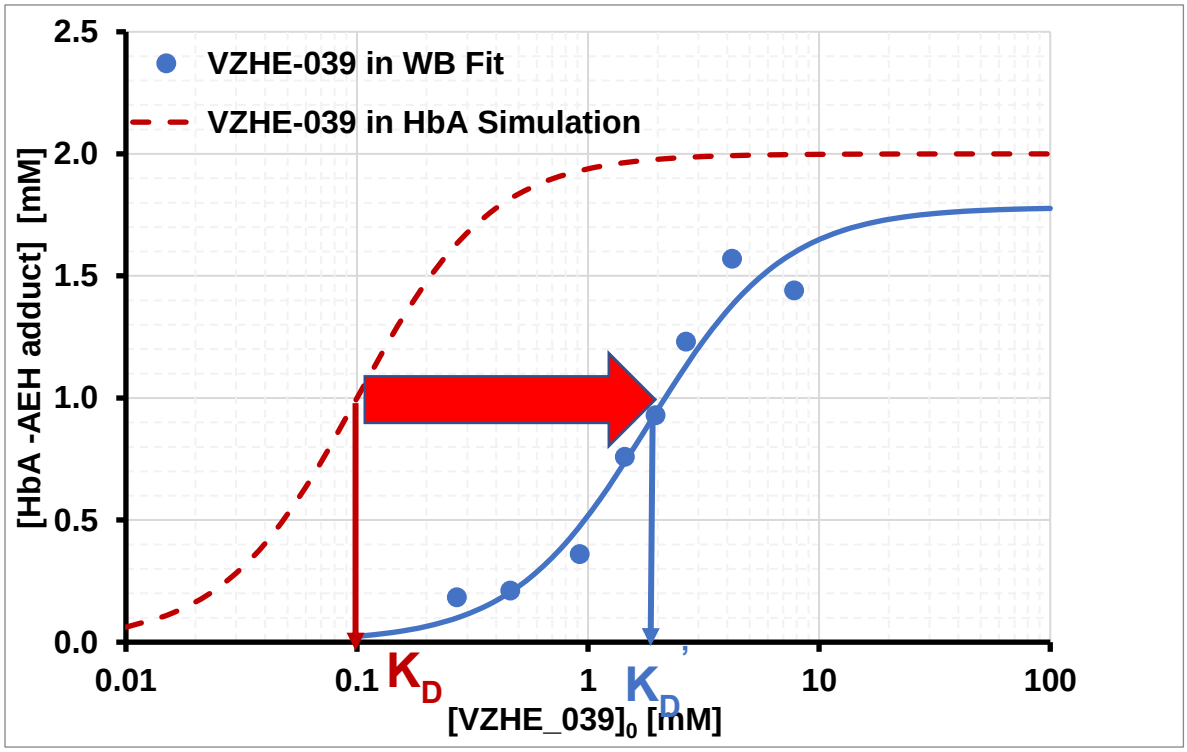

5.3.2.2.3 Time-dependency of HbA-AEH Adduct Formation in WB

The dissolution rate-limited c_p-t profiles of VZHE-039 indicated that the HbA-AEH adduct formation in RBC was slowed down by the dissolution rate as well. In order to properly characterize VZHE-039 binding kinetic in WB, a subset of low $[VZHE\text{-}039]_0$ was selected to reduce the influence of dissolution rate. Goodness-of-fit of using this subset was not as good as using the entire dataset fit by the simple kinetic binding model, reflected by a smaller r^2 (0.880) and larger COV (35%) for parameter estimates (Table 5.7). Initial ascending portion of HbA-AEH adduct – t profiles were constantly overestimated by the simple kinetic binding model. k_{on}' and k_{off}' estimates using subset data were both numerically larger than estimates using the entire dataset, which is indirect evidence of dissolution rate limitations for high $[VZHE\text{-}039]_0$.

To improve the goodness-of-fit and incorporate a dissolution step in the model, the simple dissolution kinetic binding model was established and the entire dataset was included. VZHE-039 was dissolved in WB with the same rate, characterized by k_0. As expected, with higher $[VZHE\text{-}039]_0$, it took longer for VZHE-039 to be completely dissolved in WB (Figure 5.15). The estimated dissolution times (TE) for each $[VZHE\text{-}039]_0$ were similar to the observed t_{max} from c_p – t profile, indicating k_o was properly estimated. Final point estimates of k_{on}' and k_{off}' are almost identical to results using simple kinetic binding model with subset data, indicating both approaches successfully circumvent the “nuisance” dissolution problem in the parameter estimation (Table 5.7). Moreover, the goodness-of-fit using the simple dissolution kinetic binding model was significantly improved, as reflected by r^2 (0.956), and more precise point estimates (COV 16% - 25%) (Table 5.7). The simple dissolution kinetic binding model introduced

sigmoidicity at the initial ascending portions of HbA-AEH adduct – t profiles, and the experimental data were well fitted (Figure 5.16b). The model also captured well the HbA-AEH adduct level after equilibrium (Figure 5.17b). Though high correlation between k_{on}' and k_{off}' (0.960) were observed using the dissolution kinetic binding model, precision on point estimates (COV) were improved compared to using simple kinetic binding model (Table 5.7). Therefore, the simple dissolution kinetic binding model was deemed the best among the tested modeling approaches (Table 5.7).

Both k_{on}' and k_{off}' estimates were significantly smaller than k_{on} (~300-fold) and k_{off} (~10-fold) in HbA solution, resulting in a slowing down of the overall Hb binding kinetics (prolonged $t_{1/2}^{eq}$) and lowering the apparent binding affinity (larger K_D') of VZHE-039 in WB (Table 5.7). The value for K_D' (2.3 mM) of VZHE-039 in WB was approximately 20-fold larger than it K_D (0.1 mM) in HbA solution, primarily due to significantly slower association (smaller k_{on}'), indicating that processes like PPB (94%) and/or RBC membrane binding significantly decrease association rate of VZHE-039 to Hb in WB.

Table 5.7. Final parameter estimates of time-dependency of HbA-AEH adduct formation for VZHE-039 in WB, using different kinetic binding models, and compared to the PE in HbA solution. The primary rate constants were presented as PE with (COV).

	HbA Solution	WB, Entire Dataset	WB, Subset	WB, Entire Dataset
	Simple kinetic binding model			Dissolution kinetic binding model
$[HbA]_0$ [mM]	**0.1**	2.3	**2.3**	**2.3**
r^2	**0.983**	0.938	**0.880**	**0.956**
Correlation between k_{on}' and k_{off}'	**0.888**	0.823	**0.894**	**0.960**
k_0 [mmole*hr^{-1}]	**NA**	NA	**NA**	**0.0019 (16%)**
k_{on}' [mM^{-1}*hr^{-1}]	**61 (9%)**	0.085 (10%)	**0.16 (24%)**	**0.20 (21%)**
k_{off}' [hr^{-1}]	**5.8 (13%)**	0.17 (17%)	**0.31 (35%)**	**0.46 (25%)**
K_D' [mM]	**0.095**	2.0	**2.0**	**2.3**
$t_{1/2}^{eq}$ [hr]	**0.058**	1.9	**1.0**	**0.75**

Figure 5.15. Simulation of the zero-order dissolution process using the final k_0 estimate from the simple dissolution model in WB.

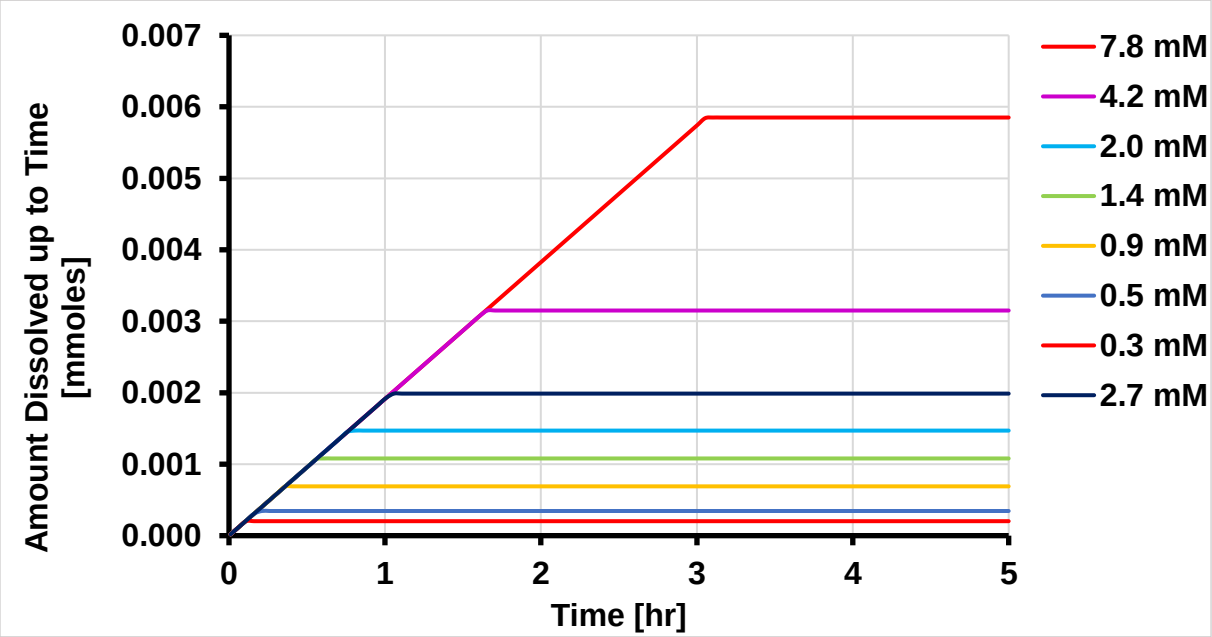

Figure 5.16. Initial portion of the time-dependency of HbA-AEH adduct formation for VZHE-039 in WB, using the simple kinetic binding model (Figure 5.16a) and the simple dissolution kinetic binding model (Figure 5.16b). Models (lines) were fit to the experimental data (symbols).

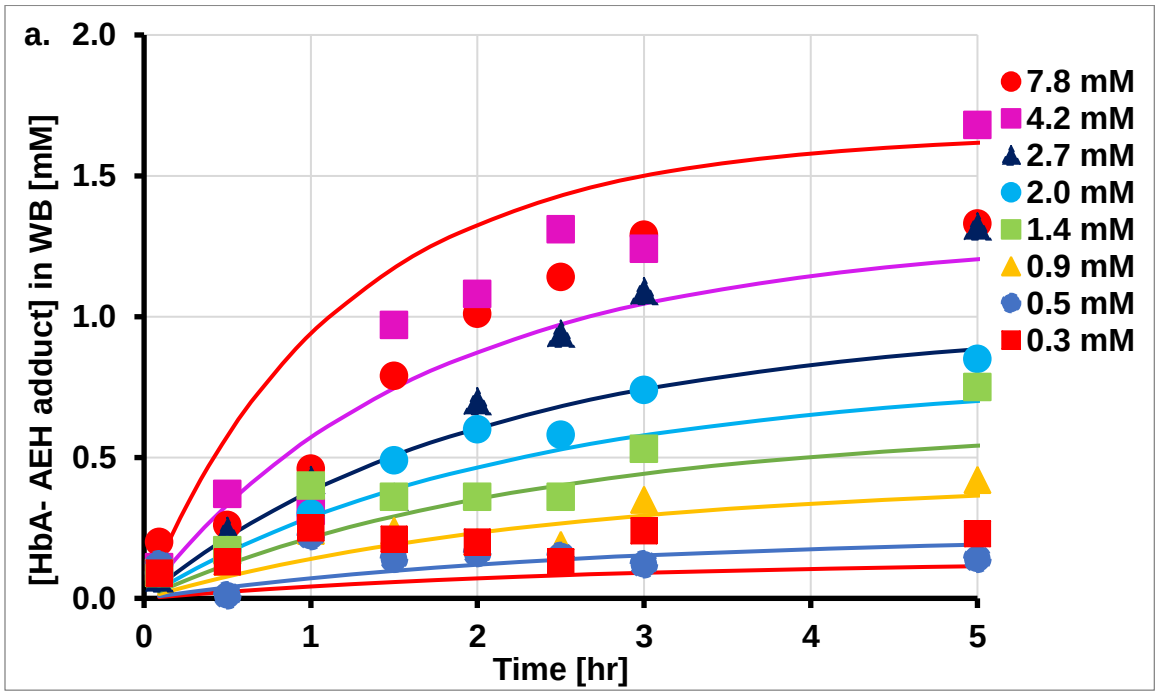

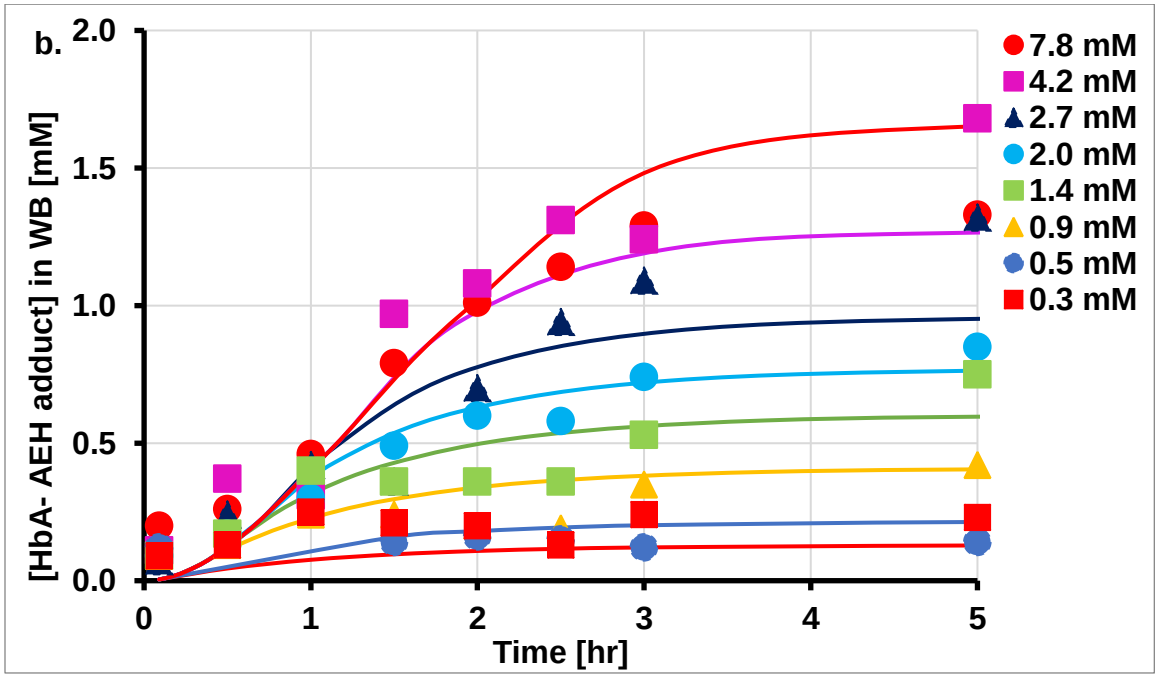

Figure 5.17. Full time-dependency of HbA-AEH adduct formation for VZHE-039 in WB, using the simple kinetic binding model (Figure 5.16a) and the simple dissolution kinetic binding model (Figure 5.16b). Models (lines) were fit to the experimental data (symbols).

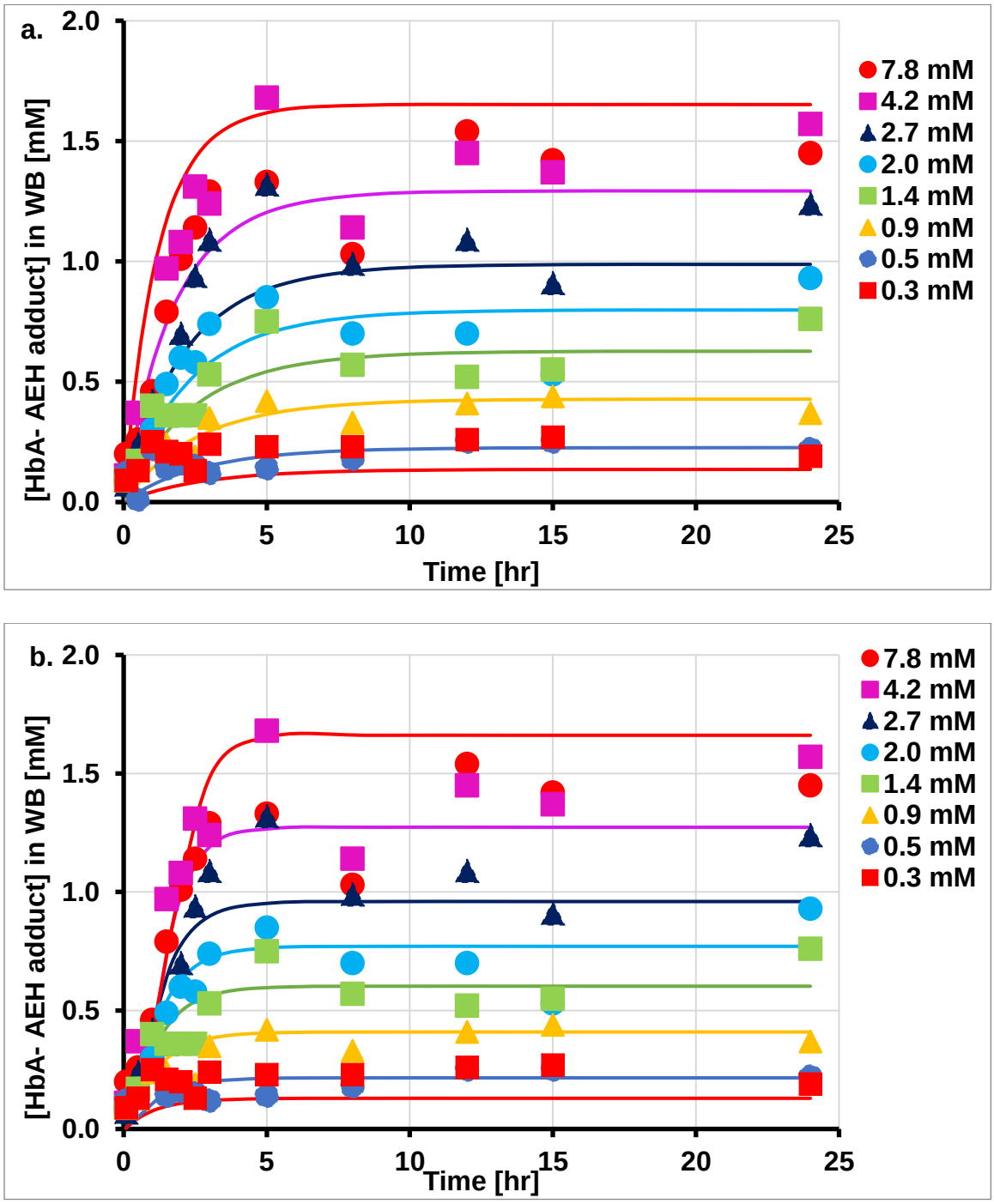

5.3.2.3 Disposition of VZHE-039 between Plasma and RBC

Plasma concentrations, c_p, of VZHE-039 and HbA-AEH adduct concentrations in WB are plotted together against time to compare the disposition of VZHE-039 in plasma and RBC.

Figure 5.18a is an example of a low $[VZHE\text{-}039]_0$ (0.3 mM). c_p rapidly decreased from time zero with a concurrent increase of HbA-AEH adduct. With time, HbA-AEH adduct concentrations surpassed c_p and achieved equilibrium within an hour, indicating rapid RBC uptake and subsequent binding to HbA.

Figure 5.18b is an example of a high $[VZHE\text{-}039]_0$ (7.8 mM). Both c_p and HbA-AEH adduct concentrations slowly increased until 5 hrs, indicating dissolution-rate limitations. In the ascending portion, VZHE-039 was dissolving into plasma and penetrating into RBC to bind Hb. After 5 hrs, c_p and HbA-AEH adduct concentrations achieved their plateaus, indicating that HbA binding achieved equilibrium, as the dissolution and distribution processes were completed, and VZHE-039 concentrations in both plasma and RBC remained constant.

Disposition of VZHE-039 at equilibrium was assessed across $[VZHE\text{-}039]_0$ concentrations (Figure 5.19). c_p increased at lower $[VZHE\text{-}39]_0$ and achieved a plateau at around 2 mM. After plateauing, c_p increased again and surpassed HbA-AEH adduct concentrations because of saturation of HbA binding sites, while the extra VZHE-039 remained in plasma. When $[VZHE\text{-}039]_0$ concentrations were lower than the maximal HbA binding capacity, c_p was lower than HbA-AEH adduct concentrations, indicating

extensive RBC partitioning, where most VZHE-039 was cleared from plasma and distributed into RBC to bind to HbA.

Figure 5.18. Time-dependent VZHE-039 disposition in plasma and RBC for low and high [VZHE-039]$_0$ (Figure a, 0.3 mM; Figure b, 7.8 mM). Smooth lines connected the experimental data (symbols) for visual inspection.

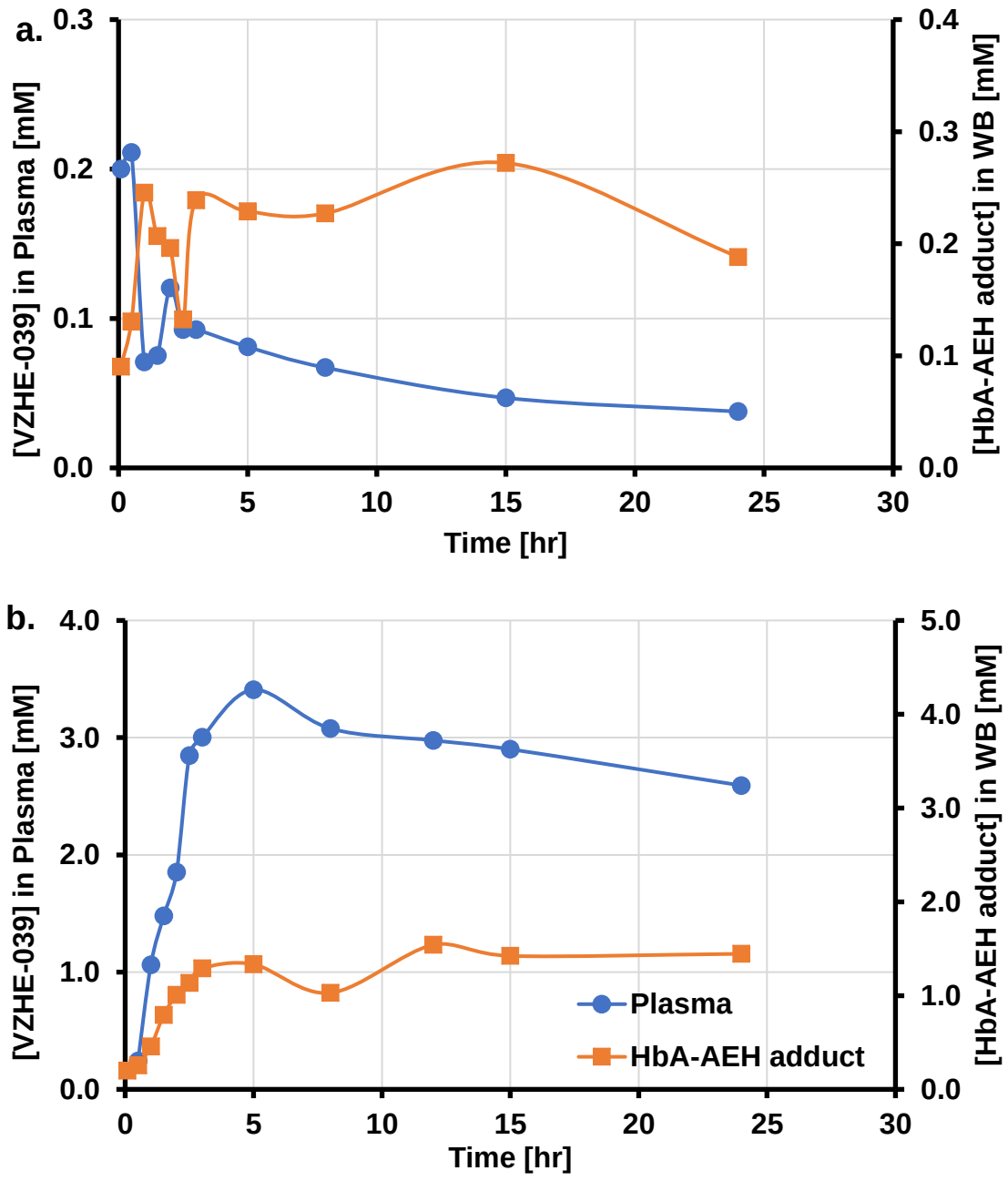

Figure 5.19. Disposition of VZHE-039 in plasma and RBC at equilibrium (at 24 hrs). The sigmoidal B_{max}-model (lines) were fit to HbA-AEH adduct in WB. Smooth dashed lines connected VZHE-039 in plasma for visual inspection.

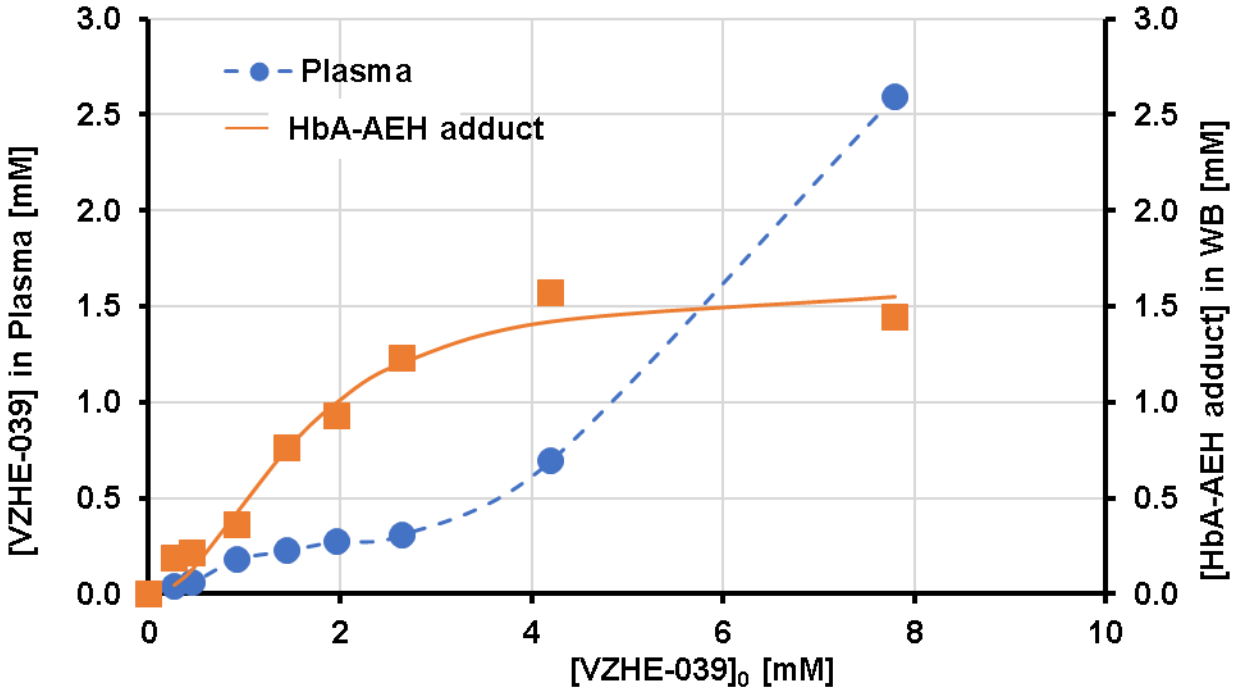

5.3.3 WB Disposition of 5-HMF

5.3.3.1 NCA Analysis of HbA-AEH adduct – t Profile

HbA-AEH adduct concentrations of 5-HMF in WB increased from time zero, peaked around 1.5 hrs and declined below eLOQ by 24 hrs (Figure 5.22). For the lowest $[5\text{-HMF}]_0$ (0.5 mM), HbA-AEH adduct was not detectable after 4 hrs.

To assess dose-proportionality using all $[5\text{-HMF}]_0$ (0.5 – 5 mM), $AUC_{0\text{-}4}^{adduct}$ were calculated. $AUC_{0\text{-}4}^{adduct}$ increased less than proportionally with $[5\text{-HMF}]_0$, described by an exponent from the power model fit of 0.73, i.e., less than 1 (Figure 5.20). AUC is a metric that describes the extent of HbA-AEH adduct formation in WB. c_{max} is a hybrid metric, describing both extent and rate of HbA-AEH adduct formation. c_{max} increased less than proportionally with $[5\text{-HMF}]_0$, and the proportionality constant was almost identical to the proportionality constant of $AUC_{0\text{-}4}^{adduct}$, indicating this nonlinearity of HbA-AEH adduct in WB caused by the extent of HbA-AEH adduct, rather than its rate (Figure 5.20).

Figure 5.20. Dose-proportionality assessment for HbA-AEH adduct of 5-HMF in WB. A power equation (dotted line) is fitted to the experimental data (symbols).

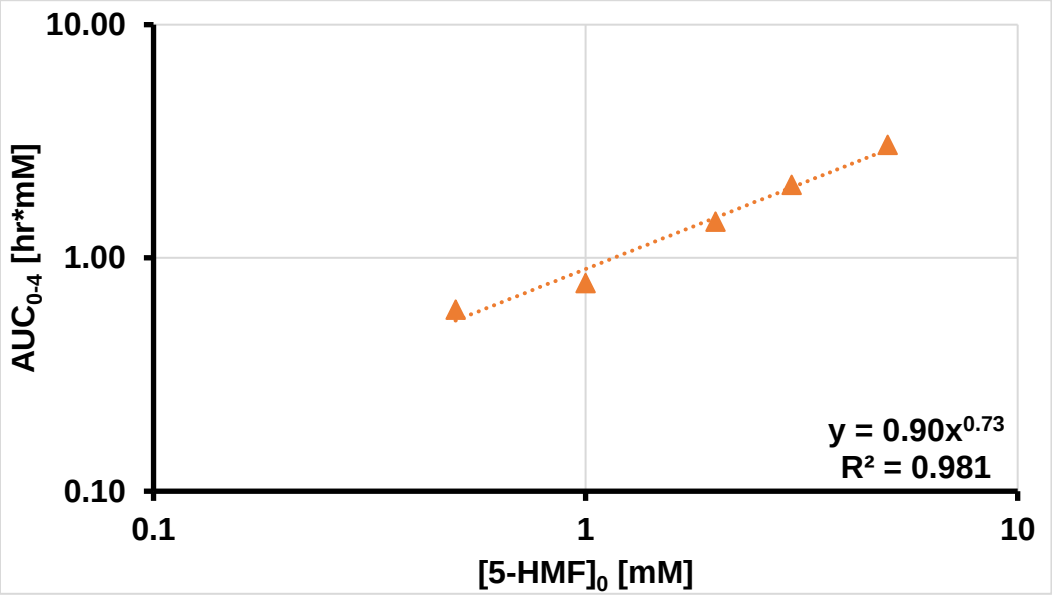

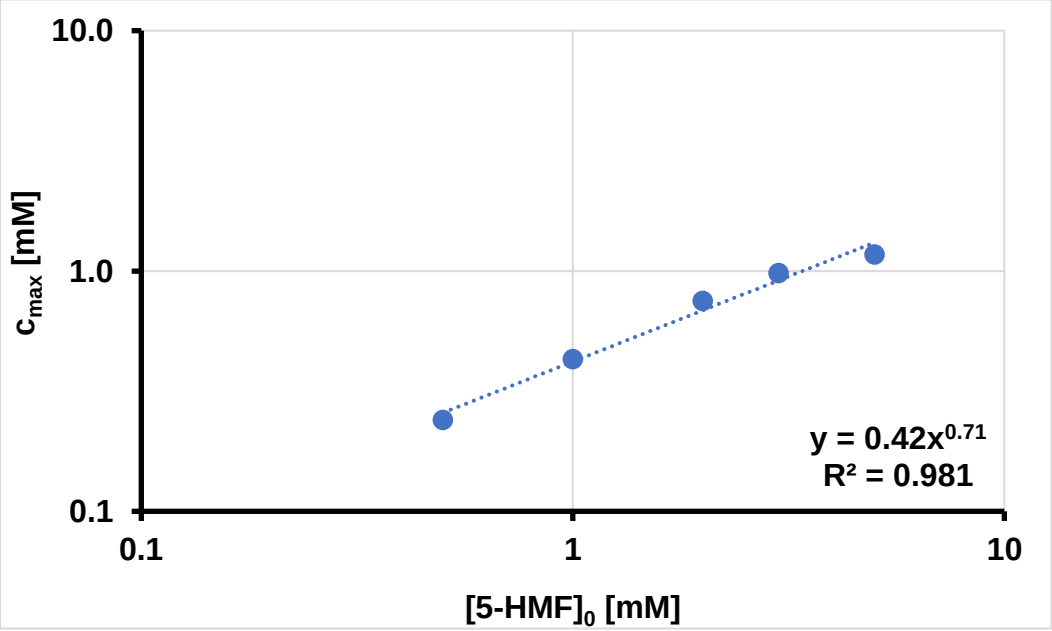

5.3.3.2 Apparent SS Concentration- and Time-dependency of HbA-AEH Adduct Formation in WB

5.3.3.2.1 Apparent SS Concentration-Dependency of HbA-AEH Adduct Formation in WB

Due to the intra-RBC metabolism of 5-HMF, equilibrium cannot be achieved in WB. Thus, the **apparent** SS binding affinity K_D' was estimated at t_{max} (1.5 hrs). In the previous 5-HMF binding studies in HbA solution (as discussed in Chapter 3), equilibrium was achieved at high $[5\text{-HMF}]_0$ (4 mM) relative to K_D (0.37 mM). In WB, saturation is expected to be achieved as well with higher $[5\text{-HMF}]_0$ (>5 mM). Therefore, for comparison sake, B_{max} was fixed to 2.0 mM, i.e., $[HbA]_0$ to mimic saturable conditions. The sigmoidal-B_{max}-model fitted the concentration-dependent experimental well with an r^2 value of 0.999. The Hill coefficient (n = 1.2 (7%)) was almost identical to the point estimate in HbA solution (n = 1.1 (36%)). However, the apparent binding affinity (K_D' = 3.0 (4%)) in WB was 8-fold lower than the binding affinity in HbA solution (Figure 5.21), as a result of rapid intra-RBC metabolism within 1.5 hrs, reducing intra-RBC 5-HMF concentrations available for HbA binding.

Figure 5.21. Apparent SS concentration-dependency HbA-AEH adduct of 5-HMF in WB and the extrapolation (dashed line) from HbA solution. A sigmoidal B_{max}-model (solid line) was fit to experimental data in WB (symbols).

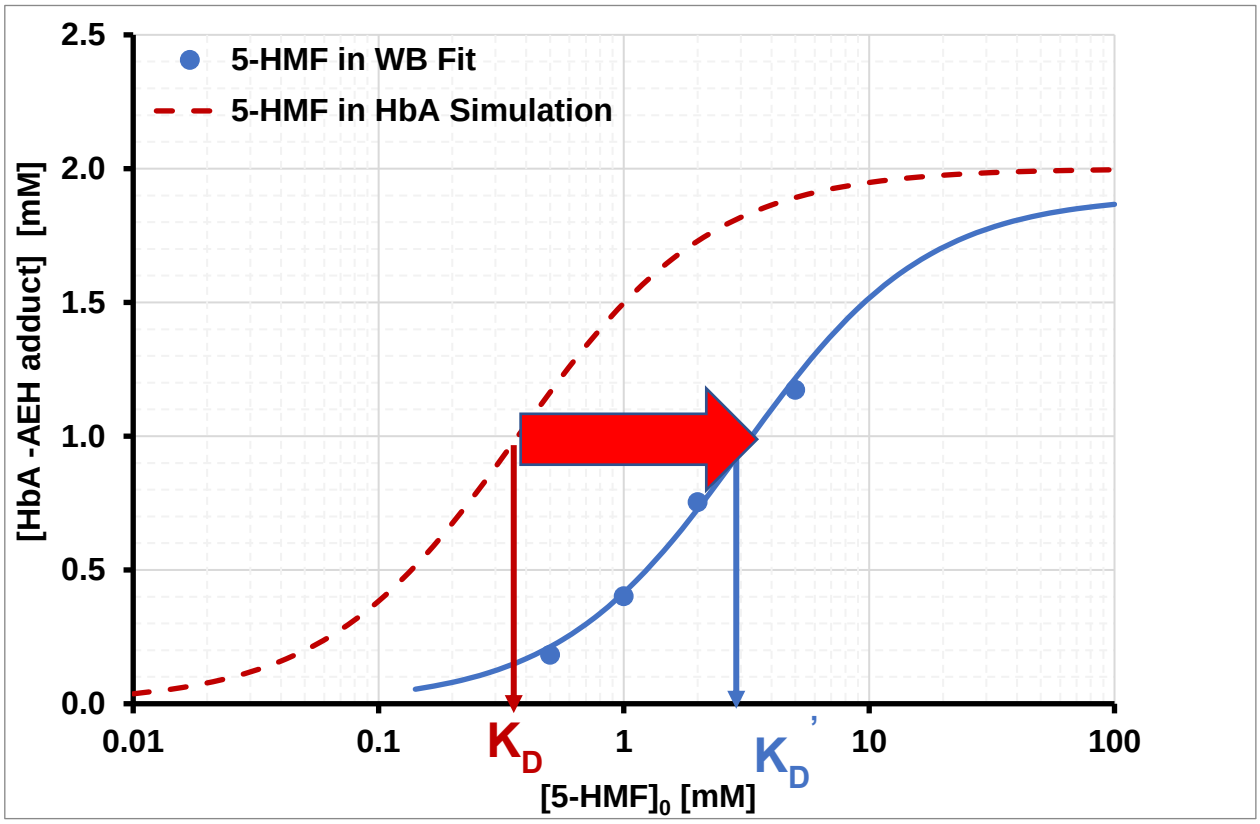

5.3.3.2.2 Time-dependency of HbA-AEH Adduct Formation in WB

Across the studied $[5\text{-HMF}]_0$ in WB, HbA-AEH adduct concentrations increased from time zero, peaked at 1.5 hrs and decreased below eLOQ at 24hrs (Figure 5.10). Unlike the time-dependent profile of 5-HMF in WB, HbA-AEH adduct concentrations were sustained in HbA solution at least for 24 hrs. Intra-RBC metabolism is the likely reason behind this major difference in time-dependency of HbA-AEH adduct profiles. 5-HMF is a substrate of ALDH enzyme, present in RBC but not in HbA solution. The simple metabolism kinetic binding model captured the overall HbA-AEH adduct changing trend with time. Goodness-of-fit of the simple metabolism kinetic binding model used in WB is less optimal than the simple kinetic binding model used for 5-HMF in HbA solution, with a smaller r^2, larger COV and high correlation of k_{on}' and k_{off}' estimates (Table 5.8).

Point estimates of k_{on}' and k_{off}' from WB are 15 – 20%, similar to k_{on} and k_{off} estimated from HbA solution, resulting in about 30% estimate of similar kinetic binding affinity ($K_D^{kinetic'} = k_{on} / k_{off}$) (Table 5.8). This suggests that the primary Hb binding mechanism for 5-HMF is not affected by WB constituents. However, due to much higher initial HbA concentrations ($[HbA]_0$ = 2 mM) in WB, the association rate in WB was significantly faster than observed with the low $[HbA]_0$ (0.2 mM) in HbA solution. The apparent half-lives of HbA association and metabolism in were less than hour in WB, while in HbA solution, the association half-life was longer than 7 hrs. On the other hand, the dissociation rate is independent of $[HbA]_0$, and therefore is almost identical (~ 6hrs) between WB and HbA solution.

In HbA solution, both association and dissociation processes are equally slow (Table 5.8). However, in WB, the dissociation process has become the rate-limiting step due to rapid metabolism in RBC and the increased $[HbA]_0$ speeding up the association rate.

k_{met}' was introduced to account for and characterize the intra-RBC metabolism of 5-HMF in WB. Final fit from the simple metabolism binding model showed a large COV (48%) for k_{met}', indicating less confidence in the precision of the PE. In addition, due to lack of experimental reference for k_{met}', and high correlation among model parameters, assessing the stability and sensitivity of the parameter k_{met}' is necessary for better validation of this simple metabolism kinetic binding model (discussed in the following section 3).

Figure 5.22. Time -dependency of HbA-AEH adduct formation for 5-HMF in WB. The simple metabolism kinetic binding model (lines) was fit to the experimental data (symbols).

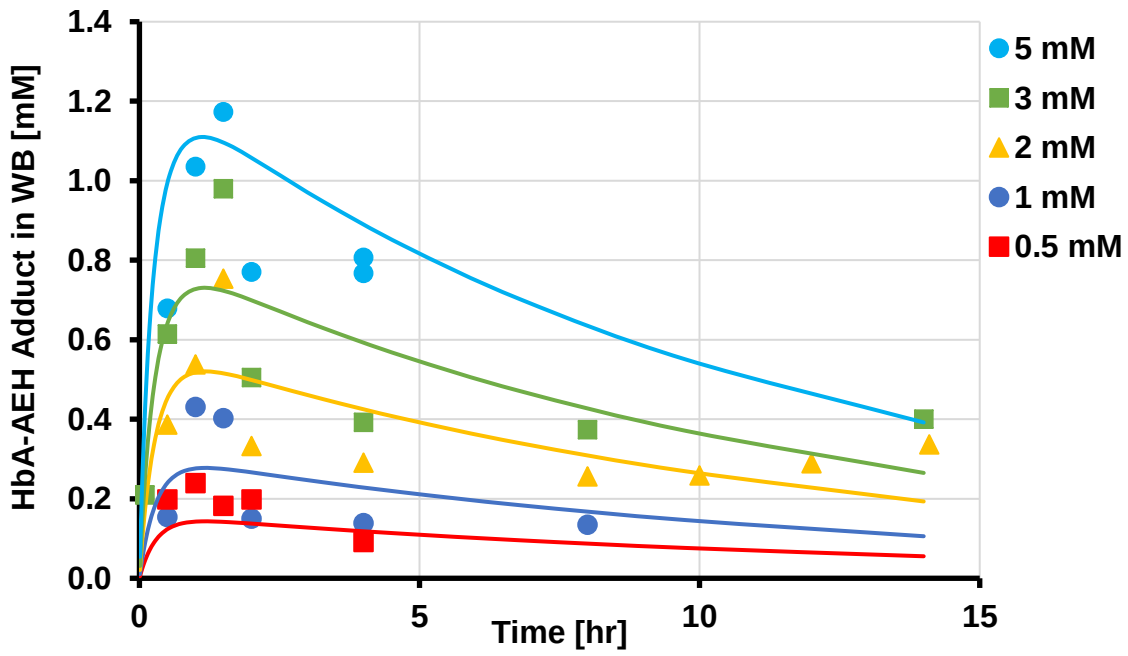

Table 5.8. Final parameter estimates of time-dependency of HbA-AEH adduct formation for 5-HMF in WB and in HbA solution, using the simple metabolism kinetic binding model and the simple kinetic binding model, respectively. The primary rate constants are presented as PE with (COV).

5-HMF		HbA Solution	WB
$[HbA]_0$	[mM]	0.2	2.0
r^2		0.957	0.918
Correlation between k_{on} and k_{off}		0.946	0.750
k_{on}' or k_{on}	$[mM^{-1}*hr^{-1}]$	0.46 (11%)	0.56 (38%)
k_{off}' or k_{off}	$[hr^{-1}]$	0.13 (25%)	0.11 (33%)
k_{met}'	$[hr^{-1}]$	0	2.2 (48%)
K_D' or K_D	[mM]	**0.28**	**0.20**
$t_{1/2}^{metabolism}$	[hr]	NA	0.32
$t_{1/2}^{association}$	[hr]	7.5	0.65
$t_{1/2}^{dissociation}$	[hr]	5.3	6.3

5.3.3.2.3 Post-hoc sensitivity analyses

The reference scenario (Figure 5.23) is based on the final point estimates from the simple metabolism kinetic binding model of 5-HMF in WB.

In this reference scenario, HbA-AEH adduct is rapidly formed in RBC and peaks at 0.54 mM at 1.2 hrs, followed by a slower and parallel decline of 5-HMF concentration in RBC. The terminal half-life is 9 hr (Figure 5.23). After 24 hrs, the metabolic reaction, i.e., metabolic conversion of 5-HMF to HMFA, is close to completion, with metabolite/HMFA concentrations close to 2 mM, i.e., $[5\text{-HMF}]_0$. HbA-AEH adduct and 5-HMF concentrations are close to zero at 24 hrs. Similar results were also observed in the experimental data, where HbA-AEH adduct peaked at 0.75 mM after 1.5 hrs and declined to zero by 24 hrs (Table 5.9).

When k_{on}' or k_{off}' was changed within their LL and UL, K_D' (which is equal to k_{off}' divided by k_{on}') was changed accordingly. On the other hand, k_{met}' does not influence the binding affinity (K_D') of 5-HMF to HbA.

Figure 5.23. Reference case: Simulation of the disposition of 5-HMF (2 mM) in WB ($[HbA]_0$ of 2.0 mM) from the simple metabolism kinetic binding model using the final PE (k_{on}' =0.56 mM^{-1} hr^{-1}, k_{off}' =0.11 hr^{-1}, k_{met}' =2.2 hr^{-1}, K_D' = 0.2 mM)

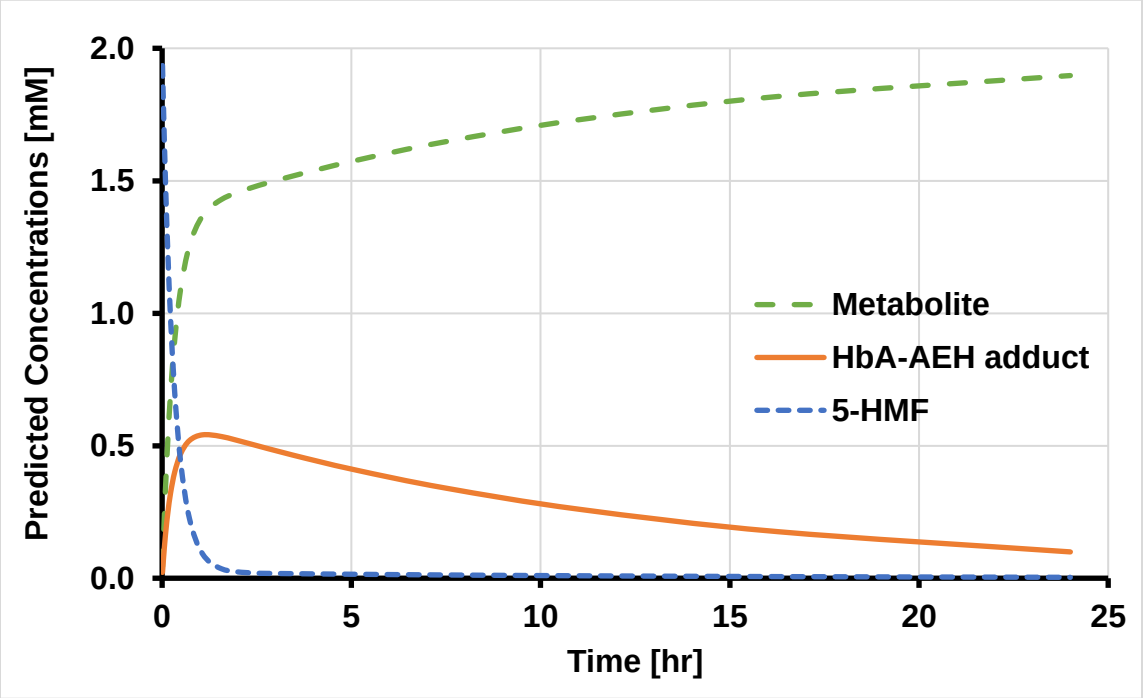

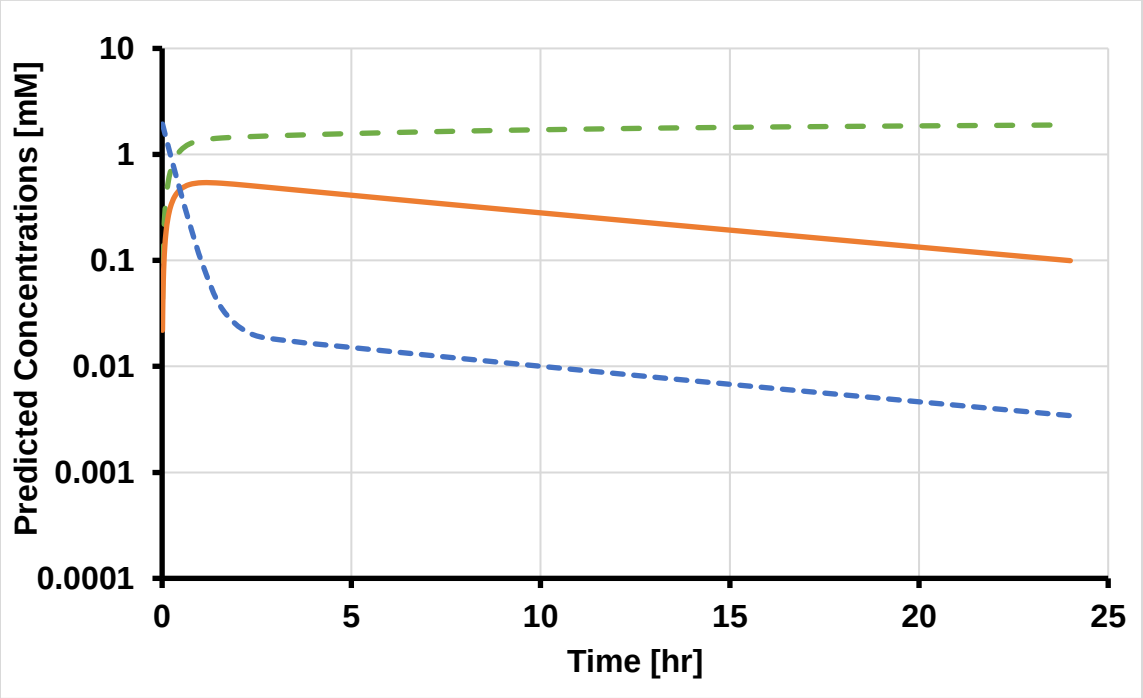

Table 5.9. Assessment of the outcome metrics for HbA-AEH adduct in RBC from sensitivity analysis of the simple metabolism kinetic binding model. Abbreviations: LL, lower limit; ST, simulation from final point estimates; EX, experimental observation; UL, upper limit; FC, fold-change.

	AUC_∞ [mM*hr]					$t_{1/2}$ terminal [hr]				
	LL	ST (AUC_{0-14})	EX (AUC_{0-14})	UL	FC	LL	ST	EX	UL	FC
k_{on}'	2.2	5.0	4.5	26	***12***	7.1	9.4	17	16	*2.2*
k_{off}'	31	5.0	4.5	2.0	***-16***	35	9.4	17	2.5	***-14***
k_{met}'	27	5.0	4.5	2.2	***-12***	16	9.4	17	7.1	*-2.3*

	t_{max} [hr]					c_{max} [mM]				
	LL	ST	EX	UL	FC	LL	ST	EX	UL	FC
k_{on}'	1.4	1.2	1.5	0.88	*-0.65*	0.19	0.54	0.75	1.1	***5.8***
k_{off}'	1.6	1.2	1.5	0.8	*-2.1*	0.58	0.54	0.75	0.46	*-1.3*
k_{met}'	2.4	1.2	1.5	0.46	***-5.2***	0.98	0.54	0.75	0.20	***-4.8***

Table 5.10. Assessment of the outcome metrics of 5-HMF in RBC from sensitivity analysis of the simple metabolism kinetic binding model.

	AUC_∞ [mM*hr]				$t_{1/2}$ terminal [hr]			
	LL	ST	UL	FC	LL	ST	UL	FC
k_{on}'	0.9	0.9	0.9	1.0	7.1	9.1	12.5	1.8
k_{off}'	0.9	0.9	0.9	1.0	33	9.1	2.5	**-13**
k_{met}'	3.6	0.9	0.2	**-16**	12	9.1	7.1	-1.7

Scenario 1 shows model predictions with the change of k_{on}' only (Figures 5.24 and 5.25). When k_{on}' is **decreased**, the association rate (binding to HbA) is reduced (Figure 5.24). Therefore, the initial decrease of 5-HMF is shallower on log-scale, where HbA-AEH adduct peaks slighter later (at 1.4 hr) with 5.8-fold lower concentrations than k_{on}' at UL (Table 5.9). AUC_{∞}^{adduct} is dramatically decreased (12-fold), because the binding affinity is decreased, where less HbA-AEH adduct is formed and more of free 5-HMF is available for the rapid metabolism in RBC. The reaction is complete at 24 hrs, where all 5-HMF is converted to metabolite (2 mM). When k_{on}' is **increased**, more HbA-AEH adduct is formed due to enhanced binding affinity (Figure 5.25). HbA-AEH adduct peaks earlier, and less 5-HMF is available to undergo metabolism. The terminal slopes of HbA-AEH adduct and 5-HMF are shallower and the (metabolic) reaction is not completed after 24 hrs. $AUC_{\infty}^{5\text{-}HMF}$ for both cases (increase or decrease of k_{on}') remains the same, because binding to Hb is reversible and the irreversible removal of 5-HMF only depends on metabolism (k_{met}') (Table 5.10). Overall, c_{max} and AUC_{∞}^{adduct} are quite sensitive to the change of k_{on}'.

Figure 5.24. Scenario 1a: Simulation of the disposition of 5-HMF (2 mM) in WB ($[HbA]_0$ of 2.0 mM) from the simple metabolism kinetic binding model by changing k_{on}' to 0.14 mM^{-1} hr^{-1} (K_D' = 0.79 mM).

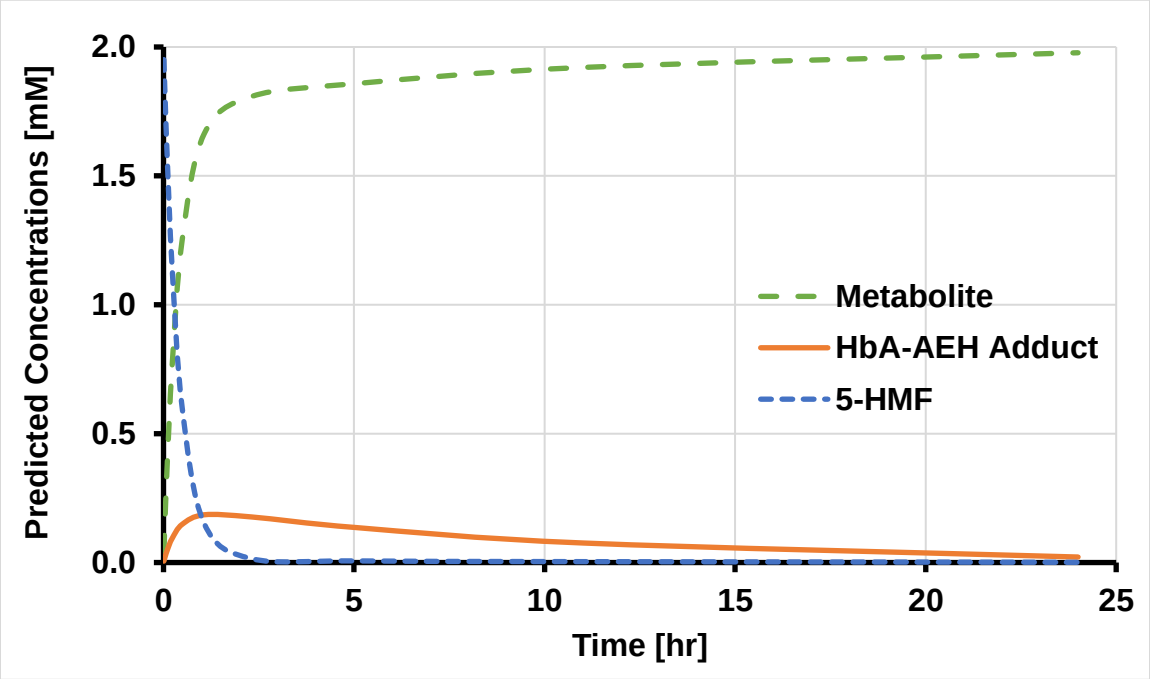

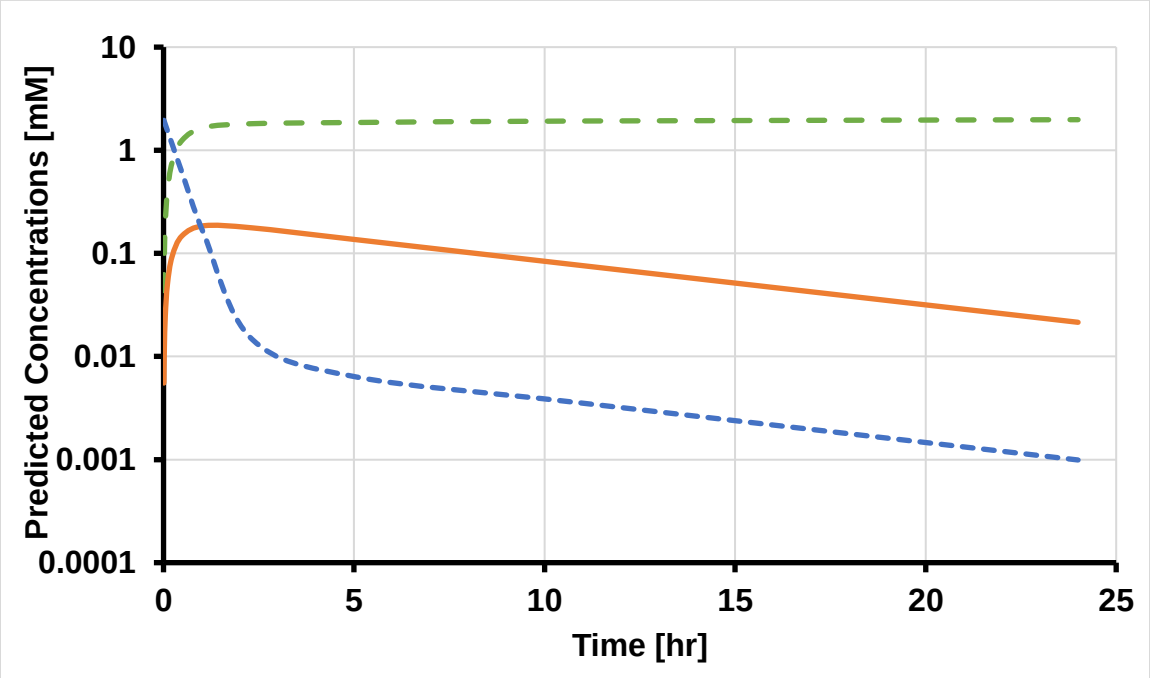

Figure 5.25. Scenario 1b: Simulation of the disposition of 5-HMF (2 mM) in WB ($[HbA]_0$ of 2.0 mM) from the simple metabolism kinetic binding model by changing k_{on}' to 2.24 mM^{-1} hr^{-1} (K_D' = 0.05 mM).

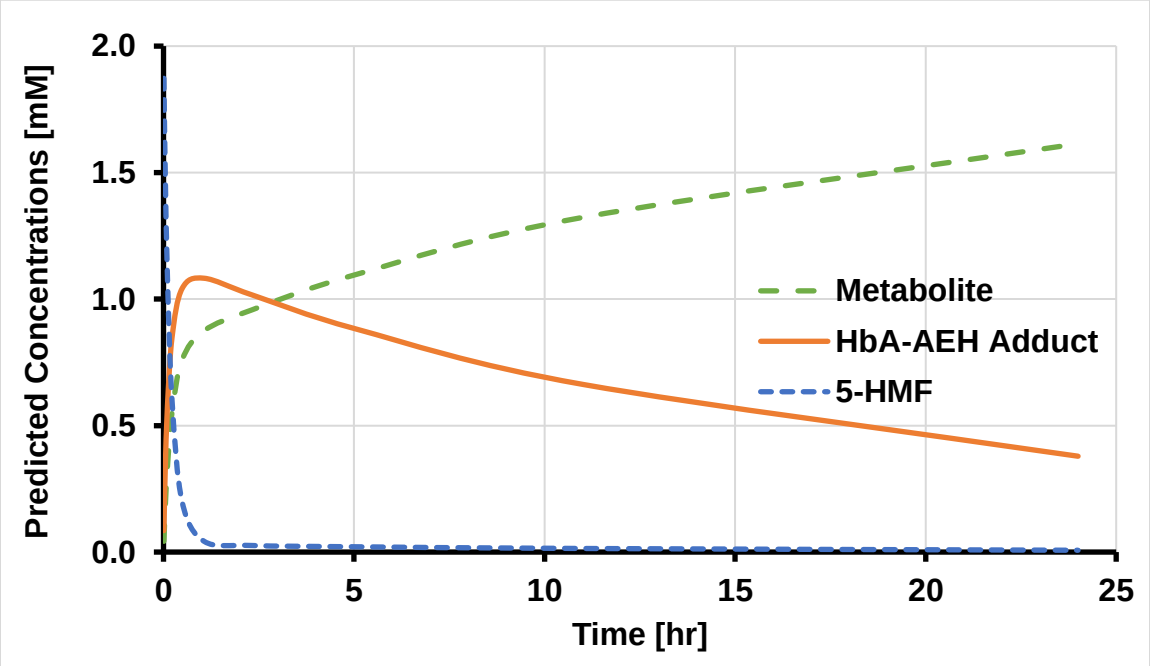

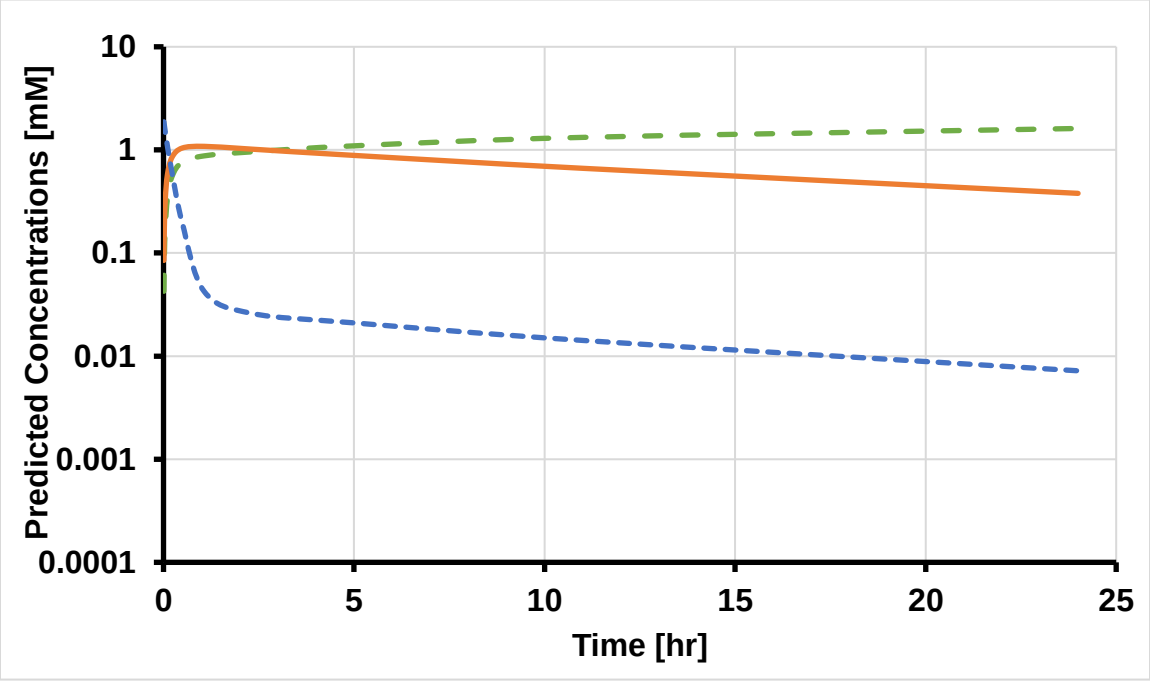

Scenario 2 are the model predictions with the change of k_{off}' only (Figure 5.26 and 5.27). Dissociation from HbA is the rate-limiting step for all simulated scenarios, where k_{off}' is the smallest among k_{on}'*HbA_0 and k_{met}'. Thus, the terminal slopes of HbA-AEH adduct and 5-HMF are predominantly driven by k_{off}' and are parallel on a log-scale in all cases. When k_{off}' is **decreased**, the dissociation rate (5-HMF release from HbA) is reduced (Figure 5.26). The terminal decline of HbA-AEH adduct and 5-HMF are significantly slower, characterized by 14-fold longer $t_{1/2}^{terminal}$ than it is of k_{off}' at upper limit (UL), and the (metabolic) reaction is incomplete at 24 hrs (Table 5.9 and 5.10). HbA-AEH adduct peaks slightly later (at 1.6 hr) with a small increase in peak level (at 0.58 mM). AUC_{∞}^{adduct} is dramatically increased (16-fold) due to the 16-fold increase in binding affinity. Vice versa, when k_{off}' is **increased**, less HbA-AEH adduct is formed, more 5-HMF becomes available for metabolism, and AUC_{∞}^{adduct} is decreases 16-fold (Figure 5.27). Dissociation from HbA is faster, where 5-HMF undergoes more rapid metabolism. The terminal slopes of HbA-AEH adduct and 5-HMF are steeper, and the (metabolic) reaction is completed at 24 hrs. Overall, $t_{1/2}^{terminal}$ and AUC_{∞}^{adduct} are quite sensitive to the change of k_{off}'.

Figure 5.26. Scenario 2a: Simulation of the disposition of 5-HMF (2 mM) in WB ($[HbA]_0$ of 2.0 mM) from the simple metabolism kinetic binding model by changing k_{off}' to 0.03 hr^{-1} (K_D' = 0.05 mM)

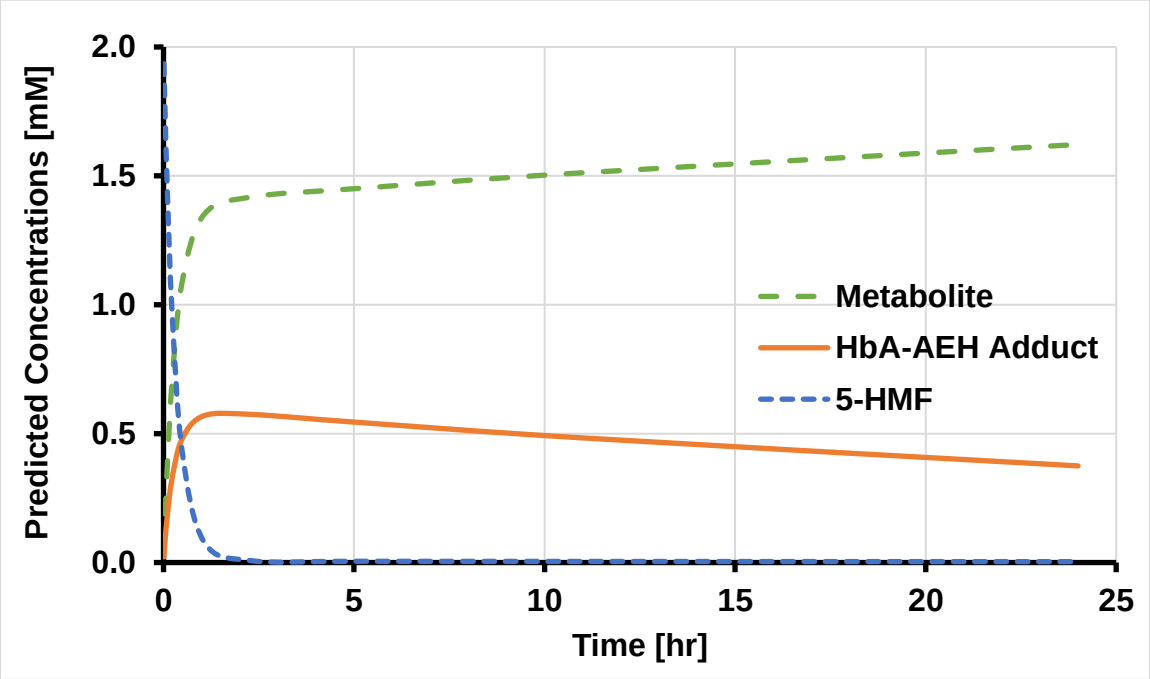

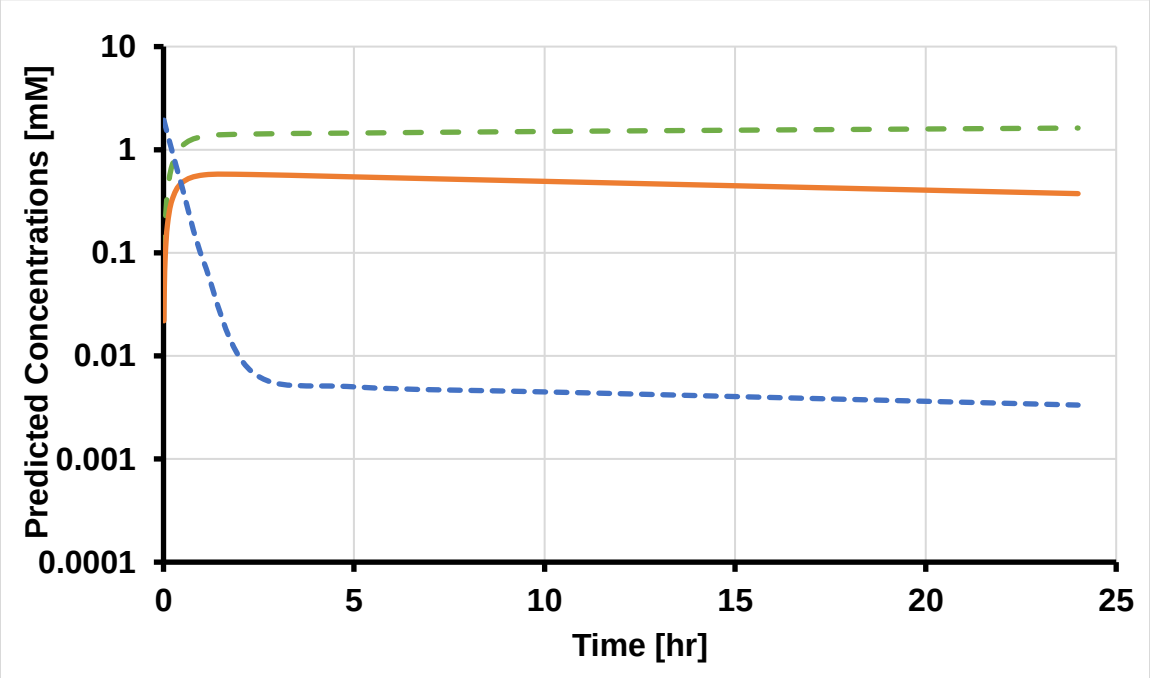

Figure 5.27. Scenario 2b: Simulation of the disposition of 5-HMF (2 mM) in WB ($[HbA]_0$ of 2.0 mM) from the simple metabolism kinetic binding model by changing k_{off}' to 0.44 hr^{-1} (K_D' = 0.79 mM)

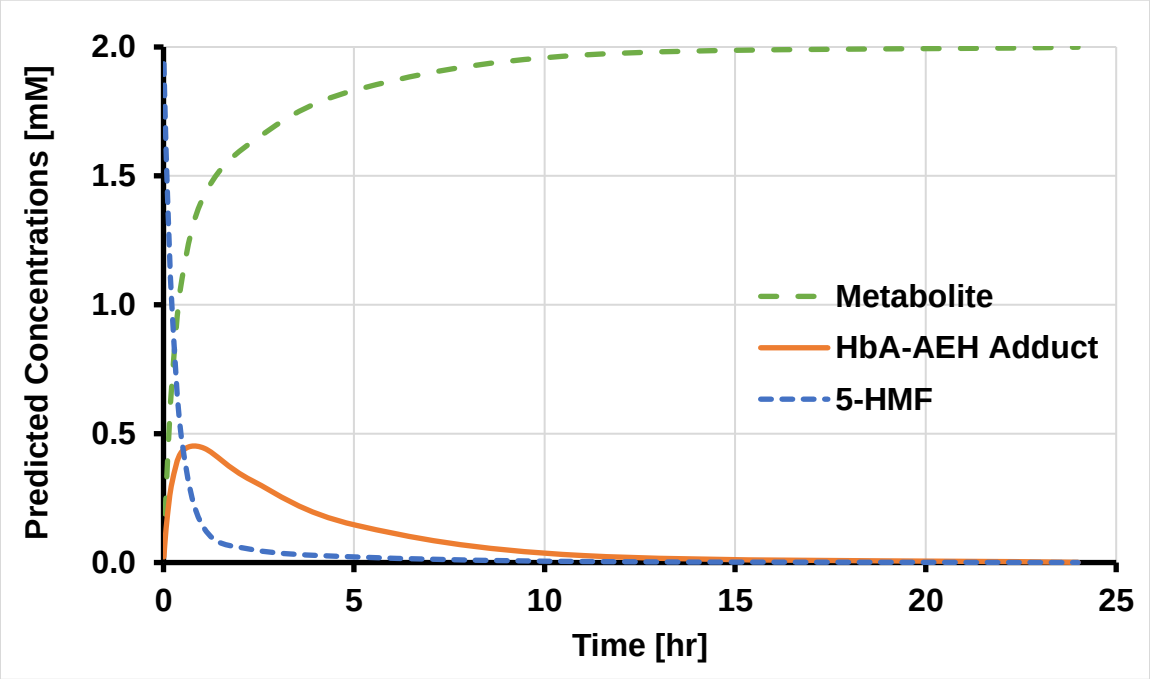

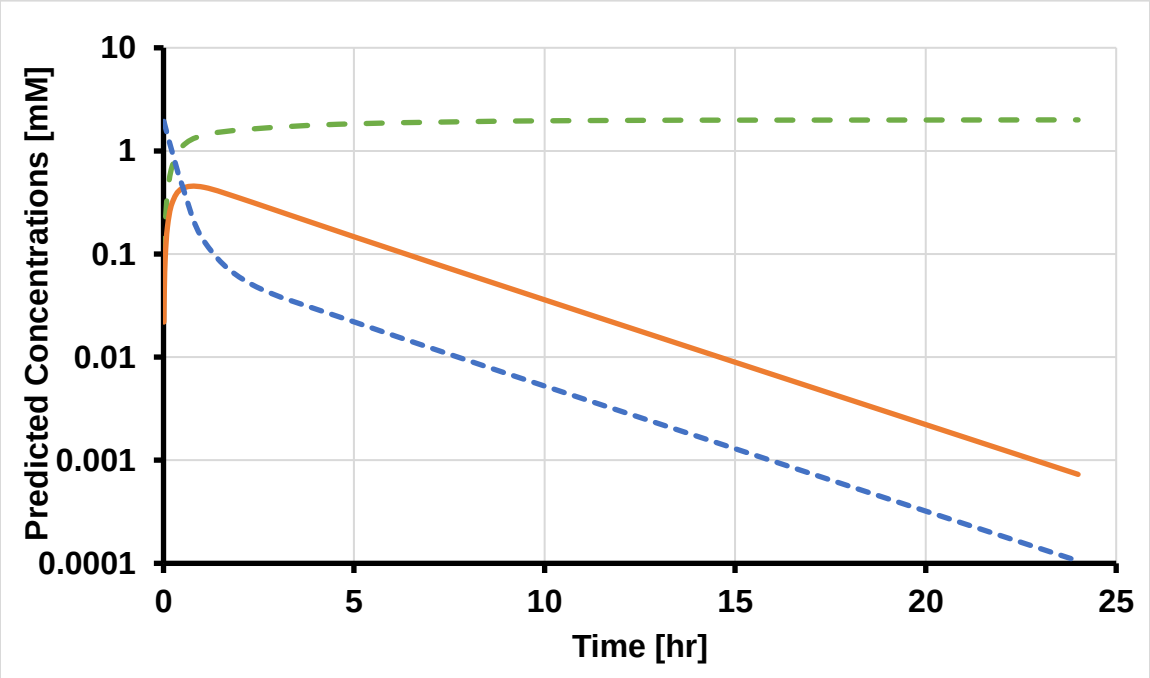

Scenario 3 includes the model predictions with a change of k_{met} only (Figure 5.28 and 5.29). When the ALDH activity is reduced, k_{met}' is **decreased**, resulting in a slower formation of metabolite from 5-HMF (Figure 5.28). Therefore, more HbA-AEH adduct is formed and remains in WB. The reaction is incomplete at 24 hrs. Although HbA binding affinity remains the same, AUC_{∞}^{adduct} is dramatically increased (by 12-fold) due to the slow metabolism in RBC. $AUC_{\infty}^{5\text{-}HMF}$ is 16-fold decreased when k_{met}' is increased 16-fold, because the metabolism of 5-HMF is an irreversible process. The initial decrease of 5-HMF is shallower on log-scale, but the terminal decrease of HbA-AEH adduct and 5-HMF are only slightly slower due to the dissociation from HbA remains as the rate-limiting step. When k_{met}' is **increased**, less HbA-AEH adduct is formed since 5-HMF is rapidly metabolized by ALDH (Figure 5.29). HbA-AEH adduct peaks much earlier (0.46 hrs) compared to k_{met}' at LL (2.4 hrs), and to a lower level (0.20 mM compared to 0.98 mM). Terminal slopes of HbA-AEH adduct and 5-HMF are steeper and the reaction is complete at 24 hrs. Overall, AUC_{∞}^{adduct} and $AUC_{\infty}^{5\text{-}HMF}$, as well as c_{max} and t_{max} are sensitive to the change of k_{met}'.

Figure 5.28. Scenario 3a: Simulation of the disposition of 5-HMF (2 mM) in WB ($[HbA]_0$ of 2.0 mM) from the simple metabolism kinetic binding model by changing k_{met}' to 0.55 hr^{-1}(K_D' = 0.20 mM)

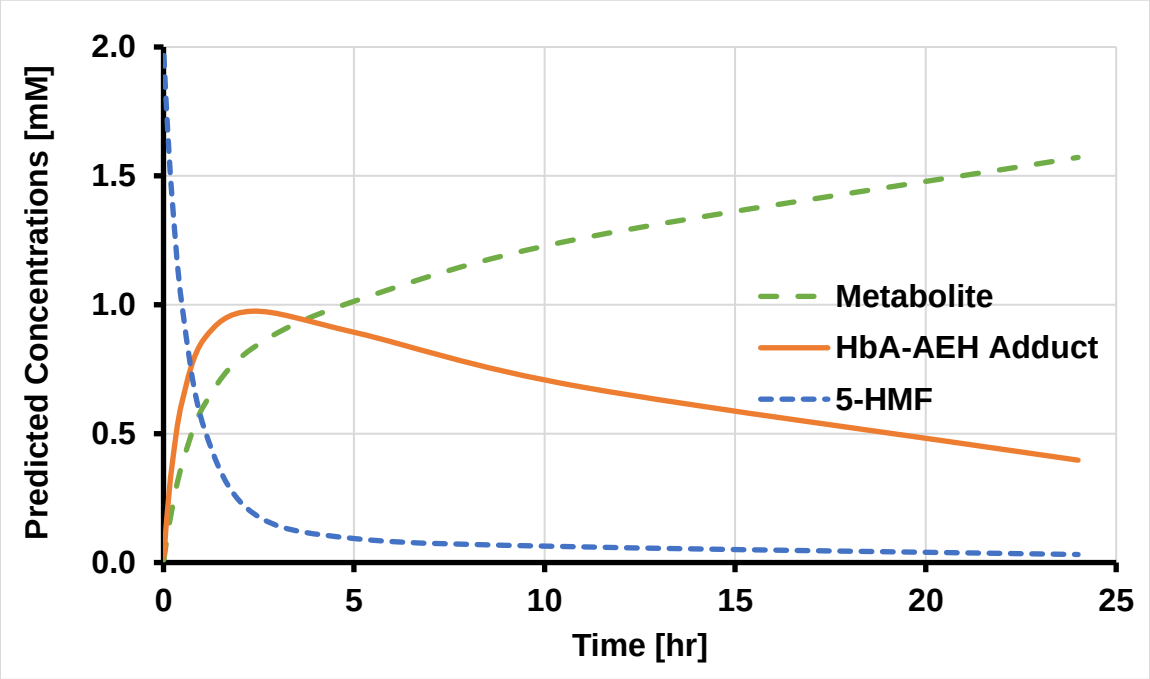

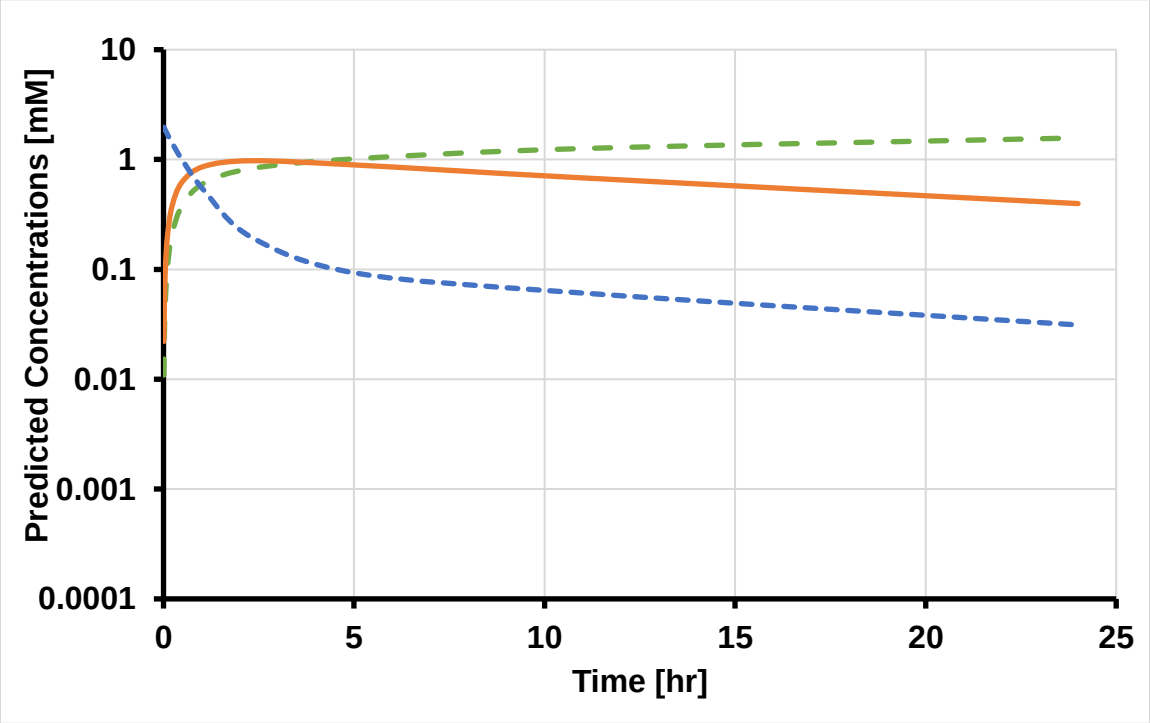

Figure 5.29. Scenario 3b: Simulation of the disposition of 5-HMF (2 mM) in WB ($[HbA]_0$ of 2.0 mM) from the simple metabolism kinetic binding model by changing k_{met}' to 8.8 hr^{-1}(K_D' = 0.20 mM)

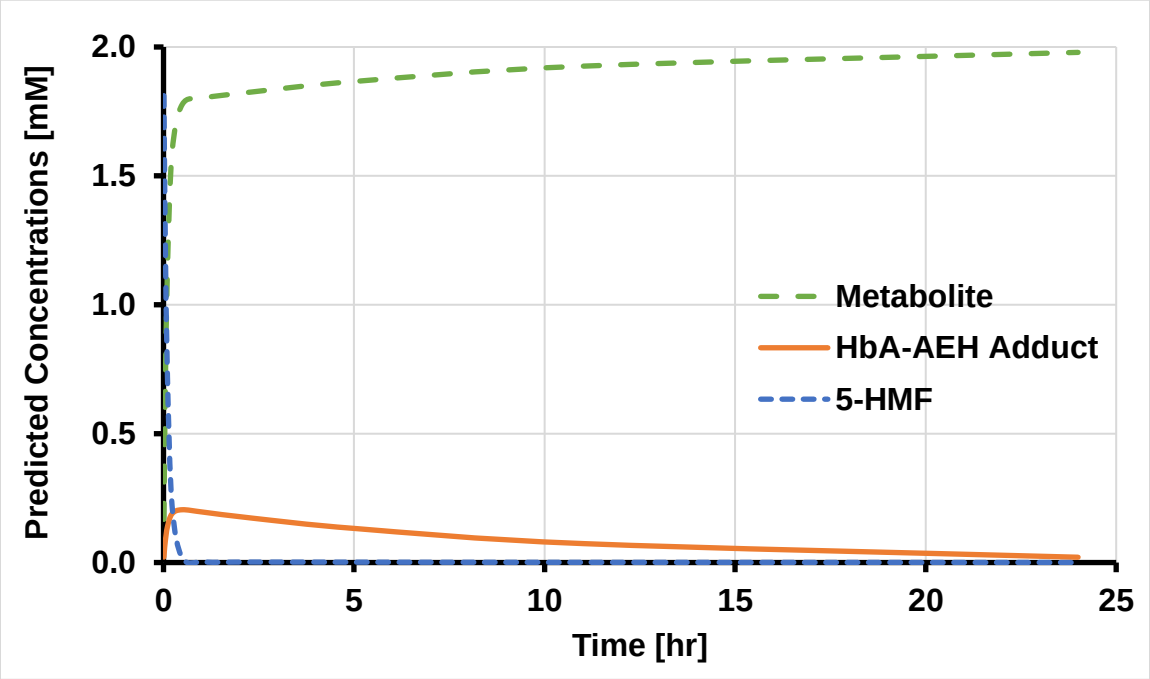

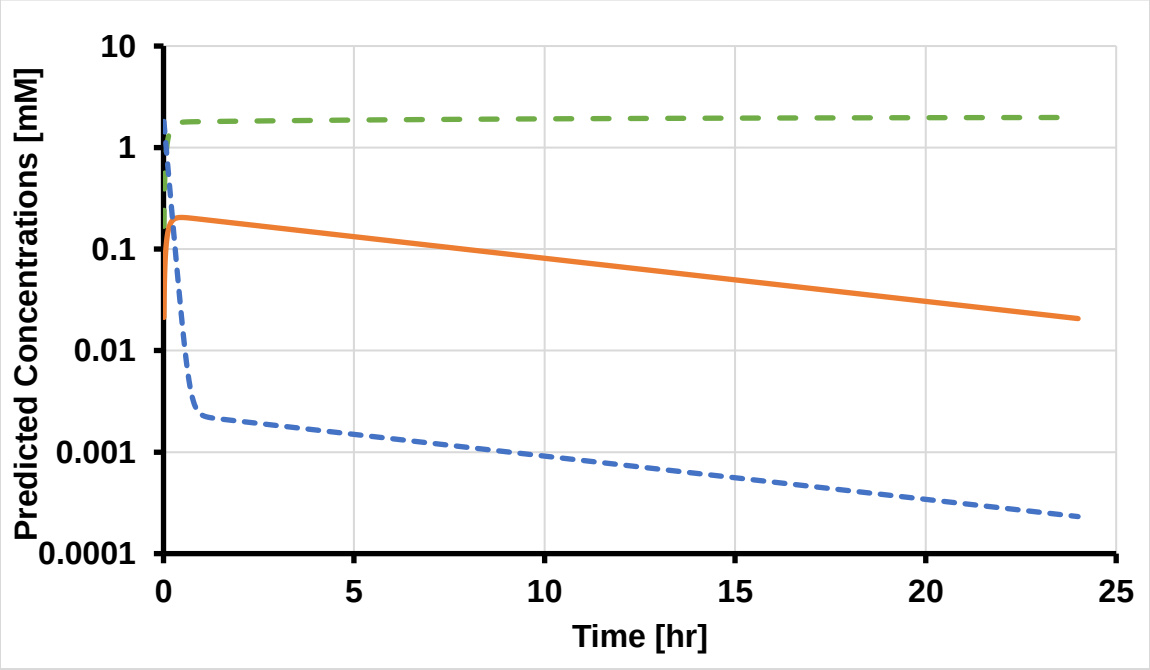

Table 5.9 and 5.10 summarize the results for sensitive analyses. The exposure of 5-HMF in RBC ($AUC_{\infty}^{5\text{-}HMF}$) remains the same with the changes of k_{on}' and k_{off}', but sensitive to k_{met}'. The exposure of HbA-AEH adduct in RBC (AUC_{∞}^{adduct}), which drives the pharmacological effect, is greatly affected by all parameters, i.e., k_{on}', k_{off}', and k_{met}'. The estimate for k_{on}' and k_{met}' has an effect on peak of HbA-AEH adduct (c_{max}), because the formation of HbA-AEH adduct competes with metabolism by ALDH. k_{off}' determines the duration of HbA-AEH adduct, since the dissociation from HbA is the rate-limiting step. Onset time (t_{max}) is not sensitive to either k_{on}' nor k_{off}', but affected by k_{met}'. The experimental $AUC_{0\text{-}14}^{adduct}$, c_{max} and t_{max} are similar to the simulation results using the final point estimates, which is a validation of the sensitivity analysis for the simple metabolism kinetic binding model (Table 5.9). $t_{1/2}^{terminal}$ was determined by the rate-limiting step, which characterized by k_{off}' for these simulated scenarios. The duration of the circulating HbA-AEH adduct and 5-HMF are similar to their reference scenarios, as k_{off}' remains the same as the rate-limiting step.

For this simple metabolism kinetic binding model, most metrics of HbA adduct exposure (including onset, duration and extent) and (intra-RBC) 5-HMF exposure are very sensitive to changes in k_{met}'. In addition, there is no external quantitative experimental reference for k_{met}', which further decreases the reliability of k_{met}' estimate. For k_{on}' and k_{off}', though high correlation and less precision (large COV) were observed for the final point estimates; both of them were similar to the external references from 5-HMF binding study in HbA solution (Table 5.8). In conclusion, k_{on}' and k_{off}' estimates from the final simple metabolism kinetic binding model of 5-HMF in WB are reliable, whereas k_{met}' is less reliable.

5.4 Discussion and Conclusions

This chapter presents studies to gain insight into *in-vitro* disposition of 5-HMF and VZHE-039 in WB, and compare the results with those obtained under similar studies conducted in HbA solution (discussed in Chapter 3) in order to explore how blood components may affect formation of HbA-AEH adduct.

For VZHE-039, no evidence of intra-RBC metabolism was observed, as the HbA-AEH adduct concentrations were sustained in WB for 24 hrs. K_D' estimated from both kinetic and SS concentration-dependent model are similar and were 15- to 20-fold larger than K_D values estimated from HbA solution, primarily due to a dramatic decrease of association rate constant to Hb. High degree of PPB (94%) and/or RBC membrane binding (non-specific binding) are believed to be responsible for the slowdown of overall kinetic binding and lower apparent binding affinity of VZHE-039 in WB, mostly by affecting k_{on}'. Due to its lipophilicity, VZHE-039 is extensively plasma protein ound and expected to bind to RBC membranes as well. These reversible binding processes are competing with its specific binding to Hb via Schiff base. They are NOT expected to irreversibly remove VZHE-039 (as is the case for 5-HMF metabolism inside RBC). Given the dramatic reduction in k_{on}' and K_D' relative to k_{on} and K_D, one or both of these binding processes are of low affinity and high capacity relative to HbA binding. This is supported by a constant, i.e., dose-invariant, and low in-vitro plasma clearance (0.005 mL/min/ 12 mL plasma), seemingly dose-proportional plasma exposures and long plasma $t_{1/2}^{terminal}$ (~20 hr). On the other hand, VZHE-039 is considered as a high affinity and low capacity Hb binder, as reflected by an infra-proportional increase of AUC^{adduct} with $[VZHE\text{-}039]_0$. This saturable Hb binding is essential for VZHE-039 to elicit its

pharmacological effects at its target site, and prolonged persistence in WB may be advantageous *in-vivo*.

For 5-HMF, it quickly binds to HbA, but in its unbound form in RBC, it is rapidly metabolized by ALDH enzyme, leading to a quick onset, short duration and lower extent of action/HbA adduct formation as shown by the irreversible decrease of HbA-AEH adduct and c_p of 5-HMF. The reduction in apparent binding affinity relative to HbA solution results from the rapid intra-RBC metabolism reducing its availability for HbA binding. After incorporating this irreversible removal of 5-HMF by ALDH metabolism by using simple metabolism binding model of 5-HMF, however, the kinetic apparent binding affinity ($K_D^{'kinetic}$=0.28 mm) is similar to K_D (0.20 mM) in HbA. Given its hydrophilic nature, it is not expected to bind to plasma and proteins or RBC membranes in any significant way. Previous studies showed that PPB of 5-HMF and metabolism in plasma are negligible(Parikh, 2013). RBC membrane binding is most likely negligible as well due to the hydrophilicity of 5-HMF (cLogP = 0.4). The final point estimate for k_{on}' in WB is almost identical to the k_{on} in HbA solution, indicating PPB/RBC membrane binding do not hinder 5-HMF transport into RBC and binding to Hb. Using a modified kinetic binding model, incorporating first-order metabolism for 5-HMF, both apparent association and metabolic processes are fast, while the terminal decrease of HbA-AEH adduct is determined by the slow dissociation of 5-HMF from Hb (Table 5.11).

Table 5.11. Summary table of VZHE-039 and 5-HMF disposition in WB.

AEH	WB						Plasma	
	AUC dose-proportionality constant	K_D'	k_{on}'	k_{off}'	k_{met}'	$K_D^{kinetic'}$	AUC dose-proportionality constant	K_m^{app}
		[mM]	[mM^{-1} hr^{-1}]	[hr^{-1}]	[hr^{-1}]	[mM]		[mM]
VZHE-039	0.79	1.5	0.20	0.46	0	2.0	0.93	NA
5-HMF	0.73	3.0	0.56	0.11	2.2	0.20	2.05	0.54

Previous studies have showed that the majority of 5-HMF was cleared from plasma at 10 hrs across $[5\text{-HMF}]_0$ (0.5 – 5 mM)(Parikh, 2013). The plasma clearance, however, decreased from 1.36 mL/min/12 mL plasma to 0.12 mL/min/12 mL plasma as $[5\text{-HMF}]_0$ increased from 0.5 mM to 5 mM(Parikh, 2013). The decreasing plasma clearance results in a supra-proportional increase of $AUC^{5\text{-HMF}}$, characterized by an power model exponent of greater than 1 (Table 5.11). This nonlinear *in-vitro* plasma kinetics of 5-HMF suggest saturable ALDH metabolism and/or saturable Hb binding. As discussed in Chapter 4, 5-HMF undergoes *in-vitro* metabolism in HLC and expected to show similar metabolism in RBC, because of the same isoform of ALDH enzymes in HLC and RBC. Only first-order metabolism was observed in HLC with a k_m larger than 90 mM, the highest studied $[5\text{-HMF}]_0$. In WB maximum $[5\text{-HMF}]_0$ of 5 mM was studied, which is much lower than the estimated k_m. Metabolic clearance by ALDH is expected to be constant within 0.5 – 5 mM of $[5\text{-HMF}]_0$. Previous plasma disposition results showed that the c_p at half-maximal clearance (K_m^{app} = 0.54 mM) was similar to HbA binding affinity of 5-HMF characterized in HbA solution (K_D=0.37 mM), indicating that the

saturable clearance from plasma is due to the saturable Hb binding (Parikh, 2013).

These plasma disposition results match to the current findings from HbA-AEH adduct profiles in WB. AUC^{adduct} of HbA-AEH adduct increased less than proportional to increasing $[5\text{-HMF}]_0$, due to the saturation of Hb binding. Along with the findings from previous c_p-t profile, the current HbA binding properties in WB provide conclusive evidence that the saturable Hb binding lead to the nonlinear plasma disposition of 5-HMF rather than saturable ALDH-mediated metabolism in RBC.

The anti-sickling effect of 5-HMF and VZHE-039 were previously tested by incubating 5-HMF or VZHE-039 in SCD blood for 2 hrs. 2 mM of 5-HMF showed 22% sickling inhibition, whereas VZHE-039 showed ~100% inhibition(Abdulmalik, 2018; Safo & Kato, 2014). After thoroughly studying their HbA binding properties, ALDH-mediated metabolism and WB disposition, we conclude that the different anti-sickling effect of 5-HMF and VZHE-039 in SCD blood is predominantly due to the ALDH-mediated metabolism.

The lower apparent binding affinity of VZHE-039 and 5-HMF in WB may require larger *in-vivo* dose for future drug development than the extrapolation from binding affinity in HbA solution, to achieve similar HbA modification level for desirable anti-sickling effect. Though both VZHE-039 and 5-HMF showed similar apparent binding affinity in WB, the WB disposition VZHE-039 favors better PK/PD properties than 5-HMF, where a linear PK and longer half-life are expected and its reversible PPB would have pharmacologic advantage over irreversible metabolism.

CHAPTER 6

OVERALL CONCLUSIONS AND FUTURE DIRECTIONS

SCD is characterized primarily by chronic, severe hemolytic anemia, leading to vascular occlusion, tissue infection, painful “crises” and, eventually, chronic organ damage that ultimately results in poor quality of life and decreased life expectancy (Piel et al., 2017). Common clinical management includes temporary administration of analgesics and blood transfusions for symptom relief. Four F.D.A.-approved drug treatment options are available for SCD, including hydroxyurea, voxelotor (GBT-440), crizanlizumab and L-glutamine.

AEH have been studied for several years and have demonstrated dramatic *in-vitro* and *in-vivo* anti-sickling effects by forming Schiff-base adducts with Hb, increasing its O_2-binding affinity and inhibiting polymerization of HbS (Safo & Kato, 2014). GBT-440 is the first AEH to be approved in 2019 by the U.S. F.D.A. for SCD treatment, confirming the clinical benefits of this novel MOA (Blair, 2020b; Vichinsky et al., 2019). The marketing approval of GBT-440 for SCD was based mainly on increased Hb levels and reduced hemolysis in SCD patients, considered to be clinically relevant benefits, rather than pertinent long-term clinical outcomes (*Multi-Discipline Review of Voxelotor*, 2019; Vichinsky et al., 2019). Regardless, the clinical studies supporting approval of GBT-440 provide encouraging evidence that AEH have SCD disease-modifying potential, mitigating the downstream adverse consequences of RBC sickling (Vichinsky et al., 2019). To aid future development of potentially more effective AEH drug candidates with better PK/PD

properties, this research encompasses a series of rationally-designed *in-vitro* studies that were conducted to screen novel synthetic AEH.

This research had the following overall objectives: 1). To fully characterize concentration- and time-dependent Hb binding of AEH (their primary MOA); 2). To investigate their ALDH susceptibility; and 3). To integrate the underlying disposition mechanisms in WB using quantitative kinetic models.

Since the rate and extent of Hb-AEH adduct formation at the target site (RBC) are expected to correlate directly with anti-sickling effect of AEH, a “universal” LC-UV/Vis assay method was developed to quantitate Hb-AEH adduct concentrations in relevant matrices, e.g., HbA solution and WB. Liquid chromatography using a weak cation-exchange column (PolyCAT A) with a linear mobile phase gradient was employed to separate the HbA-AEH adducts from free HbA, based on their differences in pI and detection of the heme part at 410 nm allowed quantitation. The assay was validated indirectly with external (free) HbA calibration curves, where a single HbA peak was observed for blank HbA solution and blank WB hemolysate at retention times of 11.0–11.5 min. Using this indirect validation, HbA calibration curves (0.0005–0.5 mM) were found to be linear (1/y weighted) with r^2 values of 0.993–0.999, with acceptable precision (RSD) and accuracy (DFN). This universal assay method was subsequently applied to AEH with different chemical structures and physicochemical properties. It successfully allowed to fully characterize HbA binding kinetics for the selected AEH as part of this research and can also be used to screen other AEH in future drug discovery.

Using HbA solutions (0.1 or 0.2 mM), experiments with an optimized sampling schedule and optimized AEH concentration ranges (based on pilot studies) showed that all AEH bind to HbA in a concentration- and time-dependent manner. The HbA-AEH adduct levels were sustained in HbA solution for most of the tested AEH (TDs, INN-310, PP-14, VZHE-039, 5-HMF), due to the absence of chemical and/or metabolic degradation in HbA solution; however, they achieved SS binding at different rates. A SS sigmoidal B_{max}-model was used to characterize the SS binding affinity (equivalent to $1/K_D$) as well as the capacity of HbA binding sites (B_{max}); it also captured potential cooperativity of HbA binding sites using the Hill coefficient (n) as measure of sigmoidicity. Furthermore, a simple kinetic binding model was used to characterize time-dependent binding profiles with association and dissociation processes (characterized by k_{on} and k_{off}) across the initial AEH concentrations, $[AEH]_0$. Using nonlinear regression methods, both models estimated relevant HbA binding properties with acceptable goodness-of-fit and parameter estimates (r^2, COV, correlation matrix, residuals); it resulted in similar K_D (from SS concentration-dependent) and $K_D^{kinetic}$ (from time-dependent) estimates.

All vanillin-derived benzaldehydes exhibited enhanced binding affinity in HbA solution - relative to their parent vanillin, primarily due to their faster k_{on} - indicating that the additional pyridinyl-methoxy side chains do increase HbA interactions (Table 6.1). In addition, the position of the pyridinyl-methoxy group alters HbA binding affinity and kinetics as demonstrated by comparing the three TD isomers: K_D and $t_{1/2}^{eq}$: TD-7 (0.15 hr) <TD-9 (0.23 hr) <TD-8 (0.55 hr) (Table 6.1). 5-HMF and 2,5-DMF, the two

furaldehydes studied, exhibited smaller K_D, i.e., higher HbA affinity, than vanillin, but larger than VZHE-039 – due to the changes on k_{off} and k_{on} (Table 6.1).

Table 6.1. Summary table of HbA binding kinetics of AEH in HbA solution and their oxidative metabolism in HLC.

AEH	Binding in HbA Solution				Metabolism in HLC	
	K_D	$K_D^{kinetic}$	k_{on}	k_{off}	$CL_{int}^{in\text{-}vitro}$	K_m
	[mM]	[mM]	[$mM^{-1}hr^{-1}$]	[hr^{-1}]	[µL/min/mg]	[mM]
5-HMF	0.37	0.28	0.46	0.13	0.036	>90
2,5-DMF	0.19	0.12	0.54	0.07	0	0
Vanillin	1.72	4.3	0.16	0.69	NA	
TD-8	0.58	0.55	0.18	0.10	0	0
TD-9	0.25	0.23	0.76	0.18	0	0
TD-7	0.19	0.15	9.8	1.5	0.88	>0.4
INN-310	0.19	0.14	5.0	0.70	1.6	>0.3
PP-14	0.16	0.10	16	2.2	NA	
VZHE-039	0.10	0.10	61	5.8	0	0
GBT-440	0.11	Faster than VZHE-039			NA	

A strong (log-log) correlation (r=0.993, n=7) was found between the k_{on} and k_{off} values among most of the tested AEH, suggesting that the current molecular design approach did accomplish (deliberately) enhancing HbA association while (inadvertently) increasing Hb dissociation as well. The chemical reaction kinetics for both formation and hydrolysis of Schiff-base involve several intermediates, and the rate-limiting step (reflected in k_{on} or k_{off}) may be determined by any of these intermediate steps (Scheme 6.1) (Kallen, 1971). The electron density on the carbon atom of the aldehyde on the AEH, and the nitrogen atom of the primary amine of Val1 on the α-chain of HbA may affect the association kinetics of AEH to Hb (k_{on}), whereas the oxygen atom of the water

molecule, the carbon and nitrogen atom of Schiff-base HbA-AEH adduct may affect the kinetics of hydrolysis process (k_{off}) (Scheme 6.1).

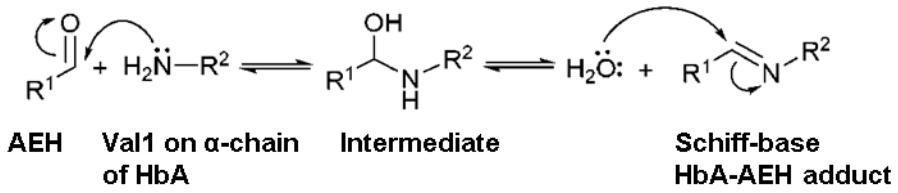

---- Scheme 6.1

Two deviations from this relationship, namely 2,5-DMF and vanillin, were observed: 2,5-DMF has two aldehyde moieties on the furan ring (rather than one for 5-HMF) and showed a slower k_{off} than 5-HMF. Vanillin, however, being the smallest benzaldehyde with fewer molecular interactions with Hb, consistently showed the slowest k_{on}. In X-ray crystallographic structural studies with benzaldehydes, key molecular features, i.e., the methoxy-pyridine ring, the ortho-hydroxyl moiety (relative to the aldehyde group) on the aromatic ring and the methyl-hydroxyl group on the pyridine ring, have been identified as key features in enhancing Hb interactions and affinity - which was confirmed by the results of the kinetic HbA binding studies - by speeding up binding kinetics, however, in both directions, i.e., by changing k_{on} and k_{off} simultaneously.

Due to their aldehyde functionality, AEH can be subject to ALDH-mediated metabolism; however, not all AEH were found to undergo oxidation in HLC, which contains the ALDH1 isoform (that is present in RBCs as well). ALDH1 is the major ALDH isoform to catalyze the oxidation of retinal (a form of vitamin A) and is efficient at oxidizing long-chain alkanals (O'Brien et al., 2005). It can also oxidize a rather broad

spectrum of both aliphatic and aromatic aldehydes with varying efficiency, including aldophosphamide, naphthalene, phenanthrene, and coumarin (Inoue et al., 1979; O'Brien et al., 2005; Vasiliou et al., 2000; Yoshida et al., 1998). The influence of side chains relative to the aldehyde group on ALDH oxidation has not been systemically studied. 5-HMF, TD-7 and INN-310 showed much lower affinity to, but a larger capacity/catalytic efficiency of the ALDH enzyme in HLC, compared to its prototypical substrate, i.e., acetaldehyde (Table 6.1). SAR studies showed that the ALDH enzyme favors TD-7 (with a meta-methoxy group) as substrate rather than its two isomers, i.e., TD-8 and TD-9 (with para-methoxy group). Interestingly, VZHE-039 did not exhibit any measurable oxidative metabolism, presumably due to the ortho-hydroxyl group on the aromatic ring, forming an intra-molecular hydrogen bond interaction with the aldehyde group, thus reducing its catalytic efficiency of ALDH. Electron density on the aromatic ring and steric hindrance may also play a role in AEH binding to and catalytic efficiency of ALDH. These metabolic findings in HLC are expected to be translatable to RBC, the site of action for AEH containing ALDH1 isoform, as demonstrated below for the disposition of AEH in WB.

To quantitatively integrate the results from HbA binding and HLC metabolism studies, apparent SS concentration- and time-dependent studies in WB (with RBC and other blood components, reflecting the physiologically relevant milieu for AEH) were designed. Normal WB (collected from healthy volunteers, Hct: 38-45%, $[HbA]_0$: 2.0-2.3 mM) was equilibrated with two prototypical AEH individually, 5-HMF (a polar furaldehyde, subject to ALDH-mediated metabolism) and VZHE-039 (a lipophilic

benzaldehyde, not subject to ALDH-mediated metabolism). $[AEH]_0$ ranges and sampling times were optimized from pilot experiments.

Protection from ALDH-mediated metabolism was found to be pivotal in sustaining HbA-AEH adduct levels in RBC, and extending the PD effects of AEH: VZHE-039 consistently showed sustained HbA-AEH adduct levels in WB for 24 hrs (Figure 6.1). On the other hand, the HbA-AEH adduct concentrations of 5-HMF in WB decreased after 1.5 hrs due to rapid metabolism in the RBC, consistent with the metabolic results in HLC (Figure 6.2, Table 6.1). Using a modified kinetic binding model, incorporating first-order metabolism for 5-HMF, both apparent association and metabolic processes are fast – as shown for 5-HMF in HbA solutions -, while the terminal decrease of HbA-AEH adduct is determined by the slow dissociation of 5-HMF from HbA (Table 6.2).

Previous studies had shown that the *in-vitro* plasma clearance ($CL_{plasma}^{in\text{-}vitro}$) of 5-HMF was high, but it decreased with increasing $[5\text{-}HMF]_0$, presumably due to saturable Hb binding and/or saturable metabolism (Parikh, 2013). In the current research, the observed saturable HbA-AEH adduct formation provides conclusive evidence that the cause of super-proportional increase for AUC of 5-HMF in plasma and the corresponding decrease in $CL_{plasma}^{in\text{-}vitro}$ with increasing $[5\text{-}HMF]_0$ is the saturable HbA binding rather than the saturable ALDH metabolism (Table 6.2).

Figure 6.1. Time-dependency of HbA-AEH adduct formation for VZHE-039 in WB. The simple dissolution kinetic binding model (lines) was fit to the experimental data (symbols), as discussed in Chapter 5.

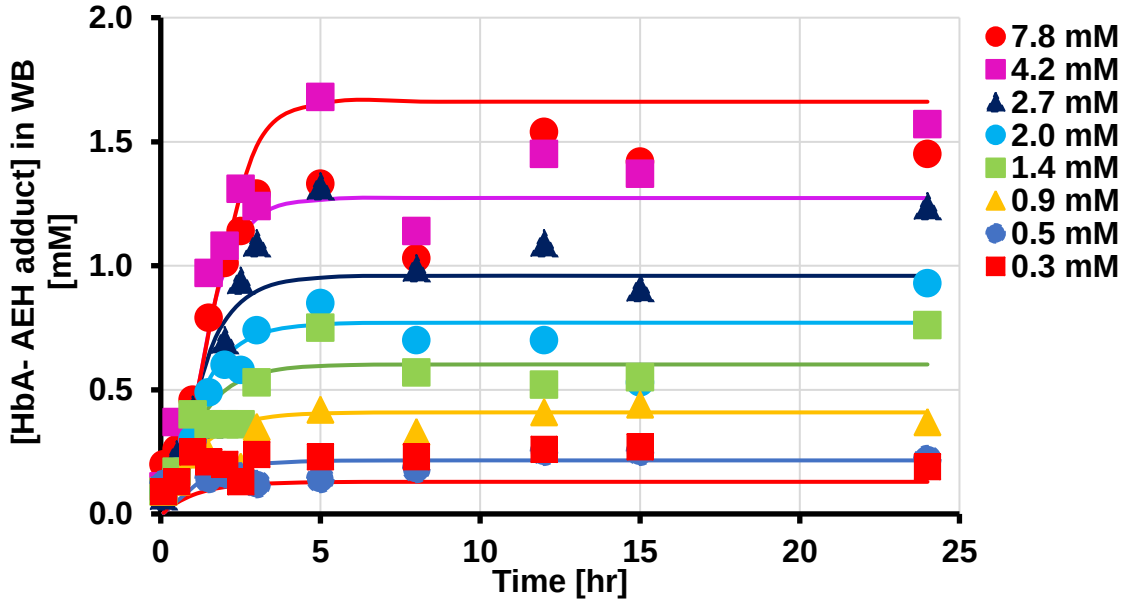

Figure 6.2. Time-dependent HbA-AEH adduct formation for 5-HMF in WB. The simple metabolic kinetic binding model (lines) was fit to experimental data (symbols) as discussed in Chapter 5.

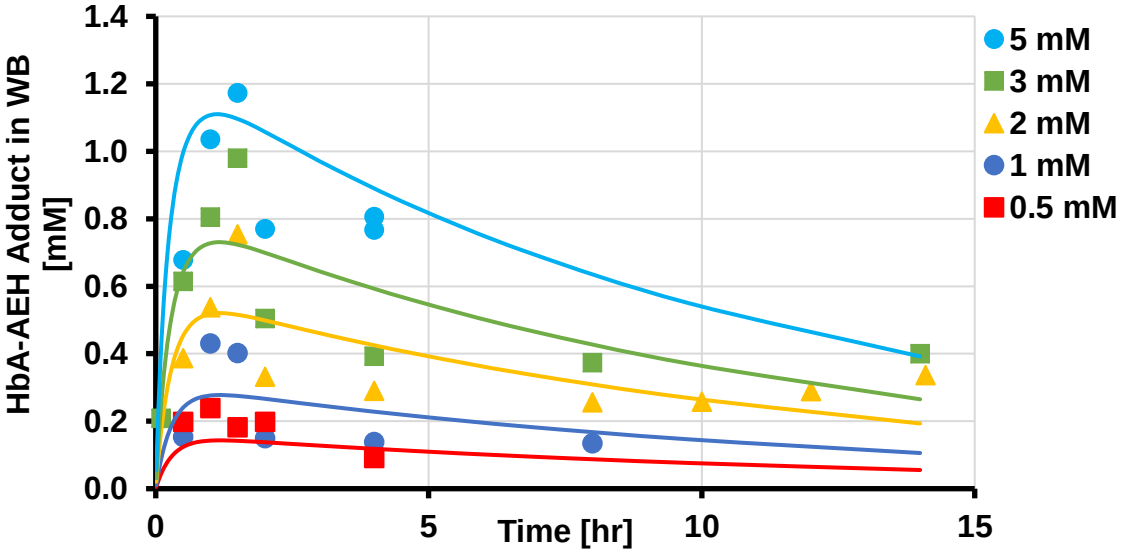

Table 6.2. Summary table of the disposition of VZHE-039 and 5-HMF in WB

AEH	HbA-AEH Adduct in HbA Solution			HbA-AEH Adduct in WB						AEH in Plasma
	$K_D^{kinetic}$	k_{on}	k_{off}	K_D'	k_{on}'	k_{off}'	k_{met}'	$K_D^{kinetic'}$	AUC dose-proportionalily constant	AUC dose-proportionality constant
	[mM]	[$mM^{-1}hr^{-1}$]	[hr^{-1}]	[mM]	[$mM^{-1}hr^{-1}$]	[hr^{-1}]	[hr^{-1}]	[mM]		
VZHE-039	0.10	61	5.8	1.5	0.20	0.46	0	2.3	0.79	0.93
5-HMF	0.28	0.46	0.13	3.0	0.56	0.11	2.2	0.20	0.73	2.1

Binding affinity and binding capacity of AEH to HbA, as well as to other blood components - such as PPB and RBC membranes - together determine the disposition of AEH in WB: Both 5-HMF and VZHE-039 exhibited an infra-proportional increase of HbA-AEH adduct exposures (AUC) with increasing $[AEH]_0$, due to their saturable HbA binding (with high affinity and low capacity relative to other WB components). Furthermore - different from 5-HMF -, $CL_{plasma}^{in\text{-}vitro}$ of VZHE-039 was low and remained constant across $[VZHE\text{-}039]_0$ due to its high PPB and likely RBC membrane binding, which appears characterized by high capacity and low affinity (i.e., reversible first-order binding) and competes with HbA binding.

In HbA solution, the HbA binding affinity for VZHE-039 was four-fold higher (smaller K_D) than for 5-HMF (Figure 6.3). However, the apparent WB binding affinity values ($1/K_D'$) for VZHE-039 and 5-HMF - characterized from SS concentration-dependency binding curves - are quite similar. However, the underlying mechanisms are quite different:

VZHE-039, due to its lipophilicity, is subject to extensive reversible PPB/RBC membrane binding, which slows down and reduces VZHE-039 available for intra-RBC HbA binding. This is reflected in a dramatically decreased value for k_{on}' in WB compared to k_{on} in HbA solution, and to a lesser extent, by a decreased k_{off}' value (Table 6.2). Similar properties are expected for GBT-440, due to its higher lipophilicity compared to VZHE-039.

On the other hand, 5-HMF, a hydrophilic compound, is not likely to bind significantly to plasma proteins and/or RBC membranes. However, as opposed to VZHE-039, it is subject to ALDH-mediated metabolism inside the RBC. Using the

metabolism binding kinetic model to account for this concurrent metabolism, the HbA association and dissociation rate constants for 5-HMF in WB and HbA solution are quite similar (Table 6.2). This demonstrates that its loss of HbA binding affinity in WB over HbA solution is due to metabolic loss of 5-HMF in the RBC.

Figure 6.3. Simulation of SS concentration-dependency of HbA-AEH adduct formation for VZHE-039 (solid line) and 5-HMF (dashed line) in HbA solution (red lines) and in WB (blue lines), using the final PE from the sigmoidal B_{max}-model (as discussed in Chapter 3 and 5) and scaled up to the same $[HbA]_0$ (2.0 mM) in WB.

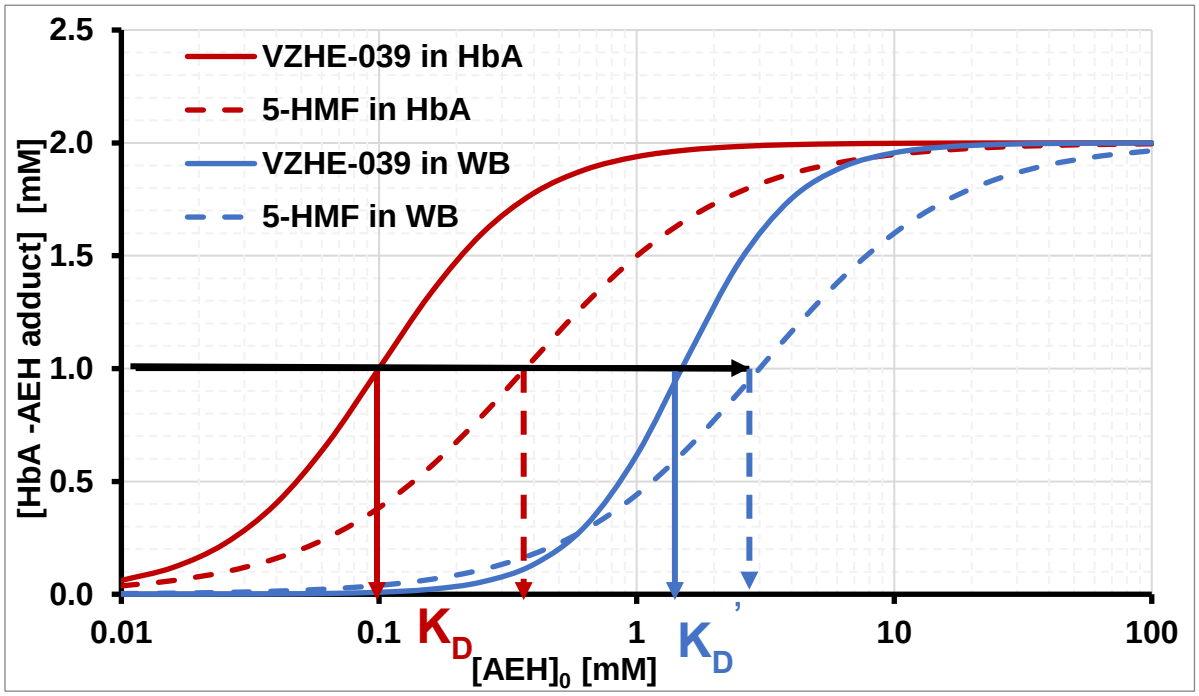

Among the tested AEH, VZHE-039 has been selected as our top candidate for further preclinical development. In HbA solution, VZHE-039 is characterized by high HbA binding affinity (K_D = 0.1 mM) and rapid binding kinetics, similar to the clinical reference compound, GBT-440 (Table 6.1). In HLC studies, VZHE-039 was also found to be resistant to ALDH-mediated metabolism – properties expected to be beneficial for sustaining its PD effect in blood, which was confirmed in the WB studies. However, the observed WB potency (K_D' of 1.5 mM) was reduced quite significantly due to nonspecific binding to plasma proteins and/or RBC membranes.

Both VZHE-039 and GBT-440 are highly bound to plasma protein, with a fraction bound in human plasma of 94% for VZHE-039 experimentally obtained from a rapid equilibrium dialysis method at a concentration of 5 μM, and 99.8% for GBT-440 measured by ultracentrifugation at concentrations of 5 and 50 μM (Abdulmalik, 2018; *Multi-Discipline Review of Voxelotor*, 2019). This high degree of PPB lowers their apparent potency in WB by competing with Hb binding (target site), but - along with the HbA binding - it also retains both compounds in the intravascular space, which is expected to lead to a reduction of their extravascular tissue distribution (small V_{dss}) and clearance (small CL_{tot}) as well, as will be discussed below.

Depending on the oral dose requirements, GI solubility of VZHE-039 is expected to be low: Our *in-vitro* studies showed that the maximal concentration of VZHE-039 that can be dissolved in 0.5 M Tris buffer (pH = 7.5) is 1.3 mM (i.e., 0.35 mg/mL). Assuming a human GI fluid volume of 250 mL, the predicted maximal dissolvable P.O. dose would be 87 mg, which is likely below its therapeutic oral doses, expected to exceed 10-20 mg/kg, i.e., 750-1500 mg. Appropriate formulation for adequate F_{oral} would be

necessary, as is the case for GBT-440 which was formulated as a 500 mg immediate-release solid oral dosage form (*Multi-Discipline Review of Voxelotor*, 2019).

GBT-440 has low solubility (0.032 mg/mL = 8 mg/250 mL, i.e., ~10 times lower than VZHE-039) in water and aqueous buffers at pH 7.0, relative to its therapeutic oral doses (1500 mg) (*Product Quality Review(s) of Voxelotor*, 2019).

VZHE-039 has shown high *in-vitro* Caco2 cell permeability and is not a substrate of efflux transporters (efflux ratio [R_e] > 0.85), consistent with trans-epithelial diffusion due to its high lipophilicity (cLog = 1.7) (Safo, 2019).

GBT-440, another lipophilic compound (cLog = 3.5), also appears to be a high permeability drug with P_{app}(B-to-A) / P_{app}(A-to-B) ratio of 1.31 in a polarized monolayer of Madin Darcy Canine Kidney MDR1 (MDCK-MDR1) cells system, indicating it is not a substrate of P-gp (*Product Quality Review(s) of Voxelotor*, 2019).GBT-440 is classified by F.D.A. as a BCS Class 2 drug (*Multi-Discipline Review of Voxelotor*, 2019). In a human mass balance study with a single radio-labeled dose of 400 mg of GBT-440 to healthy volunteers, 63% of radioactivity dose was recovered in feces, including 33% as parent drug (*Multi-Discipline Review of Voxelotor*, 2019). *In-vivo* radiolabeled studies in rats (I.V.: 2 mg/kg) showed that only approximately 6.6% of GBT-440 was excreted as unchanged form into bile and most of the dose was excreted as metabolites (77% of the dose) (*Multi-Discipline Review of Voxelotor*, 2019). These findings suggest that GBT-440 was not well absorbed from the GI tract and not subject to significant biliary excretion; about one third of the oral dose in humans does not get absorbed. A low-fat breakfast showed no significant effect on GBT-440 exposures, whereas a high-fat meal did not affect t_{max} significantly, but increased AUC by 42% and c_{max} by 45%,

demonstrating enhancement of the extent, rather than the rate of absorption (Hutchaleelaha et al., 2019; *Multi-Discipline Review of Voxelotor*, 2019). A high-fat meal is expected to stimulate bile acid secretion into the GI tract, where they help solubilizing lipophilic molecules, including GBT-440, thus increasing its GI solubility and F_{oral}. The results from both mass balance and food effect studies are consistent with its BCS class 2 designation as a poor GI solubility/high GI permeability drug.

VZHE-039 and GBT-440 are expected to be low hepatic extraction ratio compounds, as both of them are highly PPB; therefore, low first-pass metabolism is expected for both. However, their F_{oral} may be limited by GI solubility - as discussed above. *In-vitro* studies in mice showed that after oral administration of 100-200 mg/kg (non-optimized suspension), VZHE-039 exhibited a low F_{oral} of 11%-13%, whereas GBT-440 (P.O., 30 mg/kg, presumably the patented suspension) showed moderate F_{oral} of 71%, likely due to differences in their GI solubility and formulation (Table 6.3) (US 2016/0206604 A1, 2016; "Datasets obtained from Abdulmalik, Osheiza," 2018; Oksenberg et al., 2016).

Table 6.3. PK parameters for VZHE-039 and GBT-440 in mice (n = 2-3).

AEH	Dose	CL_{tot}	V_{dss}	$t_{1/2}$	F_{oral}	RBC/plasma ratio
	[mg/kg]	[mL/min/kg]	[L/kg]	[hr]	%	
VZHE-039	I.V.,12.5 - 25; P.O. 100 - 200	0.13	0.10	12	18	NA
GBT-440	I.V. 70; P.O., 30	0.11	0.10	12	71	174

Based on the results of the *in-vitro* WB disposition studies, VZHE-039 showed a constant low $CL_{plasma}^{in\text{-}vitro}$ (0.005 mL/min/12mL plasma), independent of $[VZHE\text{-}039]_0$ (0.3 – 8 mM) – reflecting non-saturable PPB/RBC membrane binding- as well as saturable HbA binding at the target site. *In-vivo* PK studies with VZHE-039 (12.5-25 mg/kg) and GBT-440 (70 mg/kg) in mice after I.V. administration showed a small V_{dss} of 0.1 ml/kg for both (Table 6.3), which is consistent with their *in-vitro* PPB/RBC membrane and Hb binding, reducing their extravascular tissue distribution (Dufu, Patel, Oksenberg, & Cabrales, 2018). GBT-440 is the main circulating moiety in human plasma and in WB accounting for 48.8% and 95% of the total radioactivity, respectively, indicating despite the high PPB of GBT-440 (99.8%), the blood-to-plasma ratio is approximately 2:1 - which further confirms its non-specific binding to RBC membranes and specific binding to Hb (target) (*Multi-Discipline Review of Voxelotor*, 2019).

GBT-440 is metabolized by CYP-450, UGT and SULT(*Multi-Discipline Review of Voxelotor*, 2019). *In-vitro* metabolism studies using recombinant isozymes indicate that the contribution of CYP3A4, CYP2C9, CYP2C19, and CYP2B6 to overall metabolism of GBT-440 was 56%, 7%, 5%, 7%, respectively (*Multi-Discipline Review of Voxelotor*, 2019). Phase 2 conjugation by UGT1A1 and UGT1A9 accounted for 8% of the overall metabolism of GBT-440 (*Multi-Discipline Review of Voxelotor*, 2019). *In-vivo* studies showed the major circulating metabolite in human plasma (as in mouse, rat and dog) is an (inactive, phase 2) O-dealkylation-sulfate metabolite that is formed by oxidation and subsequent conjugation with sulfate, accounting for 16.8% of total radioactivity in WB (*Multi-Discipline Review of Voxelotor*, 2019). A human mass balance study also showed that CYP-mediated oxidation, reduction and direct conjugation accounted for 16.9%,

11.4%, and 4.6% of the GBT-440 dose recovered in feces and urine, where 3.1% of GBT-440 was oxidized to the carboxylic acid, presumably due to ALDH-mediated metabolism (*Multi-Discipline Review of Voxelotor*, 2019).

Preliminary *in-vitro* studies with VZHE-039 (0.1 – 100 μM) in HLM showed no inhibition of several major isoforms of CYP-450 (3A4, 2C8, 2C9, 2C19, 2D6), with exception of CYP1A2 (4.7 μM) and CYP2B6 (41.4 μM). GBT-440, on the other hand, showed inhibition of major CYP-450 isozymes (CYP1A2, 2C8, 2C9, 2C19, 2D6, and 3A4) in HLM with IC_{50} values ranging from 7.9 to 148 μM, where CYP3A4, in particular showed a IC_{50} of 12.5 – 81.9 μM (Metcalf et al., 2017). In an *in-vivo* cocktail DDI study using different CYP-450 substrate drugs, exposure of midazolam (substrate of CYP3A4) increased by 63% in presence of GBT-440, indicating that GBT-440 is an inhibitor of CYP3A4 at clinically relevant doses (*Multi-Discipline Review of Voxelotor*, 2019). This study also showed a less than 1.12-fold change in exposure of caffeine (CYP1A2), warfarin (CYP2C9), and omeprazole (CYP2C19) (*Multi-Discipline Review of Voxelotor*, 2019). As GBT-440 is a known substrate of CYP3A4, which is its major metabolic elimination pathway, a reduced dose from 1,500 to 1,000 mg/daily of GBT-440 is recommended by F.D.A in concomitant use of strong CYP3A4 inhibitors (*Multi-Discipline Review of Voxelotor*, 2019).

In-vivo PK studies in mice after I.V. administration of VZHE-039 (12.5-25 mg/kg) consistently showed a low, dose-independent *in-vivo* clearance (CL_{tot}) of 0.12-0.14 mL/min/kg and a long terminal half-life ($t_{1/2}$) of 10 -13 hrs ("Datasets obtained from Abdulmalik, Osheiza," 2018). GBT-440 (I.V. 70 mg/kg) also showed a low CL_{tot} of 0.11 mL/min/kg and a long $t_{1/2}$ of 12 hrs in mice (Table 6.3) (Oksenberg et al., 2016). *In-vivo*

radiolabeled studies in rats (I.V.: 2 mg/kg) showed that metabolism is the main elimination route of GBT-440, accounting for 93% of the administered dose, while only approximately 6.6% of GBT-440 was excreted as unchanged parent drug into bile and <1% in urine (*Multi-Discipline Review of Voxelotor*, 2019).

In a human mass balance study, a single radio-labeled dose of 400 mg of GBT-440 was administrated to healthy volunteers (n = 7) on day 5 after SS was achieved with pre-administrated non-radioactive GBT-440 (Rademacher, Hutchaleelaha, Washington, Lehrer, & Ramos, 2016). 98.0% radioactivity was recovered over 23 days (*Multi-Discipline Review of Voxelotor*, 2019). 35% of radioactivity was recovered in urine and 63% in feces, where most excreted as metabolites (*Multi-Discipline Review of Voxelotor*, 2019). Only 0.08% was excreted renally unchanged (*Multi-Discipline Review of Voxelotor*, 2019), suggesting that renal elimination of parent drug is negligible and GBT-440 is almost exclusively metabolized. Low renal clearance is expected due to the high PPB (99.8%) preventing GBT-440 from being filtered in the glomeruli and any drug reaching the tubuli being reabsorbed due to its high lipophilicity.

In humans, GBT-440 followed dose-proportional PK for doses up to 2,800 mg (i.e., 37 mg/kg) (Hutchaleelaha et al., 2019). The terminal plasma $t_{1/2}$ in healthy volunteers was around 61–85 hrs, while, in SCD patients, it was shorter (~36 hrs), most likely due to low Hb level and less RBC in SCD patients, resulting in less GBT-440 bound to Hb and RBC membranes, resulting in more free drug in blood available for hepatic clearance (Hutchaleelaha et al., 2019).

Upon once daily dosing of therapeutic doses, SS concentrations of GBT-440 in plasma and blood were reached by day 8 in SCD patients. The accumulation ratio of

$AUC_{0\text{-}24h}$ at SS was approximately 3-fold, suggesting an accumulation half-life exceeding 24 hrs, consistent with the terminal half-life after single doses, as mentioned above (*Multi-Discipline Review of Voxelotor*, 2019). At steady-state after 1,000 mg/day in SCD patients (n=6), average c_{max}^{SS} of GBT-440 were measured to be 483 µg/mL (1.43 mM), 8.1 µg/mL (0.024 mM), and 221 µg/mL (0.66 mM) in RBC, plasma, and WB, respectively (Howard et al., 2019) – clearly demonstrating the preference of GBT-440 for RBC accumulation. Compared to its K_D (0.11 mM) from the *in-vitro* HbA binding study in HbA solution, these *in-vivo* SS peak concentrations in RBC (1.43 mM) are much larger. However, this doesn't account for the non-specific binding to RBC membranes, which are high for lipophilic compounds such as GBT-440, nor PPB (f_b of 99.6% for GBT-440 and 94% for VZHE-039). Comparing the *in-vivo* SS peak WB concentrations (0.66 mM) to the apparent K_D' in WB HbA binding studies of 2.3 mM, which includes nonspecific binding, (see Table 6.2) suggests that less than 50% of Hb had bound GBT-440 *in-vivo*. This is consistent with *ex-vivo* measurements of "modified HbS" concentrations at therapeutic doses in SCD patients, which suggests that only 25-30% of HbS was modified in achieving clinical efficacy. (*Multi-Discipline Review of Voxelotor*, 2019)

In summary, both VZHE-039 and GBT-440 exhibit or are expected to exhibit high GI permeability and presumably low hepatic first-pass metabolism due to high PPB. Their F_{oral}, however, is limited by poor GI solubility at therapeutic doses. Small V_{dss} and low CL_{tot} were observed for both VZHE-039 and GBT-440 in mice, due to their high PPB/RBC membrane binding and Hb binding, retaining them in blood. Due to the low CL_{ren} of GBT-440, hepatic CYP-mediated oxidative metabolism (with secondary

conjugation) was the main route of elimination. Overall, in muine PK studies, the systemic PK properties (after I.V. administration) of VZHE-039 and GBT-440 are quite similar.

Observed MOA-related differences between VZHE-039 and GBT-440 in preclinical development include: In HbA solution, at saturating concentrations, VZHE-039 exhibited 100% HbA modification whereas GBT-440 modified only ~50% of HbA - consistent with one molecule of HbA binding two molecules of VZHE-039, but only one molecule of GBT-440, as discussed in Chapter 3. In addition, VZHE-039 has a secondary, O_2-independent anti-sickling MOA over GBT-440 due to interactions with the surface-located αF-helix of Hb to directly weaken HbS polymer interactions (Ahmed et al., 2020; Oder et al., 2016; Pagare et al., 2018). It is expected that GBT-440-modified HbS tetramers may still transition to the DeoxyHb T-state in areas of severe regional hypoxia with GBT-440 incorporated into fibers, leading to local sickling. On the other hand, VZHE-039-bound to the DeoxyHb T-state of HbS would destabilize fiber formation and prevent sickling, which may be clinically advantageous (Ahmed et al., 2020; Oder et al., 2016; Pagare et al., 2018).

For future discovery of novel AEH, enhanced HbA binding affinity and kinetics as well as resistance to ALDH-mediated metabolism are pivotal criteria to improve their potency and PK/PD properties and meet dose requirement for the intended sustained PD effects. To increase Hb binding affinity ($K_D = k_{off}/k_{on}$), increasing k_{on} and/or decreasing k_{off} is desirable. Current molecular modifications of vanillin to identify and investigate novel AEH successfully increased their k_{on} (deliberately) but also (inadvertently) increased their k_{off}. There is a need to keep k_{off} small while increasing k_{on}.

Keeping k_{off} small will also slow down the overall Hb binding kinetics ($t_{1/2}^{eq}$= ln(2)/(HbA_0*k_{on}+k_{off})). This slow dissociation from HbA is desirable and makes RBC (target site) into deep compartment, which will be beneficial to hold AEH on Hb and prolong its PD effect. Lipophilicity in general is expected to decrease the apparent binding affinity of AEH (e.g. VZHE-039, GBT-440) in WB due to non-specific binding to PPB and RBC membranes. However, a possible benefit of this off-target, nonspecific, high capacity binding is drug retention in the blood, prolonging the *in-vivo* persistence of AEH in blood. Poor GI solubility can be a problem for lipophilic AEH (e.g. VZHE-039, GBT-440), reducing their F_{oral}, which can be overcome by appropriate formulations and/or improving dose potency. Other druggability issues, including PPB, other metabolic routes, and DDI liabilities also need to be considered to meet dose requirement for desirable anti-sickling effects.

LIST OF REFERENCES

Abdulmalik, O. (2018). Unpublished Data from Personal Communication.

Abdulmalik, O., Safo, M. K., Chen, Q., Yang, J., Brugnara, C., Ohene-Frempong, K., … Asakura, T. (2005). 5-hydroxymethyl-2-furfural Modifies Intracellular Sickle Haemoglobin and Inhibits Sickling of Red Blood Cells. *British Journal of Haematology*, *128*(4), 552–561.

Adducts, B., Zaugg, R. H., Walder, J. A., & Klotz, M. (1977). Schiff of Hemoglobin, *252*(23), 8542–8548.

Ahmed, M. H., Ghatge, M. S., & Safo, M. K. (2020). Hemoglobin: Structure, Function and Allostery. In U. Hoeger & J. R. Harris (Eds.), *Vertebrate and Invertebrate Respiratory Proteins, Lipoproteins and other Body Fluid Proteins* (pp. 345–382). Cham: Springer International Publishing.

Akinsheye, I., & Klings, E. S. (2010). Sickle cell anemia and vascular dysfunction: the nitric oxide connection. *Journal of Cellular Physiology*, *224*(3), 620–625.

Ataga, K. I., Kutlar, A., Kanter, J., Liles, D., Cancado, R., Friedrisch, J., … Rother, R. P. (2017). Crizanlizumab for the prevention of pain crises in sickle cell disease. *New England Journal of Medicine*, *376*(5). https://doi.org/10.1056/NEJMoa1611770

Bender, M. A., & Hobbs, W. (2014). Sickle Cell Disease-Gene Reviews. NCBI Bookshelf.

Blair, H. A. (2020a). Crizanlizumab: first approval. *Drugs*, 1–6.

Blair, H. A. (2020b). Voxelotor: First Approval. *Drugs*, *80*(2), 209–215.

Booth, C., Inusa, B., & Obaro, S. K. (2010). Infection in sickle cell disease: a review. *International Journal of Infectious Diseases*, *14*(1), e2–e12.

Bosron, F., & Li, T. (1986). Special Articles Genetic Polymorphism of Human Liver Alcohol and Aldehyde Dehydrogenases , and their Relationship to Alcohol Metabolism and Alcoholism. *Hepatology*, *6*(3), 502–510.

Bragg, W. L., & Perutz, M. F. (1952). The structure of haemoglobin. *Proceedings of the Royal Society of London. Series A. Mathematical and Physical Sciences*, *213*(1115), 425–435.

Brian W. METCALF, San Francisco, C. (US). (2016). *US 2016/0206604 A1*.

Bunn, H. F., & Forget, B. G. (1986). *Hemoglobin--Molecular, Genetic, and Clinical Aspects*. (J. Dyson, Ed.). W.B. Saunders Company.

Burchall, G., & Maxwell, E. (2010). Haemoglobin Stanleyville II modifies sickle disease phenotype. *Pathology*, *42*(3), 310–312.

Charache, S., Terrin, M. L., Moore, R. D., Dover, G. J., Barton, F. B., Eckert, S. V, … Anemia, I. of the M. S. of H. in S. C. (1995). Effect of hydroxyurea on the frequency of painful crises in sickle cell anemia. *New England Journal of Medicine*, *332*(20), 1317–1322.

ClinicalTrials.gov. (2020).

Cokic, V. P., Smith, R. D., Beleslin-Cokic, B. B., Njoroge, J. M., Miller, J. L., Gladwin, M. T., & Schechter, A. N. (2003). Hydroxyurea induces fetal hemoglobin by the nitric

oxide–dependent activation of soluble guanylyl cyclase. *The Journal of Clinical Investigation*, *111*(2), 231–239.

Cox, S. E., Hart, E., Kirkham, F. J., & Stotesbury, H. (2020). L-Glutamine in sickle cell disease. *Drugs of Today (Barcelona, Spain: 1998)*, *56*(4), 257–268.

Cretegny, I., & Edelstein, S. J. (1993). Double Strand Packing in Hemoglobin S Fibers. *J Mol Biol*, *230*, 733–738.

Datasets obtained from Abdulmalik, Osheiza. (2018).

Deshpande, T. M., Pagare, P. P., Ghatge, M. S., Chen, Q., Musayev, F. N., Venitz, J., … Safo, M. K. (2018). Rational Modification of Vanillin Derivatives to Stereospecifically Destabilize Sickle Hemoglobin Polymer Formation. *Acta Crystallographica Section D*, *74*(10), 956–964.

Disease-modifying therapies for prevention of vaso-occlusive pain in sickle cell disease. UpToDate, Inc. Accessed June-06. (2020).

Driffield, M., Chan, D., Macarthur, R., MacDonald, S., Brereton, P., & Wood, R. (2005). Single Laboratory Validation of a Method for the Determination of Hydroxymethylfurfural in Honey by using Solid-Phase Extraction Cleanup and Liquid Chromatography. *Journal of AOAC International*, *88*(1), 121–127.

Drugbank.ca. Accessed June-07. (2020).

Dufu, K., Patel, M., Oksenberg, D., & Cabrales, P. (2018). GBT440 improves red blood cell deformability and reduces viscosity of sickle cell blood under deoxygenated conditions. *Clinical Hemorheology and Microcirculation*, *70*(1).

Ekins, S., Ring, B. J., Grace, J., Mcrobie-belle, D. J., & Wrighton, S. A. (2001). Present and Future in vitro Approaches for Drug Metabolism. *Journal of Pharmacological and Toxicological Methods*, *44*(1), 313–324.

FDA.gov/drugs/drug-interactions-labeling [online]. Accessed June-07. (2020).

Foster, J. A., Houston, J. B., Hallifax, D., Foster, J. A., Houston, J. B., Comparison, D. H., … Hallifax, D. (2010). Comparison of Intrinsic Clearances in Human Liver Microsomes and Suspended Hepatocytes from the Same Donor Livers : Clearance-Dependent Relationship and Implications for Prediction of in vivo Clearance. *Xenobiotica*, *41*(2), 124–136.

Foti, A., Hartmann, T., Coelho, C., Santos-Silva, T., Romão, M. J., & Leimkühler, S. (2016). Optimization of the expression of human aldehyde oxidase for investigations of single-nucleotide polymorphisms. *Drug Metabolism and Disposition*, *44*(8), 1277–1285.

Ge, S., & Lee, T. (1997). Kinetic Significance of the Schiff Base Reversion in the Early-Stage Maillard Reaction of a Phenylalanine - Glucose Aqueous Model System. *Journal of Agricultural and Food Chemistry*, *2*(1), 1619–1623.

Han, J., Saraf, S. L., & Gordeuk, V. R. (2020). Systematic review of voxelotor: a first-in-class sickle hemoglobin polymerization inhibitor for management of sickle cell disease. *Pharmacotherapy: The Journal of Human Pharmacology and Drug Therapy*.

Hardt-Stremayr, M., Bernaskova, M., Hauser, S., Kunert, O., Guo, X., Stephan, J., … Wintersteiger, R. (2012). Development and Validation of an HPLC Method to

Determine Metabolites of 5-hydroxymethylfurfural (5-HMF). *Journal of Separation Science*, *35*(19), 2567–2574.

Horecker, B. L., & Kornberg, A. (1948). The Extinction Coefficients of The Reduced Band of Pyridine Nucleotides. *J. Biol. Chem*, *175*(1), 385–390.

Howard, J., Hemmaway, C. J., Telfer, P., Layton, D. M., Porter, J., Awogbade, M., … Lehrer-Graiwer, J. (2019). A phase 1/2 ascending dose study and open-label extension study of voxelotor in patients with sickle cell disease. *Blood*.

Hutchaleelaha, A., Allen, E., Washington, C., Siu, V., Oksenberg, D., Gretler, D. D., … Graiwer, J. L. (2019). Pharmacokinetics and Pharmacodynamics of Voxelotor (GBT440) in Healthy Adults and Patients with Sickle Cell Disease. *British Journal of Clinical Pharmacology*, *85*, 1290–1302.

Ilesanmi, O. O. (2010). Pathological basis of symptoms and crises in sickle cell disorder: implications for counseling and psychotherapy. *Hematology Reports*, *2*(1).

Inoue, K., Nishimukai, H., & Yamasawa, K. (1979). Purification and Partial Characterization of Aldehyde Dehydrogenase from Human Erythrocytes. *Biochimica et Biophysica Acta*, *569*(2), 117–123.

Itala, L., Seppa, K., Turpeinen, U., & Sillanaukee, P. (1995). Separation of Hemoglobin Acetaldehyde Adducts by High-Performance Liquid Chromatography Cation-Exchange Chromatography. *Analytical Biochemistry*, *224*, 323–329.

Jelski, W., Zalewski, B., & Szmitkowski, M. (2008). The Activity of Class I, II, III, and IV Alcohol Dehydrogenase (ADH) Isoenzymes and Aldehyde Dehydrogenase (ALDH)

in Liver Cancer. *Digestive Diseases and Sciences*, *53*(9), 2550–2555.

Jia, L., & Lliu, X. (2007). The Conduct of Drug Metabolism Studies Considered Good Practice (II): In Vitro Experiments. *Current Drug Metabolism*, *8*(8), 822–829.

Kallen, R. G. (1971). The Mechanism of Reactions Involving Schiff Base Intermediates. Thiazolidine Formation from L-Cysteine and Formaldehyde. *Journal of the American Chemical Society*, *93*(23), 6236–6248.

Kaufman, D. P., & Lappin, S. L. (2019). Physiology, Fetal Hemoglobin. In *StatPearls [Internet]*. StatPearls Publishing.

Kutlar, A., Kutlar, F., Wilson, J. B., Headlee, M. G., & Huisman, T. H. J. (1984). Quantitation of Hemoglobin Components by High-Performance Cation-Exchange Liquid Chromatography : Its Use In Diagnosis and in the Assessment of Cellular Distribution of Hemoglobin Variants, *53*, 39–53.

Lane, P. A., Buchanan, G. R., Desposito, F., Pegelow, C. H., Vichinsky, E. P., Wethers, D. L., & Woods, G. M. (2002). Health supervision for children with sickle cell disease. *Pediatrics*, *109*(3), 526–535.

Ley, K. (2001). Functions of selectins. In *Mammalian Carbohydrate Recognition Systems* (pp. 177–200). Springer.

Lin, A.-S., Qian, K., Usami, Y., Lin, L., Itokawa, H., Hsu, C., … Lee, K.-H. (2008). 5-Hydroxymethyl-2-furfural, a Clinical Trials Agent for Sickle Cell Anemia, and its Mono/di-glucosides from Classically Processed Steamed Rehmanniae Radix. *Journal of Natural Medicines*, *62*(2), 164–167.

Liu, Z. J., Sun, Y. J., Rose, J., Chung, Y. J., Hsiao, C. D., Chang, W. R., … Wang, B. C. (1997). The First Structure of an Aldehyde Dehydrogenase Reveals Novel Interactions between NAD and the Rossmann Fold. *Nature Structural Biology*, *4*(4), 317–326.

Man, Y., Goreke, U., Kucukal, E., Hill, A., An, R., Liu, S., … Little, J. A. (2020). Leukocyte adhesion to P-selectin and the inhibitory role of Crizanlizumab in sickle cell disease: A standardized microfluidic assessment. *Blood Cells, Molecules, and Diseases*, 102424.

Manikandan, P., & Nagini, S. (2017). Cytochrome P450 Structure, Function and Clinical Significance: A Review. *Current Drug Targets*, *19*(1), 38–54.

Marchitti, S. A., Brocker, C., Stagos, D., & Vasiliou, V. (2008). Non-P450 aldehyde oxidizing enzymes: the aldehyde dehydrogenase superfamily. *Bone*, *4*(6), 697–720.

Menez, J. F., Berthou, F., Meskar, A., Picart, D., Le Bras, R., & Bardou, L. G. (1984). Glycosylated Haemoglobin: High-Performance Liquid Chromatographic Determination of 5-(hydroxymethyl)-2-furfuraldehyde after Haemoglobin Hydrolysis. *Journal of Chromatography A*, *297*, 339–350.

Metcalf, B., Chuang, C., Dufu, K., Patel, M. P., Silva-Garcia, A., Johnson, C., … Li, Z. (2017). Discovery of GBT440, an Orally Bioavailable R-State Stabilizer of Sickle Cell Hemoglobin. *ACS Medicinal Chemistry Letters*, *8*(3).

Mezey, E., Rawles, J. W., Rhodes, D. L., & Potter, J. J. (1987). Characterization of Human Erythrocyte Aldehyde Dehydrogenase. *Biochemical Pharmacology*, *36*(21), 3715–3722.

Michail, K., Matzi, V., Maier, A., Herwig, R., Greilberger, J., Juan, H., … Wintersteiger, R. (2007). Hydroxymethylfurfural: an Enemy or a Friendly Xenobiotic? A Bioanalytical Spproach. *Analytical and Bioanalytical Chemistry*, *387*(8), 2801–2814.

Multi-Discipline Review of Voxelotor. (2019). *FDA*.

Nader, E., Grau, M., Fort, R., Collins, B., Cannas, G., Gauthier, A., … Connes, P. (2018). Hydroxyurea therapy modulates sickle cell anemia red blood cell physiology: Impact on RBC deformability, oxidative stress, nitrite levels and nitric oxide synthase signalling pathway. *Nitric Oxide - Biology and Chemistry*, *81*.

Niihara, Y., Koh, H. A., Tran, L., Razon, R., Macan, H., Stark, C., … Adams-Graves, P. (2014). A phase 3 study of l-glutamine therapy for sickle cell anemia and sickle ß0-thalassemia. American Society of Hematology Washington, DC.

O'Brien, P., Siraki, A., & Shangari, N. (2005). Aldehyde Sources, Metabolism, Molecular Toxicity Mechanisms, and Possible Effects on Human Health. *Critical Reviews in Toxicology*, *35*(7), 609–662.

Obied, T. (2010). in-Vitro Metabolism and Protein Binding of 5-Hmf, a Potential Antisickling Agent. *Ph.D. Dissertation, Virginia Commonwealth University*.

Oder, E., Safo, M. K., Abdulmalik, O., & Kato, G. J. (2016). New developments in anti-sickling agents: can drugs directly prevent the polymerization of sickle haemoglobin in vivo? *British Journal of Haematology*, *175*(1), 24–30.

Oksenberg, D., Dufu, K., Patel, M. P., Chuang, C., Li, Z., Xu, Q., … Archer, D. R. (2016). GBT440 increases haemoglobin oxygen affinity , reduces sickling and prolongs

RBC half-life in a murine model of sickle cell disease. *British Journal of Haematology*, *175*(July), 141–153.

Ou, C.-N., & Rognerud, C. L. (1997). Rapid Analysis. *Clinical Chemistry*, *20*(February), 72–76.

Ou, C.-N., Buffone, G. J., & Reimer, G. L. (1983). High-performance liquid chromatography of human hemoglobin in a new cation exchanger. *Journal of Chromatography*, *266*, 197–205.

Overturf, G. D. (1999). Infections and immunizations of children with sickle cell disease. *Advances in Pediatric Infectious Diseases*, *14*, 191–218.

Pagare, P. P., Ghatge, M. S., Musayev, F. N., Deshpande, T. M., Chen, Q., Braxton, C., … Safo, M. K. (2018). Rational Design of Pyridyl Derivatives of Vanillin for the Treatment of Sickle Cell Disease. *Bioorganic and Medicinal Chemistry*, *26*(9), 2530–2538.

Parikh, A. (2013). In-vitro PK/PD Profiling and Modeling of the Anti-Sickling Agents, 5-Hydroxymethyl Furfural (5-HMF) and Novel Synthetic Allosteric Effectors of Hemoglobin (AEH) in Human Whole Blood. *Ph.D. Dissertation. Vriginia Commonwealth University*.

Piccin, A., Murphy, C., Eakins, E., Rondinelli, M. B., Daves, M., Vecchiato, C., … Smith, O. P. (2019). Insight into the Complex Pathophysiology of Sickle Cell Anaemia and Possible Treatment. *European Journal of Haematology*.

Piel, F. B., Steinberg, M. H., & Rees, D. C. (2017). Sickle Cell Disease. *New England*

Journal of Medicine, *376*(16), 1561–1573.

Poillon, W N, Kim, B. C., Labotka, R. J., Hicks, C. U., & Kark, J. A. (1995). Antisickling effects of 2, 3-diphosphoglycerate depletion.

Poillon, William N, & Kim, B. C. (1990). 2, 3-Diphosphoglycerate and intracellular pH as interdependent determinants of the physiologic solubility of deoxyhemoglobin S.

Product Quality Review(s) of Voxelotor. (2019). *FDA*.

Rademacher, P., Hutchaleelaha, A., Washington, C., Lehrer, J., & Ramos, E. (2016). Absorption, Metabolism and Excretion of GBT440, a Novel Hemoglobin S (HbS) Polymerization Inhibitor for the Treatment of Sickle Cell Disease (SCD), in Healthy Male Subjects. *Blood*, *128*(22), 2487.

Reactions of Arenes.Electrophilic Aromatic Subsitution [online]. Accessed June-10. (2020).

Rhoda, M.-D., Martin, J., Blouquit, Y., Garel, M.-C., Edelstein, S. J., & Rosa, J. (1983). Sickle cell hemoglobin fiber formation strongly inhibited by the stanleyville II mutation (α78 Asn→ Lys). *Biochemical and Biophysical Research Communications*, *111*(1), 8–13.

Rivera, A. (2007). Reduced sickle erythrocyte dehydration in vivo by endothelin-1 receptor antagonists. *American Journal of Physiology-Cell Physiology*, *293*(3), C960–C966.

Roberts, J. D., Spodick, J., Cole, J., Bozzo, J., Curtis, S., & Forray, A. (2018). Marijuana use in adults living with sickle cell disease. *Cannabis and Cannabinoid Research*,

3(1), 162–165.

Ryzlak, M. T., & Pietruszko, R. (1987). Purification and characterization of aldehyde dehydrogenase from human erythrocytes. *Archives of Biochemistry and Biophysics*, *255*(2), 409–418.

Safo, M. K. (2019). *Unpublished Data from Personal Communication*.

Safo, M. K., & Abraham, D. J. (2003). X-ray crystallography of hemoglobins. In *Hemoglobin Disorders* (pp. 1–19). Springer.

Safo, M. K., Ahmed, M. H., Ghatge, M. S., & Boyiri, T. (2011). Hemoglobin-Ligand Binding: Understanding Hb Function and Allostery on Atomic Level. *Biochimica et Biophysica Acta - Proteins and Proteomics*, *1814*(6), 797–809.

Safo, M. K., & Kato, G. J. (2014). Therapeutic strategies to alter the oxygen affinity of sickle hemoglobin. *Hematology/Oncology Clinics of North America*, *28*(2), 217–231.

Safo, M. K., Pagare, P. P., Ghatge, M. S., Casu, C., Ghiaccio, V., Anabaraonye, N., … Abdulmalik, O. (2019). PP-14, a Novel Structurally-Enhanced Antisickling Allosteric Hemoglobin Effector, Increases Oxygen Affinity and Disrupts Hemoglobin S Polymer Formation. *Blood*, *134*(S1).

Scott, J. P., Hillery, C. A., Brown, E. R., Misiewicz, V., & Labotka, R. J. (1996). Hydroxyurea therapy in children severely affected with sickle cell disease. *The Journal of Pediatrics*, *128*(6), 820–828.

Smith, W. R., & Alsalman, A. J. (2013). Methadone prescribing in the sickle cell patient. In *Handbook of Methadone Prescribing and Buprenorphine Therapy* (pp. 263–276).

Springer.

Sobota, A., Sabharwal, V., Fonebi, G., & Steinberg, M. (2015). How we prevent and manage infection in sickle cell disease. *British Journal of Haematology*, *170*(6), 757–767.

Standefer, J. C., & Eaton, R. P. (1983). Evaluation of a Colorimetric Method for Determination of Glycosylated Hemoglobin. *Clinical Chemistry*, *29*(1), 135–140.

Sun, K., D'Alessandro, A., Ahmed, M. H., Zhang, Y., Song, A., Ko, T.-P., … Xia, Y. (2017). Structural and Functional Insight of Sphingosine 1-Phosphate-Mediated Pathogenic Metabolic Reprogramming in Sickle Cell Disease. *Scientific Reports*, *7*(1), 15281.

Sun, K., Zhang, Y., D'Alessandro, A., Nemkov, T., Song, A., Wu, H., … Xia, Y. (2016). Sphingosine-1-phosphate promotes erythrocyte glycolysis and oxygen release for adaptation to high-altitude hypoxia. *Nature Communications*, *7*, 12086.

Tamouza, R., Neonato, M.-G., Busson, M., Marzais, F., Girot, R., Labie, D., … Charron, D. (2002). Infectious complications in sickle cell disease are influenced by HLA class II alleles. *Human Immunology*, *63*(3), 194–199.

Thom, C. S., Dickson, C. F., Gell, D. A., & Weiss, M. J. (2013). Hemoglobin variants: Biochemical properties and clinical correlates. *Cold Spring Harbor Perspectives in Medicine*, *3*(3).

Turpeinen, U., Stenman, U., & Roine, R. (1989). Lipuid-Chromatographic Determination of Acetylated Hemoglobin. *Clinical Chemistry*, *35*(1), 33–36.

Uniport.org. Accessed June-01. (2020).

Upadhya, B., Ntim, W., Brandon Stacey, R., Henderson, R., Leedy, D., O'Brien, F. X., & Knovich, M. A. (2013). Prolongation of QT c intervals and risk of death among patients with sickle cell disease. *European Journal of Haematology*, *91*(2), 170–178.

Uwaezuoke, S. N., Ayuk, A. C., Ndu, I. K., Eneh, C. I., Mbanefo, N. R., & Ezenwosu, O. U. (2018). Vaso-occlusive crisis in sickle cell disease: current paradigm on pain management. *Journal of Pain Research*, *11*, 3141–3150.

Vasiliou, V., Pappa, A., & Petersen, D. R. (2000). Role of Aldehyde Dehydrogenases in Endogenous and Xenobiotic Metabolism. *Chemico-Biological Interactions*, *129*, 1–19.

Vasillou, V., Pappa, A., & Estey, T. (2004). Role of human aldehyde dehydrogenases in endobiotic and xenobiotic metabolism. *Drug Metabolism Reviews*, *36*(2), 279–299.

Vichinsky, E., Hoppe, C. C., Ataga, K. I., Ware, R. E., Nduba, V., El-Beshlawy, A., … Howard, J. (2019). A Phase 3 randomized trial of voxelotor in sickle cell disease. *New England Journal of Medicine*, *381*(6), 509–519.

Wahl, S., & Quirolo, K. C. (2009). Current issues in blood transfusion for sickle cell disease. *Current Opinion in Pediatrics*, *21*(1), 15–21.

Ware, R. E., & Aygun, B. (2009). Advances in the use of hydroxyurea. *ASH Education Program Book*, *2009*(1), 62–69.

Washington, C., Green, M., Inati, A., Estepp, J. H., Brown, Abboud, M., … Gordeuk, victor r. (2018). Pharmacokinetics (PK) of voxelotor (GBT440) using population

pharmacokinetic (PPK) and physiologically based pharmacokinetic (PBPK) modeling in pediatric subjects with sickle cell disease (SCD). *HemaSphere. [Abstract No. PF713]*, *2*(Suppl 2), 306.

Wohlford, G. F., Safo, M. K., & Venitz, J. (2015). In-vitro Oxidative and Reductive Metabolism of Allosteric Effectors of Hemoglobin (AEH) in Human Liver Cytosol (HLC) Using NAD+ and NADH as Cofactors. *18th Annual VCU Pharmaceutical Sciences Reserach and Career Day*.

Wroczyński, P., & Wierzchowski, J. (2000). Aromatic aldehydes as fluoregenic indicators for human aldehyde dehydrogenases and oxidases: Substrate and isozyme specificity. *Analyst*, *125*(3), 511–516.

Xu, G. G., Pagare, P. P., Ghatge, M. S., Safo, R. P., Gazi, A., Chen, Q., … Abdulmalik, O. (2017). Design, Synthesis, and Biological Evaluation of Ester and Ether Derivatives of Antisickling Agent 5-HMF for the Treatment of Sickle Cell Disease. *Molecular Pharmaceutics*, *14*(10), 3499–3511. https://doi.org/10.1021/acs.molpharmaceut.7b00553

Yoshida, A., Rzhetsky, A., Hsu, L. C., & Chang, C. (1998). Human aldehyde dehydrogenase gene family. *European Journal of Biochemistry / FEBS*, *251*(3), 549–557.

Zhang, L., Zhu, L., Wang, Y., Jiang, Z., Chai, X., Zhu, Y., … Qi, A. (2012). Characterization and Quantification of Major Constituents of Xue Fu Zhu Yu by UPLC-DAD–MS/MS. *Journal of Pharmaceutical and Biomedical Analysis*, *62*, 203–209.

APPENDIX A

Scientist ® Model Files

1. Michaelis-Menten Kinetics Model

```
// Michaelis-Menten Kinetics Model
// AP/JV XX 2018
// S, initial substrate conc. in mM; V, initial reaction rate in nmoles/min/mg

IndVars: S
DepVars: V
Params: V0, Vmax, Km
V=V0+Vmax*S/(Km+S)
//
***
```

2. Sigmoidal-B_{max} Model

```
// Sigmoidal-Bmax Model
// AP/JV XX 2018
// AEH0, initial AEH conc. in mM; HbAEH, steady-state HbA-AEH adduct conc. in
mM

IndVars: AEH0
DepVars: HbAEH
Params: Bmax, KD, n
HbAEH=Bmax*AEH0^n/(KD^n+AEH0^n)
//
***
```

3. Reversed Sigmoidal-B_{max} Model

```
// Reversed Sigmoidal-Bmax Model
// AP/JV XX 2018
// AEH0, initial AEH conc. in mM; Hb, steady-state HbA conc. in mM

IndVars: AEH0
DepVars: Hb
Params: Bmax, KD, n
Hb=Bmax*(1-(AEH0^n/(KD^n+AEH0^n)))
//
```

4. Simple Kinetic Binding Model

```
// Simple Kinetic Binding Model
// JV, AP, TO, XX, Jun 25, 2018
//
// Assuming bimolecular, reversible interaction between AEH and Hb
// concentrations unit in mM
// kon, forward rate constant in mM-1*hr-1
// koff, backward rate constant in hr-1
//
IndVars: T, AEH0
DepVars: HbAEH
Params: kon, koff, Hb0
// Diff Equations
AEH'=koff*HbAEH-kon*Hb*AEH
HbAEH'=kon*Hb*AEH-koff*HbAEH
//
Hb=Hb0-HbAEH
// IC
t=0
AEH=kon*AEH0/kon
HbAEH=0
// Mathematically, AEH=AEH0; kon was included to fix a Scientist model bug
***
```

5. Simple Metabolism Kinetic Binding Model

```
// Simple metabolism kinetic binding model
// JV, AP, TO, XX, Mar 10, 2020
//
// Assuming bimolecular, reversible interaction between HMF and Hb, irreversible metabolism from HMF to HMFA
// concentrations in mM
// kon in mM-1*hr-1
// koff in hr-1
// kmet in hr-1
//
IndVars: T, HMF0
DepVars: HMF, Hb, HbHMF, HMFA
Params: kon, koff, Hb0, kmet
// Diff Equations
HMF'=koff*HbHMF-kon*Hb*HMF-kmet*HMF
HbHMF'=kon*Hb*HMF-koff*HbHMF
HMFA'=kmet*HMF
//
Hb=Hb0-HbHMF
// IC
t=0
HMF=kon*HMF0/kon
HbHMF=0
HMFA = 0
// Mathematically, HMF=HMF0; kon was included to fix a Scientist model bug
***
```

6. **Simple Dissolution Kinetic Binding Model**

```
// Simple Dissolution Kinetic Binding Model
// Version 3.0
// JV, XX, June.14, 2020
//
// Assuming zero-order input/dissolution of AEH, reversible interaction between AEH in and Hb
// concentrations in mM
// kon in mM-1*hr-1
// koff is first-order backward rate constant in hr-1
// V is WB volume in L
// k0 is zero order dissolution rate constant in mmole*hr-1
// TE is dissolution time in hr
//CRATE dissolution rate in mM
// Adiss the amount dissolved up to time t in mmole
////
IndVars: T, AEH0
DepVars: HbAEH
Params:  k0, V, kon, koff, Hb0
//
// Input, Absorption cpt
D=AEH0*V
TE=D/k0
DRATE2=0
DRATE1=k0
FLAG=UNIT(T-TE)
DRATE=DRATE1*(1-FLAG)+DRATE2*FLAG
CRATE=DRATE/V
//
// Differential equation
// Adiss'=DRATE
AEH'=CRATE+koff*HbAEH-kon*Hb*AEH
HbAEH'=kon*Hb*AEH-koff*HbAEH
//
Hb=Hb0-HbAEH
//
// IC
t=0
//Adiss=0
HbAEH=0
AEH=0
//
***
```

APPENDIX B

Experimental Data for *in-vitro* Concentration- and Time-Dependency HbA-AEH adduct of AEH in HbA Solution

Figure B.3.1. Representative chromatogram for water and 0.003 mM HbA solution.

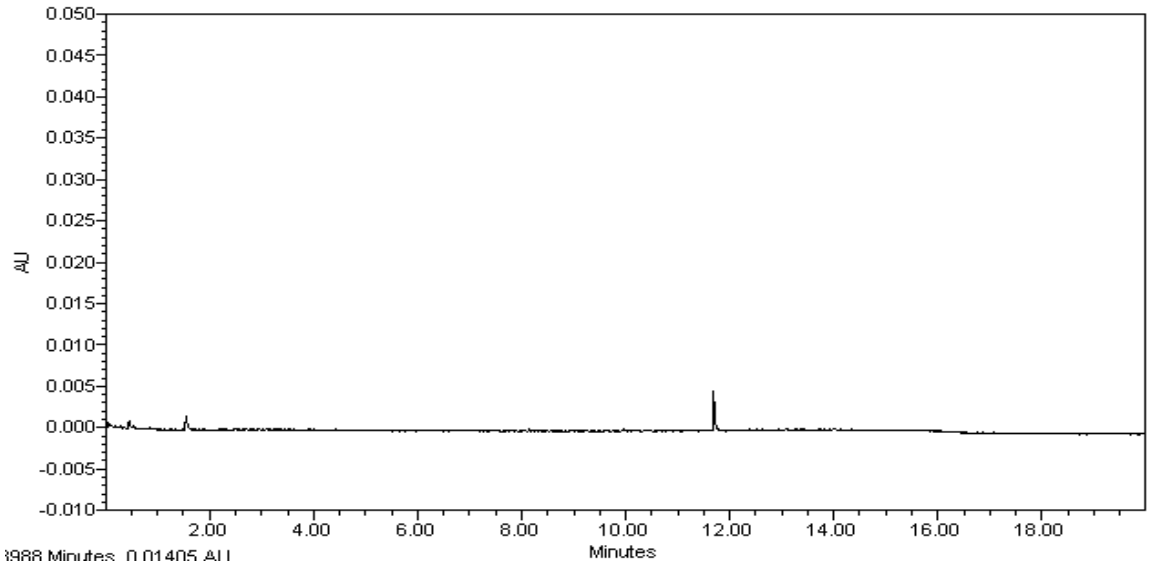

Figure B.3.2. Representative chromatogram for Hb variants.

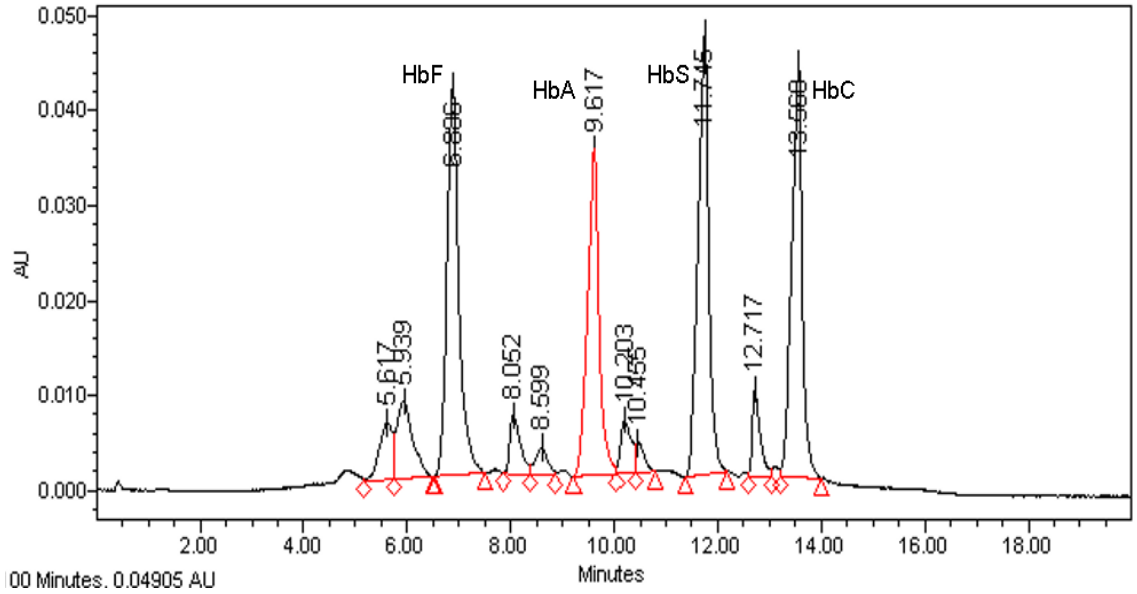

Figure B.3.3. Representative chromatogram for 2,5-DMF.

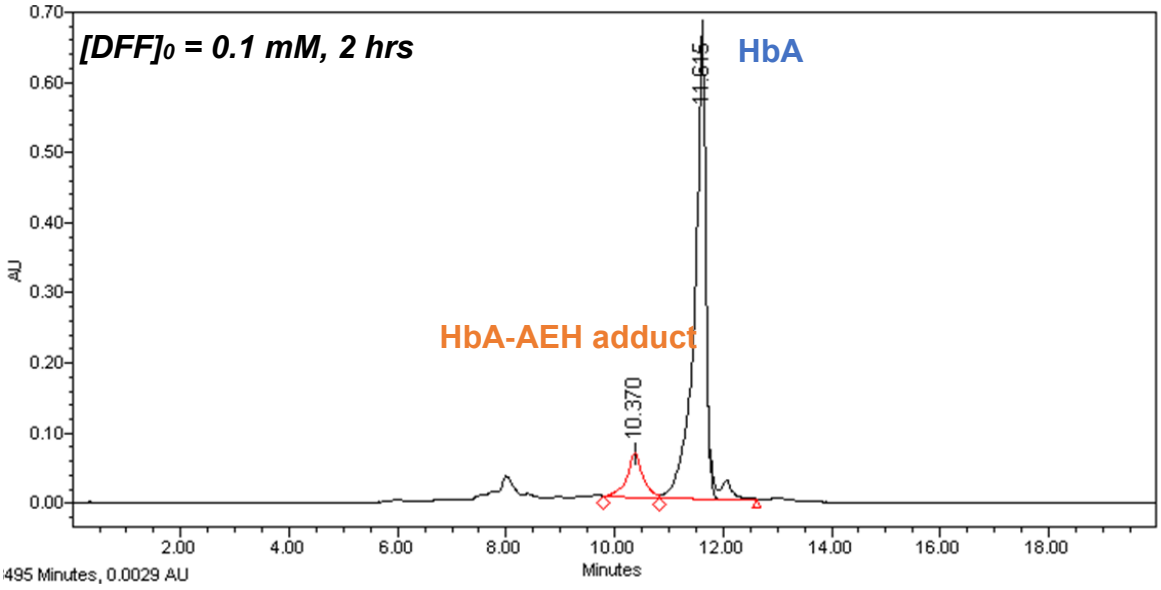

Figure B.3.4. Representative chromatogram for vanillin.

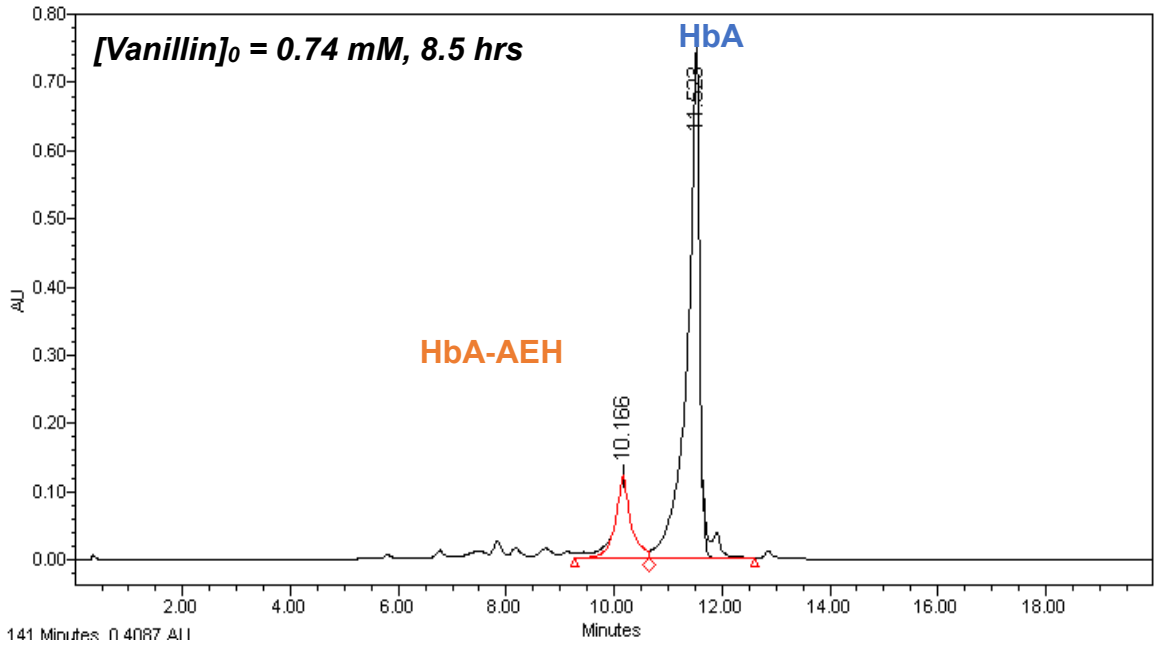

Figure B.3.5. Representative chromatogram for TD-8.

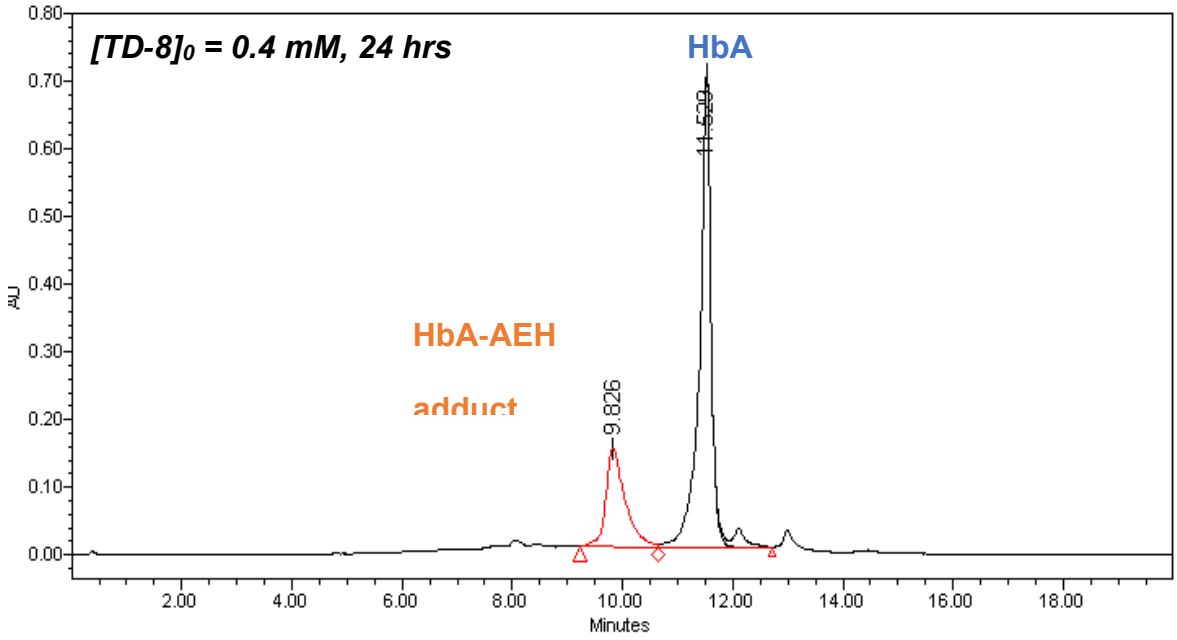

Figure B.3.6. Representative chromatogram for TD-9.

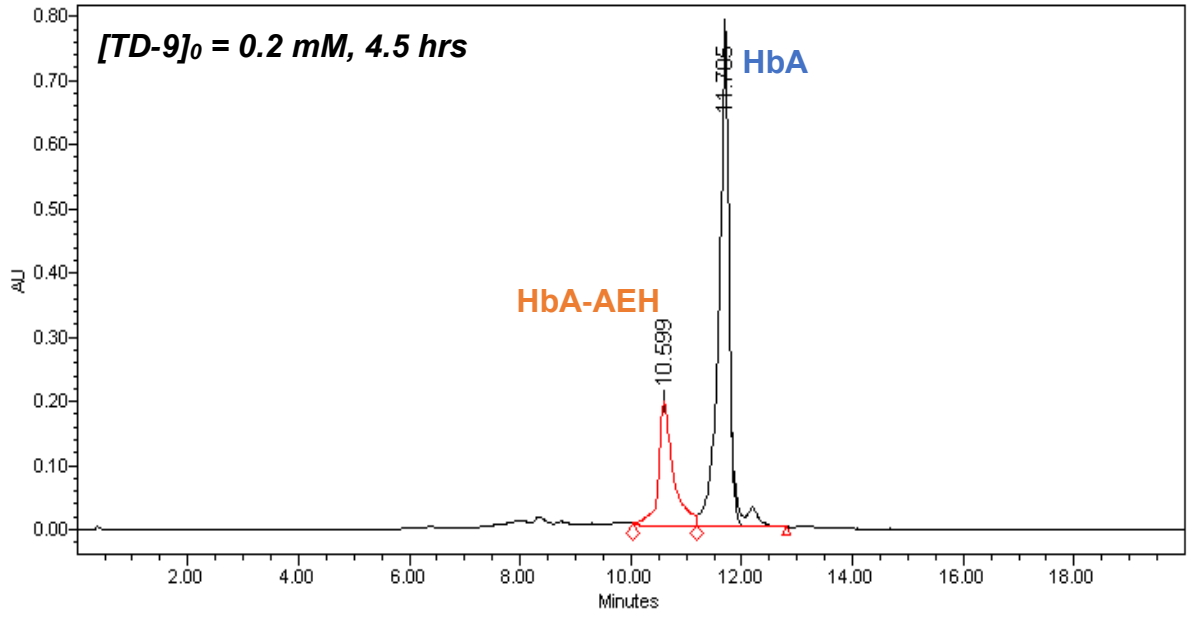

Figure B.3.7. Representative chromatogram for INN-310.

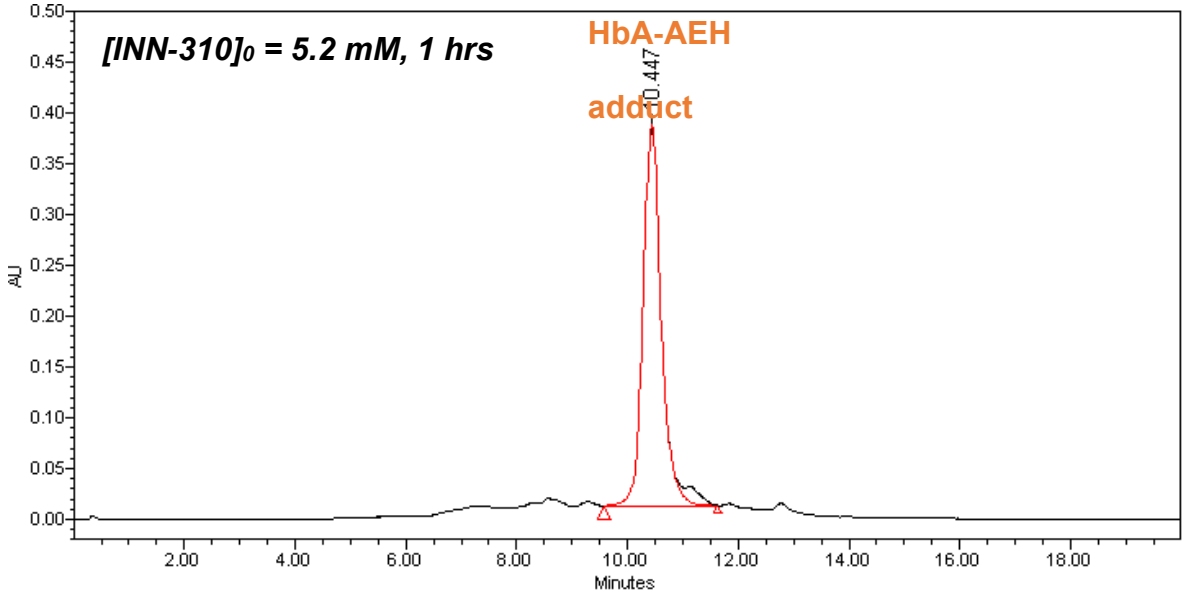

Figure B.3.8. Representative chromatogram for VZHE-039.

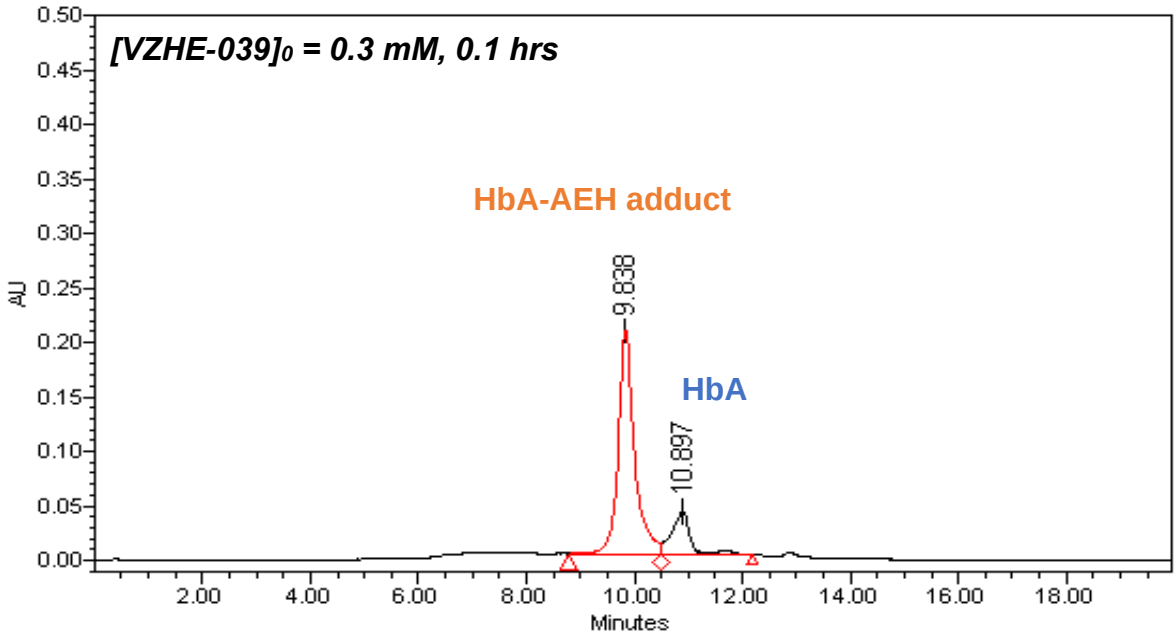

Figure B.3.9. Representative chromatogram for GBT-440.

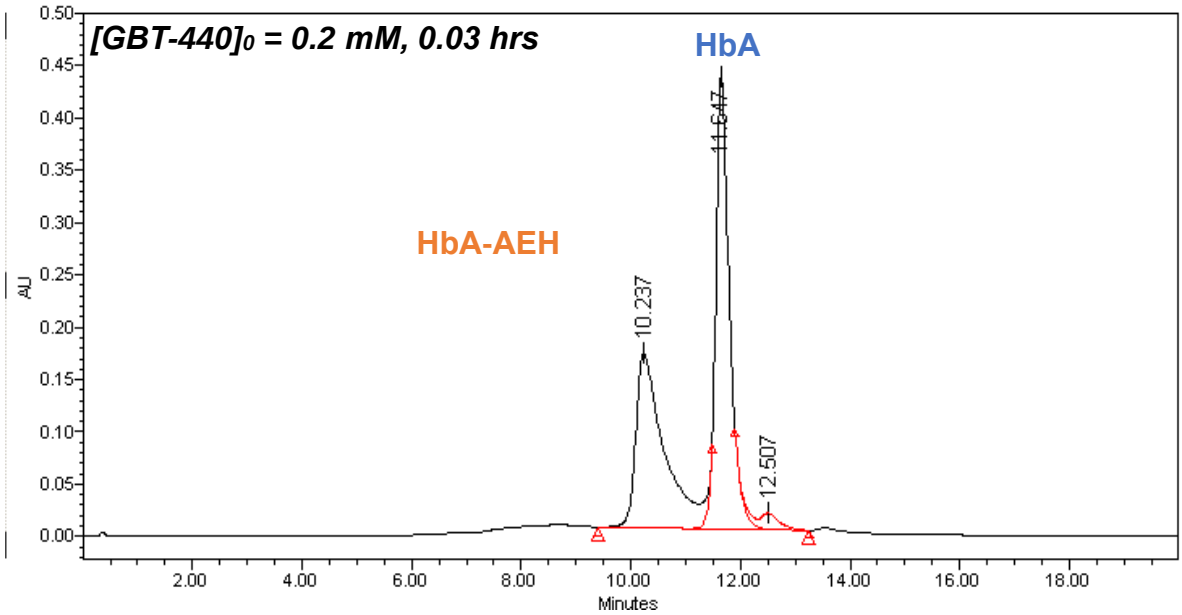

Figure B.3.10. Representative chromatogram for GBT-440 after 0.03 hrs.

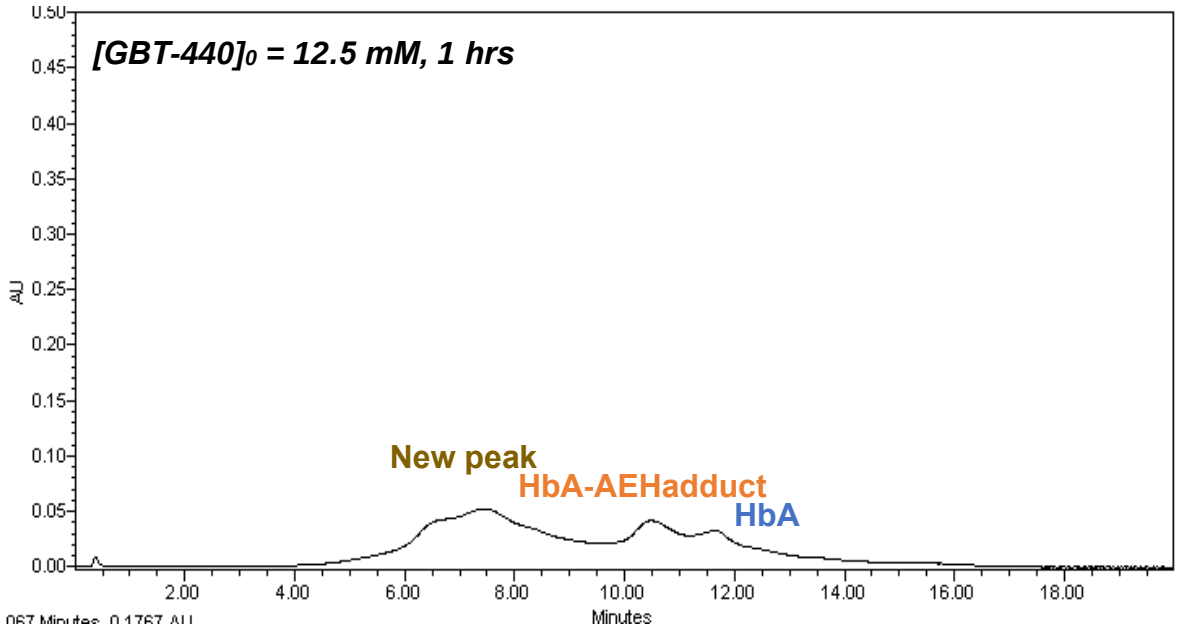

Figure B.3.11. Mass balance assessment of 2,5-DMF.

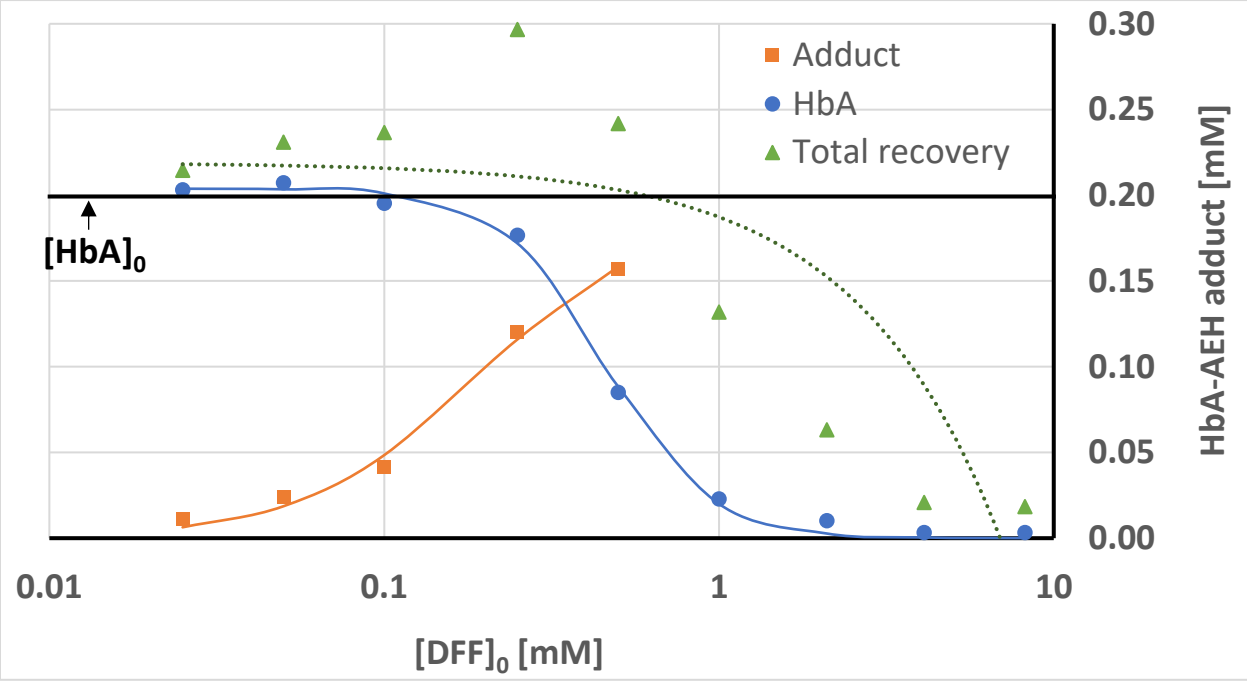

Figure B.3.12. Mass balance assessment of vanillin.

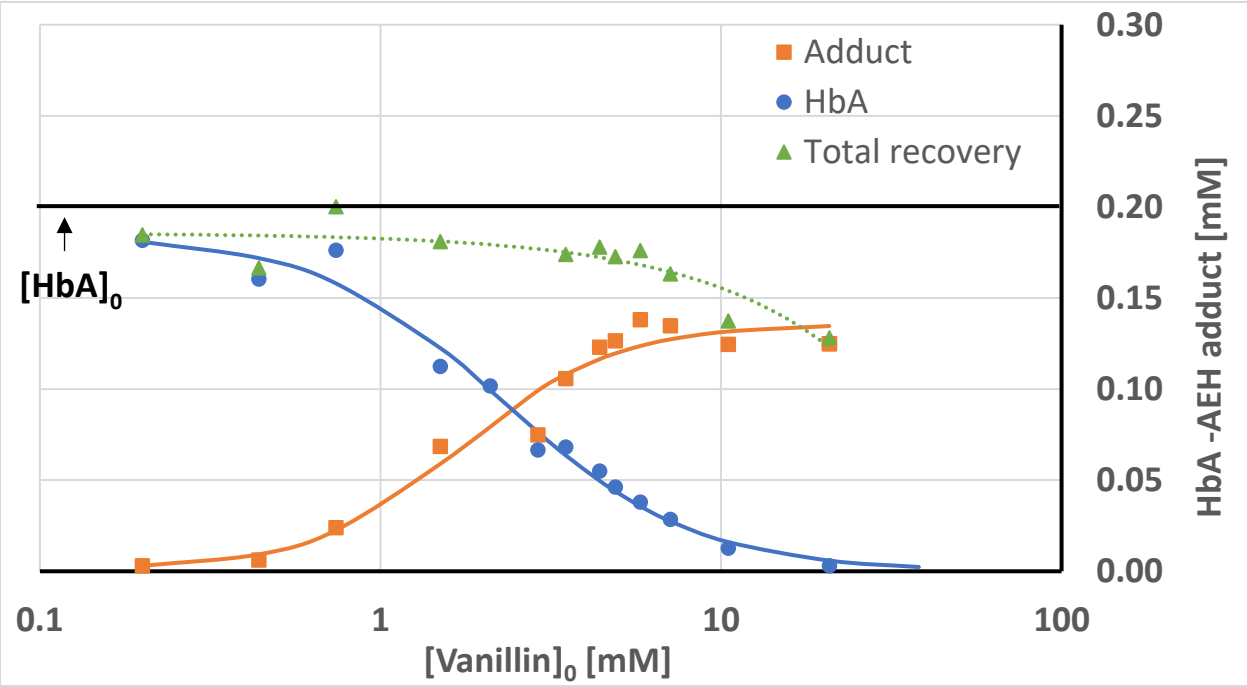

Figure B.3.13. Mass balance assessment of TD-8

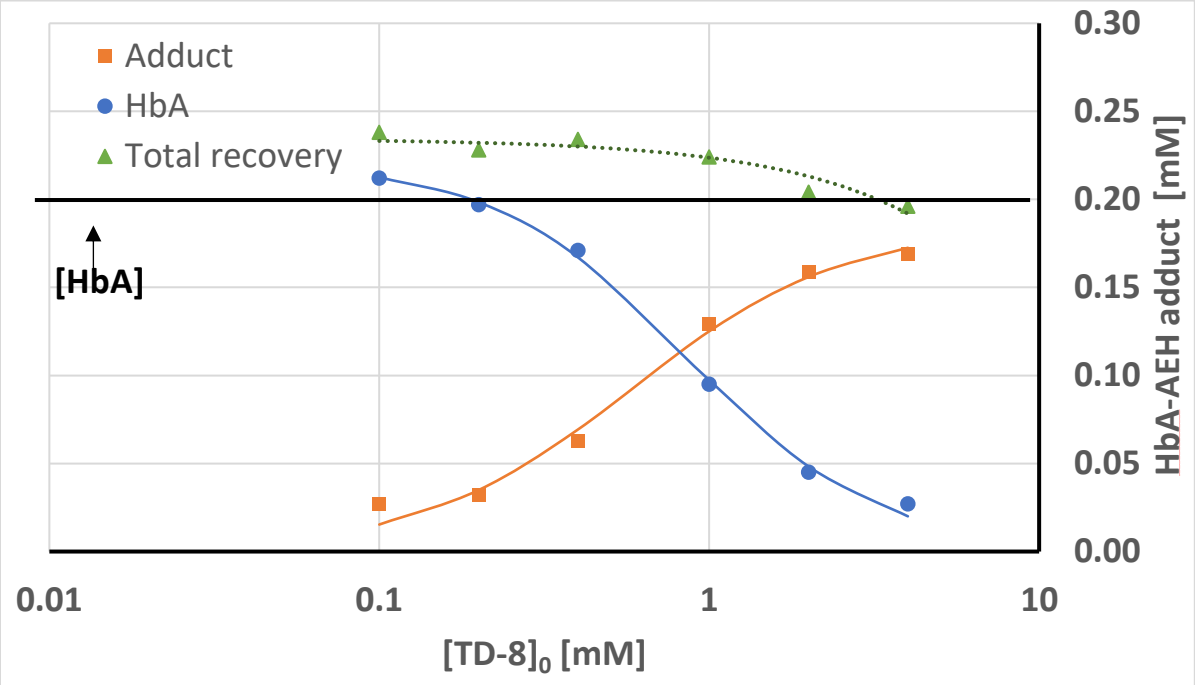

Figure B.3.14. Mass balance assessment of TD-9

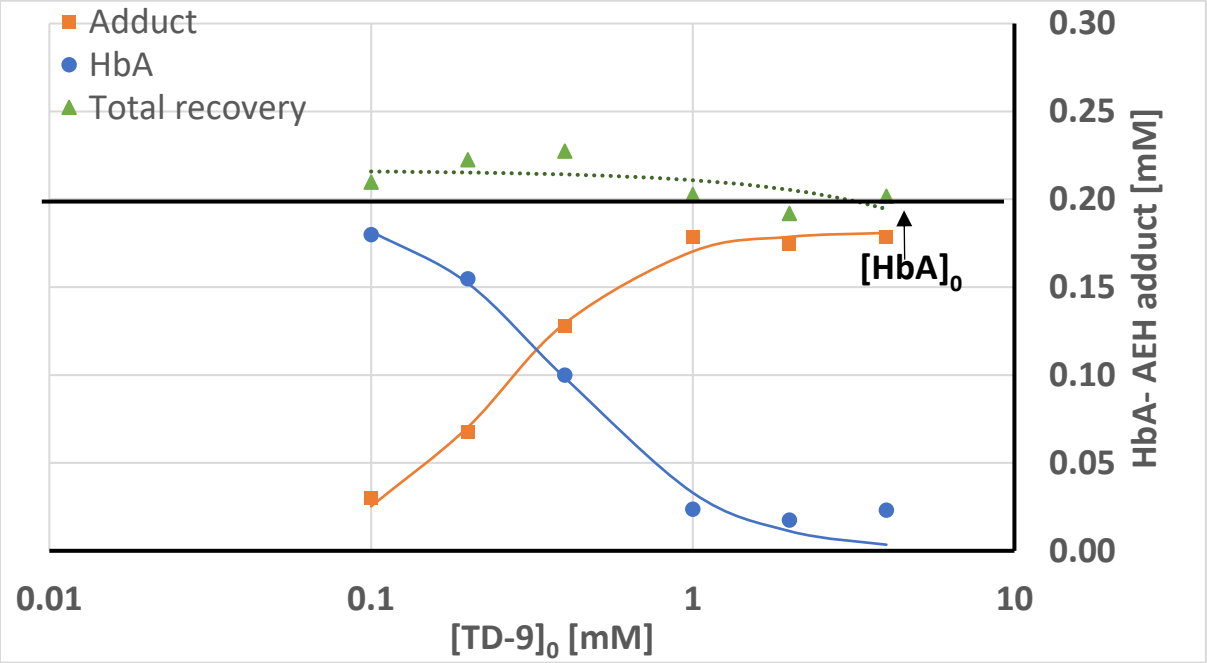

Figure B.3.15. Mass balance assessment of TD-7

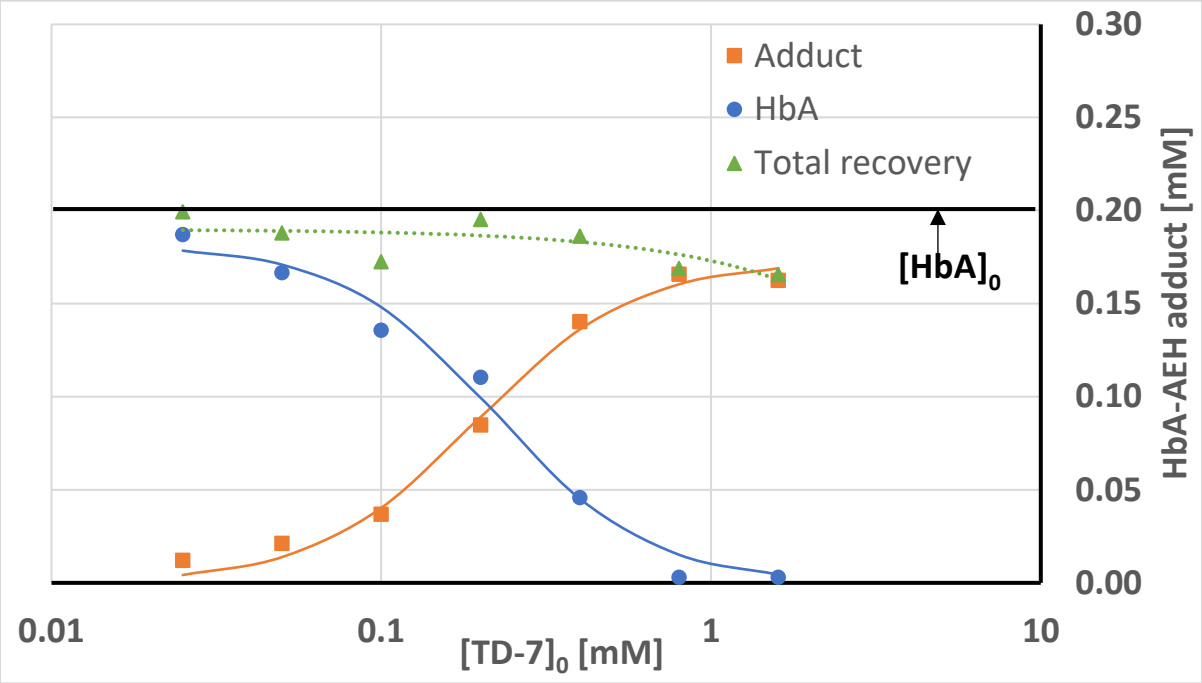

Figure B.3.16. Mass balance assessment of INN-310

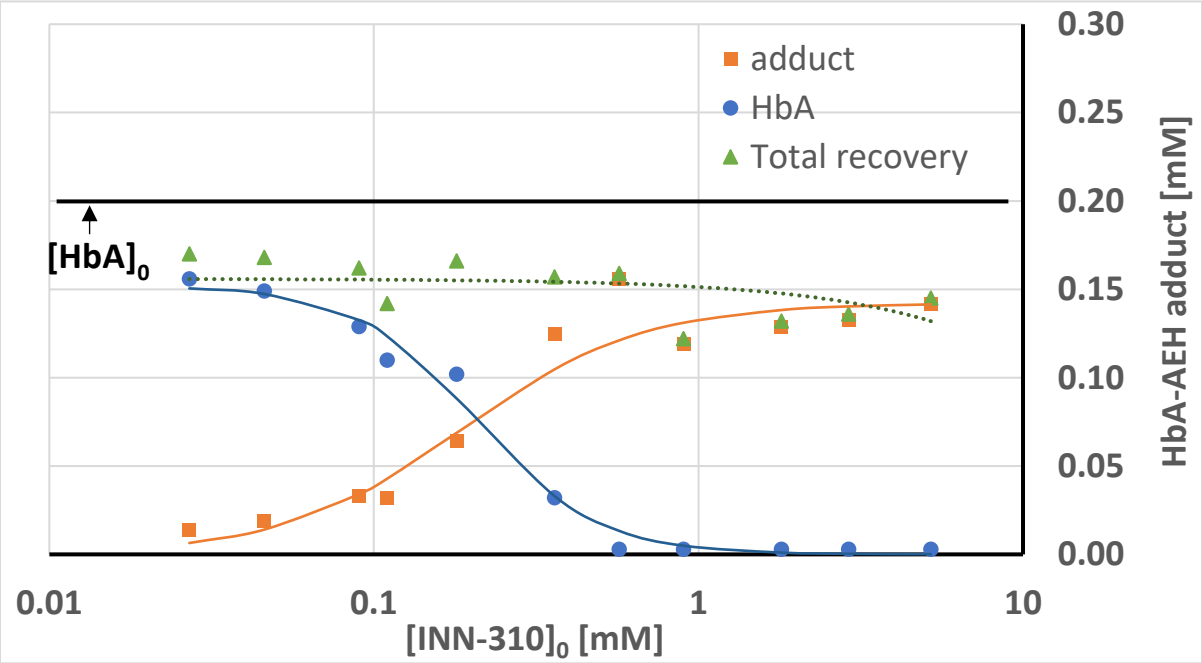

Figure B.3.17. Mass balance assessment of PP-14

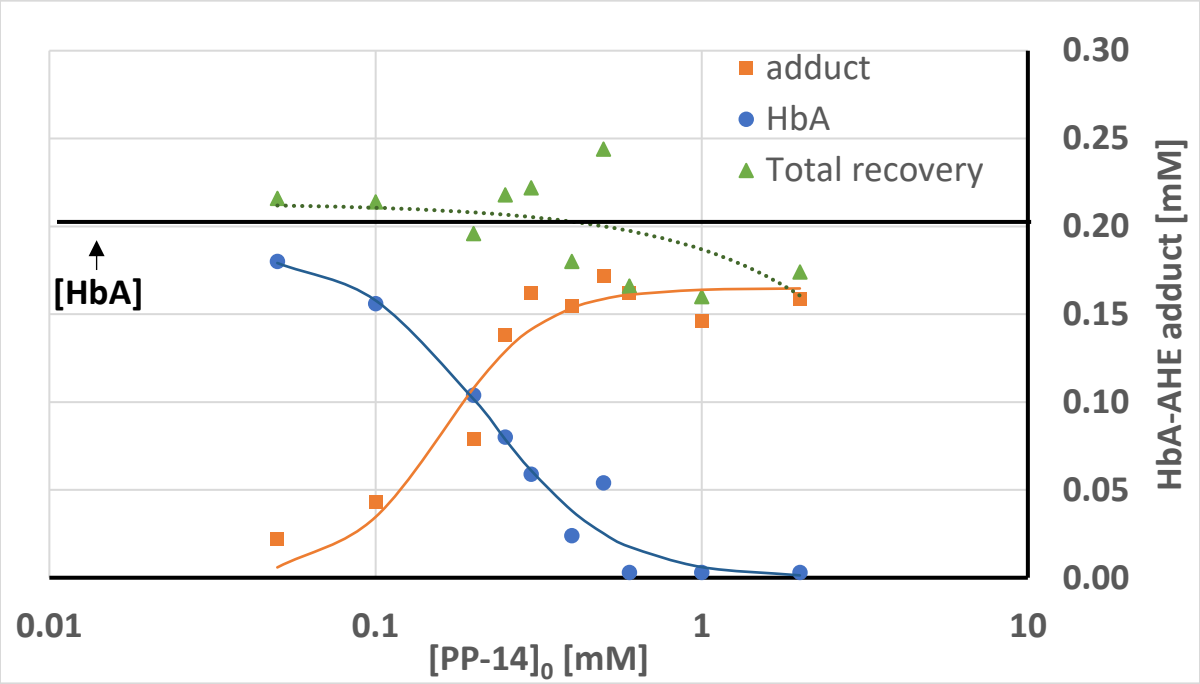

Table B.3.1. Dataset for concentration-dependency HbA-AEH adduct and HbA of 5-HMF in HbA solution.

$[5\text{-HMF}]_0$	[HbA-AEH adduct]	[HbA]
[mM]	[mM]	[mM]
0.06	0.027	0.18
0.13	0.041	0.19
0.25	0.076	0.17
0.5	0.12	0.13
1	0.15	0.066
2	0.18	0.050
4	0.18	0.030

Table B.3.2. Dataset for concentration-dependency HbA-AEH adduct and HbA of 2,5-DMF in HbA solution.

$[2,5\text{-DMF}]_0$	[HbA-AEH adduct]	[HbA]
[mM]	[mM]	[mM]
0.025	0.011	0.20
0.05	0.024	0.21
0.1	0.041	0.20
0.25	0.12	0.18
0.5	0.16	0.085
1	0.11	0.023

Table B.3.3. Dataset for concentration-dependency HbA-AEH adduct and HbA of vanillin in HbA solution.

[Vanillin]$_0$	[HbA-AEH adduct]	[HbA]
[mM]	[mM]	[mM]
0.44	0.006	0.16
0.74	0.024	0.18
1.5	0.069	0.11
2.9	0.07	0.067
3.5	0.11	0.068
4.4	0.12	0.055
4.9	0.13	0.046
5.8	0.14	0.038
7.1	0.13	0.029
11	0.12	0.013
21	0.13	Below eLOQ

Table B.3.4. Dataset for concentration-dependency HbA-AEH adduct and HbA of TD-8 in HbA solution.

[TD-8]$_0$	[HbA-AEH adduct]	[HbA]
[mM]	[mM]	[mM]
0.1	0.027	0.21
0.2	0.032	0.20
0.4	0.063	0.17
1	0.13	0.10
2	0.16	0.045
4	0.17	0.027

Table B.3.5. Dataset for concentration-dependency HbA-AEH adduct and HbA of TD-9 in HbA solution.

$[TD\text{-}9]_0$	[HbA-AEH adduct]	[HbA]
[mM]	[mM]	[mM]
0.1	0.030	0.18
0.2	0.068	0.15
0.4	0.128	0.10
1	0.18	0.02
2	0.17	0.017
4	0.18	0.023

Table B.3.6. Dataset for concentration-dependency HbA-AEH adduct and HbA of TD-7 in HbA solution.

$[TD\text{-}7]_0$	[HbA-AEH adduct]	[HbA]
[mM]	[mM]	[mM]
0.025	0.012	0.19
0.05	0.021	0.17
0.10	0.037	0.14
0.2	0.08	0.11
0.4	0.14	0.046
0.8	0.17	Below eLOQ
1.6	0.16	Below eLOQ

Table B.3.7. Dataset for concentration-dependency HbA-AEH adduct and HbA of INN-310 in HbA solution.

$[INN\text{-}310]_0$	[HbA-AEH adduct]	[HbA]
[mM]	[mM]	[mM]
0.027	0.014	0.16
0.046	0.019	0.15
0.09	0.033	0.13
0.11	0.03	0.110
0.18	0.06	0.102
0.36	0.13	0.032
0.57	0.16	Below eLOQ
0.9	0.12	Below eLOQ
1.8	0.13	Below eLOQ
3	0.13	Below eLOQ
5	0.14	Below eLOQ

Table B.3.8. Dataset for concentration-dependency HbA-AEH adduct and HbA of PP-14 in HbA solution.

$[PP\text{-}14]_0$	[HbA-AEH adduct]	[HbA]
[mM]	[mM]	[mM]
0.05	0.022	0.18
0.1	0.043	0.16
0.2	0.079	0.10
0.25	0.14	0.080
0.3	0.16	0.059
0.4	0.16	0.024
0.5	0.17	0.054
0.6	0.16	Below eLOQ
1	0.15	Below eLOQ
2	0.16	Below eLOQ

Table B.3.9. Dataset for concentration-dependency HbA-AEH adduct and HbA of VZHE-039 in HbA solution.

[VZHE-039]$_0$	[HbA-AEH adduct]	[HbA]
[mM]	[mM]	[mM]
0.03	0.009	0.066
0.04	0.016	0.064
0.06	0.020	0.058
0.08	0.027	0.044
0.12	0.046	0.041
0.25	0.071	0.010
0.35	0.061	Below eLOQ

Table B.3.10. Dataset for concentration-dependency HbA-AEH adduct and HbA of GBT-440 in HbA solution.

$[GBT\text{-}440]_0$	[HbA-AEH adduct]	[HbA]
[mM]	[mM]	[mM]
0.02	0.028	0.22
0.04	0.025	0.19
0.06	0.032	0.17
0.08	0.043	0.16
0.10	0.061	0.15
0.12	0.064	0.15
0.14	0.070	0.14
0.16	0.078	0.13
0.20	0.096	0.12
0.39	0.096	0.10
0.40	0.13	0.11
0.52	0.12	0.11
0.65	0.13	0.10
0.77	0.13	0.10
0.90	0.13	0.10
1.00	0.13	0.10
1.65	0.13	0.11
3.28	0.12	0.11
6.45	0.13	0.097
12.50	0.12	0.093

Table B.3.11. Dataset for time-dependency HbA-AEH adduct of 5-HMF in HbA solution.

T	$[5\text{-HMF}]_0$	[HbA-AEH adduct]
[hr]	[mM]	[mM]
0.03	0.0625	0.022
0.3	0.0625	0.022
1.0	0.0625	0.022
3.0	0.0625	0.024
5.0	0.0625	0.033
6.0	0.0625	0.028
7.0	0.0625	0.029
23.0	0.0625	0.030
24.0	0.0625	0.027
0.0	0.125	0.020
0.3	0.125	0.023
1.0	0.125	0.024
3.0	0.125	0.031
5.0	0.125	0.037
6.0	0.125	0.041
7.0	0.125	0.038
23.0	0.125	0.048
24.0	0.125	0.041
0.03	0.25	0.018
0.3	0.25	0.023
1.0	0.25	0.033
3.0	0.25	0.047
5.0	0.25	0.054
6.0	0.25	0.069
7.0	0.25	0.061
23.0	0.25	0.075
24.0	0.25	0.076
0.03	0.5	0.020
0.3	0.5	0.028
1.0	0.5	0.029
3.0	0.5	0.058
5.0	0.5	0.065
6.0	0.5	0.109
7.0	0.5	0.101
23.0	0.5	0.097

24.0	0.5	0.124
0.0	1	0.021
0.3	1	0.035
1.0	1	0.050
1.5	1	0.083
2.0	1	0.110
3.0	1	0.119
4.0	1	0.126
5.0	1	0.143
6.0	1	0.141
24.0	1	0.147
0.03	2	0.025
0.3	2	0.047
1.0	2	0.111
1.5	2	0.112
2.0	2	0.187
3.0	2	0.137
4.0	2	0.196
5.0	2	0.207
6.0	2	0.183
0.0	4	0.024
0.3	4	0.079
0.7	4	0.136
1.0	4	0.146
1.5	4	0.182
2.0	4	0.306
3.0	4	0.223
4.0	4	0.169
5.0	4	0.183

Table B.3.12. Dataset for time-dependency HbA-AEH adduct of 2,5-DMF in HbA solution.

T	$[2,5\text{-DMF}]_0$	[HbA-AEH adduct]
[hr]	[mM]	[mM]
6.0	0.025	0.013
24.5	0.025	0.020
25.5	0.025	0.011
1.0	0.05	0.012
2.0	0.05	0.016
4.0	0.05	0.020
6.0	0.05	0.021
24.5	0.05	0.031
25.5	0.05	0.024
0.5	0.1	0.009
1.0	0.1	0.015
2.0	0.1	0.023
4.0	0.1	0.031
6.0	0.1	0.036
24.5	0.1	0.052
25.5	0.1	0.041
0.2	0.25	0.008
0.3	0.25	0.020
0.5	0.25	0.024
1.0	0.25	0.035
2.0	0.25	0.046
4.0	0.25	0.066
6.0	0.25	0.079
24.5	0.25	0.120
0.1	0.5	0.017
0.2	0.5	0.020
0.3	0.5	0.021
0.5	0.5	0.030
1.0	0.5	0.047
2.0	0.5	0.072
4.0	0.5	0.094
6.0	0.5	0.113
24.5	0.5	0.157

Table B.3.13. Dataset for time-dependency HbA-AEH adduct of vanillin in HbA solution.

T	$[Vanillin]_0$	[HbA-AEH adduct]
[hr]	[mM]	[mM]
2.0	0.44	0.004
3.0	0.44	0.004
4.5	0.44	0.006
1.0	0.74	0.007
2.0	0.74	0.016
3.0	0.74	0.013
4.5	0.74	0.024
0.5	1.5	0.006
1.0	1.5	0.011
2.0	1.5	0.026
3.0	1.5	0.032
4.5	1.5	0.069
0.5	2.1	0.010
1.0	2.1	0.015
2.0	2.1	0.038
3.0	2.1	0.043
0.5	2.9	0.022
1.0	2.9	0.047
2.0	2.9	0.068
3.0	2.9	0.065
4.5	2.9	0.075
0.5	3.5	0.037
1.0	3.5	0.062
2.0	3.5	0.094
3.0	3.5	0.099
4.5	3.5	0.106
0.5	4.4	0.049
1.0	4.4	0.098
2.0	4.4	0.119
3.0	4.4	0.120
4.5	4.4	0.123
0.5	4.9	0.075
1.0	4.9	0.103
2.0	4.9	0.125
3.0	4.9	0.123

4.5	4.9	0.126
0.5	5.8	0.095
1.0	5.8	0.124
2.0	5.8	0.120
3.0	5.8	0.129
4.5	5.8	0.138
0.1	7.1	0.014
0.3	7.1	0.076
1.0	7.1	0.135
0.1	10.5	0.028
0.3	10.5	0.125
1.0	10.5	0.102
0.1	20.8	0.033
0.3	20.8	0.108
1.0	20.8	0.126

Table B.3.14. Dataset for time-dependency HbA-AEH adduct of TD-8 in HbA solution.

T	$[TD\text{-}8]_0$	[HbA-AEH adduct]
[hr]	[mM]	[mM]
0.1	0.1	0.009
0.5	0.1	0.013
1.0	0.1	0.015
2.0	0.1	0.017
4.0	0.1	0.020
6.0	0.1	0.023
24.0	0.1	0.027
0.1	0.2	0.013
0.5	0.2	0.016
1.0	0.2	0.017
2.0	0.2	0.021
4.0	0.2	0.029
6.0	0.2	0.031
24.0	0.2	0.032
0.1	0.4	0.012
0.5	0.4	0.018
1.0	0.4	0.021
2.0	0.4	0.030
4.0	0.4	0.048
6.0	0.4	0.060
24.0	0.4	0.063
0.1	1	0.011
0.5	1	0.020
1.0	1	0.030
2.0	1	0.063
4.0	1	0.096
6.0	1	0.115
24.0	1	0.129
0.1	2	0.010
0.5	2	0.027
1.0	2	0.050
2.0	2	0.094
4.0	2	0.132
6.0	2	0.154
24.0	2	0.159

0.1	4	0.010
0.5	4	0.035
1.0	4	0.078
2.0	4	0.123
4.0	4	0.154
6.0	4	0.182
24.0	4	0.169

Table B.3.15. Dataset for time-dependency HbA-AEH adduct of TD-9 in HbA solution.

T	$[TD\text{-}9]_0$	[HbA-AEH adduct]
[hr]	[mM]	[mM]
0.1	0.1	0.012
0.5	0.1	0.009
1.0	0.1	0.015
4.5	0.1	0.027
5.0	0.1	0.029
6.0	0.1	0.029
24.0	0.1	0.030
27.0	0.1	0.030
0.1	0.2	0.011
0.5	0.2	0.017
1.0	0.2	0.029
4.5	0.2	0.064
5.0	0.2	0.063
6.0	0.2	0.065
24.0	0.2	0.065
27.0	0.2	0.068
0.1	0.4	0.010
0.5	0.4	0.034
1.0	0.4	0.059
4.5	0.4	0.116
5.0	0.4	0.117
6.0	0.4	0.115
24.0	0.4	0.122
27.0	0.4	0.128
0.1	1	0.010
0.5	1	0.059
1.0	1	0.108
4.5	1	0.172
5.0	1	0.172
6.0	1	0.169
24.0	1	0.175
27.0	1	0.179
0.1	2	0.009
0.5	2	0.093
0.5	2	0.093

1.0	2	0.153
4.5	2	0.172
4.5	2	0.172
5.0	2	0.167
6.0	2	0.165
24.0	2	0.166
27.0	2	0.175
0.5	4	0.109
1.0	4	0.154
4.5	4	0.171
5.0	4	0.173
6.0	4	0.171
24.0	4	0.167
27.0	4	0.179

Table B.3.16. Dataset for time-dependency HbA-AEH adduct of TD-7 in HbA solution.

T	$[TD\text{-}7]_0$	[HbA-AEH adduct]
[hr]	[mM]	[mM]
0.1	0.025	0.006
0.2	0.025	0.007
0.3	0.025	0.011
0.4	0.025	0.013
0.5	0.025	0.012
0.6	0.025	0.016
0.8	0.025	0.014
1.0	0.025	0.013
1.1	0.025	0.015
2.1	0.025	0.014
5.1	0.025	0.012
0.1	0.05	0.008
0.2	0.05	0.016
0.3	0.05	0.015
0.4	0.05	0.018
0.5	0.05	0.022
0.6	0.05	0.026
0.8	0.05	0.022
1.0	0.05	0.025
1.1	0.05	0.024
2.1	0.05	0.022
5.1	0.05	0.021
0.1	0.1	0.015
0.2	0.1	0.023
0.3	0.1	0.029
0.4	0.1	0.035
0.5	0.1	0.034
0.6	0.1	0.042
0.8	0.1	0.040
1.0	0.1	0.043
1.1	0.1	0.045
2.1	0.1	0.043
5.1	0.1	0.037
0.1	0.2	0.026
0.2	0.2	0.053

0.3	0.2	0.062
0.4	0.2	0.066
0.5	0.2	0.077
0.6	0.2	0.084
0.6	0.2	0.083
0.7	0.2	0.085
0.8	0.2	0.078
1.0	0.2	0.087
1.1	0.2	0.085
0.1	0.4	0.059
0.2	0.4	0.087
0.3	0.4	0.103
0.4	0.4	0.117
0.5	0.4	0.125
0.6	0.4	0.129
0.6	0.4	0.131
0.7	0.4	0.136
0.8	0.4	0.139
1.0	0.4	0.146
1.1	0.4	0.140
0.1	0.8	0.104
0.2	0.8	0.137
0.3	0.8	0.153
0.4	0.8	0.174
0.5	0.8	0.171
0.6	0.8	0.164
0.6	0.8	0.166
0.7	0.8	0.166
0.1	1.6	0.130
0.2	1.6	0.155
0.3	1.6	0.162
0.4	1.6	0.163

Table B.3.17. Dataset for time-dependency HbA-AEH adduct of INN-310 in HbA solution.

T	$[INN\text{-}310]_0$	[HbA-AEH adduct]
[hr]	[mM]	[mM]
0.1	0.046	0.005
0.2	0.046	0.008
0.3	0.046	0.015
0.4	0.046	0.016
1.0	0.046	0.022
1.5	0.046	0.016
2.0	0.046	0.018
4.0	0.046	0.015
6.0	0.046	0.014
0.0	0.09	0.004
0.1	0.09	0.010
0.2	0.09	0.024
0.3	0.09	0.024
0.4	0.09	0.026
1.0	0.09	0.030
1.5	0.09	0.028
2.0	0.09	0.028
4.0	0.09	0.025
6.0	0.09	0.026
0.0	0.11	0.004
0.1	0.11	0.012
0.2	0.11	0.021
0.3	0.11	0.027
0.4	0.11	0.030
1.0	0.11	0.039
1.5	0.11	0.041
2.0	0.11	0.041
4.0	0.11	0.031
6.0	0.11	0.026
0.0	0.18	0.013
0.1	0.18	0.023
0.2	0.18	0.037
0.3	0.18	0.044
0.4	0.18	0.044
1.0	0.18	0.061

1.5	0.18	0.058
2.0	0.18	0.063
4.0	0.18	0.054
6.0	0.18	0.054
0.0	0.36	0.022
0.1	0.36	0.044
0.2	0.36	0.054
0.3	0.36	0.079
0.4	0.36	0.087
1.0	0.36	0.117
1.5	0.36	0.106
2.0	0.36	0.113
4.0	0.36	0.106
6.0	0.36	0.109
0.0	0.6	0.034
0.1	0.6	0.068
0.2	0.6	0.103
0.3	0.6	0.105
0.4	0.6	0.113
1.0	0.6	0.137
6.0	0.6	0.136
0.0	0.9	0.024
0.1	0.9	0.042
0.2	0.9	0.072
0.3	0.9	0.087
0.4	0.9	0.101
1.0	0.9	0.130
6.0	0.9	0.103
0.0	1.8	0.027
0.1	1.8	0.056
0.2	1.8	0.079
0.3	1.8	0.079
0.4	1.8	0.110
1.0	1.8	0.120
6.0	1.8	0.112
0.0	2.9	0.032
0.1	2.9	0.063
0.2	2.9	0.099
0.3	2.9	0.109
0.4	2.9	0.122
1.0	2.9	0.120

6.0	2.9	0.116
0.0	5.2	0.024
0.1	5.2	0.067
0.2	5.2	0.109
0.3	5.2	0.116
0.4	5.2	0.132
1.0	5.2	0.130
6.0	5.2	0.123

Table B.3.18. Dataset for time-dependency HbA-AEH adduct of PP-14 in HbA solution.

T	$[PP\text{-}14]_0$	[HbA-AEH adduct]
[hr]	[mM]	[mM]
0.1	0.05	0.016
0.2	0.05	0.017
0.2	0.05	0.016
0.3	0.05	0.021
0.4	0.05	0.019
0.5	0.05	0.018
0.6	0.05	0.019
0.7	0.05	0.021
1.0	0.05	0.019
4.0	0.05	0.022
0.0	0.1	0.017
0.1	0.1	0.031
0.2	0.1	0.028
0.2	0.1	0.030
0.3	0.1	0.034
0.4	0.1	0.034
0.5	0.1	0.033
0.6	0.1	0.033
0.7	0.1	0.039
1.0	0.1	0.040
4.0	0.1	0.043
0.0	0.2	0.036
0.1	0.2	0.058
0.2	0.2	0.058
0.2	0.2	0.055
0.3	0.2	0.065
0.4	0.2	0.063
0.5	0.2	0.065
0.6	0.2	0.065
0.7	0.2	0.076
1.0	0.2	0.076
4.0	0.2	0.079
0.1	0.25	0.061
0.2	0.25	0.077
0.3	0.25	0.100

0.5	0.25	0.087
1.0	0.25	0.103
2.0	0.25	0.101
4.0	0.25	0.138
0.1	0.3	0.059
0.2	0.3	0.093
0.3	0.3	0.092
0.5	0.3	0.133
1.0	0.3	0.117
2.0	0.3	0.141
4.0	0.3	0.162
0.1	0.4	0.101
0.2	0.4	0.118
0.3	0.4	0.142
0.5	0.4	0.145
1.0	0.4	0.156
2.0	0.4	0.194
0.0	0.5	0.071
0.1	0.5	0.114
0.2	0.5	0.140
0.2	0.5	0.131
0.3	0.5	0.148
0.4	0.5	0.157
0.5	0.5	0.153
0.6	0.5	0.157
0.7	0.5	0.100
1.0	0.5	0.158
4.0	0.5	0.172
0.1	0.6	0.085
0.3	0.6	0.155
0.5	0.6	0.150
1.0	0.6	0.123
2.0	0.6	0.151
4.0	0.6	0.162
0.0	1.0	0.072
0.1	1.0	0.118
0.2	1.0	0.128
0.2	1.0	0.151
0.3	1.0	0.142
0.4	1.0	0.129
0.5	1.0	0.141

0.6	1.0	0.146
0.0	2.0	0.073
0.1	2.0	0.112
0.2	2.0	0.135
0.3	2.0	0.151
0.4	2.0	0.165
0.5	2.0	0.164
0.6	2.0	0.159

Table B.3.19. Dataset for time-dependency HbA-AEH adduct of VZHE-039 in HbA solution.

T	$[VZHE\text{-}039]_0$	[HbA-AEH adduct]
[hr]	[mM]	[mM]
0.03	0.026	0.005
0.05	0.026	0.010
0.10	0.026	0.009
0.15	0.026	0.008
0.20	0.026	0.010
0.25	0.026	0.007
0.30	0.026	0.008
0.35	0.026	0.007
0.40	0.026	0.009
0.03	0.04	0.009
0.05	0.04	0.013
0.10	0.04	0.021
0.15	0.04	0.018
0.20	0.04	0.018
0.25	0.04	0.018
0.30	0.04	0.019
0.35	0.04	0.017
0.03	0.06	0.011
0.05	0.06	0.015
0.10	0.06	0.018
0.15	0.06	0.020
0.20	0.06	0.020
0.25	0.06	0.021
0.30	0.06	0.020
0.35	0.06	0.020
0.03	0.083	0.011
0.05	0.083	0.020
0.10	0.083	0.020
0.15	0.083	0.025
0.20	0.083	0.026
0.25	0.083	0.027
0.30	0.083	0.027
0.35	0.083	0.028
0.40	0.083	0.027
0.03	0.124	0.018

0.05	0.124	0.031
0.10	0.124	0.037
0.15	0.124	0.036
0.20	0.124	0.040
0.25	0.124	0.046
0.30	0.124	0.044
0.35	0.124	0.046
0.40	0.124	0.046
0.03	0.25	0.029
0.05	0.25	0.046
0.10	0.25	0.058
0.15	0.25	0.057
0.20	0.25	0.061
0.25	0.25	0.065
0.30	0.3	0.060
0.35	0.3	0.068
0.40	0.3	0.071
0.03	0.3	0.014
0.05	0.3	0.056
0.10	0.3	0.076
0.15	0.3	0.076
0.20	0.3	0.081
0.25	0.3	0.072
0.30	0.3	0.077
0.35	0.3	0.083
0.40	0.3	0.076

Table B.3.20. Summary of Experimental Design and Chromatographic Metrics

	Unit	**5-HMF**	**2,5-DMF**	**Vanillin**	**TD-8**	**TD-9**	**TD-7**	**PP-14**	**INN-310**	**VZHE-039**	**GBT-440**
Nominal $[HbA]_0$	[mM]	0.20	0.20	0.20	0.20	0.20	0.20	0.20	0.20	0.10	0.20
Actual $[HbA]_0$	[mM]	0.18	0.20	0.20	0.19	0.19	0.19	0.19	0.18	0.08	0.20
%DMSO	[%]	< 2%	< 2%	<5%	< 4%	< 4%	< 2%	< 2%	< 3%	< 1%	< 2%
Storage	[day]	3	4	5	6	5	14	6	23	3	5
Date		Aug-18	Jun-19	May-19	Feb-19	Feb-19	Sep-18	Apr-19	May-19	Feb-19	Mar-19
$[AEH]_0$	[mM]	0.06 - 4	0.025 - 1, (8.2)	(0.02), 0.44 - 21	(0.02, 0.04), 0.1 - 4	(0.02, 0.04), 0.1 - 4	0.025 - 1.6	(0.025), 0.05 - 2	(0.027), 0.05 - 5.2	0.03 - 0.4, (0.5, 1)	0.02 - 12.5
Time	[hr]	0.03 - 24	0.03 - 25.5	0.03 - 27	0.05 - 24	0.05 - 24	0.1 - 5.1	0.025 - 2	0.03 -6	0.025-0.65	0.03 - 4.5
Retention of Adduct	[min]	8.6	10.3	9.2	10.1	10.7	8.6	10.3	10.5	9.9	10.7
Retention of HbA	[min]	9.9	11.5	10.5	11.5	11.8	9.9	11.6	11.5	11.1	11.9
Time between peaks	[min]	1.3	1.2	1.3	1.4	1.1	1.3	1.3	1	1.2	1.2
Resolution		2.8	1.9	2.3	3.1	2.4	2.2	1.6	1.8	1.8	1.8
Time to achieve SS	[hr]	7 < t < 24	6 < t < 24	1< t < 27	6 < t < 24	1 < t < 4.5	0.5 < t < 0.6	0.3 < t < 4	0.4 < t < 1	0.4 < t < 0.5	0 < t < 0.03

APPENDIX C

Experimental Data for *in-vitro* Metabolism of AEH in Human Liver Cytosol (HLC)

Table C.4.1. Concentration-dependent oxidative metabolism of acetaldehyde in HLC

[Acetaldehyde]$_0$	**Initial Reaction Rate (v_i)**	**SD**
[mM	**[nmole/min/mg]**	
0	0.38	0.003
0.001	0.64	0.17
0.002	0.60	0.08
0.004	0.67	0.04
0.007	0.88	0.13
0.014	0.95	0.10
0.028	1.05	0.07
0.056	1.32	0.18
0.113	1.39	0.22
0.450	1.54	0.17
0.900	1.47	0.37

Table C.4.2. Concentration-dependent oxidative metabolism of acetaldehyde (0.5%DMSO) in HLC

[Acetaldehyde]$_0$	Initial Reaction Rate (v_i)	SD
[mM]	[nmole/min/mg]	
0	0.24	0.008
0.001	0.25	0.04
0.002	0.28	0.00
0.004	0.33	0.05
0.007	0.45	0.03
0.014	0.58	0.02
0.028	0.76	0.01
0.056	0.84	0.02
0.11	0.93	0.02
0.23	0.97	0.02
0.45	1.03	0.03
0.90	1.09	0.02

Table C.4.3. Concentration-dependent oxidative metabolism of ethanol in HLC

[Ethanol]$_0$	Initial Reaction Rate (v_i)	SD
[mM	[nmole/min/mg]	
0	0.47	0.06
0.1	0.64	0.12
0.2	0.68	0.02
0.4	0.80	0.02
0.7	1.07	0.03
1.4	1.35	0.05
2.8	1.60	0.01
5.6	1.87	0.05
11	2.06	0.03
23	2.26	0.02
45	2.26	0.15
90	2.44	0.21

Table C.4.4. Concentration-dependent oxidative metabolism of 5-HMF in HLC

$[5\text{-HMF}]_0$	Initial Reaction Rate (v_i)	SD
[mM]	[nmole/min/mg]	
0	0.47	0.03
1.4	0.59	0.02
2.8	0.67	0.05
4.2	0.74	0.03
5.6	0.77	0.03
11	0.90	0.05
17	1.01	0.06
23	1.14	0.05
45	1.58	0.20
68	2.08	0.16
90	3.00	0.32

Table C.4.5. Concentration-dependent oxidative metabolism of 2,5-DMF in HLC

$[2,5\text{-DMF}]_0$	Initial Reaction Rate (v_i)	SD
[mM]	[nmole/min/mg]	
0	0.47	0.04
0.003	0.54	0.01
0.007	0.66	0.14
0.013	0.83	0.26
0.026	0.80	0.05
0.052	0.95	0.04
0.104	0.69	0.02
0.208	0.69	0.18
0.420	0.53	0.06
0.830	0.65	0.24
1.670	0.47	0.01
3.330	0.39	0.16

Table C.4.6. Concentration-dependent oxidative metabolism of TD-8 in HLC

$[TD\text{-}8]_0$	Initial Reaction Rate (v_i)	SD
[mM]	[nmole/min/mg]	
0	0.65	0.08
0.02	0.70	0.07
0.04	0.60	0.14
0.08	0.64	0.10
0.12	0.58	0.07
0.15	0.60	0.09
0.18	0.55	0.06
0.24	0.54	0.12
0.30	0.52	0.10
0.36	0.48	0.09
0.48	0.41	0.05
0.60	0.46	0.09

Table C.4.7. Concentration-dependent oxidative metabolism of TD-9 in HLC

$[TD\text{-}9]_0$	Initial Reaction Rate (v_i)	SD
[mM]	[nmole/min/mg]	
0	0.62	0.07
0.004	0.64	0.00
0.01	0.70	0.03
0.02	0.58	0.09
0.03	0.64	0.07
0.05	0.64	0.20
0.09	0.54	0.02
0.18	0.46	0.05
0.30	0.44	0.04

Table C.4.8. Concentration-dependent oxidative metabolism of TD-7 in HLC

$[TD\text{-}7]_0$	Initial Reaction Rate (v_i)	SD
[mM]	[nmole/min/mg]	
0	0.44	0.05
0.01	0.47	0.04
0.02	0.51	0.03
0.04	0.51	0.05
0.08	0.56	0.07
0.14	0.59	0.07
0.18	0.67	0.04
0.37	0.79	0.09

Table C.4.9. Concentration-dependent oxidative metabolism of VZHE-039 in HLC

$[VZHE\text{-}039]_0$	Initial Reaction Rate (v_i)	SD
[mM]	[nmole/min/mg]	
0	0.55	0.02
0.21	0.53	0.04
0.38	0.45	0.03
0.41	0.54	0.00
0.53	0.47	0.02
0.74	0.53	0.04

Table C.4.10. Concentration-dependent oxidative metabolism of INN-310 (0.5%DMSO) in HLC

$[INN\text{-}310]_0$	Initial Reaction Rate (v_i)	SD
[mM]	[nmole/min/mg]	
0	0.27	0.01
0.0003	0.25	0.01
0.0006	0.26	0.01
0.001	0.25	0.01
0.002	0.27	0.01
0.005	0.26	0.01
0.009	0.26	0.03
0.02	0.30	0.01
0.04	0.33	0.03
0.08	0.38	0.03
0.15	0.49	0.03
0.30	0.75	0.04

Table C.4.11. Concentration-dependent reductive metabolism of 5-HMF in HLC

$[5\text{-}HMF]_0$	Initial Reaction Rate (v_i)	SD
[mM]	[nmole/min/mg]	
0	2.93	0.37
0.06	2.20	1.69
0.12	3.23	2.34
0.23	2.55	1.00
0.47	3.76	0.70
0.94	4.01	0.91
1.9	4.28	0.83
3.8	4.76	0.89
7.5	4.96	1.57
15	5.55	1.71
30	6.02	1.27
60	6.23	0.66

Table C.4.12. Concentration-dependent reductive metabolism of 2,5-DMF in HLC

$[2,5\text{-DMF}]_0$	Initial Reaction Rate (v_i)	SD
[mM]	[nmole/min/mg]	
0	1.84	0.41
0.003	1.36	1.82
0.007	1.81	1.83
0.013	3.64	0.53
0.026	3.67	0.15
0.052	3.87	0.75
0.104	3.20	1.46
0.208	2.76	3.22
0.42	5.18	2.83
0.83	7.65	0.59
1.67	11.35	1.11
3.33	13.26	1.15

Table C.4.13. Concentration-dependent reductive metabolism of TD-8 in HLC

$[\text{TD-8}]_0$	Initial Reaction Rate (v_i)	SD
[mM]	[nmole/min/mg]	
0	1.38	1.01
0.02	0.42	0.44
0.04	1.69	0.02
0.08	0.58	0.31
0.12	0.63	0.59
0.15	1.53	0.32
0.18	1.00	0.09
0.24	1.43	0.44
0.30	2.06	0.58
0.36	0.63	0.53
0.48	1.29	1.29
0.60	2.51	0.72

Table C.4.14. Concentration-dependent reductive metabolism of TD-9 in HLC

$[TD\text{-}9]_0$	Initial Reaction Rate (v_i)	SD
[mM]	[nmole/min/mg]	
0	1.84	0.87
0.004	1.44	0.37
0.01	1.92	0.55
0.02	0.87	0.03
0.03	0.83	0.20
0.05	1.03	0.27
0.09	1.26	0.28
0.18	1.34	0.62
0.30	0.93	0.43

Table C.4.15. Concentration-dependent reductive metabolism of TD-7 in HLC

$[TD\text{-}7]_0$	Initial Reaction Rate (v_i)	SD
[mM]	[nmole/min/mg]	
0	1.40	0.06
0.001	1.33	0.57
0.016	0.89	0.07
0.033	1.03	1.63
0.066	1.52	0.93
0.13	1.13	0.77
0.20	1.20	0.24
0.26	1.74	1.90
0.35	2.14	0.36
0.40	1.77	1.22
0.46	2.42	1.45
0.53	1.14	1.44

Table C.4.16. Concentration-dependent reductive metabolism of VZHE-039 in HLC

$[VZHE\text{-}039]_0$	Initial Reaction Rate (v_i)	SD
[mM]	[nmole/min/mg]	
0	1.52	0.67
0.019	1.42	0.76
0.038	2.12	1.13
0.075	1.33	1.38
0.15	1.27	0.72
0.30	1.31	1.46
0.45	1.96	1.43
0.6	1.57	1.05
0.8	2.12	1.43
0.9	2.23	0.82
1.0	2.34	1.02
1.2	1.67	1.06

Table C.4.17. Concentration-dependent reductive metabolism of INN-310 (0.5%DMSO) in HLC

$[INN\text{-}310]_0$	Initial Reaction Rate (v_i)	SD
[mM]	[nmole/min/mg]	
0	0.27	0.03
0.0003	0.28	0.03
0.0006	0.32	0.04
0.001	0.26	0.05
0.002	0.26	0.02
0.005	0.29	0.05
0.009	0.24	0.05
0.02	0.27	0.03
0.04	0.22	0.04
0.08	0.19	0.10
0.15	0.20	0.04
0.30	0.02	0.02

APPENDIX D

Experimental Data for *in-vitro* Disposition of VZHE-039 and 5-HMF in WB

Table D.5.1. Dataset for VZHE-039 plasma – t profile.

T	$[VZHE\text{-}039]_0$	c_p
[hr]	[mM]	[mM]
0.09	0.27	0.20
0.5	0.27	0.21
1	0.27	0.07
1.5	0.27	0.08
2	0.27	0.12
2.5	0.27	0.09
3	0.27	0.09
5	0.27	0.08
8	0.27	0.07
15	0.27	0.05
24	0.27	0.04
0.09	0.46	0.33
1.5	0.46	0.16
2	0.46	0.28
2.5	0.46	0.26
3	0.46	0.19
5	0.46	0.22
8	0.46	0.11
12	0.46	0.09
15	0.46	0.07
24	0.46	0.06
0.09	0.92	0.45
0.5	0.92	0.32
1	0.92	0.25
1.5	0.92	0.26
2	0.92	0.29
2.5	0.92	0.31
5	0.92	0.34

8	0.92	0.25
12	0.92	0.22
15	0.92	0.16
24	0.92	0.18
0.09	1.44	0.39
0.5	1.44	0.56
1	1.44	0.32
1.5	1.44	0.44
2	1.44	0.57
3	1.44	0.50
5	1.44	0.46
8	1.44	0.42
12	1.44	0.34
15	1.44	0.30
24	1.44	0.22
0.09	1.96	0.47
0.5	1.96	0.59
1	1.96	0.37
1.5	1.96	0.53
2	1.96	0.87
2.5	1.96	0.75
3	1.96	0.76
5	1.96	0.67
8	1.96	0.51
12	1.96	0.41
15	1.96	0.31
24	1.96	0.27
0.09	2.65	0.45
0.5	2.65	0.78
1	2.65	0.75
1.5	2.65	1.22
2	2.65	1.02
2.5	2.65	0.97
3	2.65	0.93
5	2.65	0.71
8	2.65	0.44
12	2.65	0.46
15	2.65	0.40
24	2.65	0.31
0.09	4.2	0.42
0.5	4.2	0.62

1	4.2	0.46
1.5	4.2	0.97
2	4.2	1.11
2.5	4.2	1.50
3	4.2	1.35
5	4.2	1.24
8	4.2	1.16
12	4.2	1.05
15	4.2	0.76
24	4.2	0.69
0.5	7.8	0.24
1	7.8	1.06
1.5	7.8	1.48
2	7.8	1.85
2.5	7.8	2.85
3	7.8	3.00
5	7.8	3.41
8	7.8	3.08
12	7.8	2.98
15	7.8	2.90
24	7.8	2.59

Table D.5.2. Dataset for concentration-dependency HbA and HbA-AEH adduct of VZHE-039 in WB.

[VZHE-039]$_0$	[HbA-AEH Adduct]	[HbA]
[mM]	[mM]	[mM]
0.27	0.19	2.61
0.46	0.21	2.24
0.92	0.36	1.86
1.44	0.76	1.57
1.96	0.93	1.31
2.65	1.23	1.45
4.2	1.57	0.53
7.8	1.44	Below eLOQ

Table D.5.3. Dataset for concentration-dependency HbA and HbA-AEH adduct of 5-HMF in WB.

[5-HMF]$_0$	[HbA-AEH Adduct]	[HbA]
[mM]	[mM]	[mM]
0.5	0.18	1.62
1	0.40	1.53
2	0.75	1.25
3	0.98	1.05
5	1.17	0.87

Table D.5.4. Dataset for time-dependency HbA-AEH adduct of VZHE-039 in WB.

T	$[VZHE\text{-}039]_0$	[HbA-AEH adduct]
[hr]	[mM]	[mM]
0.09	0.27	0.09
0.5	0.27	0.13
1	0.27	0.25
1.5	0.27	0.21
2	0.27	0.20
2.5	0.27	0.13
3	0.27	0.24
5	0.27	0.23
8	0.27	0.23
12	0.27	0.26
15	0.27	0.27
24	0.27	0.19
0.09	0.46	0.12
1.5	0.46	0.14
2	0.46	0.16
2.5	0.46	0.15
3	0.46	0.12
5	0.46	0.14
8	0.46	0.18
12	0.46	0.25
15	0.46	0.25
24	0.46	0.21
0.09	0.92	0.09
0.5	0.92	0.13
1	0.92	0.24
1.5	0.92	0.24
2	0.92	0.20
2.5	0.92	0.19
3	0.92	0.35
5	0.92	0.42
8	0.92	0.33
12	0.92	0.41
15	0.92	0.44
24	0.92	0.36
0.09	1.44	0.09
0.5	1.44	0.17

1	1.44	0.40
1.5	1.44	0.36
2	1.44	0.36
2.5	1.44	0.36
3	1.44	0.53
5	1.44	0.75
8	1.44	0.57
12	1.44	0.52
15	1.44	0.55
24	1.44	0.76
0.09	1.96	0.09
0.5	1.96	0.17
1	1.96	0.30
1.5	1.96	0.49
2	1.96	0.60
2.5	1.96	0.58
3	1.96	0.74
5	1.96	0.85
8	1.96	0.70
12	1.96	0.70
15	1.96	0.53
24	1.96	0.93
0.09	2.65	0.07
0.5	2.65	0.24
1	2.65	0.42
1.5	2.65	0.36
2	2.65	0.70
2.5	2.65	0.94
3	2.65	1.09
5	2.65	1.32
8	2.65	0.99
12	2.65	1.09
15	2.65	0.91
24	2.65	1.23
0.09	4.2	0.11
0.5	4.2	0.37
1	4.2	0.31
1.5	4.2	0.97
2	4.2	1.08
2.5	4.2	1.31
3	4.2	1.24

5	4.2	1.68
8	4.2	1.14
12	4.2	1.45
15	4.2	1.37
24	4.2	1.57
0.09	7.8	0.20
0.5	7.8	0.26
1	7.8	0.46
1.5	7.8	0.79
2	7.8	1.01
2.5	7.8	1.14
3	7.8	1.29
5	7.8	1.33
8	7.8	1.03
12	7.8	1.54
15	7.8	1.42
24	7.8	1.44

Table D.5.5. Dataset time -dependency HbA-AEH adduct of 5-HMF in WB.

T	$[5\text{-HMF}]_0$	[HbA-AEH adduct]
[hr]	[mM]	[mM]
0.5	0.5	0.20
1	0.5	0.24
1.5	0.5	0.18
2	0.5	0.20
4	0.5	0.09
0.5	1	0.15
1	1	0.43
1.5	1	0.40
2	1	0.15
4	1	0.14
8	1	0.14
0.5	2	0.39
1	2	0.54
1.5	2	0.75
2	2	0.33
4	2	0.29
8	2	0.26
10	2	0.26
12	2	0.29
14.1	2	0.34
0.1	3	0.21
0.5	3	0.61
1	3	0.81
1.5	3	0.98
2	3	0.50
4	3	0.39
8	3	0.37
14	3	0.40
0.5	5	0.68
1	5	1.04
1.5	5	1.17
2	5	0.77
4	5	0.81
4	5	0.77
6	5	1.19
8	5	0.85
14	5	0.90

VITA

Xiaomeng Xu was born on April 28, 1990 in Jinzhou, China and is a citizen of the People's Republic of China (PRC). She graduated from Shenyang Pharmaceutical University, Shenyang, Liaoning Province, China, with a Bachelor's degree in Pharmacy in 2013. Her Master's degree in Pharmaceutical Sciences with Specialization in Medicinal Chemistry was earned from the University of Pittsburgh (U PITT), Pittsburgh, PA in 2015. During the fall of 2016, she joined the Ph.D. program in Pharmaceutical Sciences at the Department of Pharmaceutics, Virginia Commonwealth University (VCU) School of Pharmacy, Richmond, VA, under the supervision of Dr. Jürgen Venitz, M.D., Ph.D.

During most of her tenure as a graduate student at VCU, Xiaomeng has been a Graduate Teaching Assistant (GTA) and conference coordinator in the Applied Pharmacokinetics course for Pharm.D. students. She has also contributed as a Graduate Research Assistant (GRA) to a project in drug discovery of novel sickle cell disease therapeutics. She has presented her research findings extramurally at annual meetings of the American Association of Pharmaceutical Scientists (AAPS), American College of Clinical Pharmacology (ACCP), and Virginia Drug Discovery Rx (VaDDRx). She also gave four formal departmental seminars and presented her research progress with three posters at the annual Fall Research Days within the School of Pharmacy, where one of her posters was selected for Podium Presentation at the 22nd Annual Pharmaceutical Sciences Research and Career Day in 2019.

Xiaomeng received the Jyotsan & Mavji Thakker Award in 2017 in recognition of demonstrated excellence in research by a first-year graduate student in VCU. She was inducted into the Rho Chi Pharmacy Honor Society as graduate student in 2018. She also received both a Rector and Rorrer Travel Award and a Phi Kappa Phi Graduate Student Award in 2019 for her continuous academic excellence and in research.

She served as secretary of the Graduate Student Association (GSA) in the Dept. of Pharmaceutics from 2017 to 2018, and a graduate student representative of the Rho Chi Pharmacy Honor Society from 2018 to 2019. She currently is an active member of AAPS, ACCP, ASCPT and has been serving as a volunteer, screening abstracts for the 2020 AAPS annual meeting.